ISSN 1520-295X

Design Recommendations for Perforated Steel Plate Shear Walls

by
Ronny Purba and Michel Bruneau

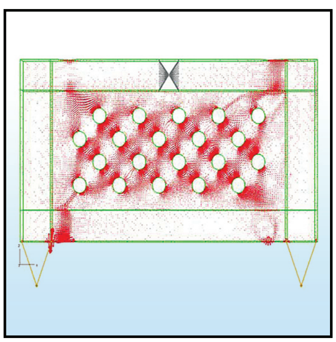
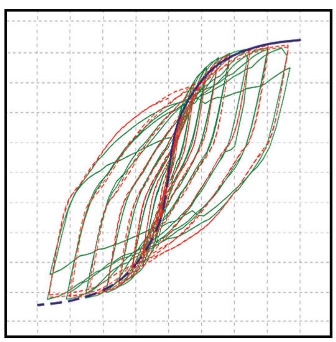
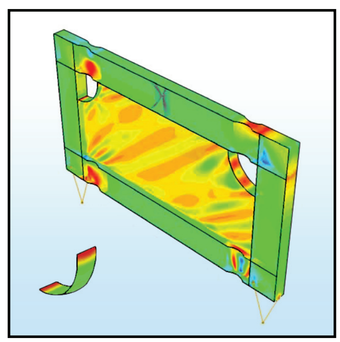
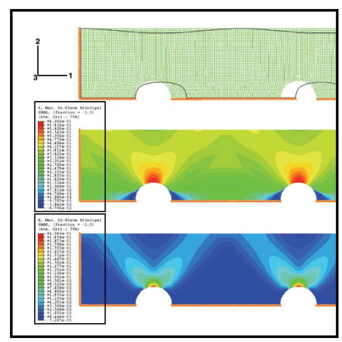

Technical Report MCEER-07-0011

June 18, 2007

This research was conducted at the University at Buffalo, State University of New York and was supported primarily by the Earthquake Engineering Research Centers Program of the National Science Foundation under award number EEC 9701471.

MCEER
EARTHQUAKE ENGINEERING TO EXTREME EVENTS

Design Recommendations for Perforated Steel Plate Shear Walls

by

Ronny Purba[1] and Michel Bruneau[2]

Publication Date: June 18, 2007
Submittal Date: August 28, 2006

Technical Report MCEER-07-0011

Task Number 9.2.2

NSF Master Contract Number EEC 9701471

1 Former Graduate Student, Department of Civil, Structural and Environmental Engineering, University at Buffalo, State University of New York
2 Professor, Department of Civil, Structural and Environmental Engineering, University at Buffalo, State University of New York

MCEER
University at Buffalo, The State University of New York
Red Jacket Quadrangle, Buffalo, NY 14261
Phone: (716) 645-3391; Fax (716) 645-3399
E-mail: *mceer@buffalo.edu*; WWW Site: *http://mceer.buffalo.edu*

Preface

The Multidisciplinary Center for Earthquake Engineering Research (MCEER) is a national center of excellence in advanced technology applications that is dedicated to the reduction of earthquake losses nationwide. Headquartered at the University at Buffalo, State University of New York, the Center was originally established by the National Science Foundation in 1986, as the National Center for Earthquake Engineering Research (NCEER).

Comprising a consortium of researchers from numerous disciplines and institutions throughout the United States, the Center's mission is to reduce earthquake losses through research and the application of advanced technologies that improve engineering, pre-earthquake planning and post-earthquake recovery strategies. Toward this end, the Center coordinates a nationwide program of multidisciplinary team research, education and outreach activities.

MCEER's research is conducted under the sponsorship of two major federal agencies: the National Science Foundation (NSF) and the Federal Highway Administration (FHWA), and the State of New York. Significant support is derived from the Federal Emergency Management Agency (FEMA), other state governments, academic institutions, foreign governments and private industry.

MCEER's NSF-sponsored research objectives are twofold: to increase resilience by developing seismic evaluation and rehabilitation strategies for the post-disaster facilities and systems (hospitals, electrical and water lifelines, and bridges and highways) that society expects to be operational following an earthquake; and to further enhance resilience by developing improved emergency management capabilities to ensure an effective response and recovery following the earthquake (see the figure below).

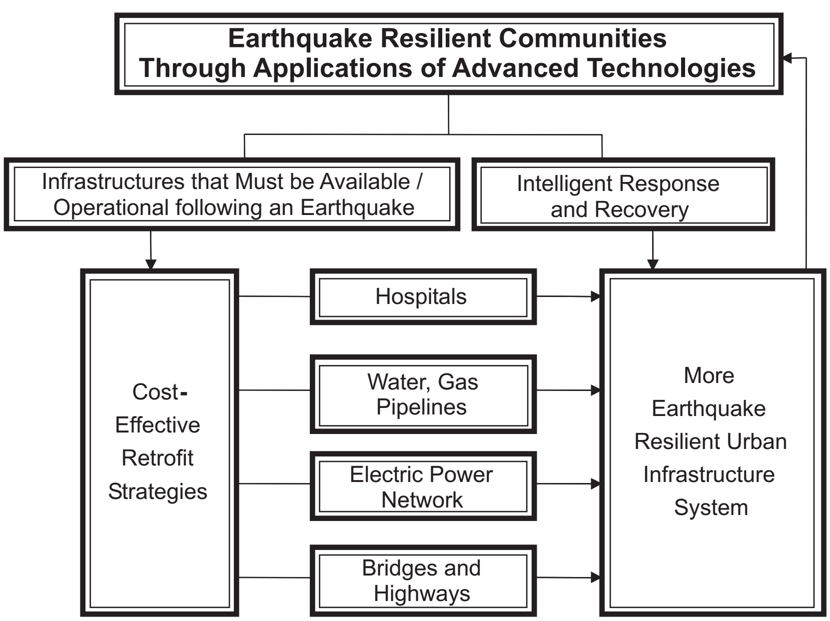

A cross-program activity focuses on the establishment of an effective experimental and analytical network to facilitate the exchange of information between researchers located in various institutions across the country. These are complemented by, and integrated with, other MCEER activities in education, outreach, technology transfer, and industry partnerships.

This report presents the results of finite element analytical studies, using monotonic pushover analysis, to investigate the behavior of unstiffened thin steel plate shear walls (SPSW) with openings on the infill plate. Two infill plate options, the perforated and the cutout corner SPSW, are investigated. First, a series of individual perforated strips were analyzed to develop a fundamental understanding of the behavior of a complete perforated SPSW. After generating a large number of data points and using fine mesh models, "smooth" curves of total uniform strip elongation versus perforation ratio were obtained. Finite element models of complete perforated SPSW were developed to verify the individual strip model results and to evaluate the effects of different infill thicknesses, perforation diameters, and material idealizations. Two finite element models of cutout corner SPSW were then developed to study the effect of a relatively thick fish plate installed perpendicularly to the flat-plate reinforcement. The effects were examined in terms of global effects, such as frame deformation and shear strength of the systems, as well as local effects adjacent to the cutout corners, such as local buckling, stress distribution, and forces applied by the cutout edge reinforcement to the beam and columns. Recommendations and considerations are proposed to help design perforated and cutout corner SPSW. This research extends work reported in "Steel Plate Shear Walls for Seismic Design and Retrofit of Building Structures" by D. Vian and M. Bruneau, MCEER-05-0010. All analyses were performed using the finite element software ABAQUS/Standard.

ABSTRACT

An analytical study using the finite element program ABAQUS/Standard was performed to investigate the behavior of unstiffened thin steel plate shear walls (SPSW) having openings on the infill plate under monotonic pushover displacement. To accommodate the passage of utilities, two designs proposed by Vian (2005), namely the perforated infill plate and the cutout corner SPSW, are revisited to investigate and resolve some concerns reported by Vian (2005).

As a sub-element that drives the behavior of the perforated infill plate of the type considered by Vian (2005), a series of individual perforated strips 2000 mm by 400 mm with 4 perforations along the strip length and perforation diameters *D* from 10 mm to 300 mm are first analyzed to develop a fundamental understanding of the behavior of complete perforated SPSW. After generating a large number of data points and using fine mesh models (maximum mesh size of 5 x 5 mm), “smooth” curves of total uniform strip elongation versus perforation ratio are obtained, improving those previously developed by Vian (2005). A series of 4000 mm by 2000 mm one-story perforated SPSW are then considered, with variation in perforation diameter, infill plate thickness, material properties idealization, and element definition. It is found that the results from the individual perforated strip analysis can accurately predict the behavior of complete perforated SPSW provided the holes diameter is less than 60% of the strip width ($D/S_{diag} \leq 0.6$). It is found that no interaction exists between adjacent strips that could affect the stress distribution within an individual strip, i.e., each strip in a SPSW behaves as an independent strip. Shear strength of the infill plate in a perforated SPSW having multiple circular perforations regularly spaced throughout the infill plate can be calculated by reducing the panel shear strength in a solid panel SPSW by a factor $\left(1-\alpha \cdot D/S_{diag}\right)$, where α is a proposed correction factor equal to 0.70.

Two cutout corner SPSW models, having flat-plate and T-section reinforcement along the cutout edges, are investigated. The global behaviors of the two models considered are not significantly different. Some local effects however are observed adjacent to the cutout corner. The flat-plate (with a minimum fish plate) is considered adequate to reinforce the cutout edges. The “corner-brace” action on the boundary frame could induce high tension/compression forces from the cutout edges reinforcement to the beams and columns, and these may require web stiffeners to prevent web crippling, web buckling, and flange bending in the boundary frame.

ACKNOWLEDGEMENTS

The financial support of the Technological and Professional Skills Development Sector Project (TPSDP) under ADB Loan Number 1792 – INO to the University of Bandar Lampung (UBL), Indonesia is gratefully appreciated.

Analytical work in this study was performed at the Center for Computational Research at the University at Buffalo, the State University of New York. This work was supported by the Multidisciplinary Center for Earthquake Engineering Research (MCEER) and the National Science Foundation (NSF).

TABLE OF CONTENTS

TABLE OF CONTENTS (cont'd)

TABLE OF CONTENTS (cont'd)

LIST OF FIGURES

LIST OF FIGURES (cont'd)

LIST OF FIGURES (cont'd)

LIST OF FIGURES (cont'd)

LIST OF FIGURES (cont'd)

LIST OF FIGURES (cont'd)

FIGURE **TITLE** **PAGE**

LIST OF FIGURES (cont'd)

LIST OF TABLES

NOTATIONS

A_b	gross cross-sectional area of beam
A_c	gross cross-sectional area of column
A_g	gross area of tension member (AISC notation)
A_n	net area of tension member (AISC notation)
b	panel width (Section 2.6)
d	panel depth (Section 2.6)
D	perforation diameter
E, E_s	Young's Modulus of steel
F_u	ultimate tensile strength of steel
F_y	yield stress of steel
h	panel thickness (Section 2.6)
h_{hinge}	height between the centerlines of floor hinge and bottom beam
H	frame story height between beam centerlines
H_{panel}	height of infill panel between beam flanges
I_c	moment of inertia of column
K_{panel}	solid (unperforated) infill plate stiffness
K_{perf}	perforated infill panel stiffness
L	frame bay width between column centerlines; length of typical perforated strip (Section 3)
L_{arch}	length of arch plate (Section 5)
M_p	plastic moment
N_r	number of perforations along the strips; number of rows of perforations
S_{diag}	strip diagonal width; spacing between perforations
t_p	panel thickness
u_x,u_y,u_z	translation in global X, Y, Z direction
V_{design}	design shear strength
V_{yf}	bare frame shear strength
V_{yp}	solid (unperforated) infill plate shear strength
$V_{yp.perf}$	perforated infill plate shear strength

W_{panel}	width of infill panel between column flanges
α	tension field inclination angle; correction factor for calculating shear strength of infill plate having multiple perforations (Section 4.8.3)
δ	axial displacement of quadrant model of typical perforated strip (Section 3); diagonal displacement of arch plate (Section 5)
Δx_i	initial imperfection on infill plate (Section 4.2.4)
ε_{max}	maximum principal strain at monitored location; monitored strain
ε_{nom}	nominal strain (engineering strain)
$\varepsilon_{\ln}^{pl}$	logarithmic plastic strain
ε_{un}	total uniform elongation of a perforated strip in tension
ε_y	yield strain of steel
ϕ_i	the i^{th} mode shape
γ_T	total interstory drift between column inflection points
η	ratio of actual-to-predicted shear strength (Section 4.8)
ν	Poisson's ratio
θ	orientation angle of SPSW perforations in infill panel
$\theta_x, \theta_y, \theta_z$	rotation in global X, Y, Z direction
σ_0	yield stress at 0.2% offset
σ_{nom}	nominal stress (engineering stress)
σ_y	yield stress (Mohr's circle)
σ_{true}	"true" stress (Cauchy stress)
τ_y	yield shear stress (Mohr's circle)
ω_i	scale factor of initial imperfection (Section 4.2.4)

ABBREVIATIONS

AISC	American Institute of Steel Construction
ASTM	American Society for Testing and Materials Standard
ATLSS	Advanced Technology for Large Structural Systems
DEF	Dissipated Energy Fraction
FEM	Finite Element Model; Finite Element Method
FLTB	Flexible Beam Laterally Braced
LTB	Lateral Torsional Buckling
LYS	Low Yield Strength
MCEER	Multidisciplinary Center for Earthquake Engineering Research
RB	Rigid Beam
RBS	Reduced Beam Section
RF	Rigid Floor
SPSW	Steel Plate Shear Walls
TFA	Tension Field Action

SECTION 1

INTRODUCTION

1.1 General

Steel plate shear walls (SPSW) have been widely used as a lateral resisting force system since first developed in early 1970s. According to Thorburn *et al*. (1983), the Nippon Steel Building in Tokyo, Japan was the first building designed using this structural system to resist lateral loads. This 20-story office building was completed in 1970. Since then the applications of SPSW as part of the structural lateral resisting system covered a wide variety of structure, ranging from low-rise hospital to high-rise residential building, from building in low seismicity zones (high wind loads) to high seismicity zones, and from new building projects to seismic retrofit project. A brief summary of these applications can be found in the original work of Thorburn *et al*. (1983) and Astaneh-Asl (2001) for buildings constructed in Japan and in United States.

The design philosophy of SPSW prior to the 1980s prevented shear buckling of the infill plate by providing thick plate and adding heavily stiffeners on the wall to ensure shear yielding occurred. After Thorburn *et al.* (1983), the design philosophy shifted to the use of unstiffened thin plates and considered the post-buckling strength of the infill plate in calculating the capacity of SPSW. This design philosophy has been widely adopted by many researchers since then (e.g., Tromposch and Kulak 1987; Caccese *et al*. 1993; Driver *et al.* 1997; Behbahanifard *et al*. 2003; Berman and Bruneau 2003 and 2005; Shishkin 2005; etc.). These researchers considered several modeling procedures to analyze SPSW, namely the strip model, the equivalent truss model, finite element analysis, plastic analysis, and the modified strip model. The researchers also reported a good correlation between analytical models and experimental results.

The advantage of SPSW systems is in the significant increase of stiffness and strength provided to buildings compared to other lateral force resisting systems. Steel plate shear walls are also lighter and more ductile than reinforced concrete shear walls, applicable for new design or retrofit project, and relatively easy to install (Astaneh-Asl 2001). In addition, SPSW are more economically attractive compared to reinforced concrete shear walls (Timler *et al*. 1998).

In some SPSW applications, the available steel for infill plate material might be thicker or stronger than required by design. This will induce relatively large forces to the surrounding frames and consequently will increase the sizes of horizontal and vertical members. Several solutions to alleviate this concern were recently proposed by changing properties of the infill plate via using light-gauge cold-rolled and Low Yield Strength (LYS) steel (Berman and Bruneau 2003a, 2005; Vian 2005), introducing vertical slits (Hitaka and Matsui 2003), or introducing multiple regularly spaced perforations (Vian 2005).

The perforated SPSW recommended by Vian (2005) is unique as the need of utility systems to pass-through the infill plate can be accommodated. Vian (2005) also proposed cutout corner SPSW, another option to accommodate passage of utilities through the infill plate without significant reduction in the strength and stiffness of the system. These new types of design improve the applicability of SPSW systems over a wider range of structures.

1.2 Statement of the Problem

Vian (2005) conducted analytical and experimental work on three SPSW specimens: solid, perforated, and cutout corner SPSW; these are briefly discussed in following section. LYS steel was used for all infill plate specimens. The analytical model of perforated SPSW was used to consider several perforation diameters using steel material typically specified in North American construction projects, and the results were compared to those obtained from the simpler perforated strip models. From these analyses, the elongation predicted by finite element model of an individual perforated strip and full SPSW, for a monitored maximum strain assumed to develop close to the perforation edges, was significantly different. This significant difference could not be explained at that time. Some jaggedness in the curves of total strip elongation versus perforation ratio calculated using the individual perforated strip model were also observed. For the cutout corner SPSW, the thick fish plate added to the “arching” flat-plate reinforcement along the cutout edges (to allow connection of the infill plate to the boundary frame) might modify behavior of the SPSW from that predicted by the idealized model. How the fish plate on the flat-plate reinforcement affect the global and local behavior of SPSW remains to be determined. Therefore, further research is needed to investigate these concerns and to propose technical solutions as appropriate.

1.3 Scope and Objectives

This research is limited to the investigation of the behavior of unstiffened thin SPSW with openings on the infill plate under monotonic pushover displacement. All analyses are performed using the finite element software ABAQUS/Standard. The two infill plate opening options recommended by Vian (2005), namely the perforated and the cutout corner SPSW, are revisited to investigate and resolve the above concerns.

Finite element models of individual perforated strip are developed in this research. This study is intended to provide an understanding of the behavior of individual perforated strips as a fundamental building block in understanding the behavior of complete perforated SPSW. Mesh refinement are performed and various meshing algorithm are considered to investigate their influence on the stress-strain distribution throughout the strip sections. A relatively large number of data points are considered to obtain smooth curves of total strip elongation versus perforation ratio. Several variations of the finite element model are developed to evaluate the effects of different boundary conditions and material idealizations.

Finite element models of complete perforated SPSW are developed to verify the appropriateness and accuracy of the individual strip model results and to investigate why prior results from panel analysis did not support the predictions from individual strip model analysis. Several variations of the complete perforated SPSW model are developed to evaluate the effects of different infill thicknesses, perforation diameters, and material idealizations. The equation proposed by previous researchers to approximate the strength of a perforated panel is re-assessed to verify its applicability for multiple perforation panels.

Two finite element models of cutout corner SPSW are developed to study the effect of a relatively thick fish plate installed perpendicularly to the flat-plate reinforcement. The effects are examined in terms of global effects, such as frame deformation and shear strength of the systems, as well as in terms of local effects adjacent to the cutout corners, such as local buckling, stress distribution, and forces applied by the cutout edge reinforcement to the beam and columns. From these analytical studies, some additional recommendations and considerations are proposed to help design perforated and cutout corner SPSW as an improvement to the recommendations previously reported by Vian (2005).

1.4 Outline of Report

Section 2 presents a brief review of previous research in SPSW, emphasizing modeling studies of this structural system. Research developing the *Strip Model* to represent the behavior of unstiffened thin steel plate shear walls is presented first, followed by research that used of finite element models to design test specimens and to verify experimental results. Research on perforated SPSW is also discussed.

Work reported in Section 3 describes the investigation on the behavior of individual perforated strips as sub-elements of perforated SPSW using the finite element software ABAQUS/Standard. The finite element modeling process, as well as work to evaluate the accuracy and convergence of the results, is first presented. The resulting finite element model is then modified to consider various perforation diameters, boundary conditions, and material idealizations.

Section 4 describes the finite element analysis of full SPSW, using more advanced and complete models to verify the appropriateness and accuracy of the individual strip model results in Section 3. Specific finite element options in ABAQUS/Standard used to capture the real panel behaviors are first described. Three different finite element models are then investigated. Models including variation in perforation diameter, infill plate thickness, and material idealization are considered, and significance of the corresponding results are assessed. The applicability of the equation proposed by previous researchers to approximate the strength of a perforated panel is re-assessed. Some design recommendations and consideration are proposed to help design perforated SPSW.

Section 5 describes additional observations on cutout corner SPSW. Two types of cutout corner SPSW are developed and investigated. Comparison on the two models analyzed is presented in terms of global effects as well as in terms of local effects adjacent to the cutout corners. Some design considerations are proposed to help design cutout corner SPSW. Finally, summary, conclusions, and recommendations for future research are presented in Section 6.

SECTION 2

PREVIOUS RESEARCH ON STEEL PLATE SHEAR WALLS

2.1 General

Numerous experimental and analytical studies have been conducted since the early 1970s to investigate the behavior of SPSW and to properly design SPSW as a lateral load resisting system. This section summarizes some of this previous research on unstiffened thin SPSW. Emphasis is placed on analytical work while some relevant experimental investigations are also reviewed. Research on the development of the *Strip Model* to represent the behavior of unstiffened thin steel plate shear walls is presented first, followed by research on using finite element models both to design test specimens and to verify experimental results. Finally, research on perforated SPSW is presented. The latter type of SPSW has gained attention in recent years from researchers (e.g., Roberts and Sabouri-Ghomi 1992 and Vian 2005) as demands for utility access through the infill plate has been expressed.

2.2 Thorburn, Kulak, and Montgomery (1983)

The first study on unstiffened thin SPSW was performed by Thorburn *et al.* (1983). The researchers introduced two analytical models to represent the behavior of unstiffened thin SPSW, namely the *Strip Model* and the *Equivalent Truss Model*. Those models considered the postbuckling strength of SPSW, adopting the original work on plate girder webs subjected to shear studied earlier by Basler (1961) and the theory of diagonal tension field action by Wagner (1931), given that the wall infill plate was allowed to buckle in shear and form a diagonal tension field to resist the applied lateral loads.

In the *Strip Model*, the infill plate was replaced by a series of tension strips (equal width), pin-ended, inclined in the direction of the tension field. Figure 2-1 illustrates the strip model used to represent any typical story and the inclination angle of the tension field α was:

$$\tan^4 \alpha = \left[\frac{1 + \dfrac{L \cdot t_p}{2 \cdot A_c}}{1 + \dfrac{H \cdot t_p}{A_b}} \right] \tag{2-1}$$

where L is the frame bay width, H is the frame story height, t_p is the panel thickness, and A_b and A_c are gross cross-sectional areas of the story beam and column, respectively.

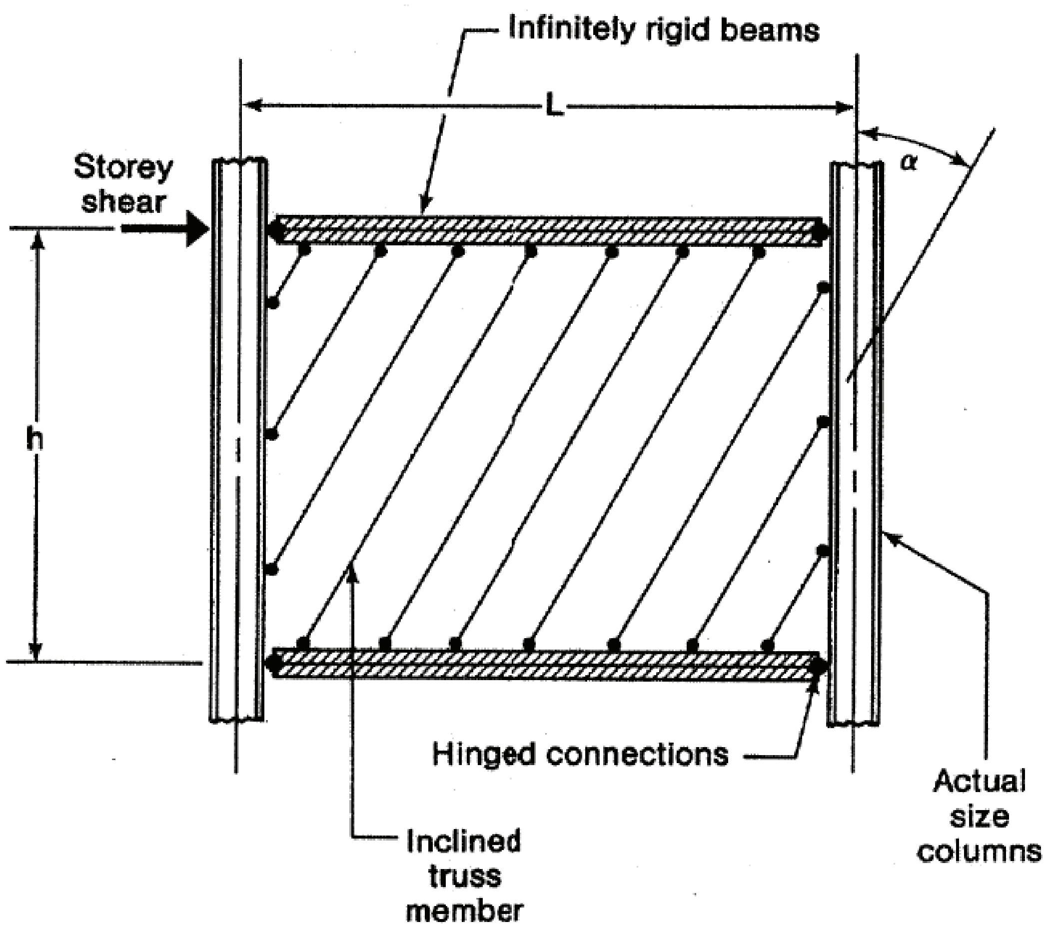

FIGURE 2-1 Schematic of SPSW Strip Model (Thorburn *et al.* 1983)

The researchers conducted analytical studies to determine the number of strips per panel that would adequately represent the infill plate behavior, and concluded that 10 strips per panel would be sufficient to represent the infill plate behavior for all shear walls investigated.

The *Equivalent Truss Model* is a simplification of the strip model by changing multiple strips into an equivalent single diagonal truss element having the same story stiffness. This model is practical to rapidly determine the story stiffness but does not provide information needed for the design of the boundary frame. A more complete review of this method can be found in the original work by Thorburn *et al.* (1983).

The researchers also conducted parametric studies to assess the influence of infill plate thickness, panel height, panel width, and column stiffness on the strength and stiffness of the infill plate. The parametric studies showed that the four parameters are inter-related and influence the effectiveness of the resulting tension zone.

2.3 Timler and Kulak (1983)

Timler and Kulak (1983) tested a single story, full scale, thin SPSW specimen to verify the analytical work of Thorburn (1983). The test specimen, shown in figure 2-2, consisted of two SPSW panels of 3750 mm bay wide by 2500 mm story high and 5 mm thick and vertically oriented beams W460X144 (W18X97) and horizontally oriented columns W310X129 (W12X87) connected by pinned joints at the four extreme corners and continuous joints at the middle intersections. A 6 mm thick “fish plate” was used to connect a 5 mm thick infill plate to the boundary frame. The specimen was loaded by quasi-static cyclic loading (cycled three times) until it reached the maximum permissible serviceability drift limit $h_s/400$, or 6.25 mm, followed by monotonic loading to failure.

The test specimen was also analyzed using the strip model technique and good correlation between predicted and measured member strains and deflections were reported. Based on this work, Timler and Kulak (1983) revised (2-1) to include the effects of column flexibility as:

$$\tan^4 \alpha = \left[\frac{1 + \dfrac{L \cdot t_p}{2 \cdot A_c}}{1 + H \cdot t_p \cdot \left(\dfrac{1}{A_b} + \dfrac{H^3}{360 \cdot I_c \cdot L} \right)} \right] \tag{2-2}$$

where I_c is the moment inertia of boundary column, and the remaining terms have been defined previously.

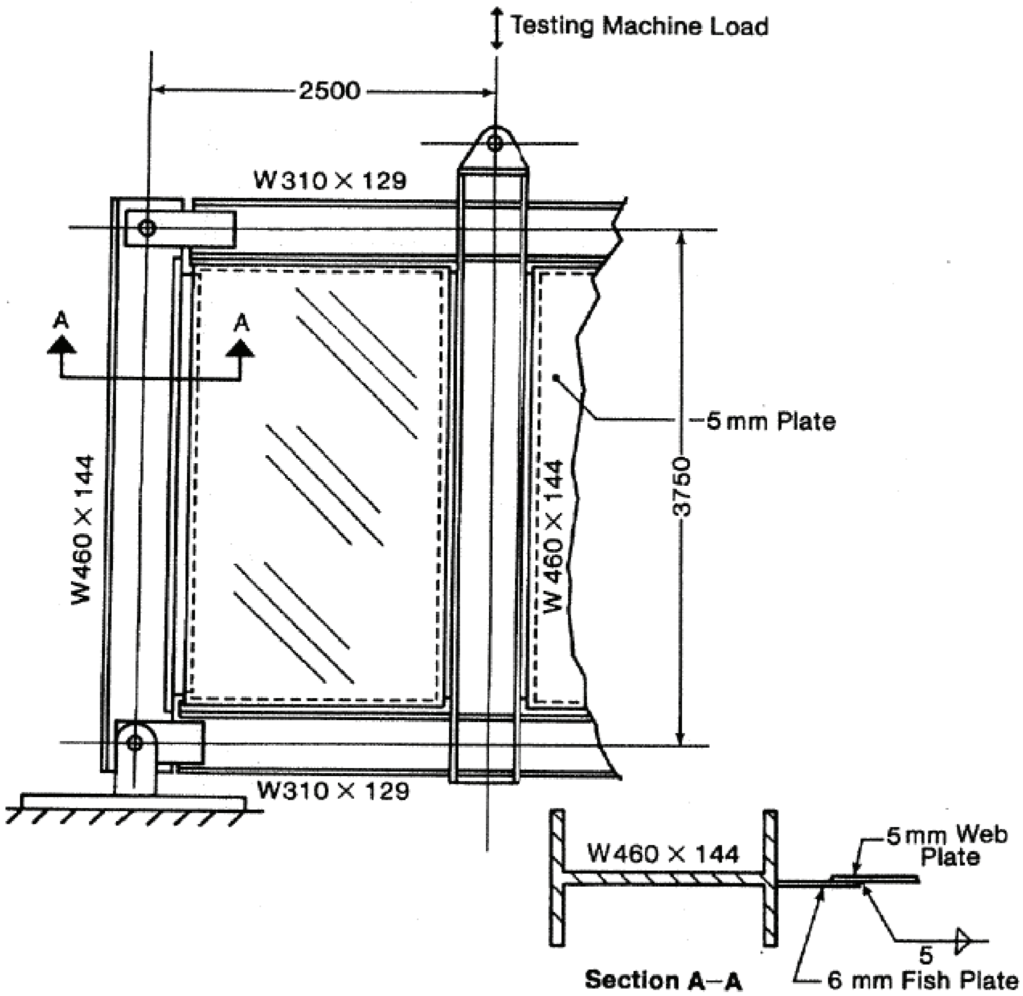

FIGURE 2-2 Schematic of Test Specimen (Timler and Kulak 1983)

In another report, Tromposch and Kulak (1987) tested a large scale SPSW somewhat similar to that tested by Timler and Kulak (1983). The researchers also used the strip model to predict the test results, and reported that the strip model was adequate in predicting the capacity of the wall and in predicting the envelope of cyclic response.

2.4 Driver, Kulak, Kennedy, and Elwi (1997, 1998a, and 1998b)

Driver *et al.* (1997, 1998a) conducted quasi-static cyclic testing on a large scale, four-story, single bay SPSW specimen with unstiffened panels, and moment-resisting beam-to-column connections. The test specimen is shown in figure 2-3, with a first story height of 1.93 m and a typical story of 1.83 m high for the remaining stories, and a bay width of 3.05 m. A relatively deep and stiff beam W530X118 (W21X55) was used at the roof level to anchor the tension field forces that would develop, while a smaller beam W310X60 (W12X40) was used for the intermediate beams. The entire four stories used W310X118 (W12X79) columns. For the infill plate, 4.8 mm and 3.4 mm plates were used for the first two stories and the next two stories, respectively. A continuous "fish plate" of 100 mm by 6 mm was added to connect the infill plates to the boundary members.

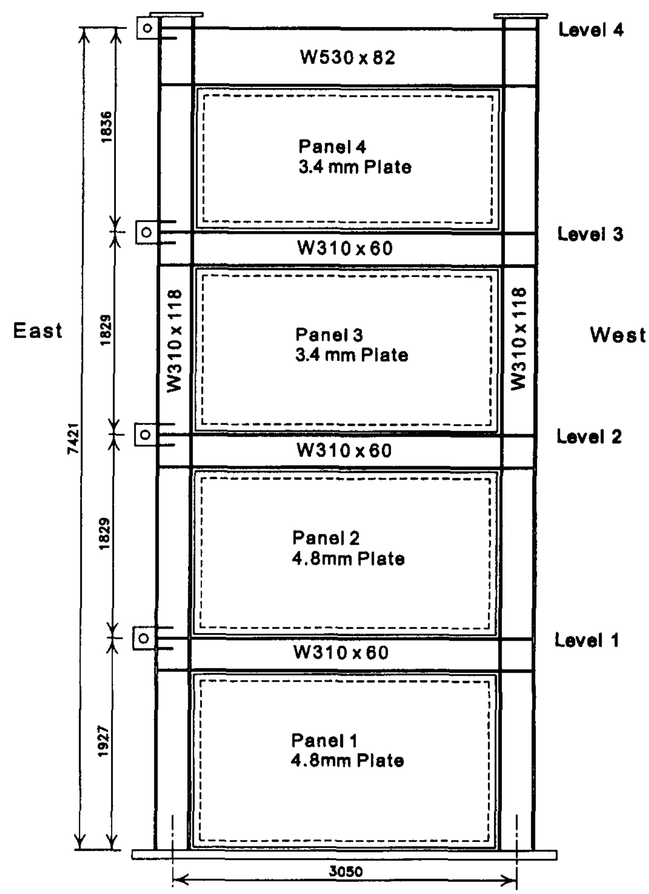

FIGURE 2-3 Schematic of Test Specimen – North Elevation (Driver *et al.* 1998a)

Driver *et al*. (1997, 1998b) also investigated the behavior of the test specimen using the finite element software ABAQUS (1994 edition). The eight-node quadratic shell element (S8R5) was used to model the infill plates with a 6×9 element mesh for the lowest panel (Panel 1), a 4×9 elements mesh for the uppermost panel (Panel 4), and a 5×9 elements mesh for the remaining two panels (Panel 2 and 3). The three-node quadratic beam element (B32) was used to model the beams and columns with 13 integration points (five in each flange and web, two common locations at the intersections) throughout the I-shaped cross section. The column element nodes were located eccentric to the centroid of the cross-section such that each node directly connected to adjacent node in the infill plate. Rigid outrigger elements were used at the tops of the columns to apply the concentric vertical loads. The beam element nodes were located at the center of the cross section, and to ensure deformation compatibility between the beams and infill plates, rigid outrigger elements by a distance equal to one-half of the beam depth were assigned at each node. The "fish plate", used in the test specimen to connect the infill plate to the surrounding frame, was not considered in the finite element model. Instead, the infill plates were connected directly to the beams and columns. The effects of this assumption to the overall behavior of steel plate shear walls were found to be small. Horizontal loads and constant vertical loads were applied to the model to replicate the test specimen load history. An elasto-perfectly plastic bilinear constitutive stress-strain relationship was applied to represent the type of steel used, with E_s = 200.000 MPa and F_y = 300 MPa. Initial imperfections of 10 mm based on the first buckling mode of the plate and residual stresses were also incorporated in the finite element model. The finite element model was restrained against out-of-plane movement at six nodes at the center of beam-to-column joints and fixed boundary conditions were applied to all the nodes along the lower edge of the model. The deformed shape of the SPSW model when loaded to a base shear of approximately 2200 kN is shown in figure 2-4.

Figure 2-5 compares the story shear versus interstory displacement of the experimental and the monotonic finite element model results for Panel 1. A good agreement between the two was observed up to a story shear of about 400 kN (one-eight of the maximum value attained). However, at higher levels, some discrepancy was observed due to the geometric nonlinearity effects, which were not taken into account in the finite element model, and the cyclic loading applied to the tested specimen that soften the structure. The finite element model overestimated

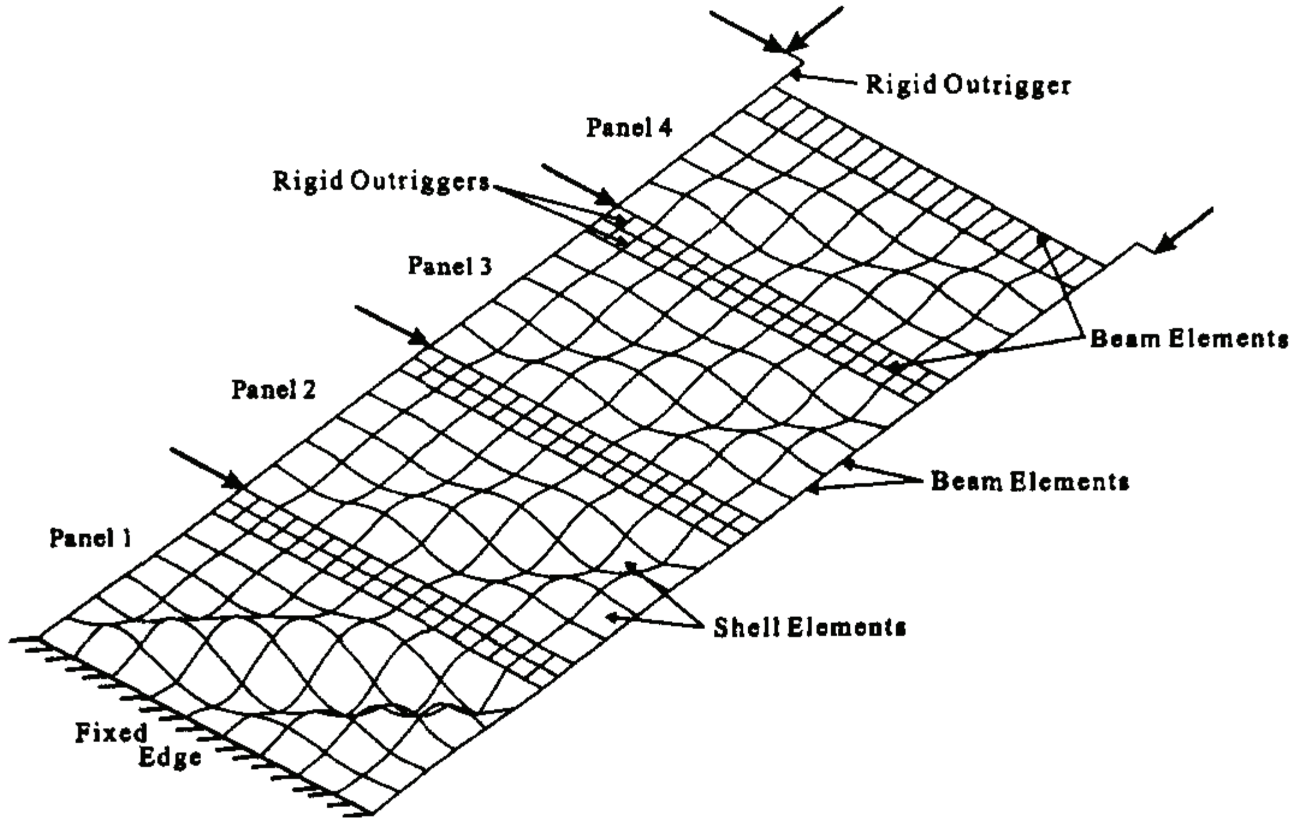

FIGURE 2-4 Finite Element Model of Test Specimen – Deformation Scale Factor = 5 (Driver *et al.* 1998b)

the stiffness of the specimen. In addition, the researchers also extended the monotonic finite element analysis by including geometric nonlinearity into the model, however, convergence of result was hard to achieve at higher levels and the finite element model accurately predicted the experimental response only at the lower levels. Base on these accurate results, it was recommended that geometric non-linearity be included, whenever feasible, in the finite element models of SPSW.

The researchers also performed cyclic analysis using the finite element model. Even though has recommended to include geometric non-linearity in the model, to avoid instability as previously stated, geometric non-linearity was not modeled in this instance. Figure 2-6 compares the hysteresis curves of experimental and cyclic finite element model results for Panel 1. Pinching on

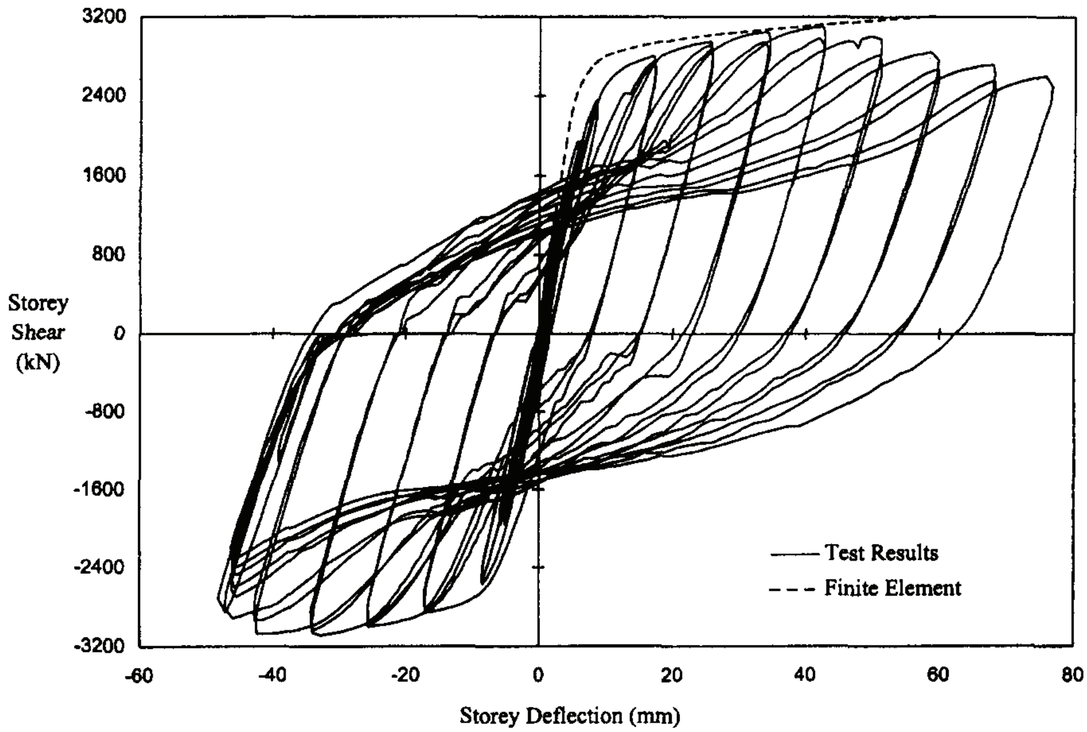

FIGURE 2-5 Comparison of Experimental and Monotonic Finite Element Model Results for Panel 1 (Driver *et al.* 1998b)

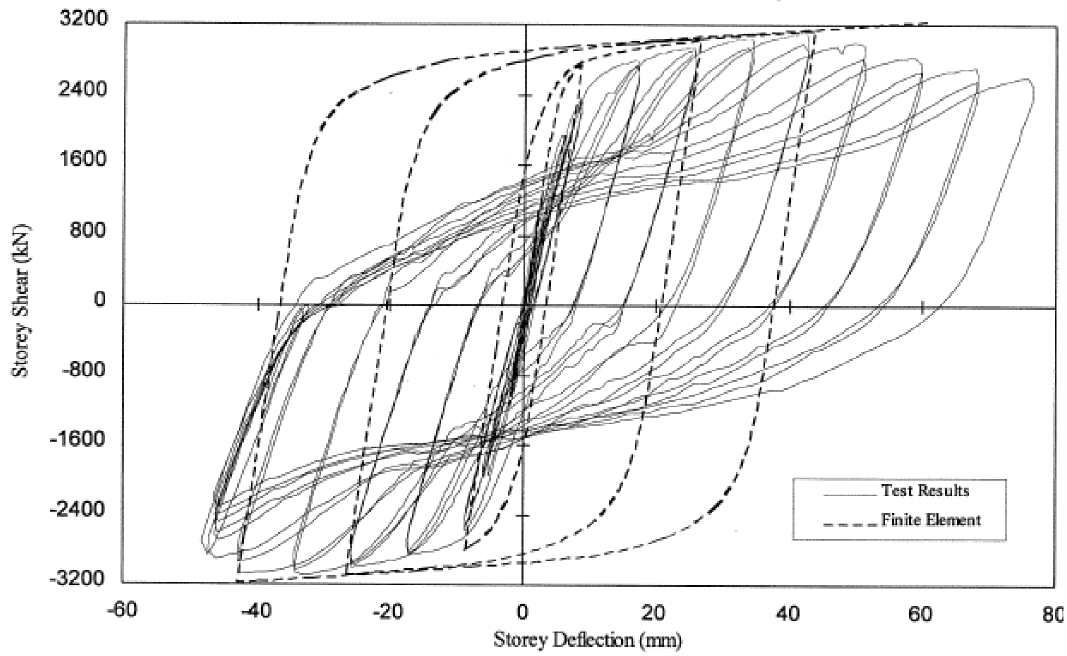

FIGURE 2-6 Comparison of Experimental and Finite Element Hysteresis Results for Panel 1 (Driver *et al.* 1997)

the experimental hysteresis curve is not duplicated by the finite element hysteresis curve. This is likely because the second order effects have been neglected in the finite element model.

Modeling the SPSW using the strip model was also investigated by the researchers, adopting the method presented earlier by Thorburn *et al.* (1983). The plane-frame strip model of the tested specimen is plotted in figure 2-7 where each infill plate is modeled using 10 strips at the calculated tension field inclination angle α. S-FRAME, a commercial three-dimension structural analysis program, was used to perform the analysis. The researchers reported that a tension field inclination angle of 45° generally can be used in the strip model. The strip model captured well the envelope of the cyclic test curves results as shown in figure 2-8, but it underestimated the initial stiffness of the specimen.

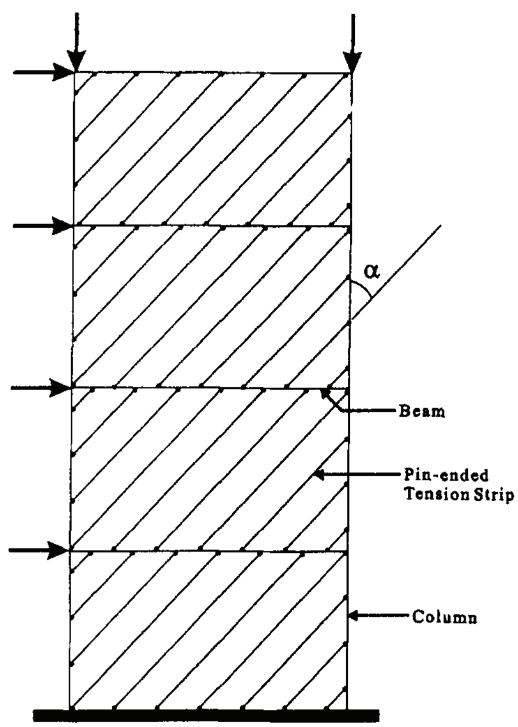

FIGURE 2-7 Plane-Frame Strip Model of Test Specimen (Driver *et al.* 1998b)

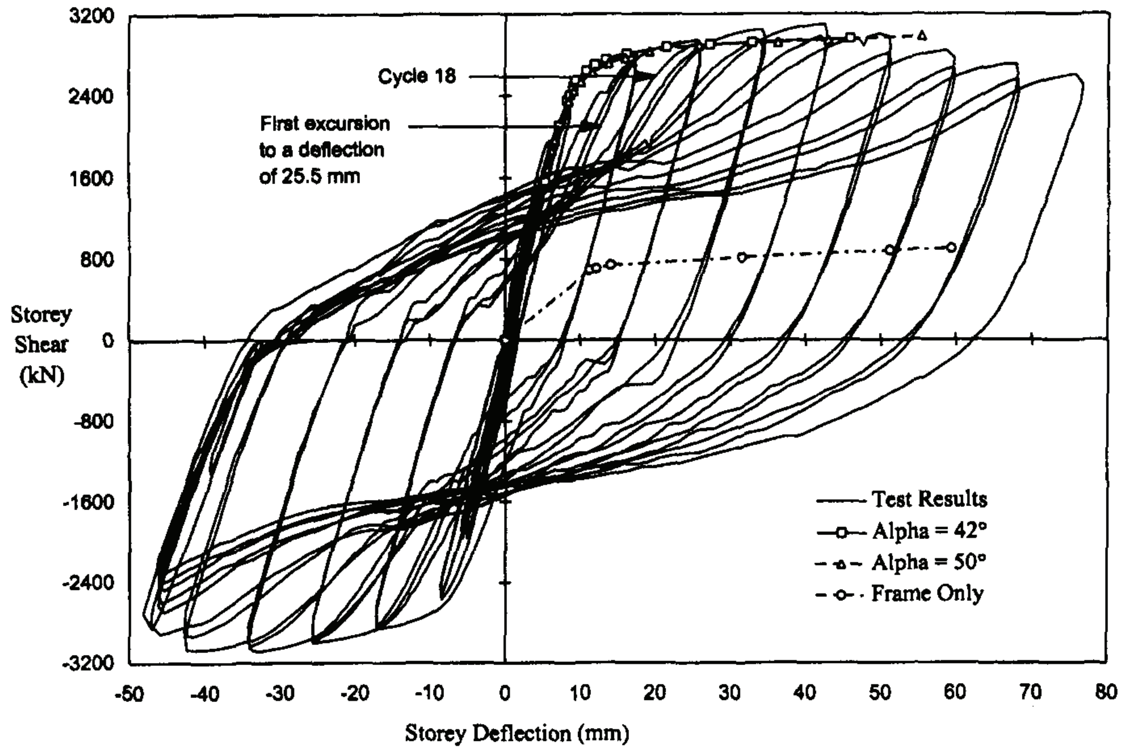

FIGURE 2-8 Comparison of Strip Model Analysis with Experimental Results for Panel 1 (Driver *et al.* 1998b)

2.5 Behbahanifard, Grondin, and Elwi (2003)

Behbahanifard *et al.* (2003) investigated a large-scale three-story unstiffened SPSW specimen both experimentally and analytically. A specimen was tested under lateral quasi-static cyclic loading in the presence of gravity loads. The test specimen was flame cut from the four-story SPSW tested by Driver *et al.* (1997) plotted in figure 2-3, and only the upper three stories were taken. A nonlinear finite element model was developed to accurately simulate the monotonic and cyclic behaviors of the test specimen.

Several changes were made to the finite element model previously developed by Driver *et al.* (1997). The four-node shell element with reduced integration (S4R element in ABAQUS 2001) was used to model all the components of the SPSW specimen, including the beams and the columns. Residual stresses and plastic deformations from the previous test were not considered in the finite element model due to their complexity. Based on Driver *et al.* (1997) recommendations, both material and geometric nonlinearity were considered in the analysis. The modified *Kinematic Hardening* material definition was used to define the inelastic (hardening) behavior of the type of steel used, with E_s = 200.000 MPa and F_y = 200 MPa. Out-of-plane movement was restrained at several nodes as shown in figure 2-9 while all the nodes along the lower edge of the model remained fixed to simulate attachment of the test specimen to the rigid base plate. Initial imperfections of 10 mm based on the first buckling mode of the plate were again used. The initial imperfections shape used in the finite element model is plotted in figure 2-10.

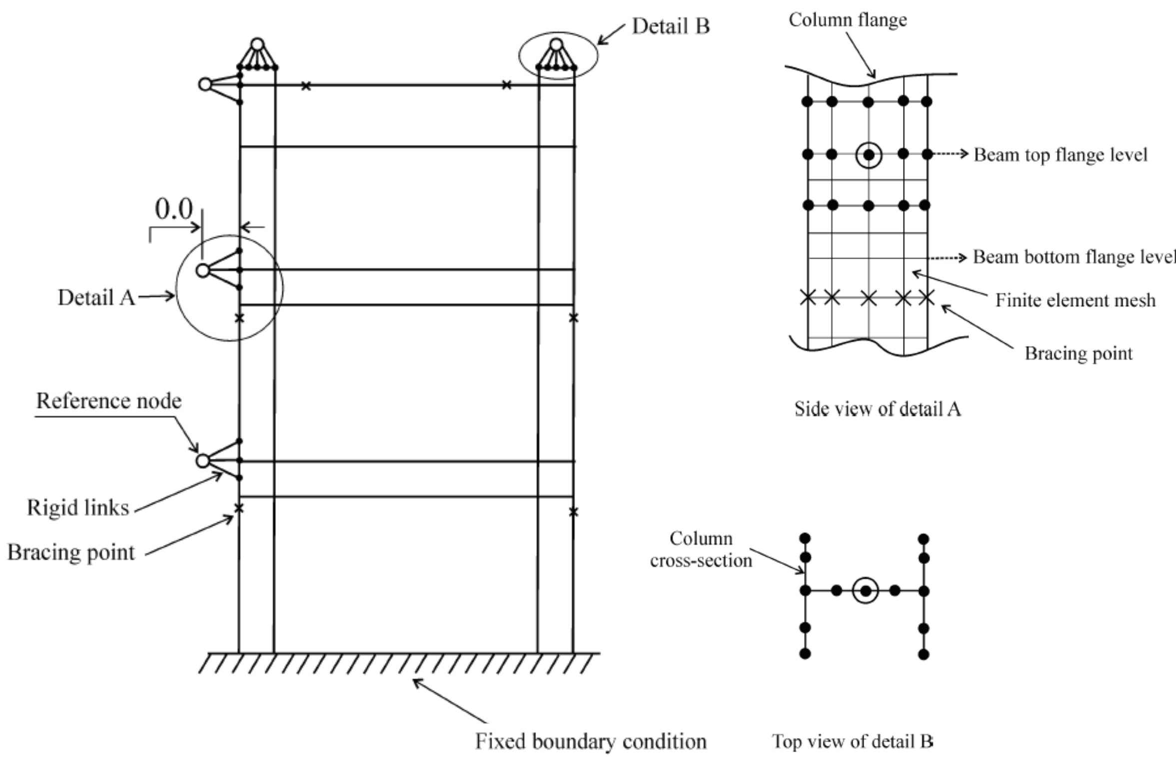

FIGURE 2-9 Boundary Conditions for the Finite Element Model (Behbahanifard *et al.* 2003)

The researchers reported that ABAQUS/Explicit (originally developed to analyze high-speed dynamic events) can be used for quasi-static problems that include complex post-buckling behavior, highly nonlinearities, and material degradation and failure. They also reported that convergence (a serious problem as a result of local buckling in the infill plate due to tension field development) in the finite element model was easier and quicker to achieve in ABAQUS/Explicit

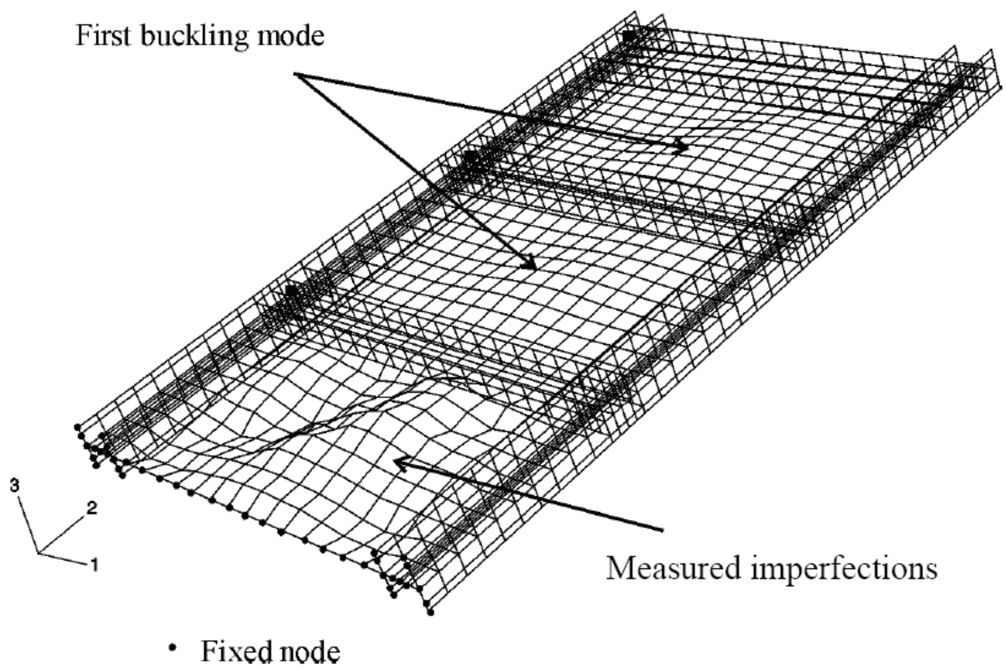

FIGURE 2-10 Imperfection Shape in Finite Element Model – Deformation Scale Factor = 5 (Behbahanifard *et al.* 2003)

(using the central difference method, no iteration involved), compared to the severe convergence difficulties experienced in ABAQUS/Standard (using Newton-Raphson iterative method). To obtain convergence, load increments of less than 10^{-5} were applied to the finite element model.

The finite element model described above was validated using the experimental results for both the monotonic (pushover) and cyclic loadings. The finite element model matched the elastic stiffness of shear wall in all stories. However after significant yielding, the finite element model underestimated the strength of the SPSW by 12% for the lowest panel (Panel 1) shown in figure 2-11. This discrepancy was attributed to previous plastic deformations not accounted for the finite element model. A good agreement between the experimental and the finite element hysteresis results was observed. Figure 2-12 shows, for the Panel 1, that the pinching of the hysteresis curves was captured reasonably well by the finite element model, and a slight stiffness difference was observed after cycle 21 because tears and cracks that developed in the specimen occurred and were not included in the finite element model.

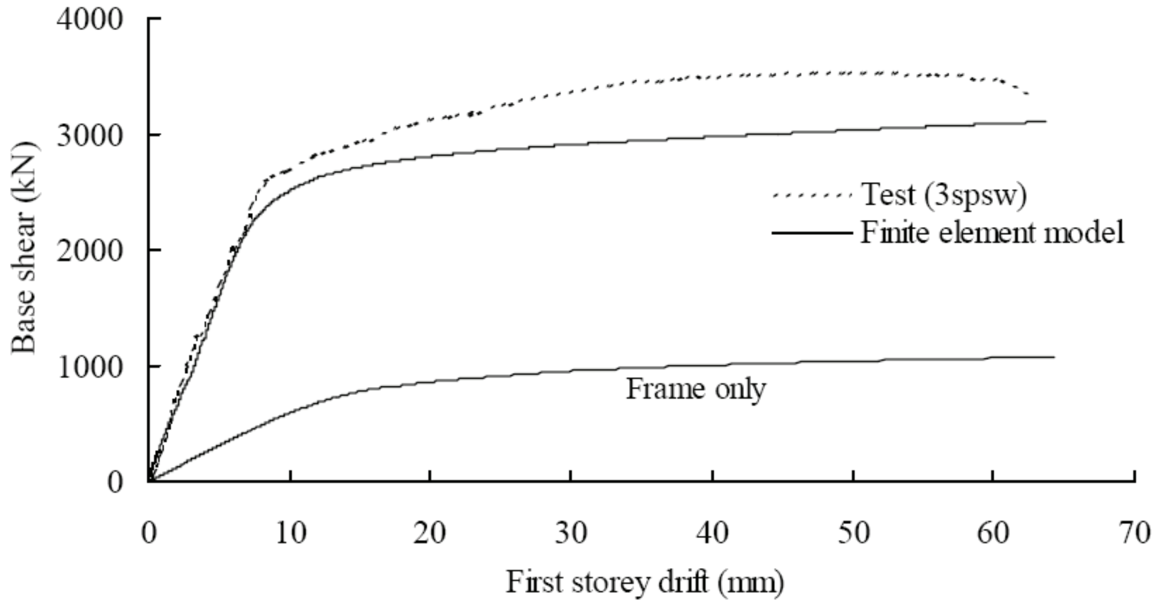

FIGURE 2-11 Monotonic Finite Element Analysis of the Three-Story Model Compared to the Envelope of Cyclic Test Results – Panel 1 (Behbahanifard *et al*. 2003)

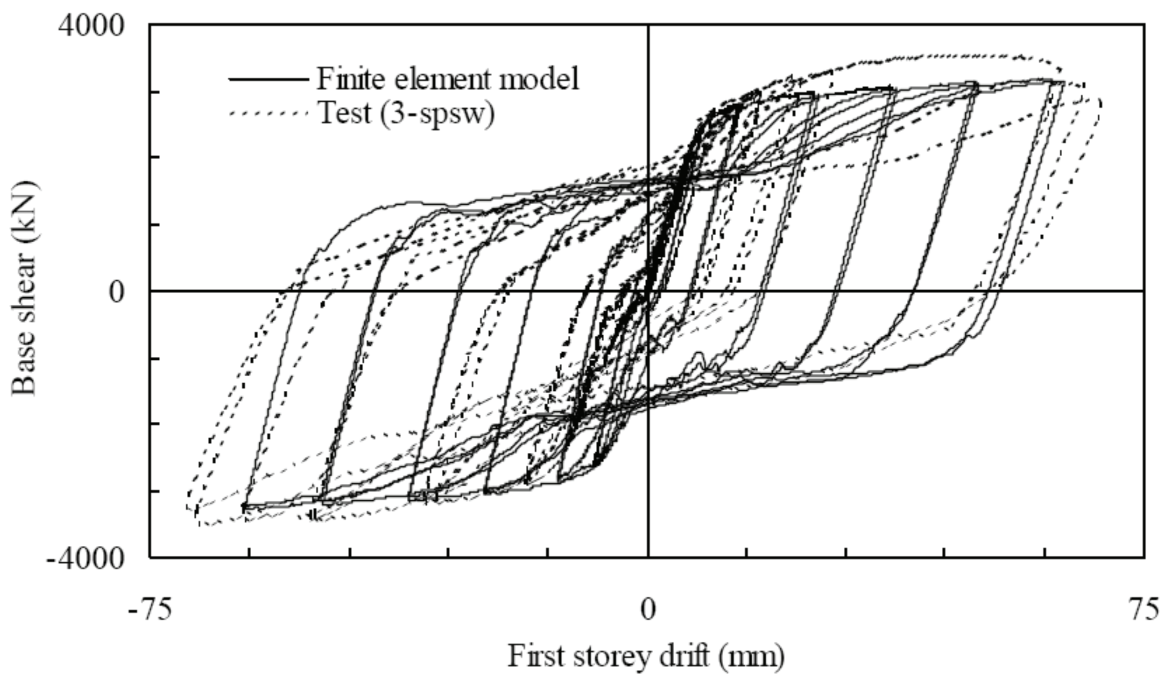

FIGURE 2-12 Comparison of Finite Element of the Three-Story Model and Experimental Hysteresis Curves – Panel 1 (Behbahanifard *et al*. 2003)

The researchers extended the three-story finite element model (FEM) to a four-story finite element model to validate the results reported by Driver *et al*. (1997). This was also done because of the discrepancy previously observed in the three-story model as a result of excluding the history of plastic deformation in the model. In terms of elastic stiffness, figure 2-13 shows agreement between the experimental and the finite element results while the finite element model underestimated the capacity of the SPSW by 7.8% on average. Figure 2-14 shows a good agreement between the experimental and finite element model hysteresis curves. Note that the researchers only compared the test results for the part of the test for which the specimen was loaded symmetrically in both directions.

The researchers also evaluated strain data of both experimental and finite element results. The strain data were measured in the flanges and webs of the boundary members. Finally, the researchers performed a parametric study to assess factors that affect the behavior of a SPSW system. A single story SPSW with rigid floor beams subjected to shear force and constant gravity load was used to examine the effect of infill plate dimensions, relative plate and column stiffness, drift magnitude, gravity and shear loads, plate and column yield strain, imperfection ratio, and local buckling. A more complete result of strain data evaluation and parametric study can be found in Behbahanifard *et al*. (2003).

2.6 Roberts and Sabouri-Ghomi (1992)

Roberts and Sabouri-Ghomi (1992) performed tests to investigate the hysteresis characteristics of unstiffened steel plate shear panels with centrally placed circular openings. Quasi-static cyclic loading tests were conducted on sixteen specimens with panel dimensions (width b and depth d) of either 300×300 mm or 450×300 mm, panel thickness h of either 0.83 mm or 1.23 mm, 0.2% offset yield stress value σ_0 of either 152 MPa or 219 MPa, and diameter of the central circular openings D of 0, 60, 105, or 150 mm. The edges of the plates were clamped by two rows of 8 mm diameter high-tensile bolts between pairs of rigid pin-ended frame members. Two diagonally opposite pinned corners of the panel were connected to the hydraulic grips where the load was applied. The schematic of test specimen is shown in figure 2-15. Results were correlated with results presented in Roberts and Sabouri-Ghomi (1991) for a similar specimen but with solid

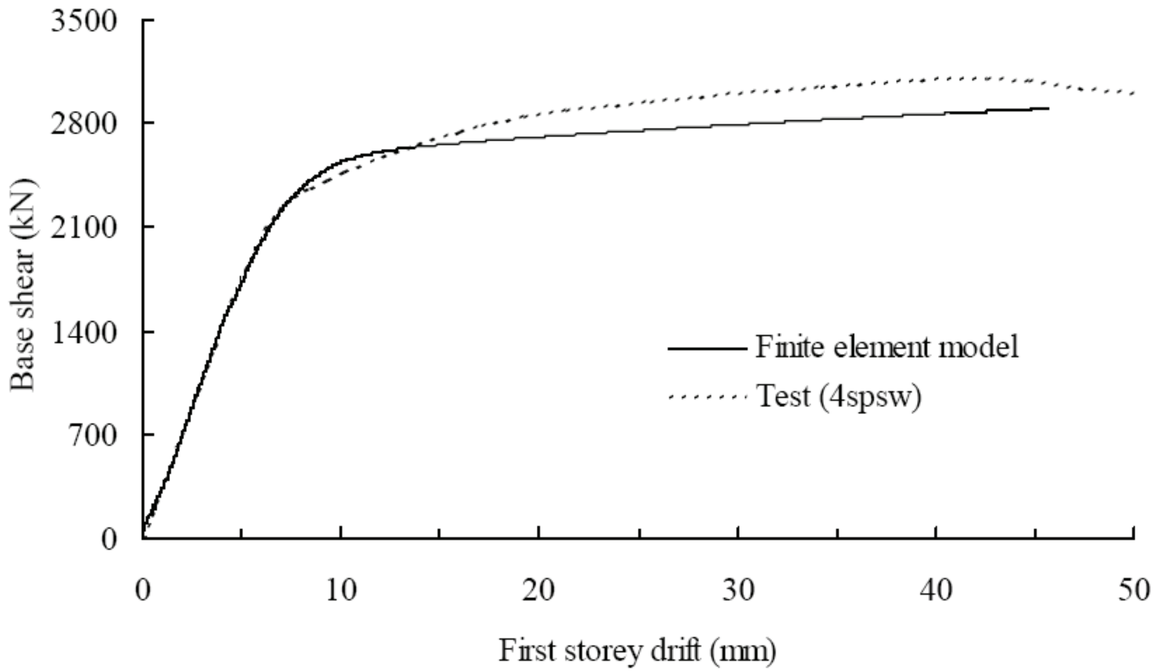

FIGURE 2-13 Monotonic Finite Element Analysis of the Four-Story Model Compared to the Envelope of Cyclic Test Results – Panel 1 (Behbahanifard *et al*. (2003)

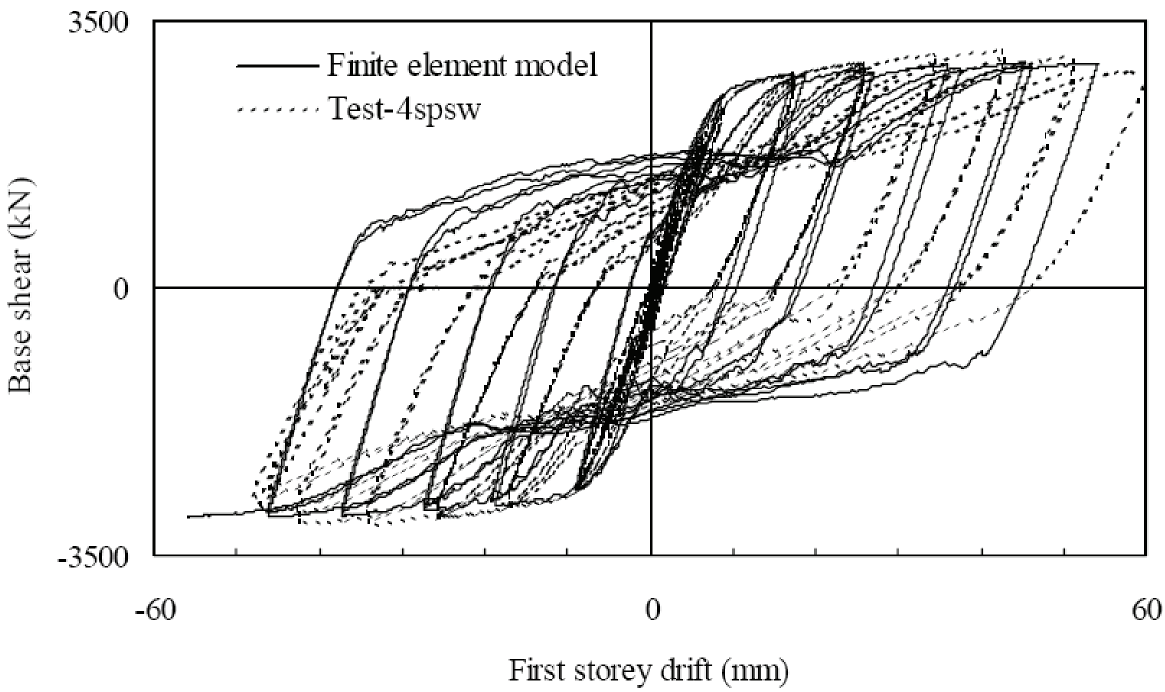

FIGURE 2-14 Comparison of Finite Element of the Four-Story Model and Experimental Hysteresis Curves – Panel 1 (Behbahanifard *et al*. 2003)

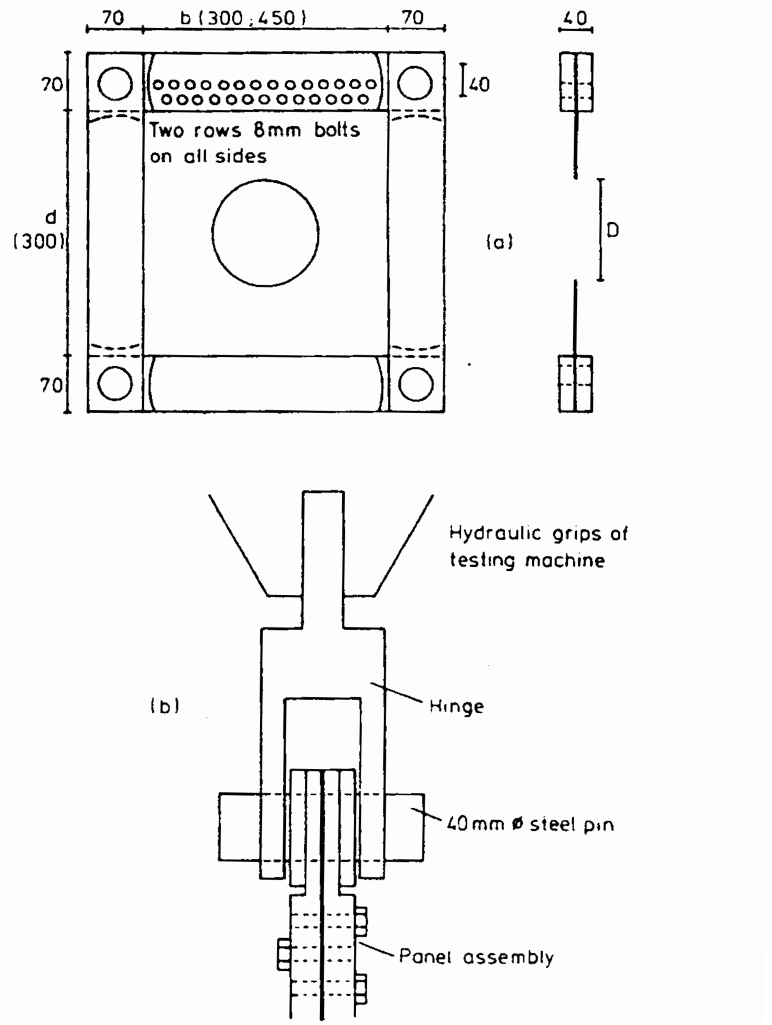

FIGURE 2-15 Schematic of Test Specimen (Roberts and Sabouri-Ghomi 1992)
(a) Perforated Shear Panel; (b) Hinge

panel. The ratio of ultimate strength and stiffness of perforated and solid panels is plotted in figure 2-16 where the ultimate strength and stiffness of panels decrease as size of perforation increase. The researchers recommended that the ultimate strength and stiffness of a perforated panel can be conservatively approximated by applying a linear reduction factor of

$$\frac{V_{yp.perf}}{V_{yp}} = \frac{K_{perf}}{K_{panel}} = \left[1 - \frac{D}{d}\right] \tag{2-3}$$

to the strength and stiffness of a similar solid panel.

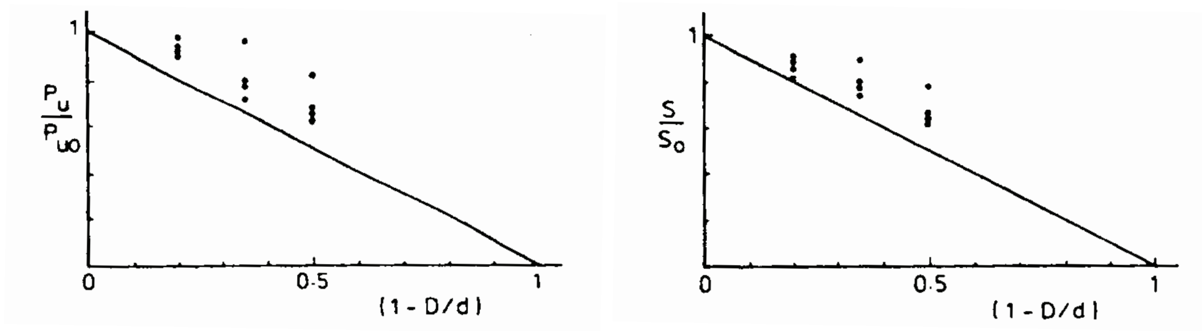

FIGURE 2-16 Variation of Strength and Stiffness of Shear Panels with Size of Opening (Roberts and Sabouri-Ghomi 1992)

The researchers also observed a reasonable agreement between experimental and theoretical hysteresis of perforated panel. The theoretical hysteresis behavior of the perforated panel was obtained by scaling the hysteresis obtained for a solid panel value using (2-3). This was considered to give a conservative assessment due to the neglect of strain hardening in the model and the simply supported boundary conditions.

2.7 Vian (2005)

Vian (2005) conducted quasi-static cyclic tests on three SPSW specimens. The first specimen consists of a single-bay, single-story frame, having rigid beam-to-column connection with reduced beam section (RBS) on the beams, and a solid infill plate of LYS steel. The other two specimens have the same boundary frame properties as the first specimen, and either multiple regularly spaced holes (perforations) in the infill plate or reinforced quarter-circle cutouts in the upper corners of the infill plate. The last two specimens were intended to accommodate the need for utility systems to pass-through the infill plate. The solid infill plate specimen was intended to be a “reference” specimen for the other two specimens. The solid panel, perforated, and cutout corner-reinforced specimens were designated as S, P, and CR specimens, respectively. The final designs of the three specimens are plotted in figures 2-17 to 2-19.

Figure 2-17 shows the final design of the solid panel specimen. The frame’s centerline dimensions were 4000 mm wide by 2000 mm high. The specimen approximately is one-half size

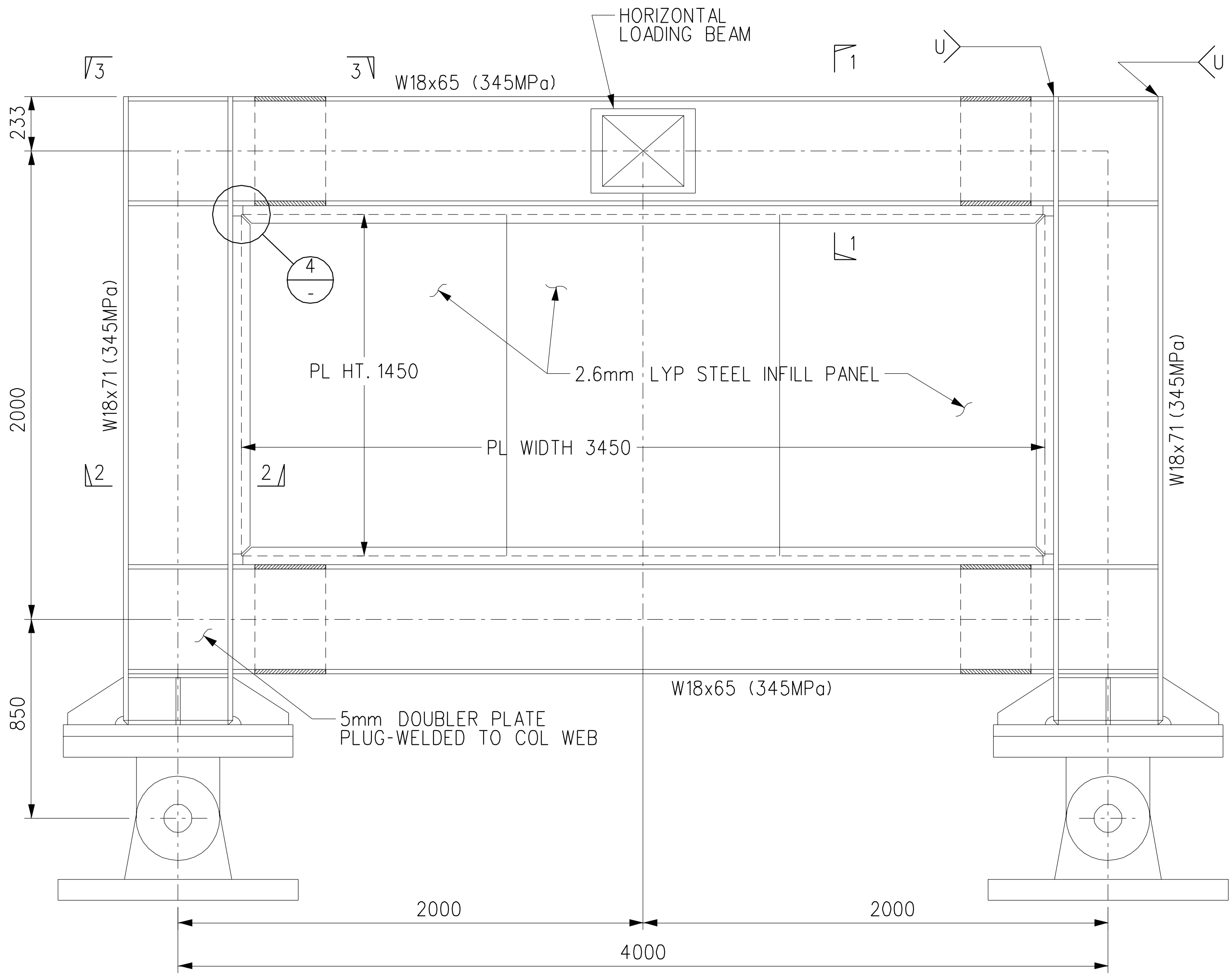

FIGURE 2-17 Basic Specimen Dimensions (Vian 2005)
(a) Overall Specimen Frame

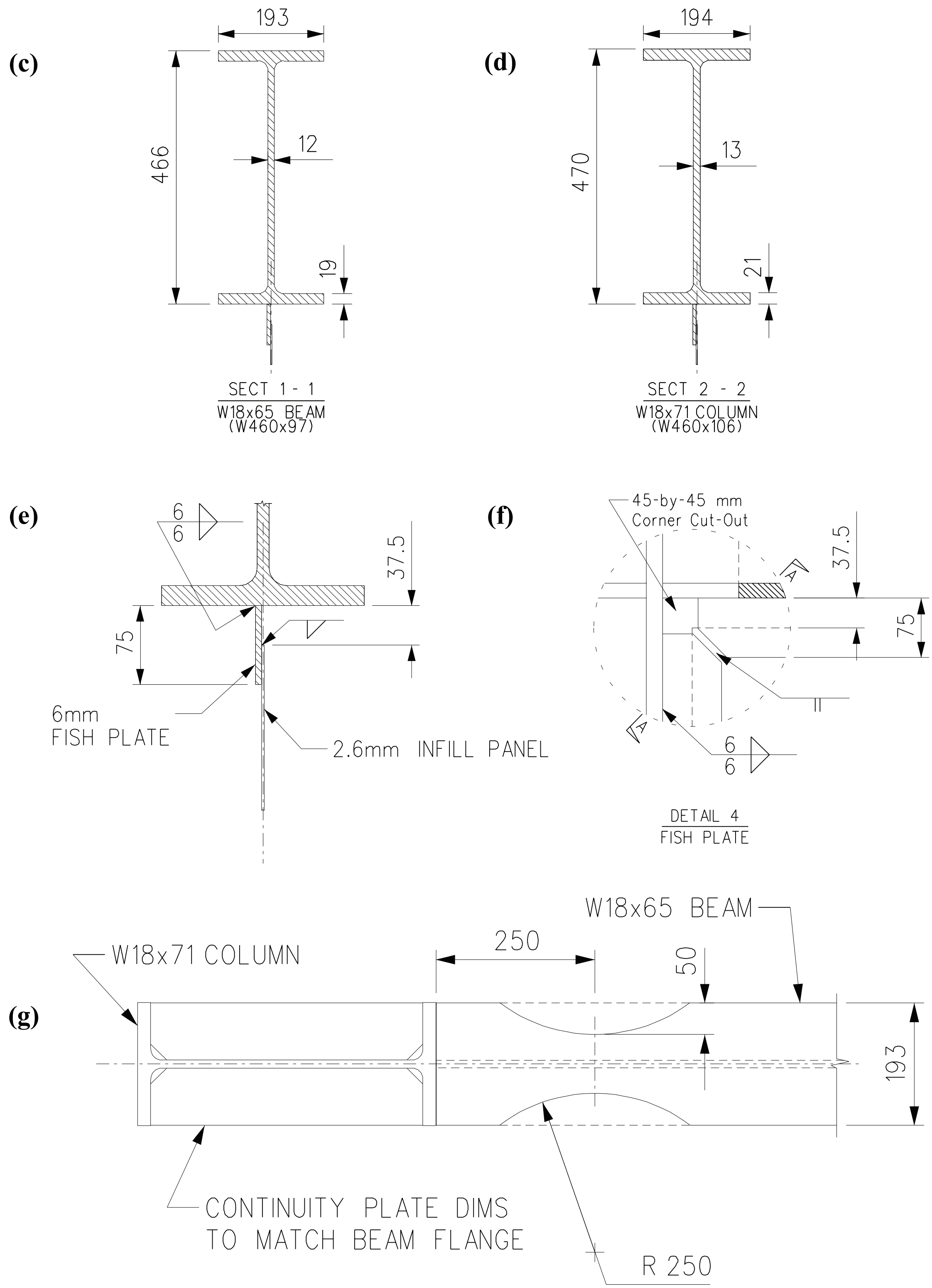

FIGURE 2-17 Basic Specimen Dimensions (Vian 2005) – Cont'd
(c) \W18x65 Beam Section; (d) Built-up W18x71 Column Section;
(e) Fishplate and Panel Section Detail; (f) Fishplate Corner Detail; (g) RBS Detailing

frame bay of the Multidisciplinary Center for Earthquake Engineering Research (MCEER) demonstration hospital project (Yang and Whittaker 2002). W18X65 and W18X71 made from ASTM A572 Gr. 50 (F_y = 345MPa) steel were used for beams and columns, respectively. RBS connections in the beams and hinges located 850 mm below the intersection point of the column and lower beam working lines were implemented. LYS with yield stress and ultimate stresses of 165 MPa and 305 MPa, respectively, was used for the infill plate of 2.6 mm thick. Figure 2-18 shows the final design of the perforated specimen. The 2.6 mm thick infill plate consisted of staggered holes arranged at a 45° angle with 300 mm center-to-center spacing along both the vertical and horizontal directions to provide panel strip width S_{diag} equal to 424.26 mm (D/S_{diag} = 0.471). The number of 200 mm perforations along the diagonal strip N_r equal to 4. Figure 2-19 shows the final design of the cutout corner specimen. Quarter-circle cutouts of 500 mm radius at the upper corners of the infill plate and flat-plate reinforcement along the cutout edges of 160 mm by 19 mm were applied. In all cases, a "fish plate" of 6 mm thick was added to facilitate attachment of the infill plate to the surrounding frame. The FEM models of the three specimens are plotted in figure 2-20(a), (b), and (c) for the same respective specimens.

In addition, another solid infill plate specimen was built and tested prior to the fabrication of the previous three specimens, to investigate the fabricator's workmanship in assembling the LYS infill plate panel from three separated pieces using seam welds. Vian (2005) observed that substantial deficiencies in fabrication and "inadequate" overall quality of workmanship occurred. Therefore, for the subsequent specimens these problems were corrected. The two solid panels, the latter "benchmark" and the previous "reference" specimens, were designated as S1 and S2, respectively.

Experimental and analytical hysteresis of specimen S2, P, and CR are shown in figure 2-21(a), (b), and (c), respectively. The monotonic pushover curves are also shown in the figures. Specimen S2 and P were tested to a maximum interstory drift of 3% while specimen CR was tested to a maximum interstory drift of 4%. Excellent agreement between the experimental and cyclic analytical hysteresis of specimen S2 was observed until the final cycle. Although the analytical model of specimens P and CR somewhat underestimated the experimental strength, good agreement in overall behavior between the experimental and cyclic analytical results was

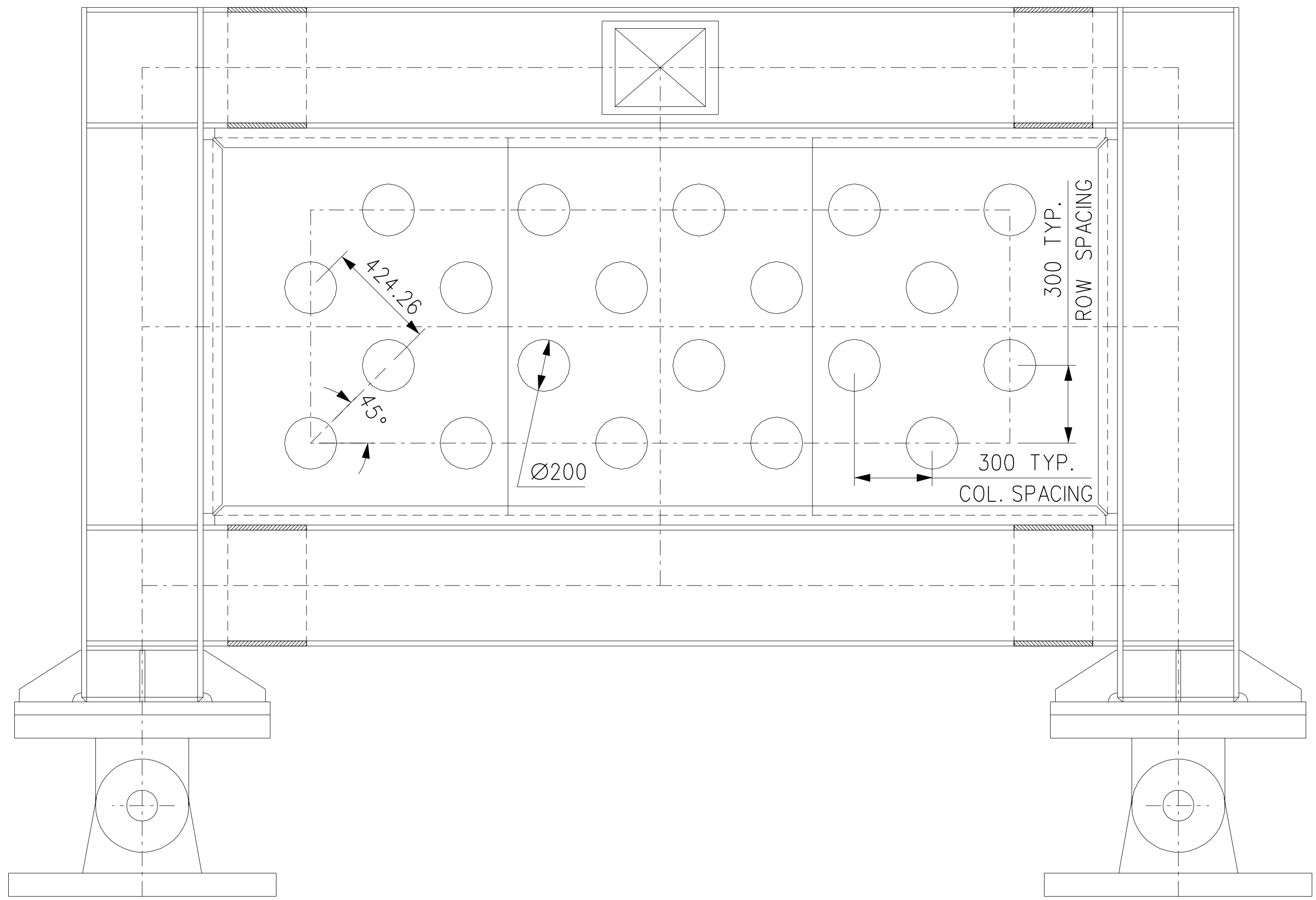

FIGURE 2-18 Specimen P Final Dimensions: Perforation Layout *D* = 200 mm (Vian 2005)

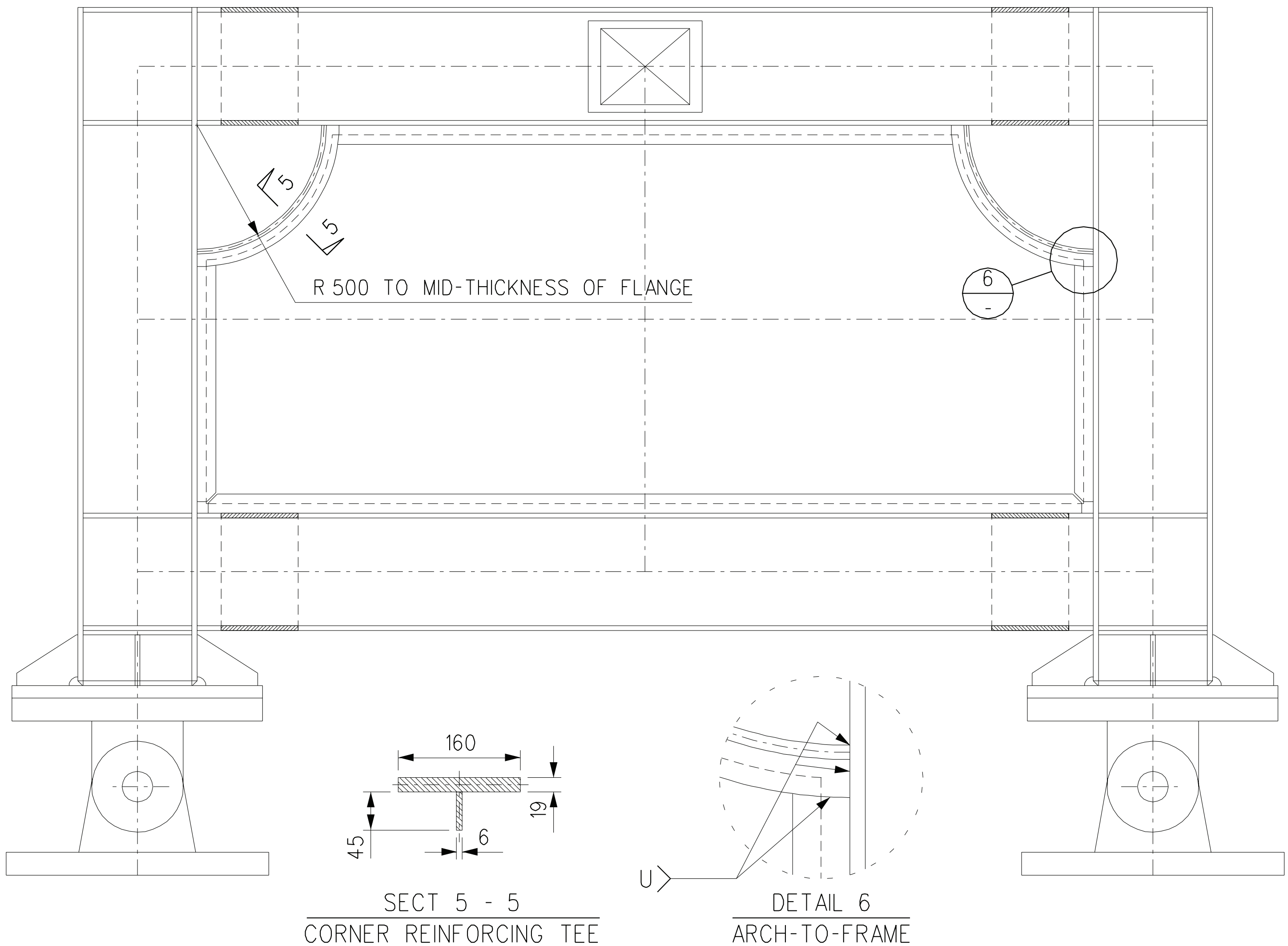

FIGURE 2-19 Specimen CR Final Design (Vian 2005)

(a)

(b)

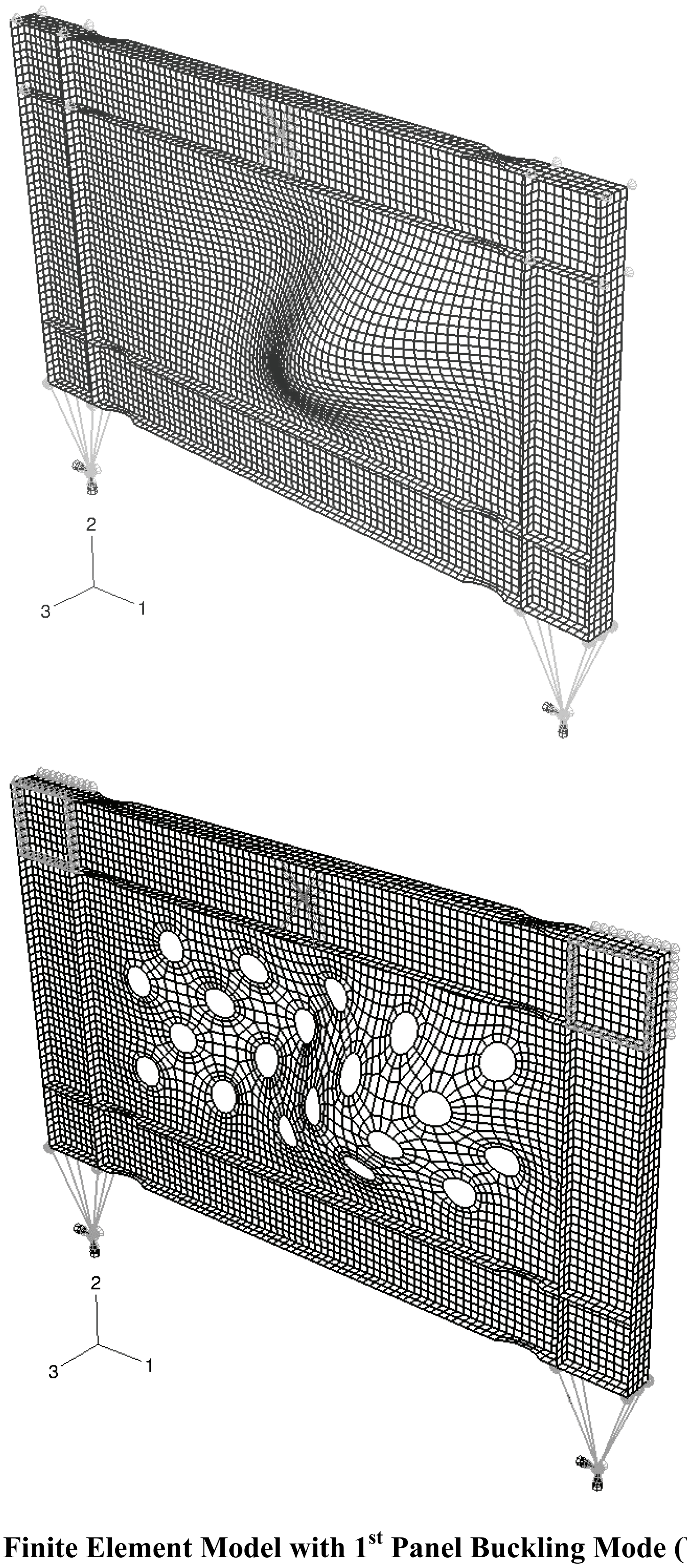

FIGURE 2-20 Finite Element Model with 1st Panel Buckling Mode (Vian 2005)
(a) Specimen S; (b) Specimen P

(c)

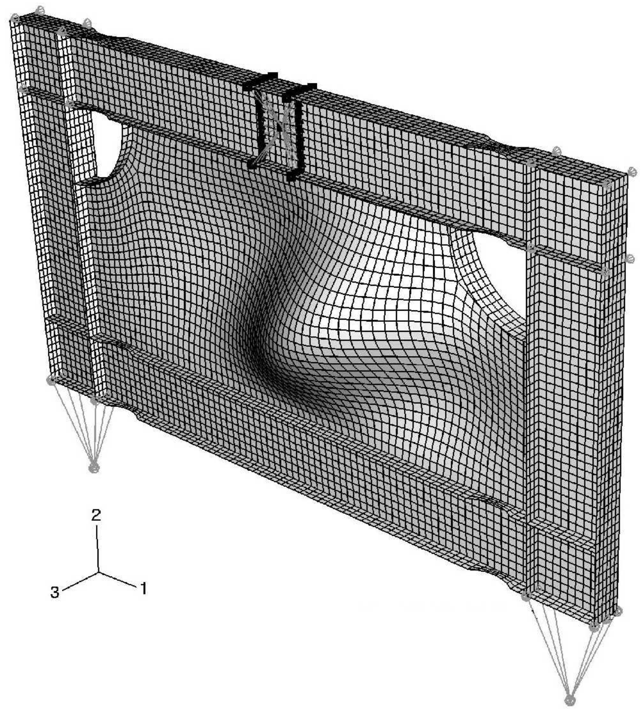

FIGURE 2-20 Finite Element Model with 1st Panel Buckling Mode (Vian 2005) – Cont'd (c) Specimen CR

(a)

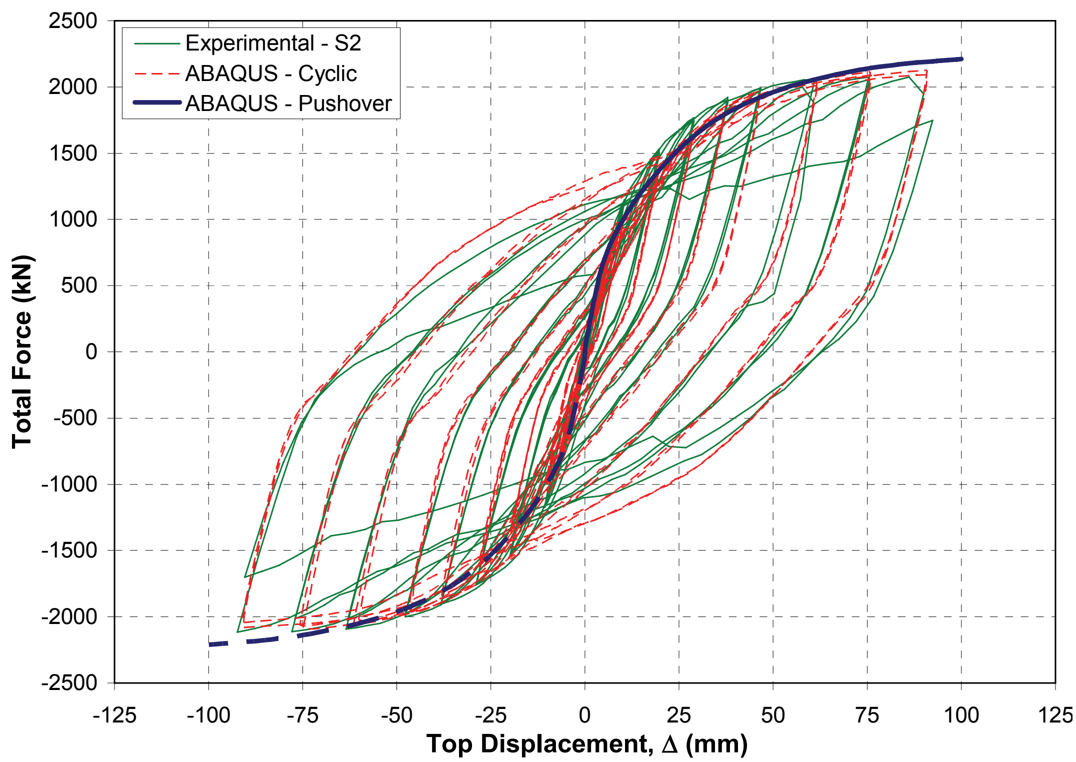

FIGURE 2-21 Specimen Hysteresis of Experimental and Analytical Results (Vian 2005) (a) Specimen S2;

(b)

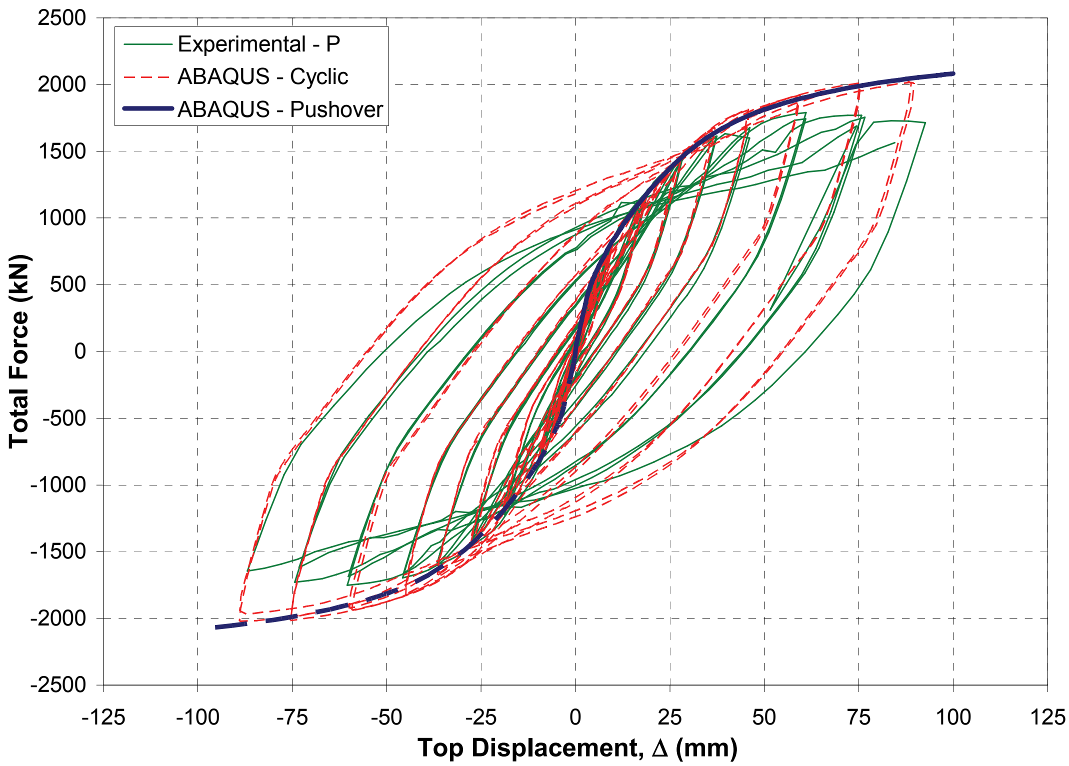

(c)

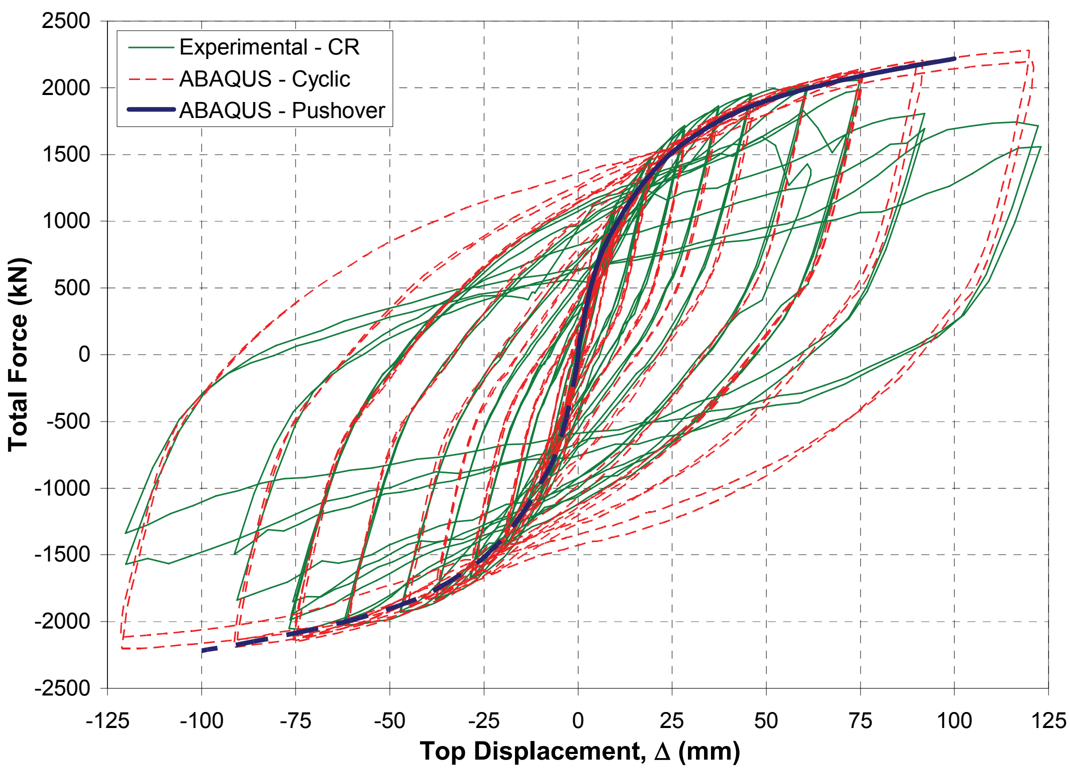

FIGURE 2-21 Specimen Hysteresis of Experimental and Analytical Results (Vian 2005) (b) Specimen P; (c) Specimen CR

observed. Loading assembly rotation, subsequent column twisting, distortion of the top beam and lateral support frames, RBS connections fractures (on the CR specimen) account for the discrepancy between experimental and analytical results at large drifts as the FEM model was not developed to consider such distortions and material failure.

The analytical model of the perforated SPSW was further extended to consider holes with 100, 150, 200 mm diameter in infill plates of ASTM A36 (F_y = 248 MPa) and A572 Gr. 50 (F_y = 345MPa) steels which are commonly specified in North American construction projects. The results were compared to the results for individual perforated strips having perforation diameters varying between 0 (no hole) to 200 mm. The resulting total uniform strip elongation ε_{un} and normalized strip elongation $\varepsilon_{un}/(Nr{\cdot}D/L)$ versus perforation ratio D/S_{diag} are plotted in figures 2.22 and 2.23, respectively, for both material grades used. ε_{max} is the maximum principal local strain shown in the figures. The rational for the normalization procedure is described in Vian (2005). Vian (2005) reported that the jaggedness in the curves shown in figure 2-22 might be an artifact of the coarseness of the chosen mesh and recommended further research to investigate the effects of mesh refinement on stress-strain distribution adjacent to perforations on the assumed limit states. Vian (2005) also reported that the elongation predicted by the finite element model of an individual perforated strip and full SPSW model, for monitored maximum strain assumed close to perforations edges, was significantly different. Further research was recommended to determine the factors that affect this behavior and to improve the design recommendations proposed for perforated SPSW. Section 3 and 4 of this report are intended to investigate those concerns and to resolve these issues.

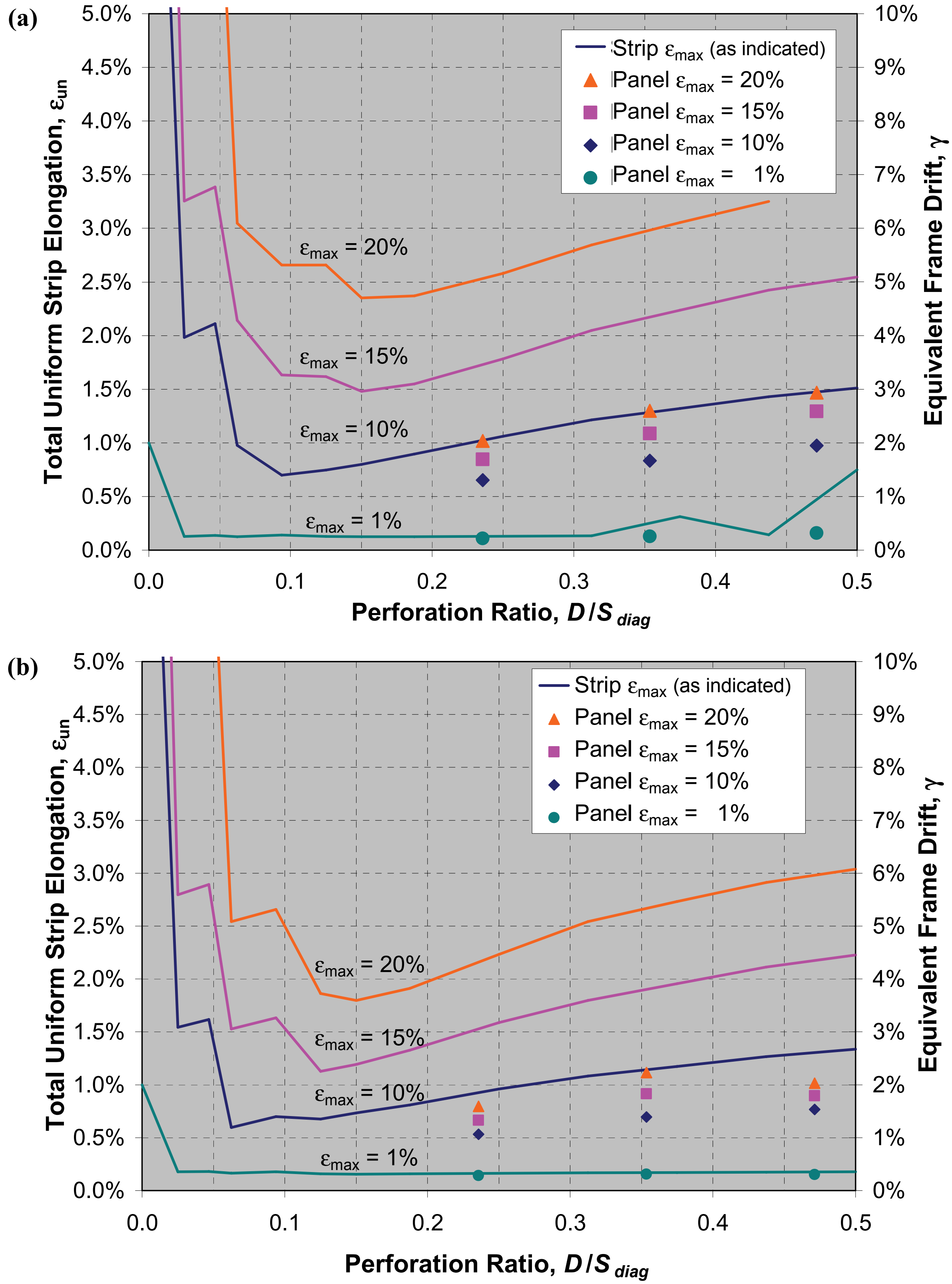

FIGURE 2-22 Total Uniform Distributed Strip Elongation ε_{un} versus Perforation Spacing Ratio D/S_{diag} (a) Idealized A36 Steel; (b) Idealized A572 Steel (Vian 2005)

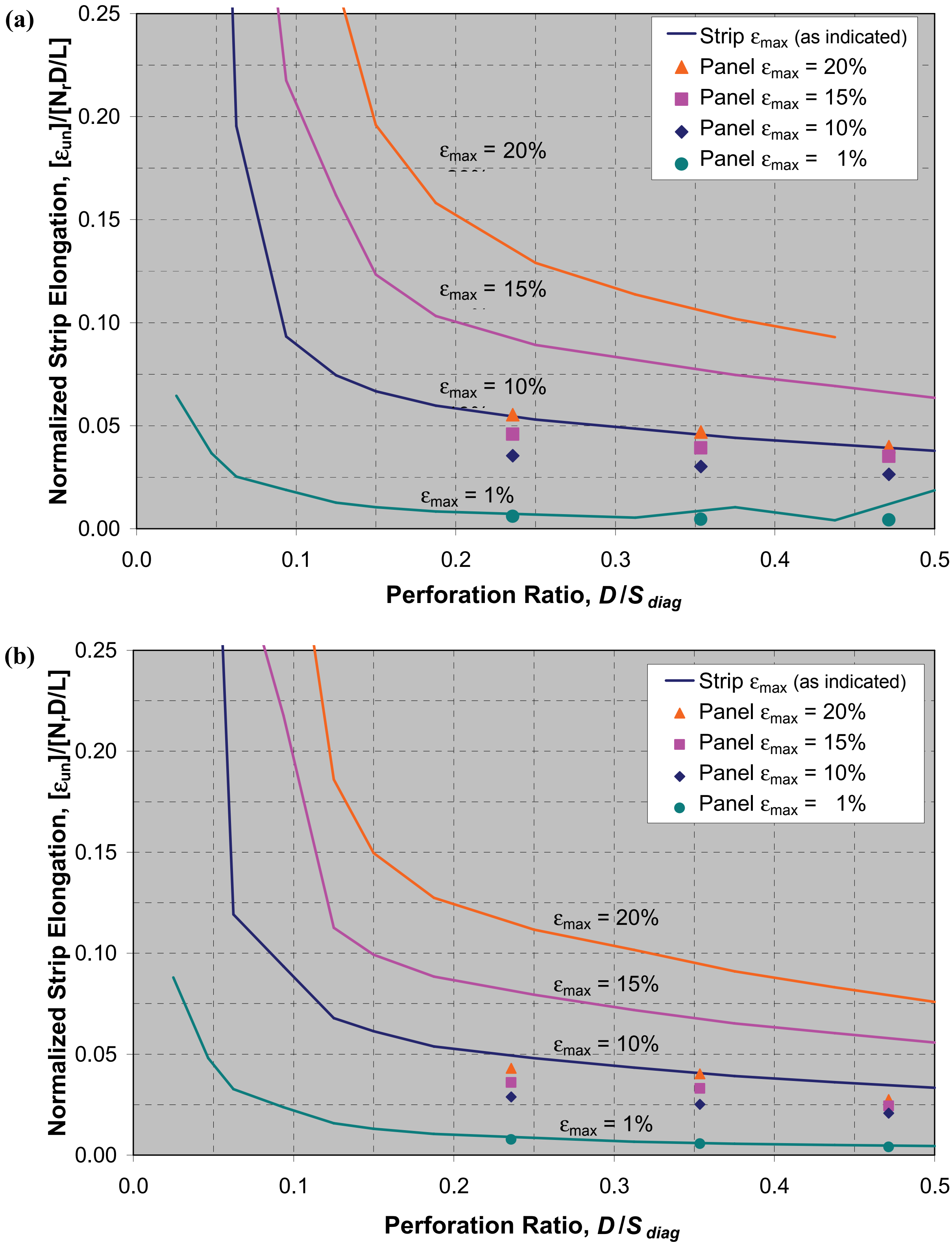

FIGURE 2-23 Normalized Strip Elongation $\varepsilon_{un}/(N_r D/L)$ versus Perforation Spacing Ratio D/S_{diag} (a) Idealized A36 Steel; (b) Idealized A572 Steel (Vian 2005)

SECTION 3

ANALYSIS OF PERFORATED STEEL PLATE SHEAR WALLS USING STRIP MODEL

3.1 General

This section describes investigation on the behavior of individual perforated strips as a sub-element of perforated SPSW using the finite element software ABAQUS/Standard. Several key features of assembling a comprehensive finite element model, such as modeling process, element definitions, and material definitions, are concisely discussed first. After evaluating the accuracy and convergence of the resulting finite element model, perforated strips 400 mm wide with 100 mm diameter holes are first examined and results are presented in terms of stress-strain distributions throughout the strip section as well as in terms of global deformations. The model is then modified to consider various perforation diameters, boundary conditions, and material idealizations. These studies are intended to develop an understanding of the behavior of individual perforated strips as a fundamental building block in understanding the behavior of complete SPSW in the next section.

3.2 Finite Element Description of Strip Model

Examples of the type of perforated panel layouts considered here, in which holes are uniformly distributed throughout the infill plate of a SPSW are shown in figure 3-1 for a four-story building frame. One possible perforation layout is detailed in figure 3-2 with perforations of diameter D are equally spaced of diagonal width S_{diag}, arranged at an angle θ with respect to the beam axis which in this case is considered 45°. Vian (2005) defines a "typical" panel strip as "the region within a tributary width of $\frac{1}{2}S_{diag}$ on either side of a perforation layout line"; in figure 3-2, the region is shaded differently. One infill plate may consist of several strips which depend on the frame dimensions and the perforation layout. Single strips having particular dimensions and perforation layout are investigated in this section using finite element analysis as explained in the following sections.

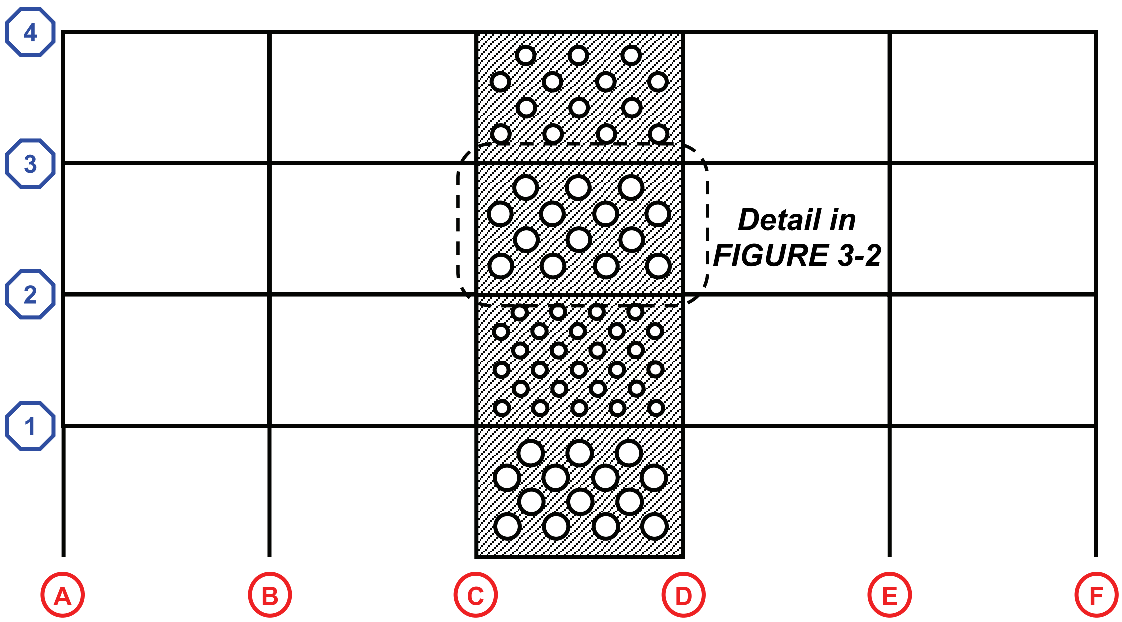

FIGURE 3-1 Arbitrary Schematic Examples of Possible Perforated SPSW Infill Panels in Four Story Building Frame (Vian 2005)

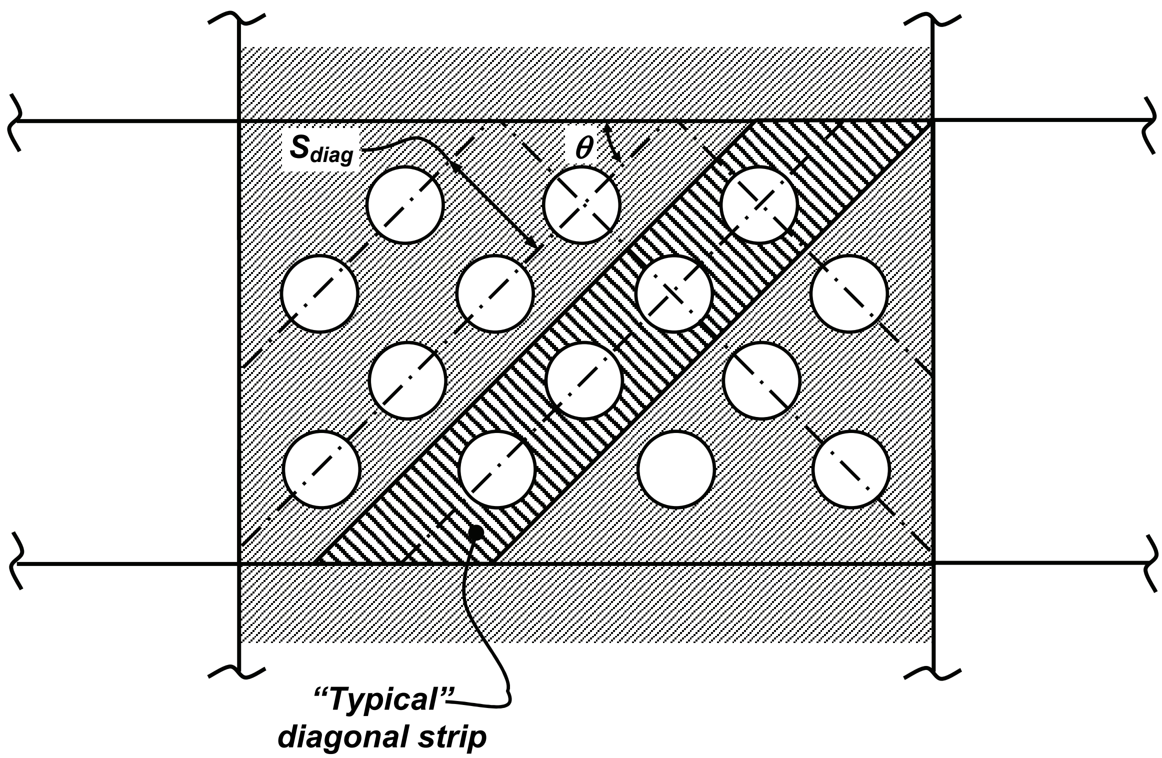

FIGURE 3-2 Schematic Detail of 3rd Story Panel and "Typical" Diagonal Strip (Vian 2005)

3.2.1 Typical Perforated Strip Models

Typical perforated strip dimensions of length L equal to 2000 mm, diagonal width S_{diag} equal to 400 mm, number of perforations along the diagonal strip N_r equal to 4, and plate thickness t_p equal to 5 mm are studied in this section. These dimensions are similar to those Vian (2005) investigated for a range of perforation diameters. Here finite element analyses were performed for strips having a perforation diameter D ranging from 10 to 300 mm, corresponding to a perforation ratio D/S_{diag} varying from 0.025 to 0.75. For the strip geometry selected, a perforation diameter increment of 10 mm was chosen for analyses between the limit values of 10 mm and 300 mm, to obtain a relatively large number of data points and thus relatively smooth curves in the plots that express the variation of behavior for various perforation diameters than the ones that were previously developed by Vian (2005).

Current design philosophy of SPSW allows the infill plates to buckle in shear and form diagonal tension strips to resist lateral loads. Due to that buckling during the inelastic stage, as a first step in this study, the continuity between strips was assumed to be such that there is no interaction between adjacent strips that could affect the stress distribution within an individual strip. Each strip therefore behaves as an independent strip. This assumption is then revisited in a latter section. The typical geometry of an individual perforated strip is shown in figure 3-3.

Because the strip geometry and loading are symmetrical about horizontal and vertical axes through the center of the strip, a quadrant model can be used to represent the full-strip model, as shown schematically in figure 3-3(b). To maintain equilibrium and proper displacements, constraints are specified along the symmetric boundaries such that displacements are restrained in the vertical direction along the horizontal boundary, and that displacements are restrained in the horizontal direction along the left vertical boundary. Note that as described in the previous paragraph, the top edge which is the interface edge to adjacent strip remains un-restrained.

A monotonic incremental displacement δ was applied to the strip models uniformly along the right-edge until the strips reached a displacement δ equal to 50 mm, or a total uniform strip elongation ε_{un} ($=\delta/L$) of 5%. During the analysis, total uniform strip elongations were noted when the maximum principal local strain ε_{max} reached values of 1, 5, 10, 15, and 20% somewhere in the strips.

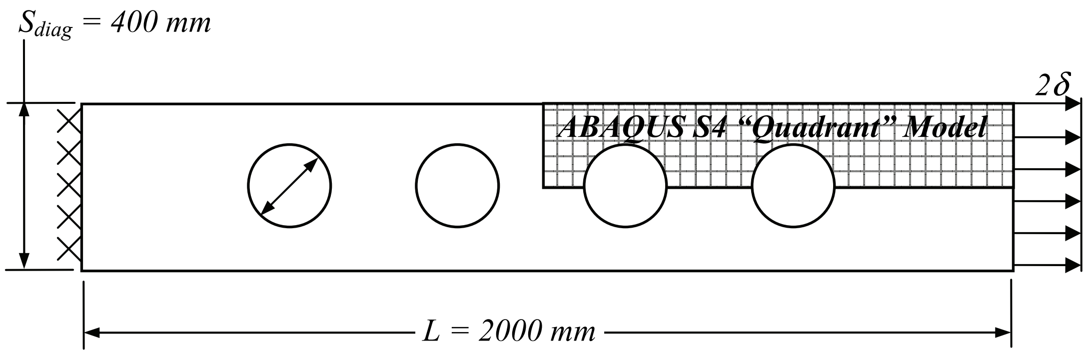

(a) Geometry of Perforated Strip

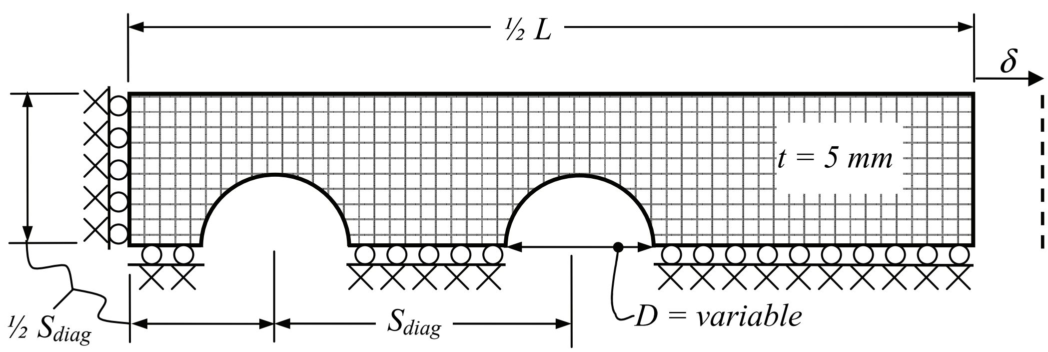

(b) Schematic Representation of "Quadrant" Part – ST1 Model (*not actual mesh*)

FIGURE 3-3 Analyzed Typical Strip Model Geometries (Vian 2005)

3.2.2 Element Definitions

Isoparametric 4-node shell element S4 was used in the finite element models. The S4 shell element is a fully integrated, general-purpose shell element. Each node has six degrees of freedom, three translations (u_x, u_y, u_z) and three rotations (θ_x, θ_y, θ_z). The S4 element is not sensitive to element distortion, can avoid parasitic locking, and does not have hourglass modes in either the membrane or bending response of the element; hence, the element does not require hourglass control (HKS 2004b). The S4 shell element together with a relatively small mesh size was selected to provide reasonable solution accuracy in this study.

This element allows transverse shear deformation by applying thick shell theory as the shell thickness increases. Conversely as the thickness decreases, it becomes discrete Kirchhoff thin shell element with transverse shear deformation becoming very small. Moreover, this element also accounts for finite (large) member strains and large rotations, geometric and material nonlinearities, and changes in thickness by inputting a specific Poisson's ratio $\nu = 0.3$ for steel (HKS 2004b).

The transverse shear calculation is performed at the center of the element and assumed constant over the element thickness. Hence, transverse shear strain, force, and stress will not vary over the area of the element (HKS 2004b). Nevertheless, in ABAQUS/Standard the default output points through the thickness of a shell section are the points that are on the bottom and top surfaces of the shell section for integration with Simpson's rule (HKS 2004b). Nine integration points were used through a single layer shell and output was taken at the top surfaces.

3.2.3 Material Definitions

ASTM A572 Gr. 50 ($F_y = 345$MPa) steel was selected and its behavior was represented by an idealized tri-linear stress-strain model as shown in figure 3-4. ABAQUS/Standard defines stress-strain material properties in terms of "true" stress (Cauchy stress) and logarithmic plastic strain, σ_{true} and $\varepsilon_{\ln}^{pl}$, respectively. The specified nominal stress (σ_{nom}) and nominal strain (ε_{nom}) values obtained from coupon tests were therefore converted using the following relationships (HKS 2004b):

$$\sigma_{true} = \sigma_{nom} \cdot (1 + \varepsilon_{nom}) \tag{3-1}$$

$$\varepsilon_{\ln}^{pl} = \ln(1 + \varepsilon_{nom}) - \frac{\sigma_{true}}{E} \tag{3-2}$$

where E is Young's modulus taken as 200.000 MPa. Note that these equations are valid only for an isotropic material. The "true" stress versus logarithmic plastic strain of ASTM A572 Gr. 50 steel is plotted in figure 3-5.

To define the inelastic (hardening) behavior, the *Combined Hardening* model was used. This hardening model is a nonlinear combination of *Isotropic Hardening* and *Kinematic Hardening* models. The Von Mises yield criteria was used.

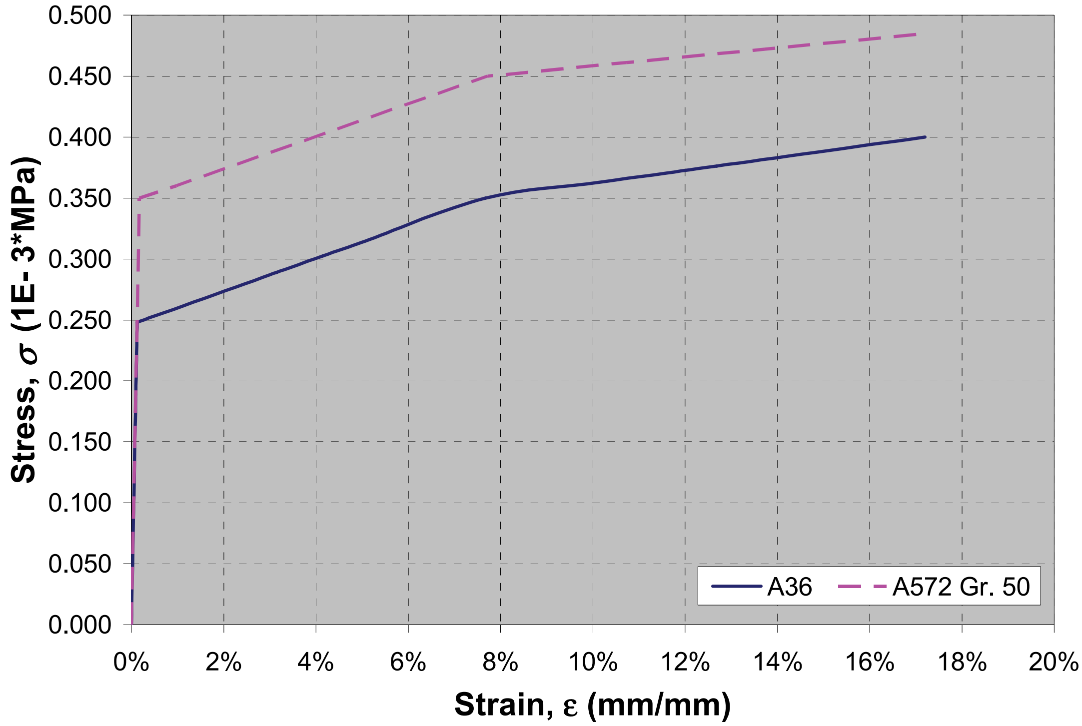

FIGURE 3-4 Idealized Tri-Linear Stress-Strain Models for A36 and A572 Steels (Vian 2005)

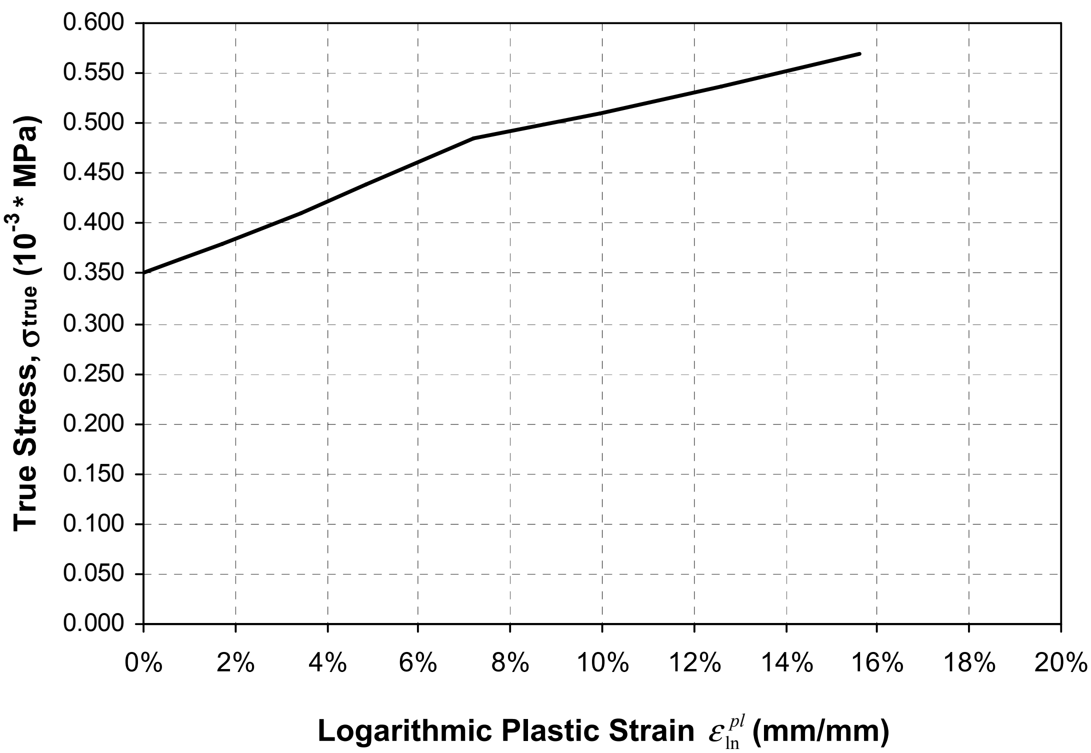

FIGURE 3-5 True Stress σ_{true} versus Logarithmic Plastic Strain $\varepsilon_{\ln}^{pl}$ of Idealized Tri-Linear Stress-Strain Curve for A572 Gr. 50 Steel (*ABAQUS Definition*)

3.3 Meshing Algorithm and Mesh Refinement

Vian (2005) reported that some jagged curves shown in figure 2-22 might be an artifact of the coarseness of the chosen mesh and recommended further research to investigate the effects of mesh refinement on stress-strain distribution adjacent to perforations on the assumed limit states. In addition, meshing algorithm on how to mesh a complex shape (i.e., regions around the perforations) might also affect stress-strain distributions. One of the objectives of this section, therefore, is to study the influence of mesh refinement and meshing algorithm on stress-strain distributions throughout the strip section. The study of meshing algorithm is described first and followed by the study of mesh refinement.

To study the meshing algorithm, three finite element models using transition zones close to the perforations shown in figure 3-6 were studied. The transition zone is the area bounded by half-circular or half-rectangular shapes in a distance equal to the radius of perforation offset from the tip of the perforations (i.e., 50 mm). Note that part (c) is a modification of part (a) by dividing the half-rectangular zone into 4-quadrant regions. Incidentally, this meshing algorithm has been commonly used in finite element textbooks and references (e.g., Schiermeier *et al*. 1996; Cook *et al*. 2001; Fillippa 2004). In addition to the three previous models, a model without any transition zone was also studied for comparison. Note that if no significant difference results among all the models considered, the latter model is desirable because ABAQUS will directly mesh the entire region without human-intervention, which expedites the meshing process.

The models used for this meshing algorithm study were meshed with a maximum 10 x 10 mm size for quadrilateral elements using the *Free Meshing Technique* and *Medial Axis Algorithm* options of ABAQUS/CAE. The transition zones were created using the *Partition* feature of the *Part Module*. Note that the finite element model of the quadrant part shown in figure 3-3(a) was generated using only one *Part* and obviously one *Assembly* in the ABAQUS/CAE.

The results of meshing algorithm (including the model without a transition zone) are compared in table 3-1 along with the relative CPU time to run each model and number of elements. The table presents the stress (S11) and strain (E11) monitored at the edge of the right perforation and total reaction forces (RF11) in the horizontal direction monitored at the left edge when the strip

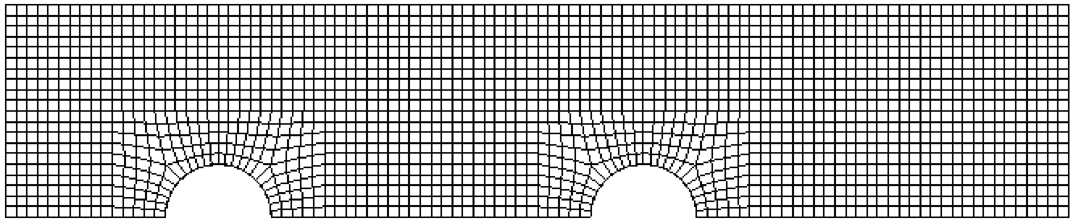

(b)

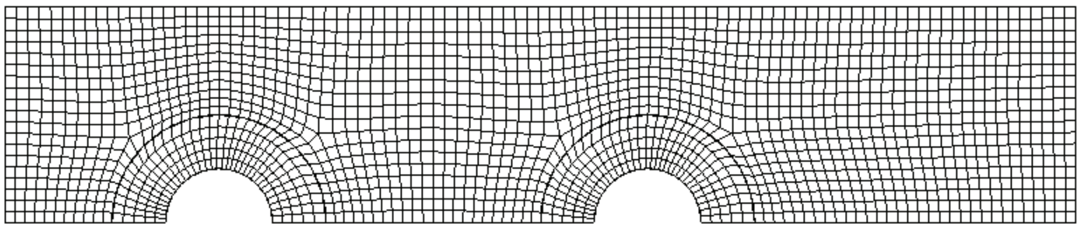

(c)

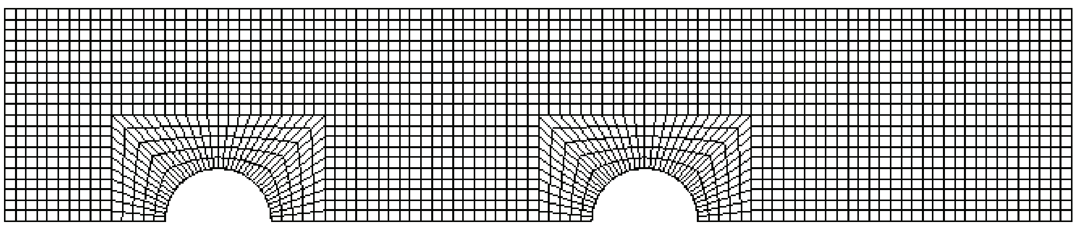

(d)

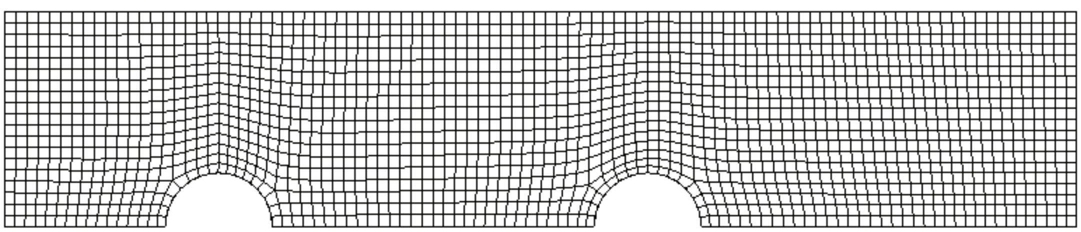

(e)

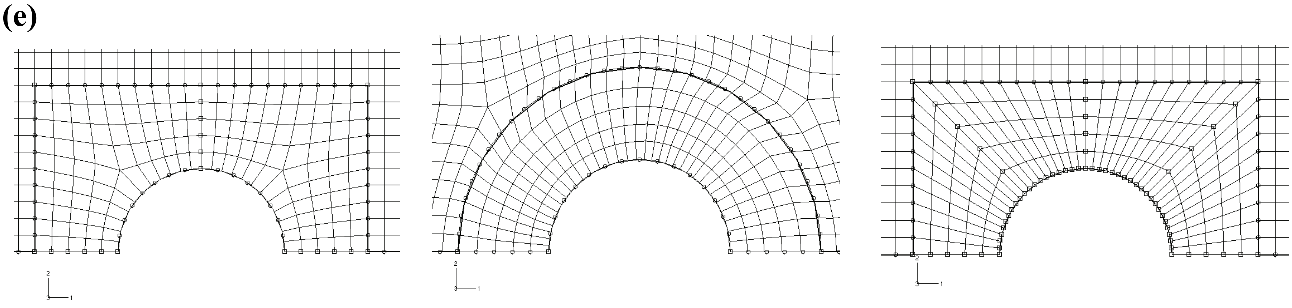

FIGURE 3-6 Meshing Algorithms (a) Rectangular Transition Zone; (b) Circular Transition Zone; (c) 4-Quadrant Transition Zone; (d) without any Transition Zone; (e) Zoom View of Rectangular, Circular, and 4-Quadrant Transition Zones (*left to right*)

reached 2% elongation. The monitored values of all models considered are close to each other and it is concluded that all models provide the same accuracy.

TABLE 3-1 Mesh Accuracy of Several Considered Models at 2% Strip Elongation

Transition Zone	Number of Elements[(1)]	S11 (MPa)	E11 (%)	RF11[(2)] (kN)	CPU Time (hh:mm:ss)
Rectangular	1904	623.16	18.76	329.26	00:08:40
Circular	1886	622.02	18.53	330.05	00:08:33
4-Quadrant	2000	624.41	18.69	328.97	00:09:17
No Transition	1819	609.41	18.58	329.33	00:08:10

Note: 1) A maximum 10 x 10 mm mesh size
2) Total reaction forces in the horizontal direction monitored at the left edge of the strip

To study the influence of mesh refinement, four finite element models with maximum mesh size varying from coarse mesh of 20 x 20 mm to very fine mesh of 2.5 x 2.5 mm were studied. The four-quadrant transition zone was used in each model so considered and the *Enrichment* or *h-refinement* revision method was applied such that the refined mesh size of an element or the square root of the refined area of an element is approximately half of that the previous one (Cook *et al*. 2001).

The results of mesh refinement are compared in table 3-2 for the same monitored value. In addition, the result of individual strip model used by Vian (2005) is also presented in the table. Mesh refinement significantly changed the monitored strain value; E11 is equal to 16.96% and 19.51% for the coarse mesh (20 x 20 mm) and very fine mesh (2.5 x 2.5 mm), respectively. However, the improvement in accuracy for monitored strain less significantly altered after the mesh was further refined beyond 5 x 5 mm; for example, E11 is equal to 19.35% and 19.51% for the 5 x 5 mm and 2.5 x 2.5 mm mesh, respectively. Therefore, the accuracy of the models was considered to have “converged” at a 5 x 5 mm mesh size.

TABLE 3-2 Mesh Convergence of Several Considered Models at 2% Strip Elongation

Model(1)	Number of Elements	S11 (MPa)	E11 (%)	RF11 (kN)	CPU Time (hh:mm:ss)
Coarse Mesh (20 x 20 mm)(2)	520	619.77	16.96	330.23	00:01:54
Vian Model (10 x 10 mm)	1872	609.77	18.66	329.22	00:08:32
Normal Mesh (10 x 10 mm)	2000	624.41	18.69	328.97	00:09:17
Fine Mesh (5 x 5 mm)	8000	617.17	19.35	328.16	00:46:11
Very Fine Mesh (2.5 x 2.5 mm)	32000	608.77	19.51	327.85	03:53:40

Note: 1) Except for Vian model, the four-quadrant transition zone was used.
2) A maximum mesh size

On the basis of these results and computation time needed to obtain them, the models considered later in this section use 5 x 5 mm mesh size without any transition zone close to the perforations (except that after further review, for relatively small and big perforation diameter (i.e., $D \leq 60$ and ≥ 250 mm), a rectangular transition zone is used as needed by ABAQUS to mesh the regions close to the perforations correctly, without element distortion).

3.4 Behavior of Perforated Strip Model

Strip deformations, maximum in-plane principal stress contours, and strain contours are shown in figure 3-7 for the case having a 100 mm perforation diameter when maximum principal local strain ε_{max} reached a value of 20% somewhere in the strip. As shown in the figure, the in-plane principal stress and strain contours are uniform at the right edge of the strip. However, holes in the strip disturbed the “regularity” of the stress and strain flows and high stress and strain concentrations developed at the perforation edge and zones of yielding radiate out from this location at approximately 45° angles to the left and right of the perforations.

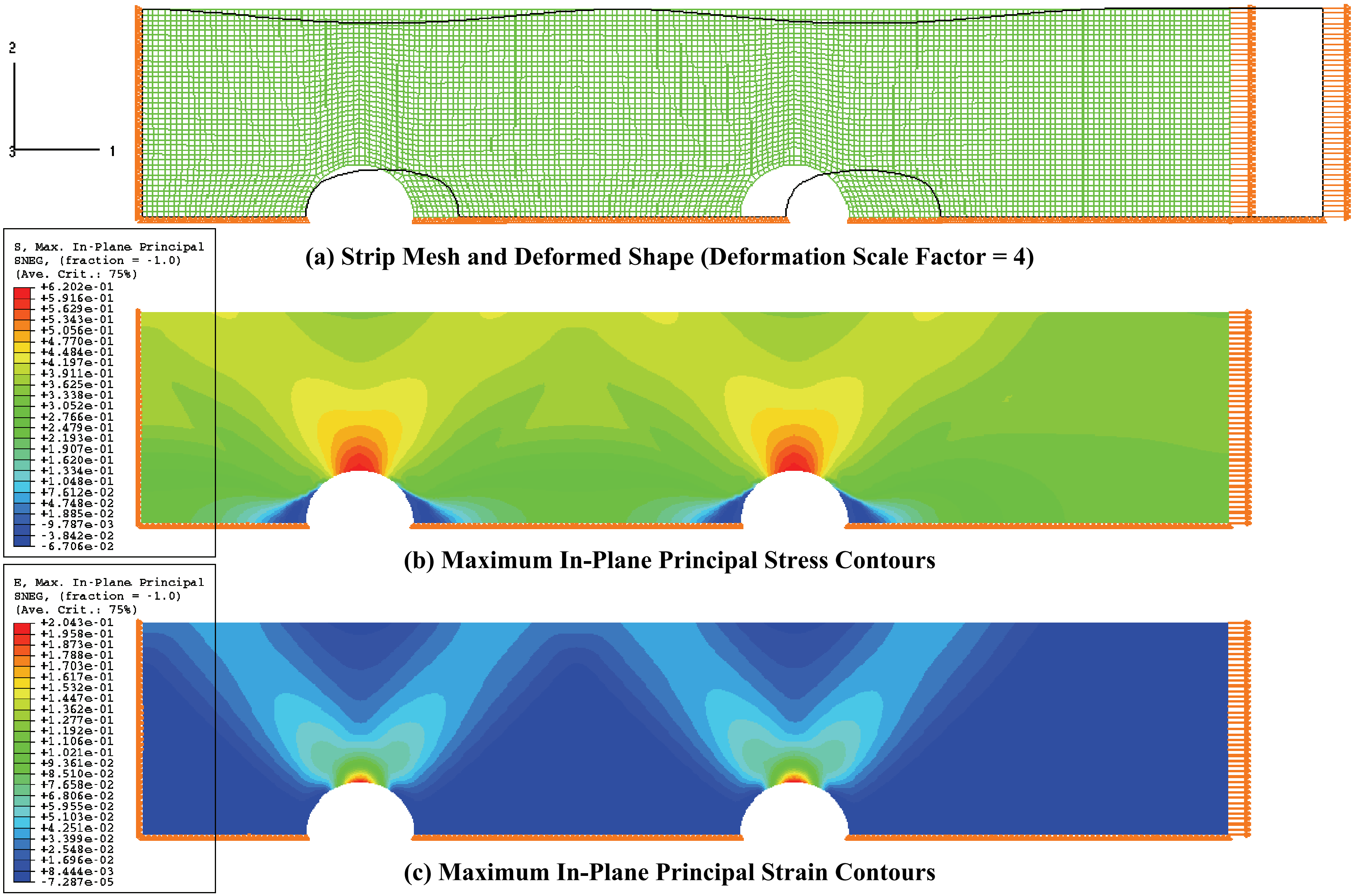

(a) Strip Mesh and Deformed Shape (Deformation Scale Factor = 4)

(b) Maximum In-Plane Principal Stress Contours

(c) Maximum In-Plane Principal Strain Contours

FIGURE 3-7 Typical Strip Analysis Results at 20% Maximum Local Strain
ST1 Model, Idealized Trilinear Stress-Strain Curve A572 Gr. 50 Steel, D = 100 mm (D/S_{diag} = 0.25)

This phenomenon can be explained by reviewing the stress distributions in the 1-1 and 2-2 direction plotted in figures 3-8(a) and (b), respectively. The figures show that stresses at shell elements close to the perforation edges are mainly dominated by S11. For example, S11 of element K shown in figure 3-8(c) is equal to 619 MPa while S22 is only 34.5 MPa. This makes element K stretches in the 1-1 direction and, because of Poisson's-ratio effect, it shrinks in the 2-2 direction. The combination of these two effects pulls down the shell elements on top of element K; as this condition repeats itself, amplifying the "pull" to each subsequent adjacent element, by the time element H is reached, S22 has increased to 134 MPa while S11 slightly decreased to be 512 MPa. By element C, however, S22 has decreased close to zero (compression stress of 7 MPa at the center of the element) while S11 is equal to 356 MPa. Therefore, stress increases in the 1-1 direction due to stress concentration also created *pull-down forces* in the 2-2 direction. This explains why the unrestrained top edge (the interface edge to the adjacent strip) adjacent to the perforations moved inward (as shown in figure 3-7a) in addition to rightward movement. For example, when the right tip of strip has deformed 21.5 mm to the right, the top edge on average has deformed 3.75 mm inward. In an actual SPSW the interface between adjacent strips correspond to a buckle "ridge", and this inward pull towards the hole due to Poisson's-ratio effect would locally reduce the amplitude of the ridge.

Between the perforations above the level of the perforation edges, no stress concentration occurred, elements developed roughly equal S11 stresses. However, below the level of the perforation edges, S11 is relatively smaller compared to that above the level of perforation edges. For example, element F experienced S11 equal to 312 MPa while element J only experienced S11 equal to 232 MPa. This phenomenon occurred because low axial compression forces developed in the elements close to the two perforations edges at the level of element J and with corresponding *push-up forces* in the 2-2 direction. Insignificant inward deformation of the top edge away from the perforations confirms this behavior.

Between the two cross sections, elements E and G experienced compression stresses in the 2-2 direction in combination with tension stresses in the 1-1 direction. This made element E and G experience large maximum principal stresses. The contribution of compression S22 stress and tension S11 stress facilitate the occurrence of yielding as can be shown using a Mohr's circle

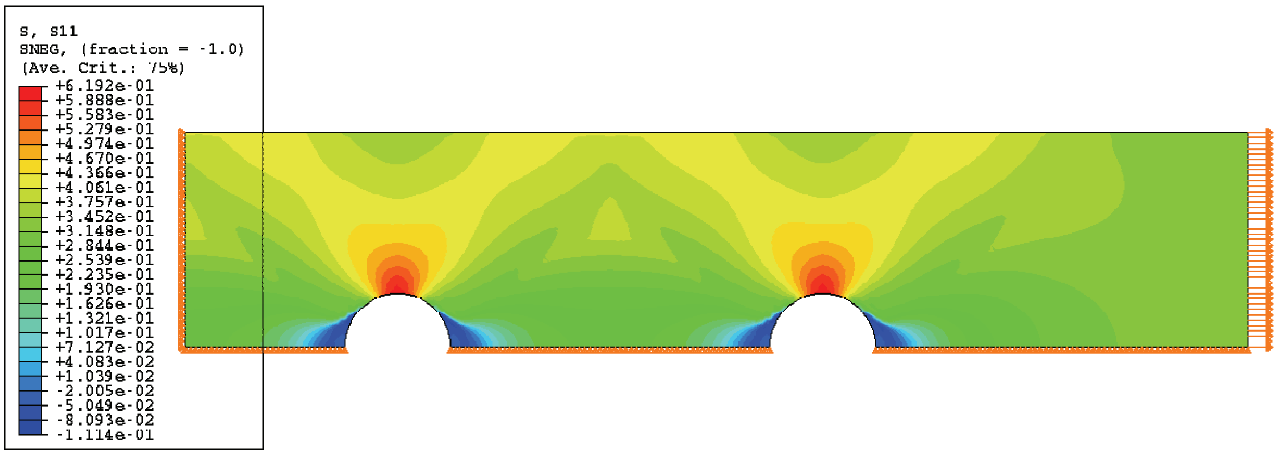

(a) Stress in the 1-1 Direction (S11)

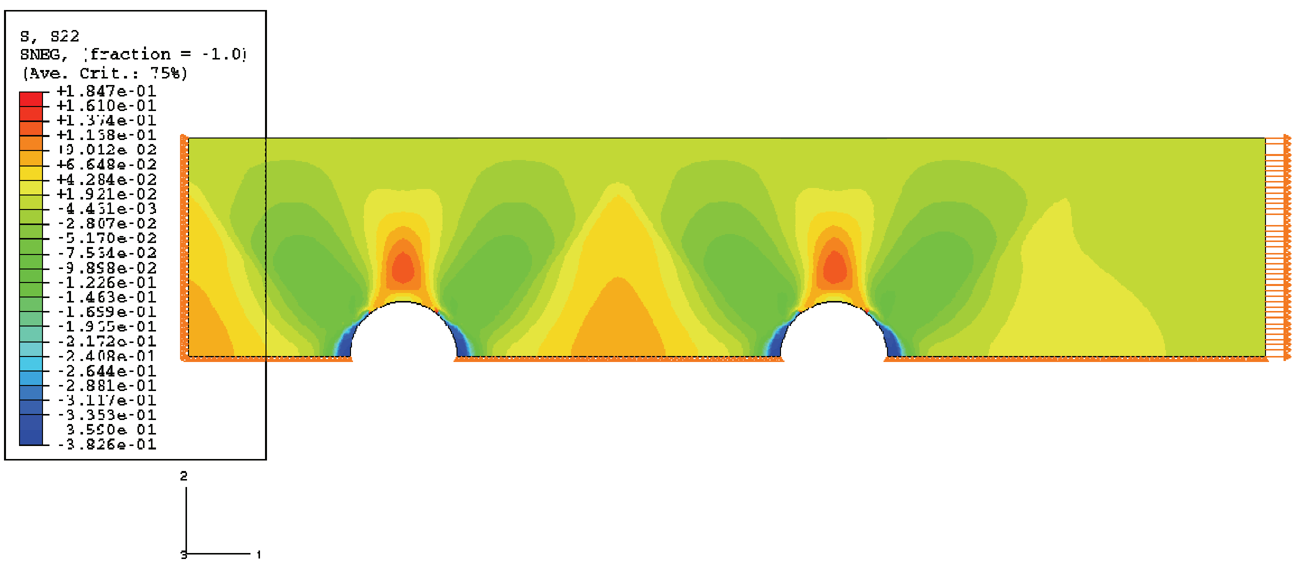

(b) Stress in the 2-2 Direction (S22)

FIGURE 3-8 Stress Distribution of the 100 mm Perforated Strip

(figure 3-8d) with the yielding point defined when the combination of stresses make the circle intersect $\tau_y = \sigma_y/2$. This phenomenon of large maximum principal stresses is experienced by elements positioned at an approximate 45° angle from the perforations as seen in figure 3-7.

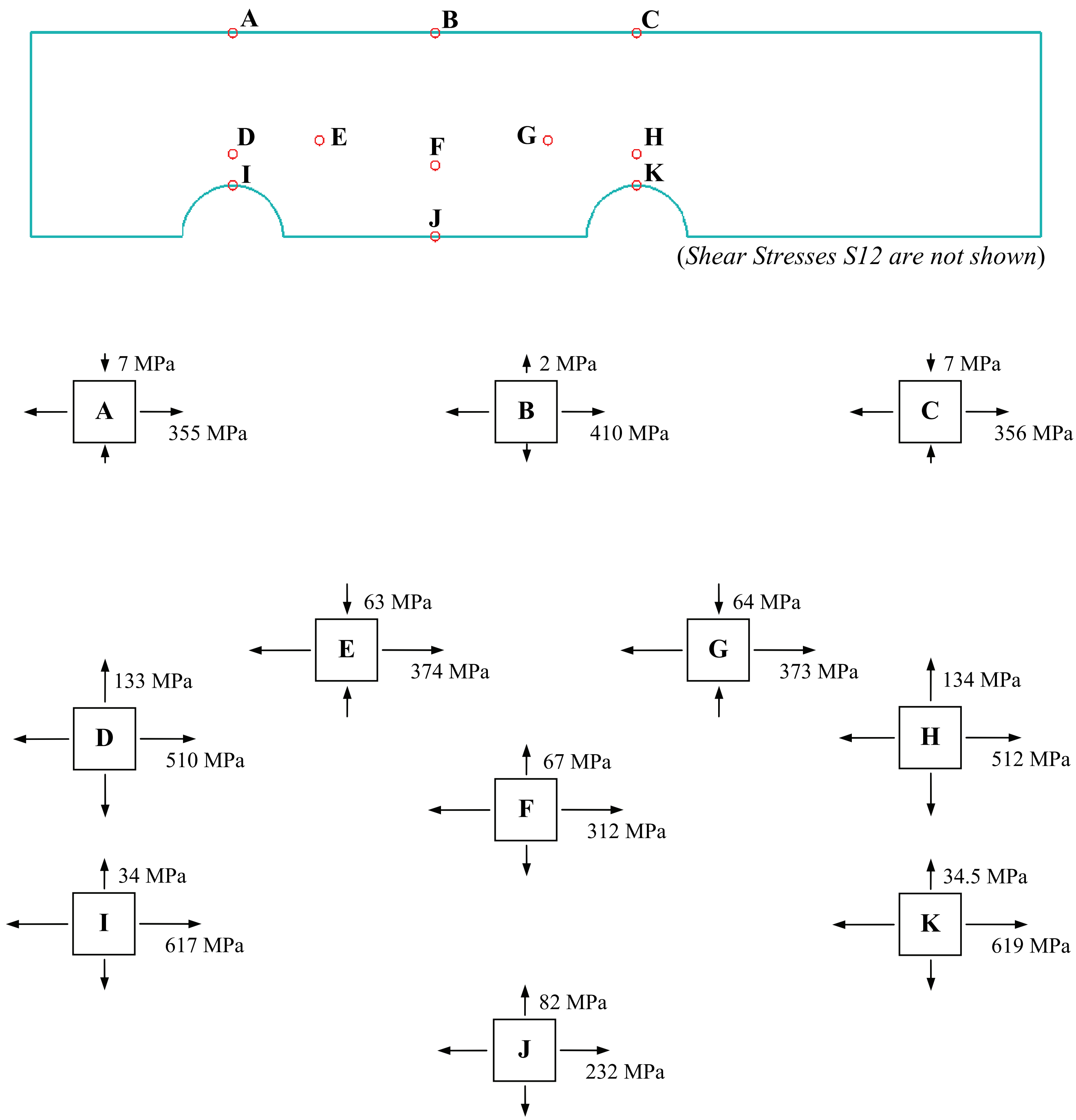

FIGURE 3-8 Stress Distribution of the 100 mm Perforated Strip – Cont'd
(c) Stress at Point of Interest

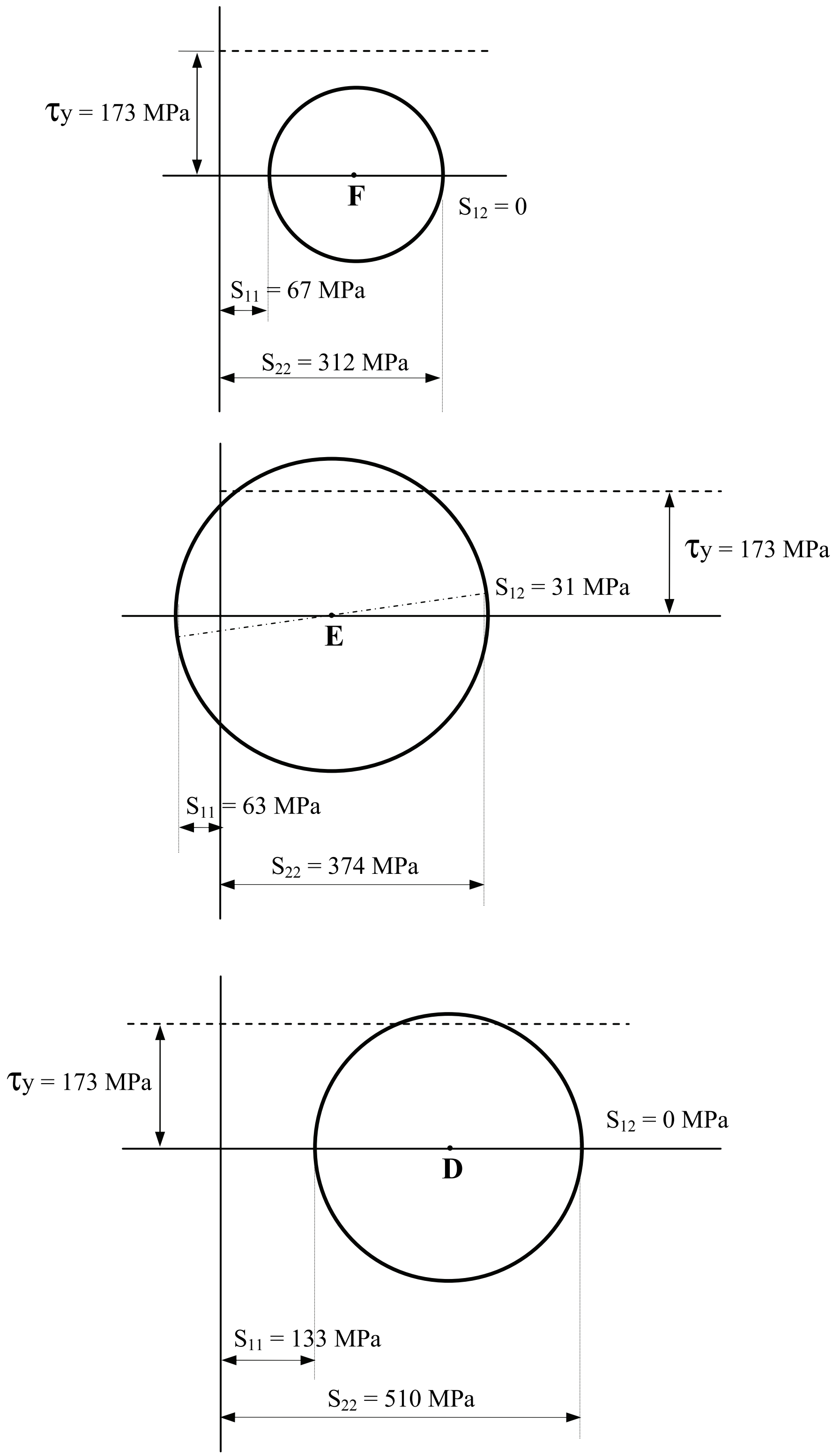

FIGURE 3-8 Stress Distribution of the 100 mm Perforated Strip – Cont'd
(d) Mohr's Circle at Element D, E and F

3.4.1 Perforated Strip as a Tension Member

The behavior of tension member is often described in terms of two key limit states: *fracture on net section* or *yielding on gross section*. For effective global element ductility of a tension member, it is important that yielding on gross section precede net section fracture as the applied axial load is increased (Dexter *et al.* 2002), i.e.:

$$F_u \cdot A_n \geq F_y \cdot A_g \tag{3-3}$$

where A_n is the net strip area; A_g is the gross strip area; F_u is the ultimate tensile strength; F_y is the yield strength. If (3-3) is satisfied, yielding in the net section due to localized high stress concentration developing there will have a chance to spread throughout the member and allow yielding to occur in the gross section as well. However, if (3-3) is not satisfied, inelastic deformations will remain localized to the region close to the perforation while the gross section remains elastic under increasing tensile load. Thus, failure would occur at the net section before the development of adequate total member elongation.

Substituting $A_n = \left(S_{diag} - D\right) \cdot t_p$ and $A_g = S_{diag} \cdot t_p$ into (3-3) and the equation can be rewritten as

$$\frac{D}{S_{diag}} \leq \left(1 - \frac{F_y}{F_u}\right) \tag{3-4}$$

For the A572 Gr. 50 (F_{y} = 50 ksi, F_{u} = 65 ksi) steel used in this study, (3-4) simplifies to $D/S_{diag} \leq 0.23$. This equation was used to examine the trend in maximum local strain in the strip for various perforation ratios as plotted in figure 3-9. Even though this equation assumes uniform longitudinal stress distribution across the net area when the ultimate stress is reached, it does not correspond to what has been observed by the authors (e.g., the axial stresses vary from 619 MPa to 356 MPa between elements K and C in Fig. 3-8) as further described in subsequent sections.

Figure 3-9 displays the maximum principal local strain ε_{max} in the strip versus perforation ratio D/S_{diag} when the strip has been elongated from 1% to 5%. The maximum principal local strain increases significantly as a function of perforation ratios over the range D/S_{diag} = 0.025 to 0.2 (which corresponds to D = 10 mm to 80 mm in this case), but then decreases gradually as the perforation ratio increases from D/S_{diag} = 0.2 to 0.6 (D = 80 mm to 240 mm), and resumes increasing slightly above D/S_{diag} = 0.6. Note that the increasing and decreasing parts are roughly separated by the D/S_{diag} = 0.23 limit (increasing on its left side of this limit and decreasing on its right side).

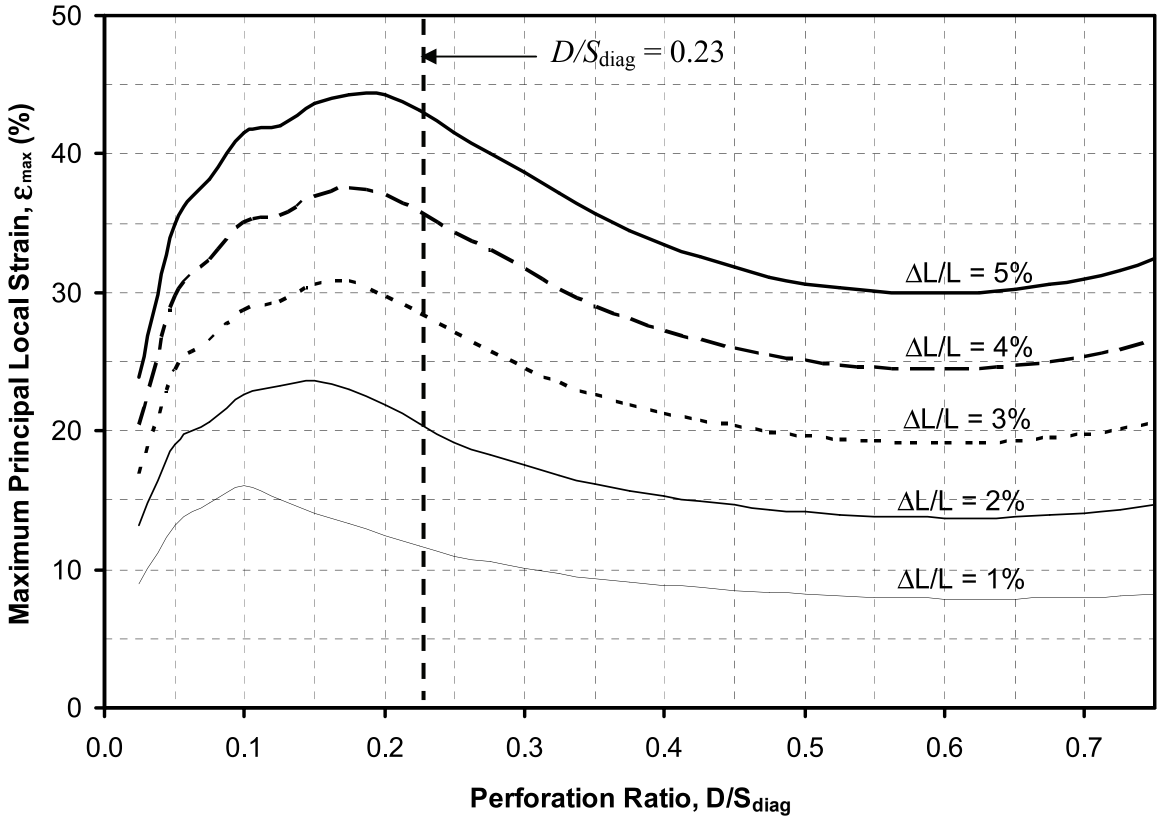

FIGURE 3-9 Maximum Local Strain ε_{max} versus Perforation Ratio D/S_{diag} (Idealized Stress-Strain Curve A572 Grade 50 Steel)

For the zone where perforation ratio $D/S_{diag} \leq 0.23$, yielding originally occurred in the elements close to the perforation edge would progressively be distributed to the gross section as the tensile load increases. As a result and because of strain hardening, the net section has a significant capacity to stretch beyond the point for which the strip has reached the monitored total strips elongation; as the perforation ratio increases, the decreased net section obviously has to stretch more to reach the same monitored elongation. However, for the zone where perforation ratio $D/S_{diag} \geq 0.23$, yielding will be localized to the region close to the perforation while the gross section remains progressively more elastic. By the time the monitored total strip elongation is reached, the shell element close to the perforation edges has reached higher strain and plastic deformation. As perforation diameter further increases, this target limit strain is reached earlier, corresponding to a lesser magnitude of total member elongation. However, note that in SPSW applications even though gross section yielding cannot develop in some cases, the spread of localized yielding, and repetition of it at multiple holes for the perforated plate configuration considered, still make it possible for the perforated plate to reach target total elongations adequate to meet the maximum drift demands for actual SPSW.

3.4.2 Effect of Holes on Strip Global Deformation

The effect of holes on strip global deformation is illustrated in figure 3-10 where uniform distributed strip elongation ε_{un} versus perforation ratio D/S_{diag} are plotted at 1, 5, 10, 15, and 20% maximum principal local strain. At higher monitored strain ε_{max} equal to 10% to 20%, the total strip elongation decreases significantly at small perforation ratios (i.e. D/S_{diag} = 0.025 to 0.1 or D = 10 mm to 40 mm), and then gradually increases between D/S_{diag} = 0.1 and 0.6 (D = 40 mm to

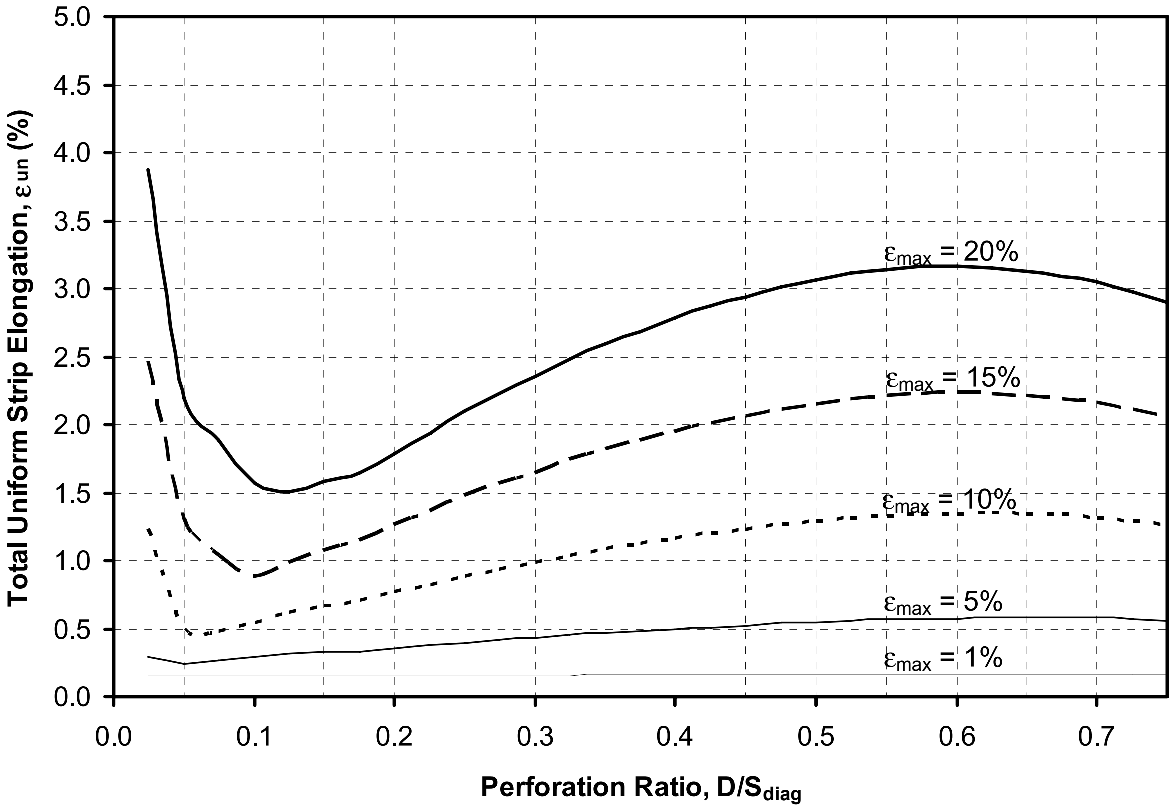

FIGURE 3-10 Uniform Distributed Strip Axial Strain ε_{un} versus Perforation Ratio D/S_{diag} (ST1 Model, Idealized Stress-Strain Curve A572 Grade 50 Steel)

240 mm) before slightly decreasing again for $D/S_{diag} > 0.6$. At the lower monitored local strain levels (i.e. ε_{max} = 1% and 5%), the total strip elongation remains almost constant for the entire range of perforation diameters.

One might argue that an increase in perforation diameter (for $D/S_{diag} \geq 0.23$) leading to an increase in total strip elongation (for the same monitored local strain) is counterintuitive. For example, to reach a 20% maximum local strain, the strip having a 100 mm perforation diameter has elongated 21.0 mm (ε_{un} = 2.10%) but the strip with 200 mm perforation diameter strip elongated even more (as much as 30.7 mm for ε_{un} = 3.07%) before this local strain limit was reached. Note that in this case, ε_{un} equal to $2 \cdot \delta / L$. To explain this behavior, it is first useful to compare the respective area of strip stressed beyond the yield point ($\varepsilon_y = 1.725 \times 10^{-3}$) for different strips, such as the strips having 100 and 200 mm diameter holes in figure 3-11. While it was originally suspected that the greater elongation of the strip having 200 mm diameter holes might have been attributed to the longer length over which yielding spread (as a percentage of total plate length), figure 3-11 actually shows that this is not the case. The area over which inelastic behavior develops (i.e., inelastic area) for the strip having 100 mm diameter holes is larger than that for the strip having 200 mm diameter holes. The percentage of inelastic area over strip net area is about 60% and 43% for the strip having 100 and 200 mm perforations, respectively. Note that these percentages become 58% and 36% if the inelastic area is divided by the gross strip area (i.e., a constant value of 1000 mm × 200 mm = 200.000 mm^2 in this case). However, the magnitude of the inelastic strain develop within these areas of inelastic deformations differs very significantly. One way to capture this difference is by comparing the energy dissipated by plastic deformation (ALLPD – *ABAQUS definition*) for both plates. Even though the inelastic area of the 100 mm perforated strip are bigger than that of the 200 mm perforated strip as shown in figure 3-11, its plastic deformation energy (ALLPD equal to 5530 kNmm) is smaller than for the 200 mm perforated strip (ALLPD equal to 5734 kNmm). This confirms that shell elements close to a bigger perforation edge stretched more than those close to a smaller perforation edge.

To provide additional insight into this behavior, a variation of figure 3-10 is plotted in figure 3-12 by normalizing the total strip elongation by the factor $N_r.D/L$, which is the ratio of perforated

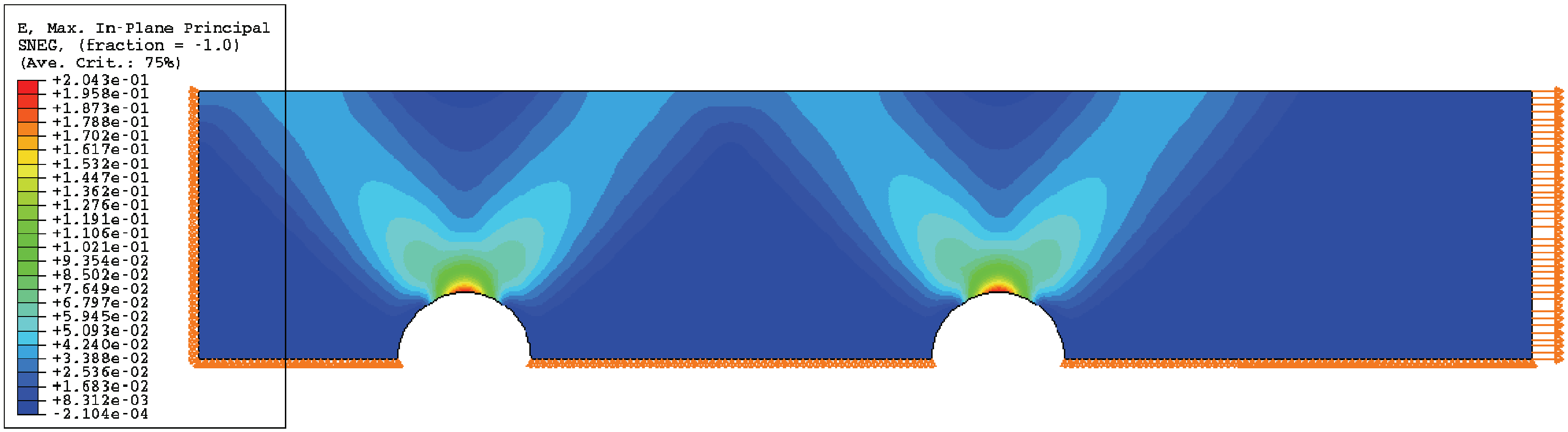

(a) Maximum In-Plane Principal Strain Contours, D = 100 mm (D/S_{diag} = 0.25)

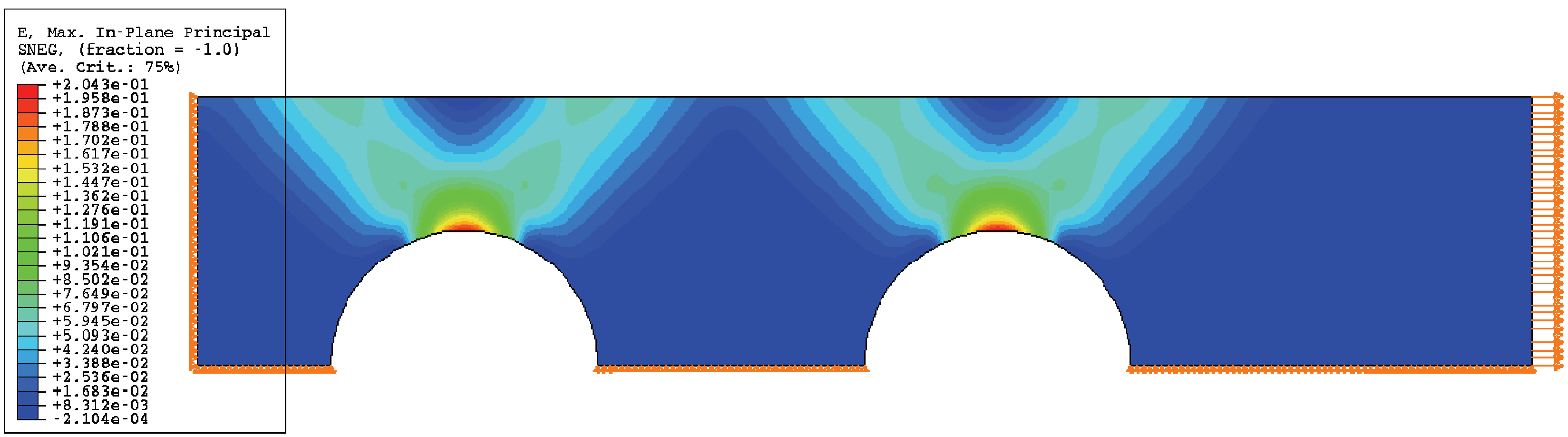

(b) Maximum In-Plane Principal Strain Contours, D = 200 mm (D/S_{diag} = 0.50)

FIGURE 3-11 Strain Comparison at 20% Maximum Local Strain
ST1 Model, Idealized Trilinear Stress-Strain Curve A572 Gr. 50 Steel

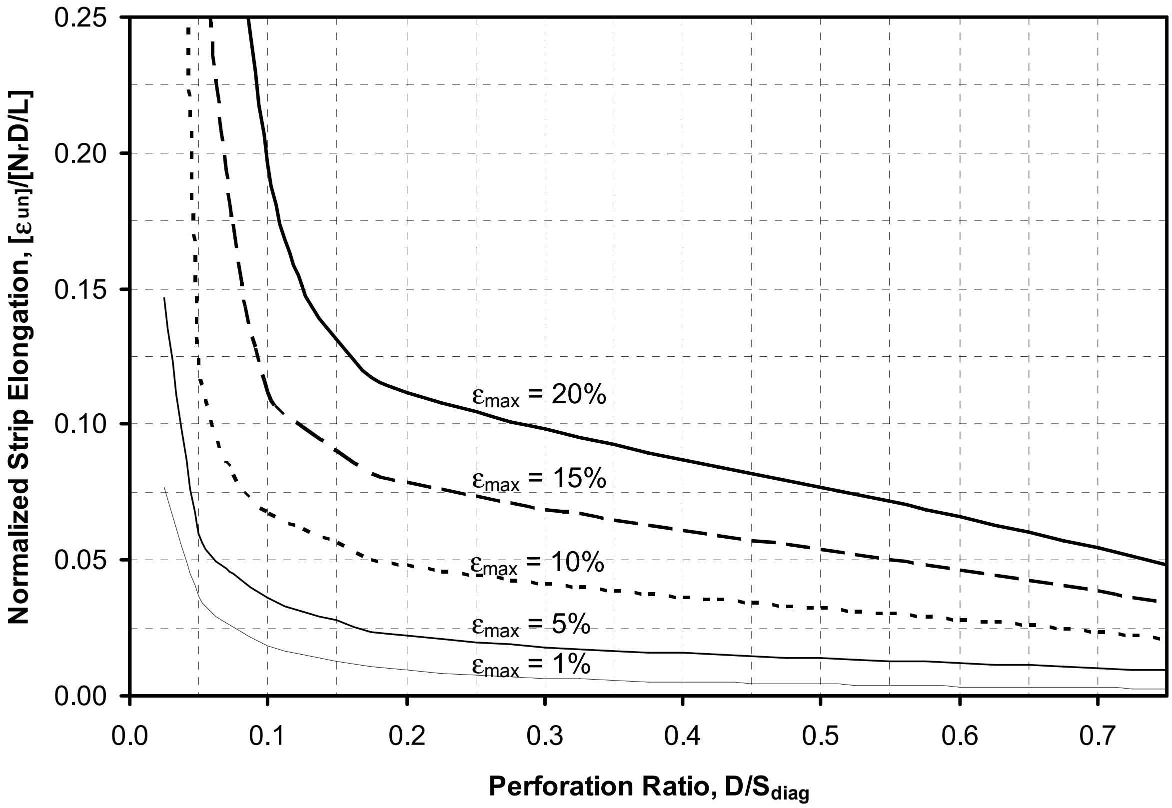

FIGURE 3-12 Normalized Strip Elongation $[\varepsilon_{un}]/[N_r \cdot D/L]$ versus Perforation Ratio D/S_{diag} (ST1 Model, Idealized Stress-Strain Curve A572 Grade 50 Steel)

length to overall length in a strip (Vian 2005). Simultaneously, the vertical axis is expressed as $2 \cdot \delta / N_r.D$, which is the total strip displacement divided by a total length of perforations over the entire strip. As shown in the figure, for all cases the normalized strip elongation gradually decreases as the perforation ratio increases.

3.5 Effect of Boundary Conditions

It was previously assumed in Section 3.2.1 that no interaction exists between adjacent strips occurred, and that each strip therefore behaves as an independent strip. However, to investigate the significance of this assumption, it is instructive to also consider (for comparison purposes), strips fully restrained laterally, as a worst case of the possible interaction that could develop with adjacent strips. Considering this hypothesis, a new model was developed as shown in figure 3-13. The interface edge is idealized such that it is restrained against displacement in the vertical direction, which is the only difference from figure 3-3(b), while the other properties remain the same. To distinguish this model and the previous model, they are labeled ST2 and ST1, respectively. The behavior of ST2 model was examined in this section and afterward compared to that of the ST1 model for the same range of perforations.

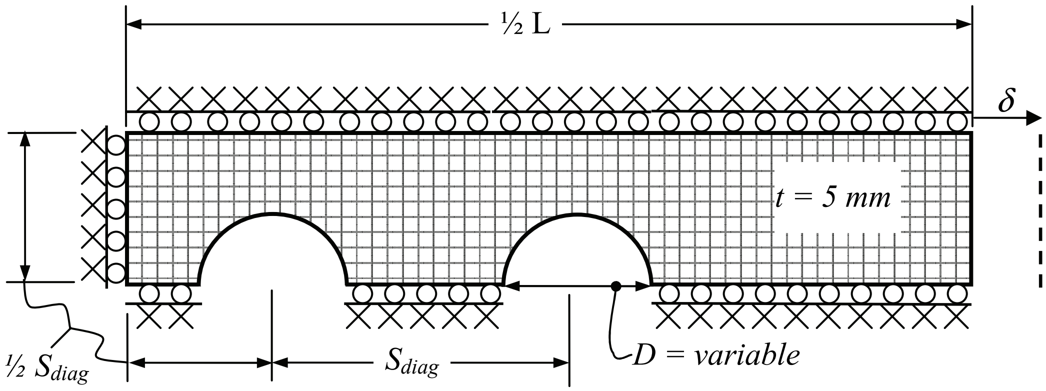

FIGURE 3-13 Schematic Representation of "Quadrant" Part – ST2 Model (*modified from* Vian 2005)

Typical plate deformations, in-plane principal maximum stress contours, and strain contours of the ST2 model are shown in figure 3-14 for 100 mm perforation diameter when maximum principal local strain ε_{max} reached 20%. The ST2 stress and strain contours are significantly different from the ST1 contours. In this case, the stress and strain concentrations are initiating at the perforations edges but then zone of yielding are radiating vertically to the top edge. This is because the vertical restraints at the top edges prevented deformations of the shell elements in the 2-2 direction due to Poisson's-ratio effect, and only allowed movement in the 1-1 direction. As a result, higher stress and strain are localized in the elements that line up from the perforations to the top edge.

Study of holes effects to the strip global deformation were also conducted within ST2 model with the same range of perforation diameters and monitoring procedures as for the ST1 case. The results in terms of the uniform strip elongation ε_{un} and the normalized strip elongation $\varepsilon_{un}/(N_r \cdot D/L)$ are plotted as a function of perforation ratio in figures 3-15 and 3-16, respectively. For comparison, the normalized strip elongation $\varepsilon_{un}/(N_r \cdot D/L)$ of the two models was compared at ε_{max} equal to 15% and 20%, and plotted in figures 3-17 and 3-18, respectively. It is observed from those figures, that the normalized strip elongation is higher for the ST2 model than for the ST1 model for the entire range of perforations and monitored strain. For example, for the perforation

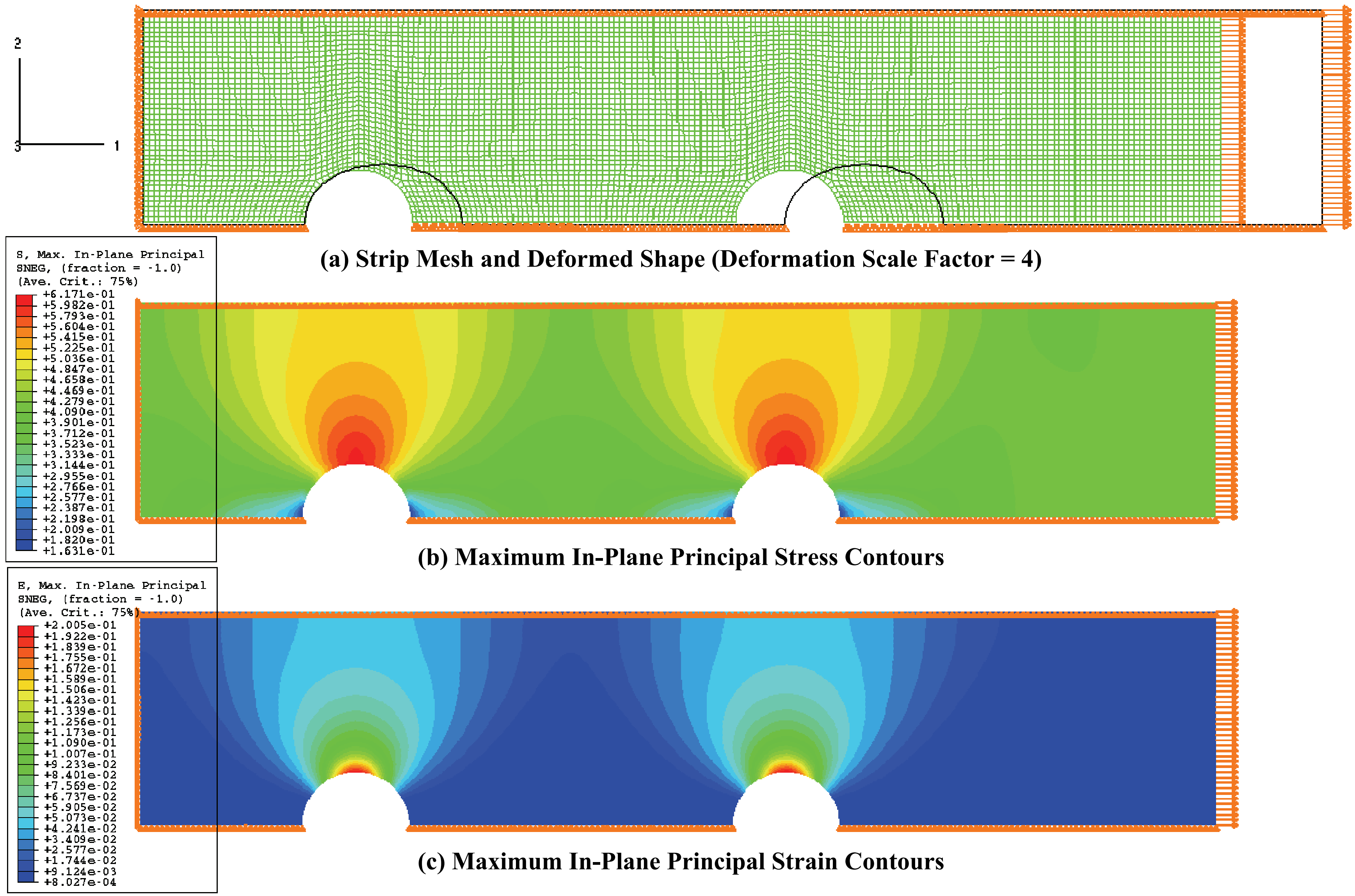

(a) Strip Mesh and Deformed Shape (Deformation Scale Factor = 4)

(b) Maximum In-Plane Principal Stress Contours

(c) Maximum In-Plane Principal Strain Contours

FIGURE 3-14 Typical Strip Analysis Results at 20% Maximum Local Strain
ST2 Model, Idealized Trilinear Stress-Strain Curve A572 Gr. 50 Steel, D = 100 mm (D/S_{diag} = 0.25)

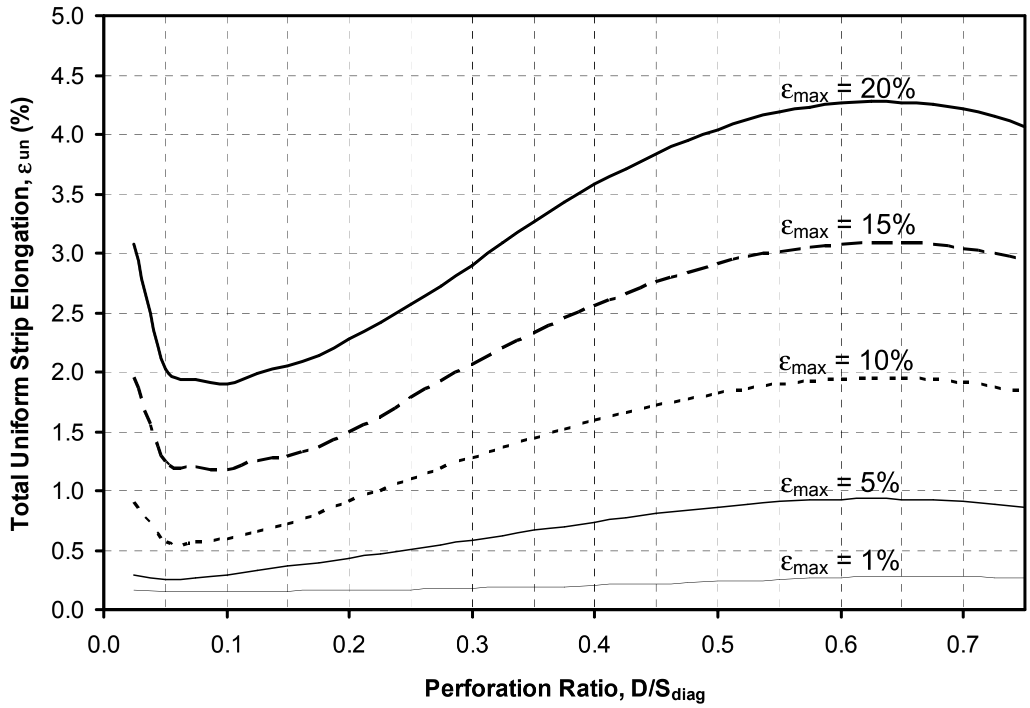

FIGURE 3-15 Uniform Distributed Strip Axial Strain ε_{un} versus Perforation Ratio D/S_{diag} (ST2 Model, Idealized Stress-Strain Curve A572 Grade 50 Steel)

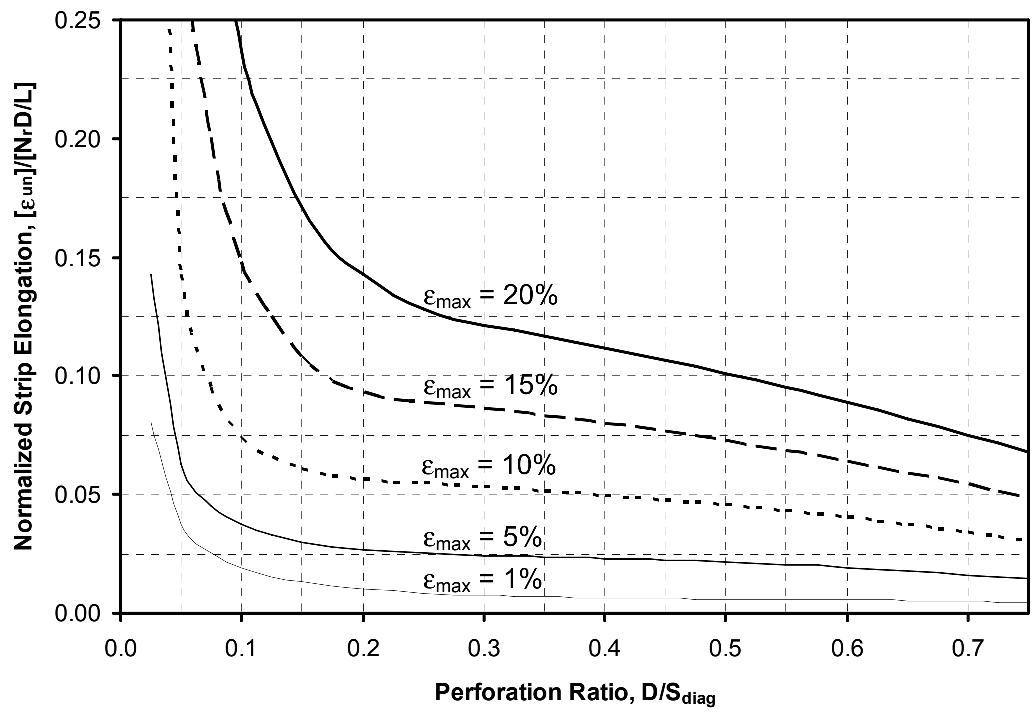

FIGURE 3-16 Normalized Strip Elongation $[\varepsilon_{un}]/[N_r \cdot D/L]$ versus Perforation Ratio D/S_{diag} (ST2 Model, Idealized Stress-Strain Curve A572 Grade 50 Steel)

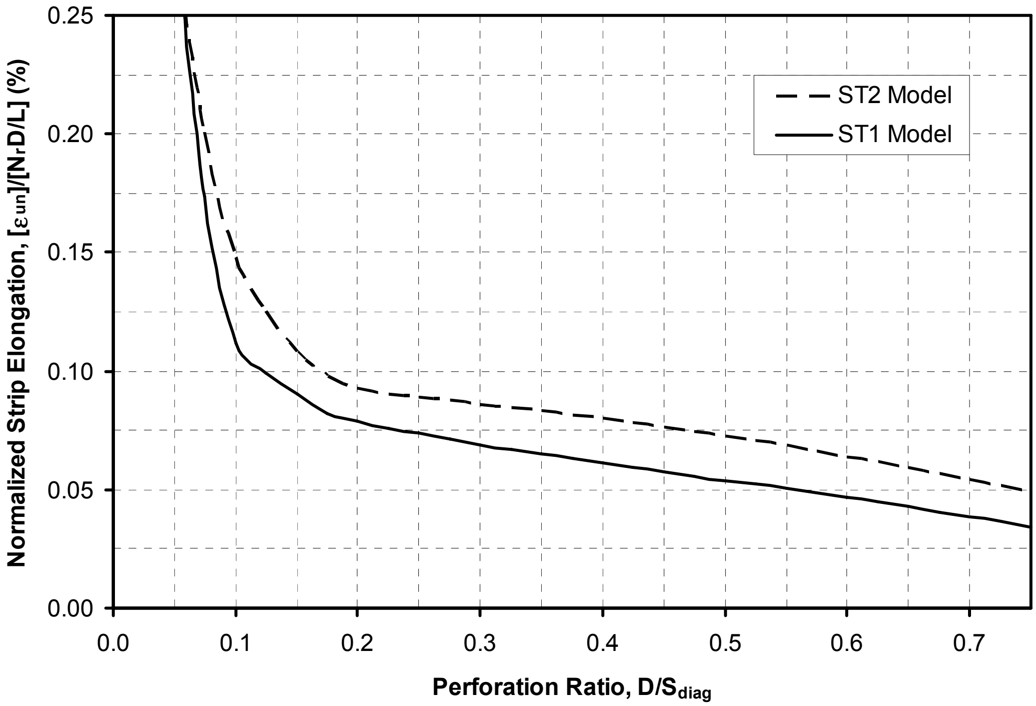

FIGURE 3-17 Comparison of Normalized Strip Elongation [ε_{un}]/[$N_r \cdot D/L$] versus Perforation Ratio D/S_{diag} at ε_{max} = 15% for Two Different Finite Element Models

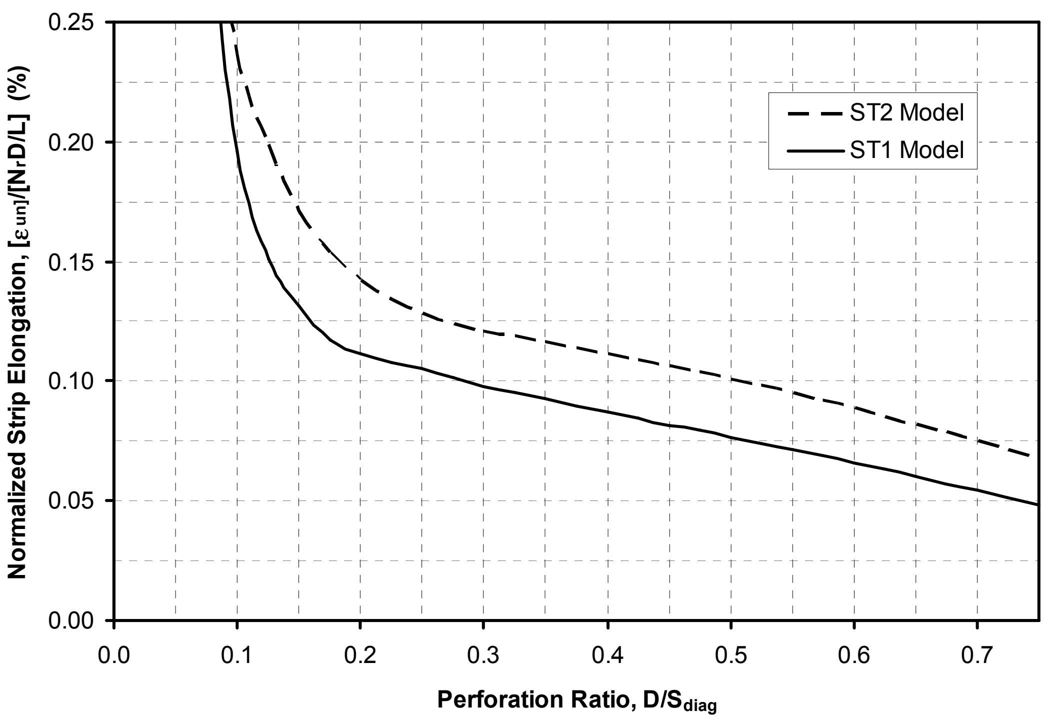

FIGURE 3-18 Comparison of Normalized Strip Elongation [ε_{un}]/[$N_r \cdot D/L$] versus Perforation Ratio D/S_{diag} at ε_{max} = 20% for Two Different Finite Element Models

ratio D/S_{diag} = 0.250 (which corresponds to D = 100 mm), the normalized strip elongation of the ST2 model are 0.09 (ε_{un} = 1.78%) and 0.13 (ε_{un} = 2.57%) at 15 and 20% maximum principal local strain, respectively. On average, these values are 1.3 times higher than those of the ST1 model which are 0.07 (ε_{un} = 1.48%) and 0.10 (ε_{un} = 2.10%) for the same respective monitored strains. These results indicate that because the ST2 model has more constraints, it required higher tensile load (or strip elongation) to reach the same monitored strain than for the ST1 model. Overall, the differences in results remain small and not of concern in the perspective of SPSW behavior. However, it is believed that the boundary conditions of model ST1 are more representative of those that exist in SPSW, and results in Section 4 will confirm this postulate.

3.6 Effect of Material Idealizations

In this section, to investigate how the response of perforated SPSW could be affected by the model assumed for type of steel used, three material models were defined to represent various ways to express the constitutive stress-strain relationship of A572 Gr.50 steel. They are the idealized tri-linear stress-strain model used by Vian (2005), the monotonic uniaxial non-cyclic stress-strain model shown in figure 3-19 (from Salmon and Johnson 1995), and an elasto-perfectly plastic bilinear stress-strain model with F_y = 345MPa and ε_y = 0.17%. This latter bilinear model is considered to examine how the absence of strain hardening could affect the strip global deformation.

The first material model is the one that was applied to the ST1 model of figure 3-3 and for which corresponding response and behavior was reported in Section 3.4. This section describes the behavior of two modified-ST1 models using the last two material models. Note that parameters for the two additional models are converted to "true" stress and logarithmic plastic strain by using (3-1) and (3-2) before inputting to ABAQUS input files. The "true" stress versus logarithmic plastic strain of the monotonic uniaxial non-cyclic stress-strain of ASTM A572 Gr. 50 steel is plotted in figure 3-20. In ABAQUS/Standard, perfectly plastic behavior is defined by inputting a single yield stress and strain (HKS 2004b). The same analysis as previously performed for the ST1 model was also conducted for the two new models and results were compared to that of the ST1. To distinguish them, the two new models are labeled ST1R and ST1B for the monotonic real (R) and bilinear (B) material models, respectively.

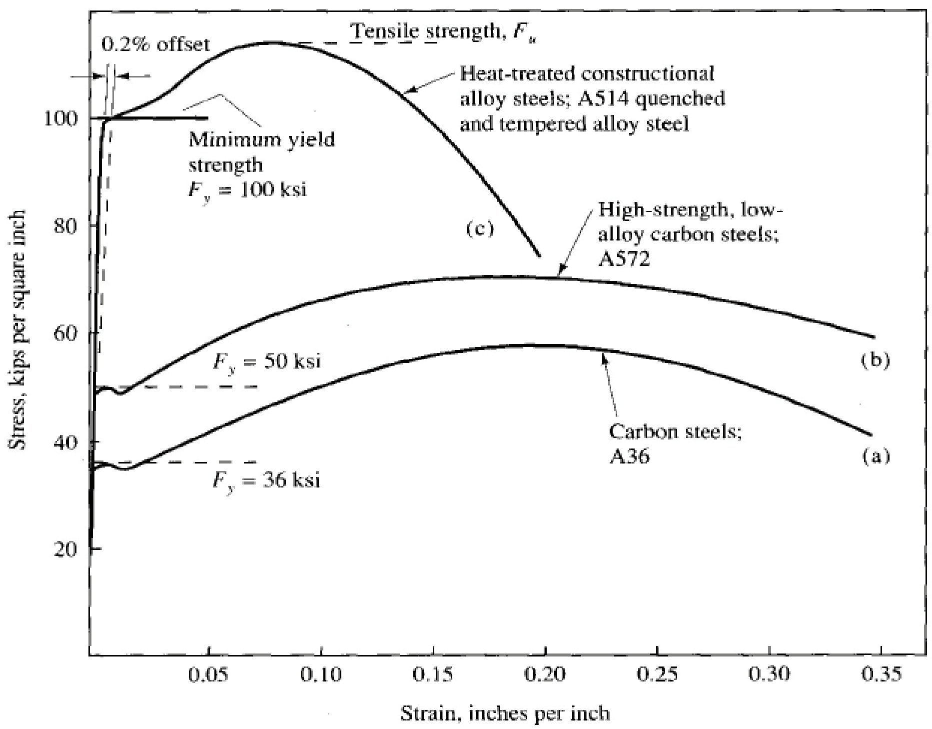

FIGURE 3-19 Monotonic Uniaxial Non-Cyclic Stress-Strain Curves for Various Steels (Salmon and Johnson 1995)

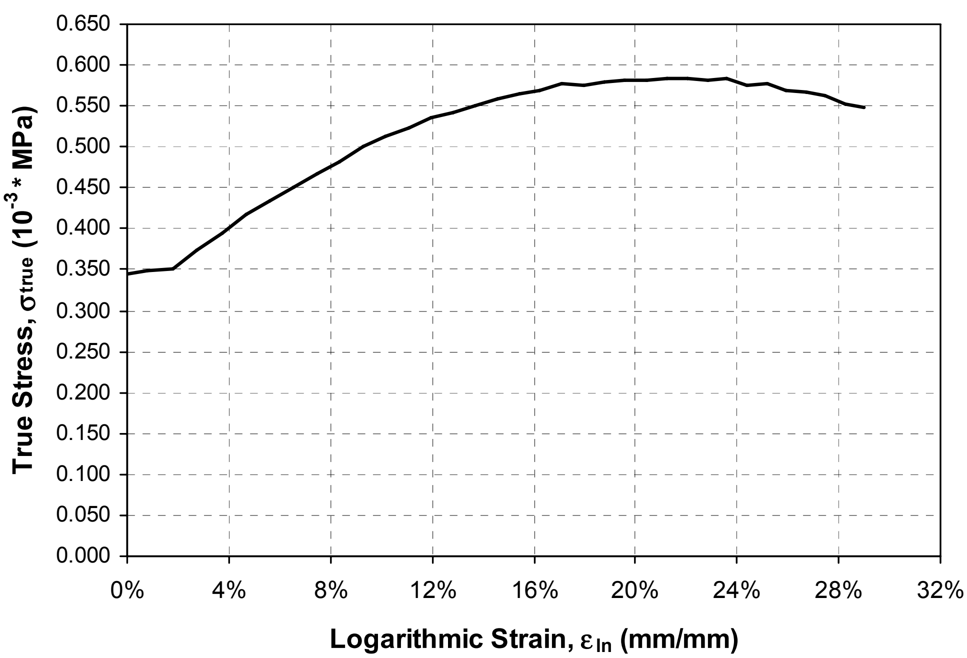

FIGURE 3-20 True Stress σ_{true} versus Logarithmic Plastic Strain $\varepsilon_{\ln}^{pl}$ of Monotonic Uniaxial Non-Cyclic Stress-Strain for A572 Gr. 50 Steel (*ABAQUS Definition*)

Plate deformations, in-plane principal maximum stress contours, and strain contours of the ST1R and ST1B model for the strip having a 100 mm perforation diameter when maximum principal local strain ε_{max} reached 20% are shown in figures 3-21 and 3-22, respectively. As expected, the STIR model behaves similar to the ST1 model where high stress and strain concentrate at the perforation edges and then zone of yielding radiate to the top edges at approximately 45° angles with respect to the horizontal axis. Inward deformations at the top edge also are near identical. However, in the ST1B model, yielding is significantly more concentrated close to the perforations and spreads to much fewer adjacent elements.

The uniform strip elongation ε_{un} and the normalized strip elongation $\varepsilon_{un}/(N_r{\cdot}D/L)$ versus perforation ratio D/S_{diag} corresponding to the two new models are plotted in figures 3-23 to 3-26, respectively. Finally, the normalized strip elongation $\varepsilon_{un}/(N_r{\cdot}D/L)$ of the three analyzed models was compared at ε_{max} equal to 15% and 20%, and plotted in figures 3-27 and 3-28, respectively. Among the three material models, ST1B elongated significantly less than the ST1 and ST1R models for each target local strain. For example, for perforation ratio D/S_{diag} equal to 0.25 (D = 100 mm), the normalized strip elongations of the ST1B model are 0.03 (ε_{un} = 0.56%) and 0.04 (ε_{un} = 0.72%) at 15 and 20% maximum principal local strain, respectively. On average, these values are only one-third of the ST1 and ST1R values. On the other side, the ST1 and ST1R are in good agreement; the difference between the two is less than 4%.

This confirms the importance of duly modeling strain hardening in the material model to properly capture the spread of yielding needed in this system to allow the strips to reach the total ductile elongation needed to accommodate the drift demands in perforated SPSW.

3.7 Summary

The finite element program ABAQUS/Standard was used to investigate the behaviors of individual perforated strips. Mesh accuracy and mesh convergence study were first done on the 100 mm perforated strip model (ST1 Model with the idealized tri-linear stress-strain material model and no interaction between adjacent strips). The non-linear behavior of various perforated strip models with perforation diameter varying from 10 to 300 mm was then considered. The

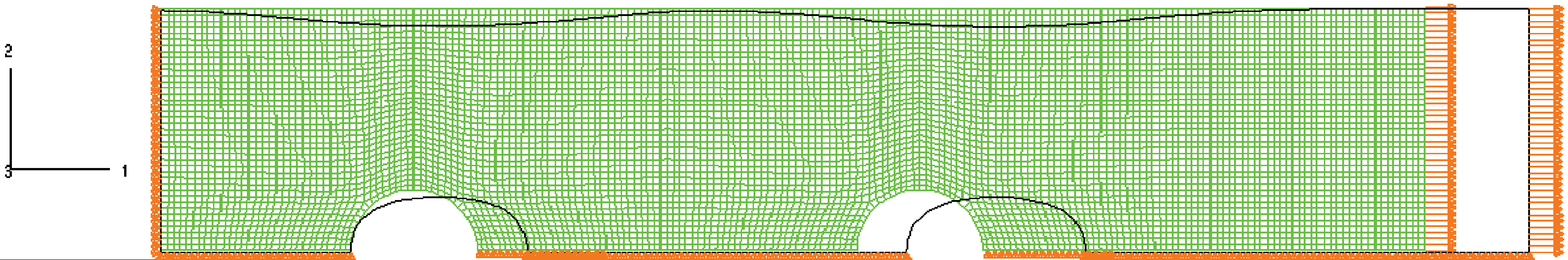

(a) Strip Mesh and Deformed Shape (Deformation Scale Factor = 4)

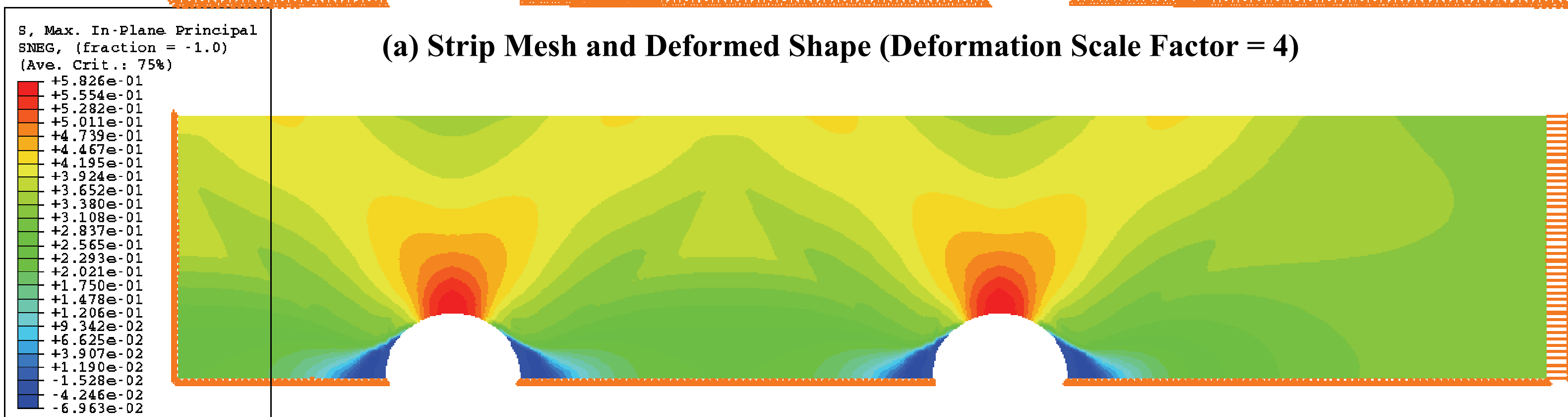

(b) Maximum In-Plane Principal Stress Contours

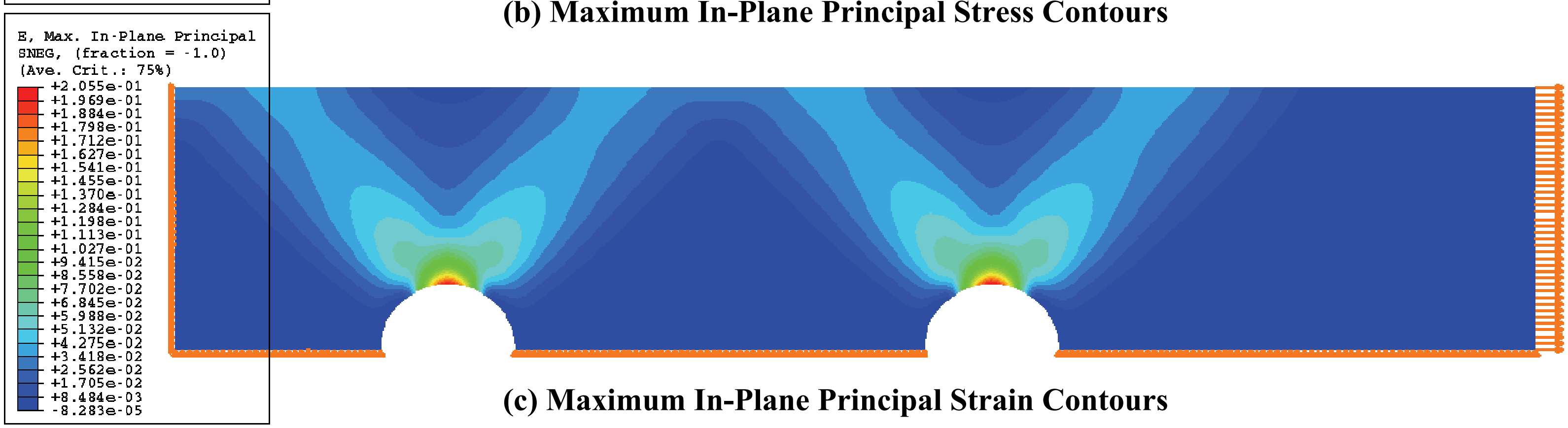

(c) Maximum In-Plane Principal Strain Contours

FIGURE 3-21 Typical Strip Analysis Results at 20% Maximum Local Strain
ST1R Model, Real Stress-Strain Curve A572 Gr. 50 Steel, D = 100 mm (D/S_{diag} = 0.25)

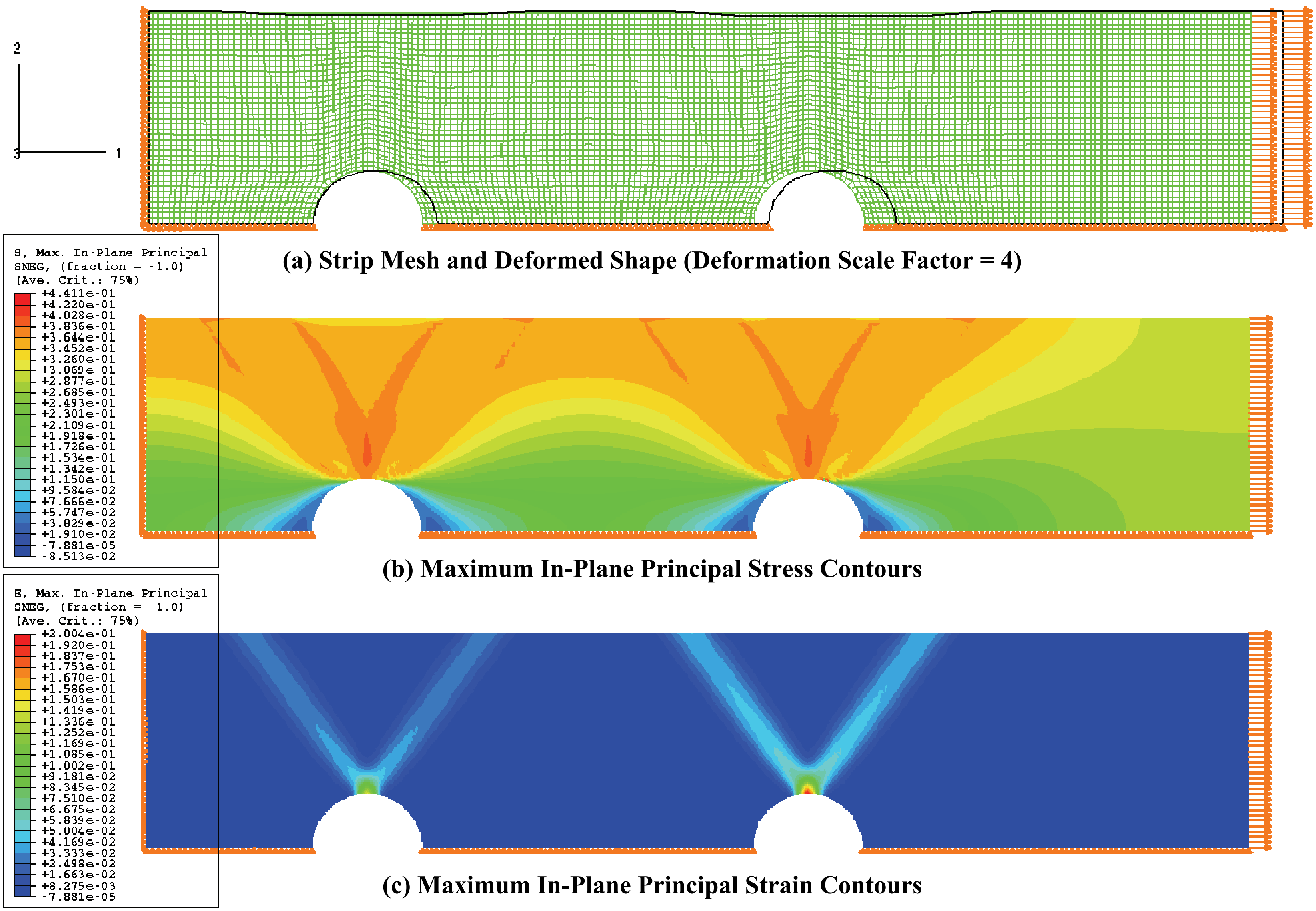

(a) Strip Mesh and Deformed Shape (Deformation Scale Factor = 4)

(b) Maximum In-Plane Principal Stress Contours

(c) Maximum In-Plane Principal Strain Contours

FIGURE 3-22 Typical Strip Analysis Results at 20% Maximum Local Strain
STIB Model, Bilinear Stress-Strain Curve A572 Gr. 50 Steel, *D* = 100 mm (D/S_{diag} = 0.25)

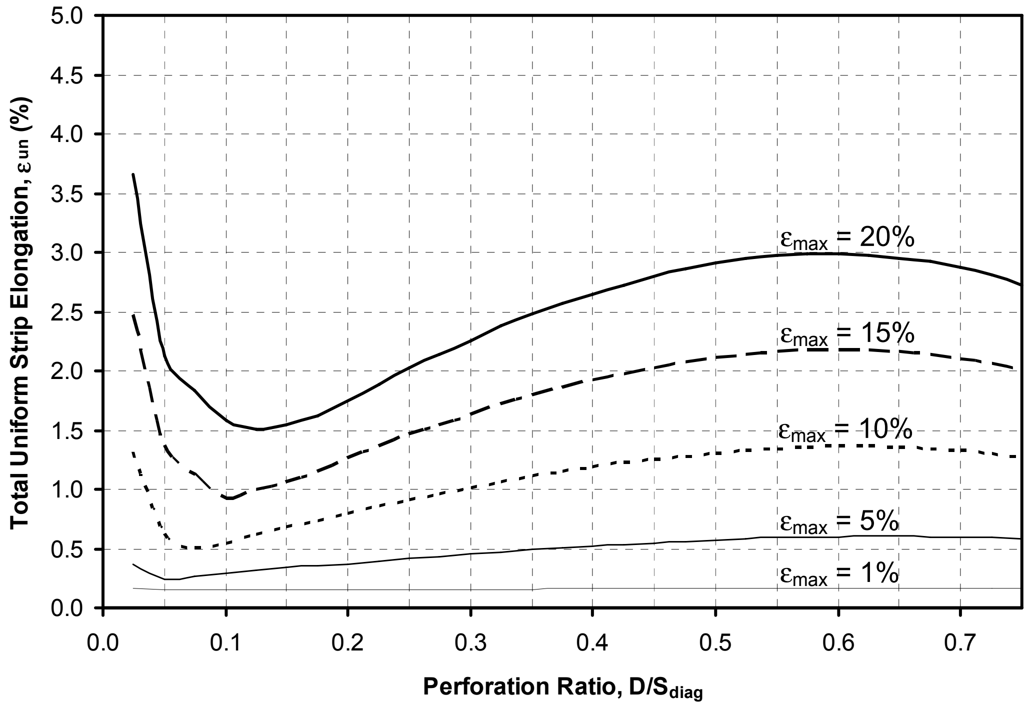

FIGURE 3-23 Uniform Distributed Strip Axial Strain ε_{un} versus Perforation Ratio D/S_{diag} (ST1R Model, Real Stress-Strain Curve A572 Grade 50 Steel)

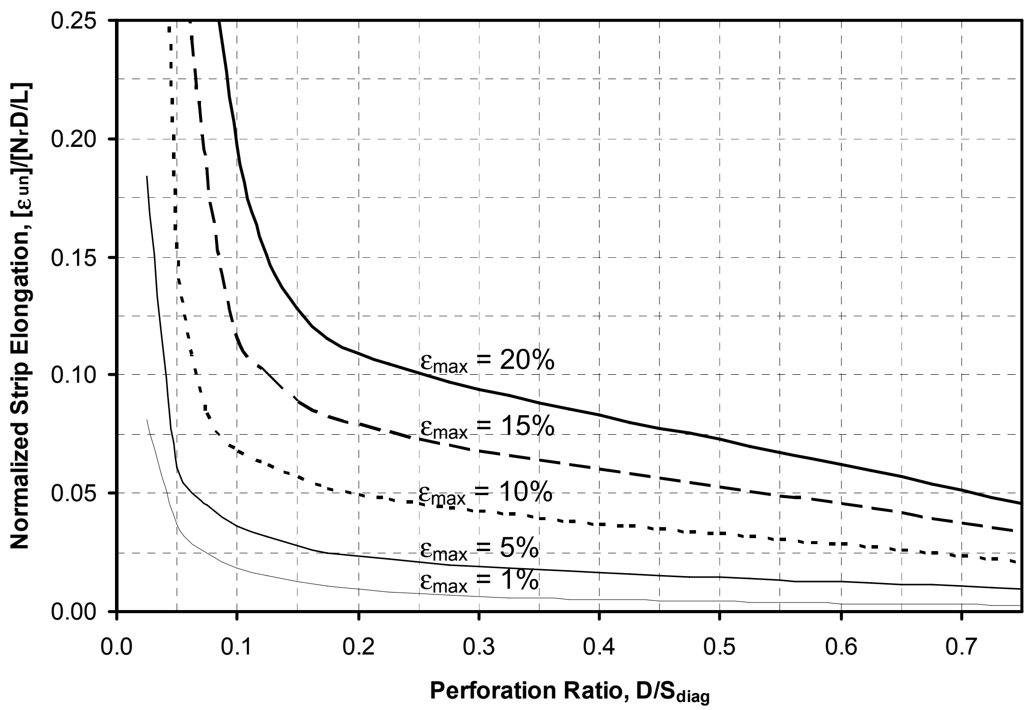

FIGURE 3-24 Normalized Strip Elongation $[\varepsilon_{un}]/[N_r \cdot D/L]$ versus Perforation Ratio D/S_{diag} (ST1R Model, Real Stress-Strain Curve A572 Grade 50 Steel)

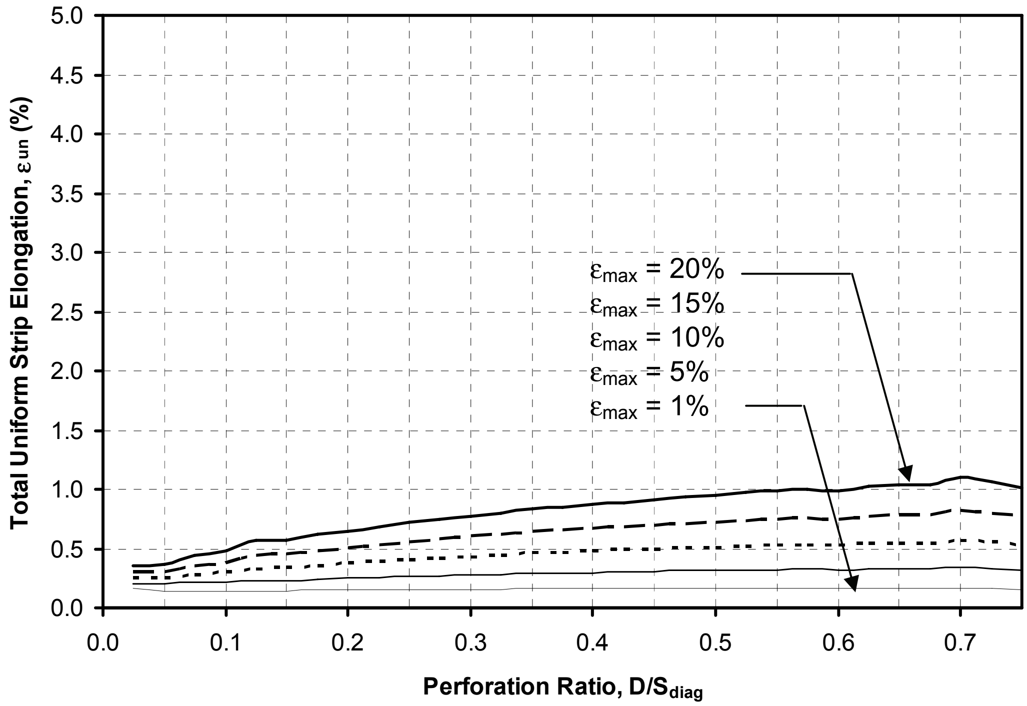

FIGURE 3-25 Uniform Distributed Strip Axial Strain ε_{un} versus Perforation Ratio D/S_{diag} (ST1B Model, Bilinear Stress-Strain Curve A572 Grade 50 Steel)

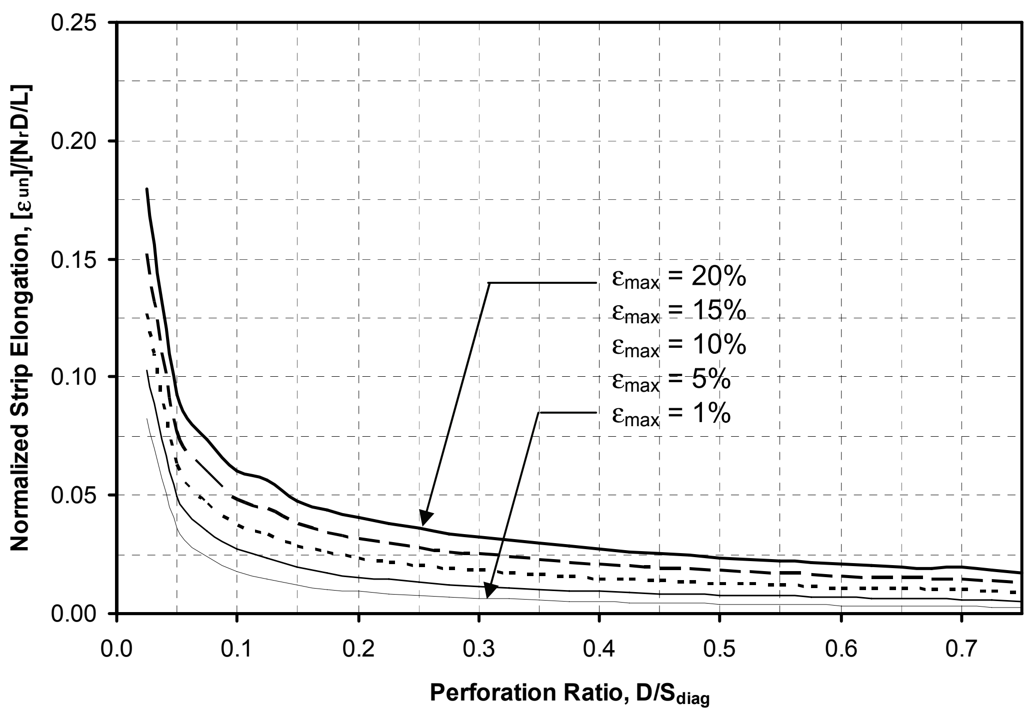

FIGURE 3-26 Normalized Strip Elongation $[\varepsilon_{un}]/[N_r \cdot D/L]$ versus Perforation Ratio D/S_{diag} (ST1B Model, Bilinear Stress-Strain Curve A572 Grade 50 Steel)

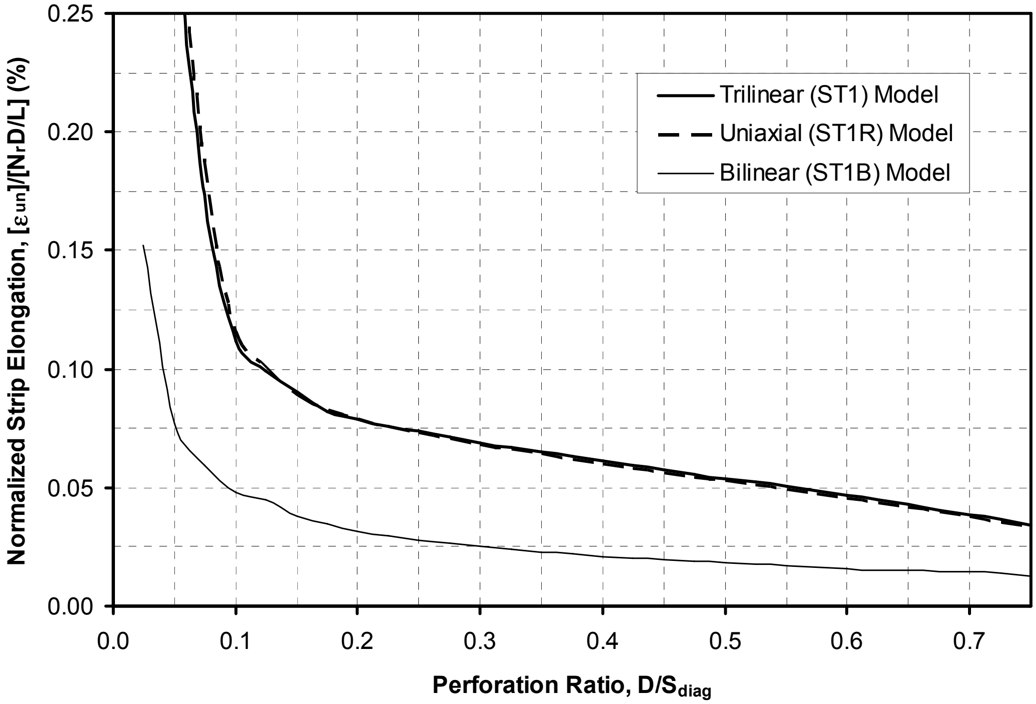

FIGURE 3-27 Comparison of Normalized Strip Elongation [ε_{un}]/[$N_r \cdot D/L$] versus Perforation Ratio D/S_{diag} at ε_{max} = 15% for Three Different Material Models

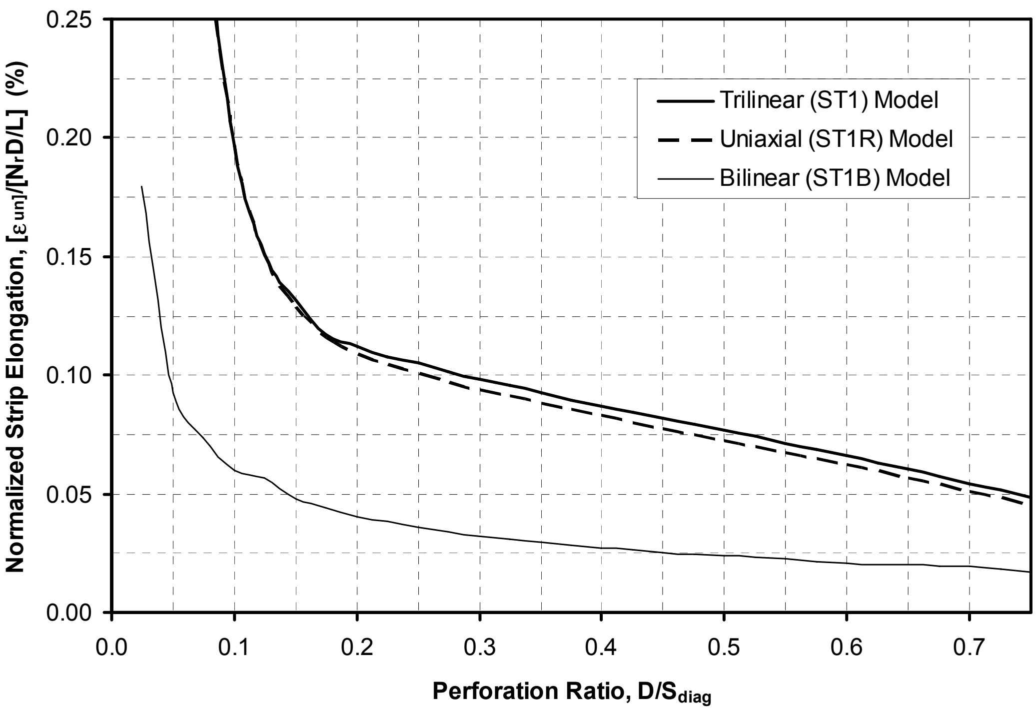

FIGURE 3-28 Comparison of Normalized Strip Elongation [ε_{un}]/[$N_r \cdot D/L$] versus Perforation Ratio D/S_{diag} at ε_{max} = 20% for Three Different Material Models

results were presented in terms of stress-strain distribution throughout the strip section as well as in terms of global deformation. Considering a large number of data points and fine mesh (maximum mesh size of 5 x 5 mm), “smooth” curves of total uniform strip elongation versus perforation ratio were developed thus enhancing and expanding results previously reported by Vian (2005). Three different models were then developed to study the effect of boundary conditions and material idealizations; the ST2 model developed to consider the possible interaction between adjacent strips, the ST1R applied the monotonic real material model, and the ST1B applied bilinear material model. Notable changes in stress and strain distribution were observed when modifying the boundary conditions or when eliminating the strain hardening from the material model.

The strip elongation of the ST2 model is 1.3 times higher than that of the ST1 model and the model without strain hardening (ST1B) elongated only one-third of the model with strain hardening (ST1 and ST1R) when the limit states of 15 and 20% was reached. The ST1 and ST1R model are in good agreement; the difference between the two is less than 4% at the same limit states. These studies provide preliminary knowledge useful in understanding the behavior of a complete wall in Section 4.

SECTION 4

ANALYSIS OF PERFORATED STEEL PLATE SHEAR WALLS

4.1 General

The preceding section described the finite element analysis of individual perforated strips as key elements to understand the behavior of perforated SPSW. This section describes the finite element analysis of full SPSW, using these more advanced and complete models to verify the appropriateness and accuracy of the individual strip model results. Specific finite element options in ABAQUS/Standard utilized to capture the real panel behaviors are also described. Finite element considerations discussed include geometry modeling and mesh algorithm, element definition, initial imperfection, boundary conditions, and stability of models. Three different models analyzed are investigated. Models including variation in infill thickness, perforation diameter, material idealization, and element definitions are considered, and significance of the corresponding results are assessed. The applicability of the equation proposed by previous researchers to approximate the strength of a perforated panel is re-assessed. Finally, some design recommendations and consideration are presented.

4.2 Finite Element Description of Panel Model

Panel dimensions studied in this section are similar to the specimen that Vian (2005) investigated as shown in figure 2-18. The frame's centerline dimensions were 4000 mm wide by 2000 mm high. I-shaped sections W18X65 and W18X71 were used for beams and columns, respectively. Reduced Beam Section (RBS) connections and hinges located 850 mm below the intersection point of the column and lower beam working lines were implemented. Staggered holes on 2.6 mm thick infill plate were arranged at a 45° angle with 300 mm center-to-center spacing along both the vertical and horizontal directions.

4.2.1 Geometry Modeling and Meshing Algorithm

ABAQUS/CAE, a graphical preprocessor program, was utilized to define a Finite Element Model (FEM) of the described specimen. Geometry modeling started using the *Part Module* by defining each "plate" of the specimen, i.e. flanges, webs, panel zones, and infill plate independently in its own coordinate system (however, plates that have the same dimensions and material properties only needed to be defined once). The resulting model consisted of nine such parts. This approach facilitated the development of new models with minor differences from the original model, i.e. such as when changing the diameter of holes.

Using the *Assembly Module* tools, the parts were then positioned, relative to each other in a global coordinate system, thus creating one final assembly (note that some parts were used more than once). At this point the parts are not yet connected to each other though one part may touch other parts, i.e. beam flanges and its web. Two approaches are possible to connect the parts: the *Tie Constraints* option allows effectively merging the interface nodes, whereas the *Merge/Cut Instances* tool allows creating a single combined mesh by assembly of compatible meshes between the parts (HKS 2004a). The later option was chosen for the models described here. This option merged the various parts into one single model and removed any duplicated nodes along intersecting boundaries of adjacent parts. This option also eliminated the need for tie constraints that are more computationally demanding (HKS 2004a).

The "fish plate", used in the test specimen to connect the infill plate to the surrounding frame, was not considered in the finite element model. Instead, the infill plates were connected directly to the beams and columns. The effects of this assumption to the overall behavior of steel plate shear walls were found to be small (Driver *et al.* 1997).

Meshes were then generated on the merged model within the *Mesh Module* after "seeding" every edge by specifying the number of elements desired along that edge (*Edge by Number* rule, HKS 2004a). The models were meshed entirely using quadrilateral elements, first on the frame members (beams and columns) followed by the infill plate. This sequence was needed; without this sequence, resulting meshes were distorted, especially at the beams and columns flange connected to the infill plate, because the adjacent parts were meshed using different techniques. The frame members were meshed using the *Structured Meshing Technique*. This technique is most appropriate for simple regions that have no holes, isolated edges, or isolated vertices like the flanges and webs of beams and columns. Note that the total number of elements within the mesh region will be even if a four-sided region is meshed with all quadrilateral elements (HKS 2004a). The perforated infill plate region, due to its complexity, can only be meshed using the *Free Meshing Technique*. Note that a transition zone close to the perforations was not needed in the FEM model of the specimen. However, it was needed for a small perforation diameter model (i.e., D = 50 and 100 mm) as was the case for the strip models as described in the previous section.

Unlike structured meshing technique, free meshing technique uses no preestablished mesh patterns, making it nearly impossible to predict the mesh pattern based on the region shape. To reduce the mesh distortion within the free meshing region, the *Medial Axis Control Algorithm* together with *Minimizing the Mesh Transition* option were applied where ABAQUS/CAE automatically creates internal partitions that divide the region into simple “structured” mesh regions and then automatically determines the number of elements (i.e., seeds) along the boundaries of the smaller regions. In general, the mesh so created is not guaranteed to match the number of elements that was previously specified (i.e., “seeded”) along the boundaries of the principal region. Afterward, there could be a problem where meshes are distorted along those principal boundaries that coincide with the *Structured* mesh region boundaries (i.e., at the interface of the infill plate and the boundary frame). To overcome that distortion problem, it is helpful to use the *Fully Constrained* seeds along those share boundaries such that the number of elements along edges are pre-determined and they cannot be altered by the mesh generation process (HKS 2004a).

4.2.2 Element Definitions

The entire infill plate and boundary elements were meshed using the S4R shell elements, a four-node doubly curved general-purpose conventional shell element with reduced integration and hourglass control. Reduced integration together with hourglass control can provide more accurate results, as long as the provided elements are not distorted (relatively close to being square in shape), and significantly reduce running time especially in three dimensions. If hourglass occurs, a finer mesh may be required or concentrated loads must be distributed over multiple nodes (HKS 2004b).

The S4R shell element basically has the same behavior as the S4 shell element described in Section 3.2.3. The difference between the two is the number of integration points. The S4R shell element has only one integration point (in the middle of an element) compared to four integration points for the S4 shell element. Later in this section, a comparison study is done to compare the results obtained by the two different element definitions.

4.2.3 Material Definitions

ASTM A572 Gr. 50 (F_y = 345MPa) steel was used for the entire infill plate and boundary elements. For comparison, to the results for individual strip models in Section 3, the infill plate in the full SPSW is modeled using the same idealized tri-linear stress-strain curve used in Section 3 to represent the behavior of A572 Gr. 50 steel. Moreover, knowing that the infill plate can only yield in tension, and immediately buckles in compression, a unidirectional constitutive stress-strain relationship is used for the infill plate. The cyclic stabilized backbone stress-strain curve shown in figure 4-1 (equivalent to Steel "A" in the ATLSS study from Kauffmann *et al*. 2001) was used in the boundary elements for the same steel grade. Note that these specified nominal stress and strain values were also converted to "true" stress (Cauchy stress) and logarithmic plastic strain using (3-1) and (3-2).

4.2.4 Initial Imperfections

Initial imperfections were applied in the models to help initiate panel buckling and development of tension field action (TFA). ABAQUS offers three ways to define an imperfection: as a linear superposition of buckling eigenmodes, from the displacements of a static analysis, or by specifying the node number and imperfection values directly (HKS 2004b). The first option was chosen for the models described here.

An eigenvalue buckling analysis was first run on the "perfect" structure to request the first twenty eigenmodes. Postbuckling analysis was subsequently run after introducing imperfections in the geometry by adding these buckling modes to the "perfect" geometry where ABAQUS interprets the imperfection data through nodal displacements. The imperfection thus has the form

$$\Delta x_i = \sum_{i=1}^{M} \omega_i \, \phi_i \qquad (4\text{-}1)$$

where ϕ_i is the i^{th} mode shape and ω_i is the associated scale factor (HKS 2004b). The resulting imperfection scale factor magnitudes corresponded to only a few percent of the shell thickness. The lowest buckling modes are frequently assumed to provide the most critical imperfections, so usually a higher scale factor is assigned to the lowest eigenmodes, progressively decreasing for the higher eigenmodes.

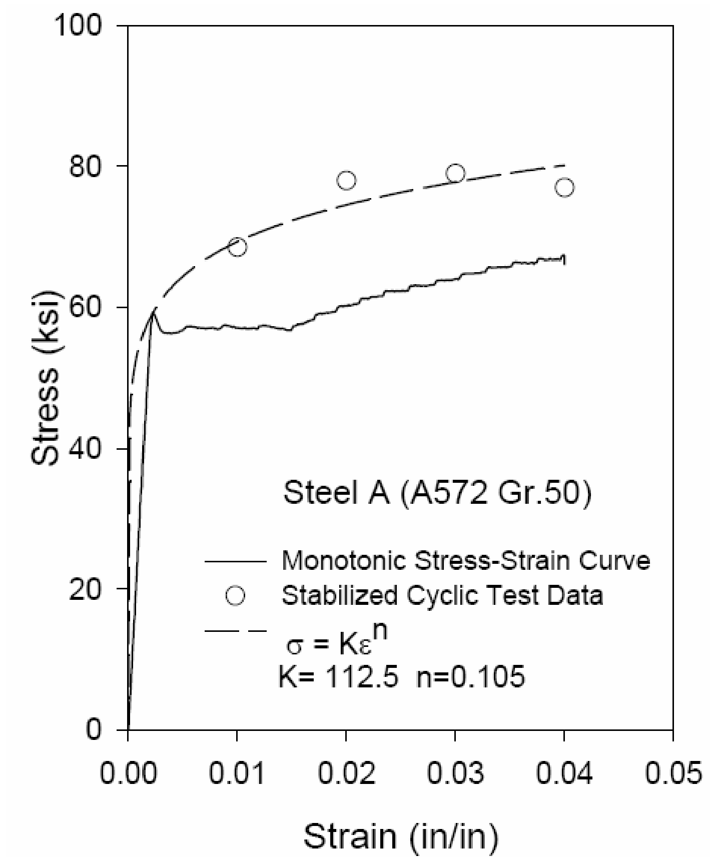

FIGURE 4-1 Stabilized Backbone Stress-Strain Curve (Steel A – Kauffmann *et al.* 2001)

4.2.5 Boundary Conditions, Constraint, and Loading

Instead of explicitly modeling the hinges at the base of the specimen in the ABAQUS model, Vian (2005) used *CONN3D2* connector elements, and the same approach was used here. This connector is a three-dimensional (3D), 2-node connector element with six DOFs in each node, three displacements and three rotations. The connector links reference nodes at the location of the hinges center, 850 mm below the centerline of bottom beam, to the corner nodes at the tip of each column flange and at the intersection of the flanges and web. Twelve *CONN3D2* connector elements were utilized in the model.

The *BEAM* connection type was assigned to these connector elements. This connection type is an *Assembled Connection* created from two *Basic Connection* components, *JOIN* (constraining translation) and *ALIGN* (constraining rotation). The result is effectively a rigid beam connection between two nodes (HKS 2004b). At the two reference nodes, only rotation about the axis perpendicular to the plane of the wall is allowed, to replicate the hinge rotation in Vian test specimen. In addition, the exterior nodes of the flange elements around the perimeter of the panel zones at the top of columns were restrained against out-of-plane movement. These boundary conditions are similar to those Vian used in his models to replicate the experimental setting of his tests. Further on in this section, these boundary conditions will be changed to investigate the impact of various lateral restraints and constraints on SPSW behavior.

A monotonic pushover displacement was applied to a reference node located at the middle centerline of the top beam. A *Kinematic Coupling Constraints* was used to constrain both the translational and rotational motion of coupling nodes to the reference node. The coupling nodes are defined as the nodes at the flanges and web of the top beam 300 mm apart around the reference node. The resulting finite element model is shown in figure 4-2.

4.3 Non-Linear Stability and Lateral Torsional Buckling

Geometric non-linearities mainly arise, in this model, from the large-displacements exhibited in the infill plate and local buckling of the infill plate may lead to unstable conditions. Although the S4R shell elements described in Section 4.2.2 are able to accommodate large-displacements, instability of the entire model may still occur. ABAQUS/Standard can overcome this unstable condition using *Stabilize* option in which the program provides an additional artificial damping to the model during a nonlinear static analysis. The artificial damping factor is determined in such a way that the extrapolated dissipated energy for the step is a small fraction of the extrapolated strain energy. The fraction is called the *dissipated energy fraction* (DEF) and has a default value of 2.0×10^{-4} (HKS 2004b).

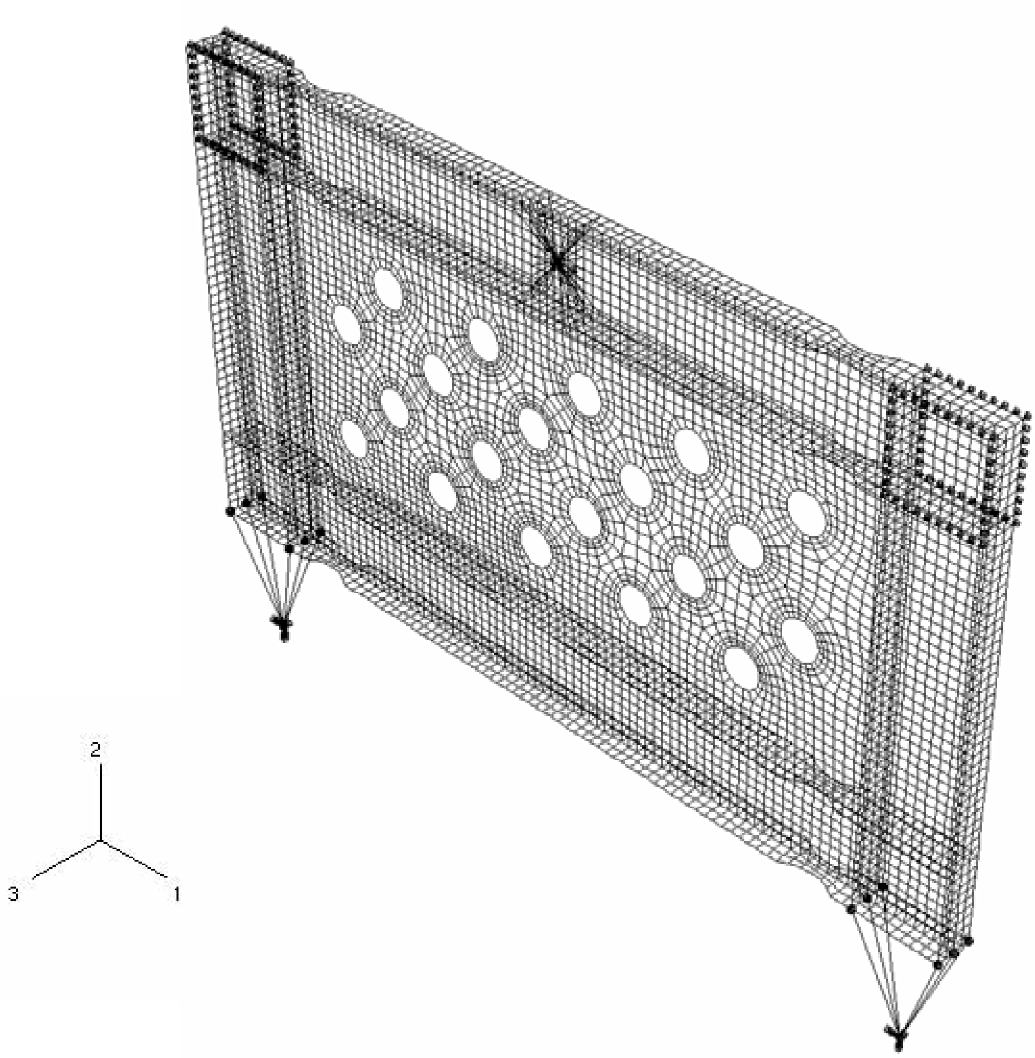

FIGURE 4-2 Finite Element Model of the Specimen (Coarse Mesh)

ABAQUS/Standard then uses Newton's method to solve the nonlinear equilibrium equations. The solution is usually obtained as a series of “time” increments from 0.0 to 1.0, with iterations to obtain equilibrium within each increment. The program can automatically adjust the time increment to permit convergence of results without unstable responses due to the higher degree of nonlinearity in the system, in this case related to infill plate buckling. In addition, for models having very thin infill plates, the increment should be defined small to ensure that any obtained solution is not too far from the equilibrium state that is being sought (HKS 2004b).

When using the stabilization feature, one should ensure that the ratio between the viscous damping energy (ALLSD – *ABAQUS definition*) and the total strain energy (ALLSE) does not exceed the DEF value or any reasonable value (HKS 2004b). After running the FEM model, results shown in figure 4-3 confirmed that, over the entire time increments/period, ALLSD was significantly smaller than ALLSE. The ratio between the two at time equal to 1.0 is 0.048 and though this ratio is somewhat bigger than the maximum recommended DEF value, the analyses are considered to satisfy the stability requirements for the purpose of this project.

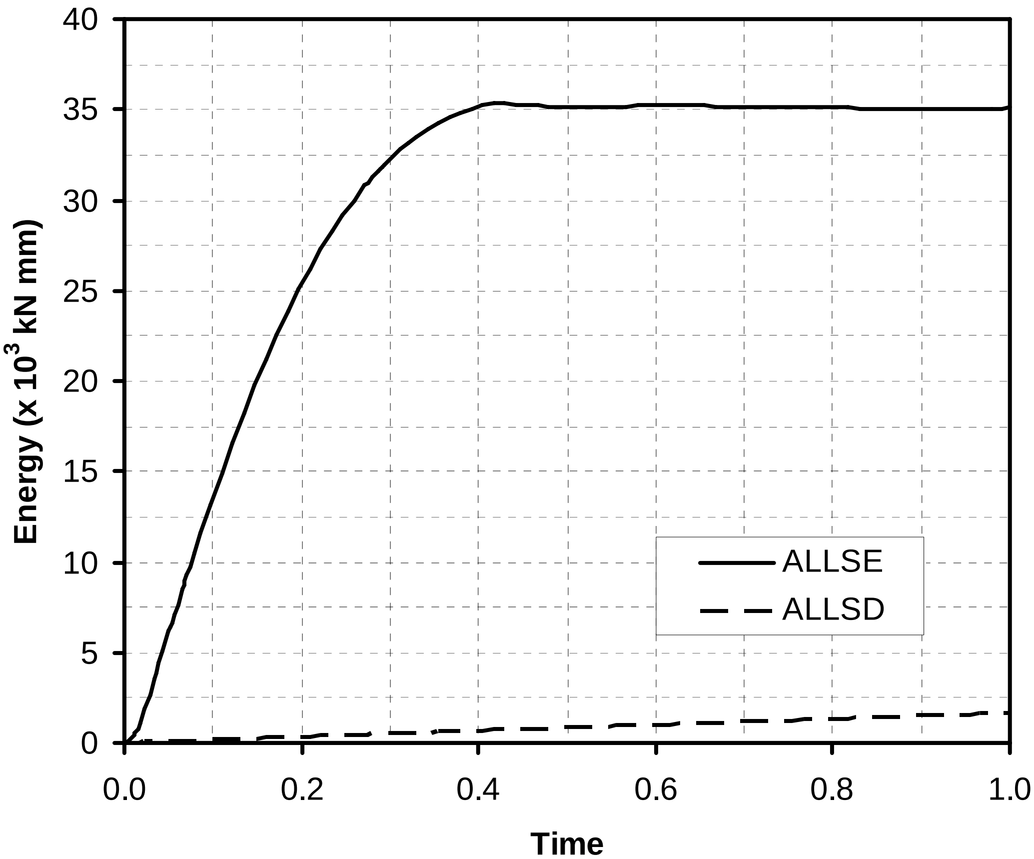

FIGURE 4-3 Strain Energy (ALLSE) and Viscous Damping Energy (ALLSD) versus Time Increment

Note that for the boundary conditions described in Section 4.2.5, at large in-plane drifts, Lateral Torsional Buckling (LTB) was observed to develop primarily at the top beam and slightly at the bottom beam, as shown in figure 4-4. This buckling and twisting phenomenon on the beams also affects the columns displacement as the left column deformed in a manner not parallel to the right

(a)

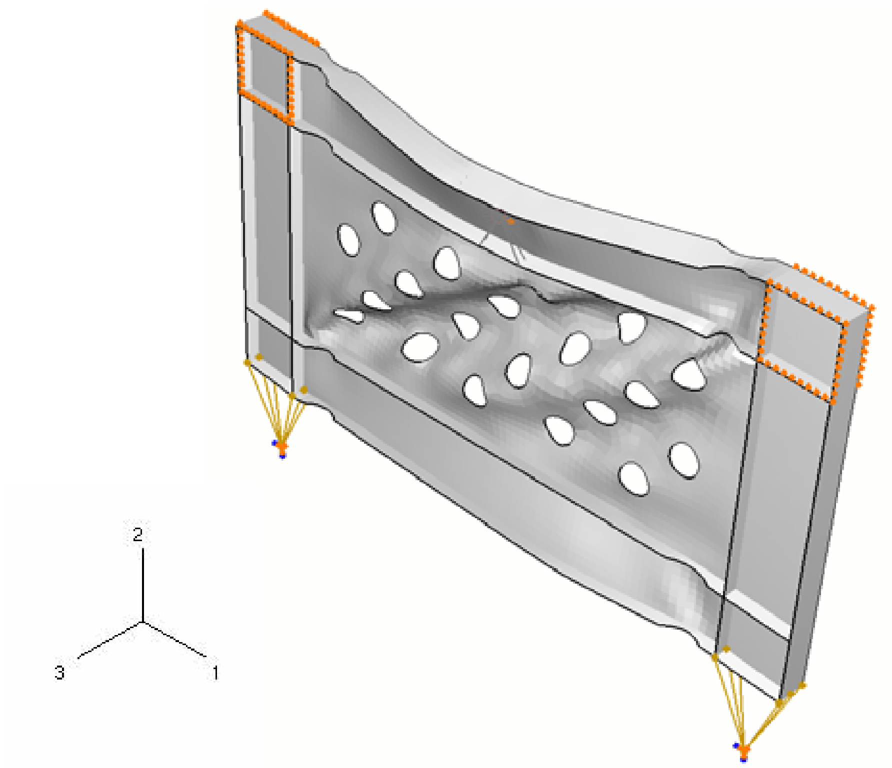

(b)

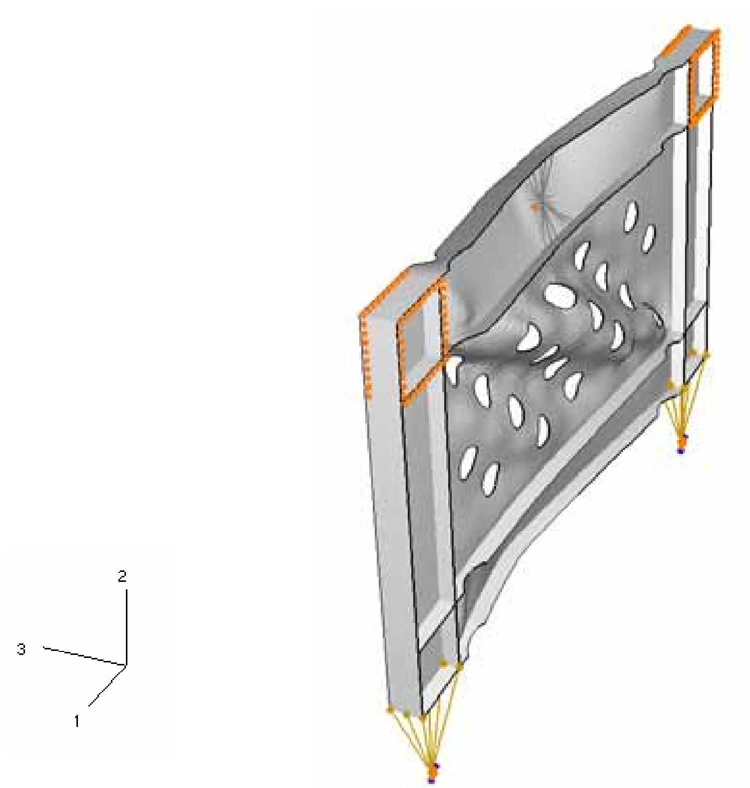

FIGURE 4-4 Deformed Shape with Lateral Torsional Buckling at the Beams (a) Front View; (b) Rear View (at 20% Maximum Local Strain, Deformation Scale Factor = 1.0)

column. To overcome this condition, the models considered later in this section use a lateral support constraining the out-of-plane movement of the nodes at the tip of the beams flanges so called boundary nodes.

4.4 Imperfection Sensitivity

A sensitivity study to investigate impact of the magnitude and type of imperfections on analytical results was conducted to determine the proper scale factor ω_i (described in Section 4.2.4) to be included in the model to allow a correct postbuckling analysis. An eigenvalue buckling analysis was first run on a modified FEM model for which lateral supports to the tip of the beam flanges were added and the first two eigenmodes of that "perfect" geometry are plotted in figure 4-5. A series of postbuckling analysis with a scale factor ω_i varying in a magnitude from 0 (no imperfection) to 2, 5, 10, 15 and 20% of shell thickness for the first mode (and a decreasing percentage for higher eigenmodes) was subsequently performed and the results are presented in figure 4-6.

Figures 4-6(a) and (b) show the frame drifts (interstory drifts) attained when one point (any point) in the infill plate reaches maximum local strain ε_{max} of 1% and 15%, respectively, as a function of the scale factor ω_i. In both figures, those frame drifts decrease significantly as imperfections are introduced, and then stabilize to a constant value (at about 0.29% and 4.11% when ε_{max} = 1% and 15%, respectively) as the scale factor ω_i increases. This confirmed that the absence of initial imperfections significantly change the frame response. For example, to get the same maximum local strain (i.e., ε_{max} = 1% and 15% in the infill plate) with the imperfection model (i.e., ω_i = 5%), then with the "perfect" model, the frame needs to reach 48% and 9% larger drifts, for the respective maximum local strain.

From figure 4-6, one could question why, at higher strains in the infill plate, the initial imperfections did not seem to matter anymore. This phenomenon could be explained by observing the shear history of the two cases plotted in figure 4-7. At lower strain ε_{max} = 1%, the "perfect" infill plate remains flat carrying the increasing load by panel shear mechanism. As a

(a)

(b)

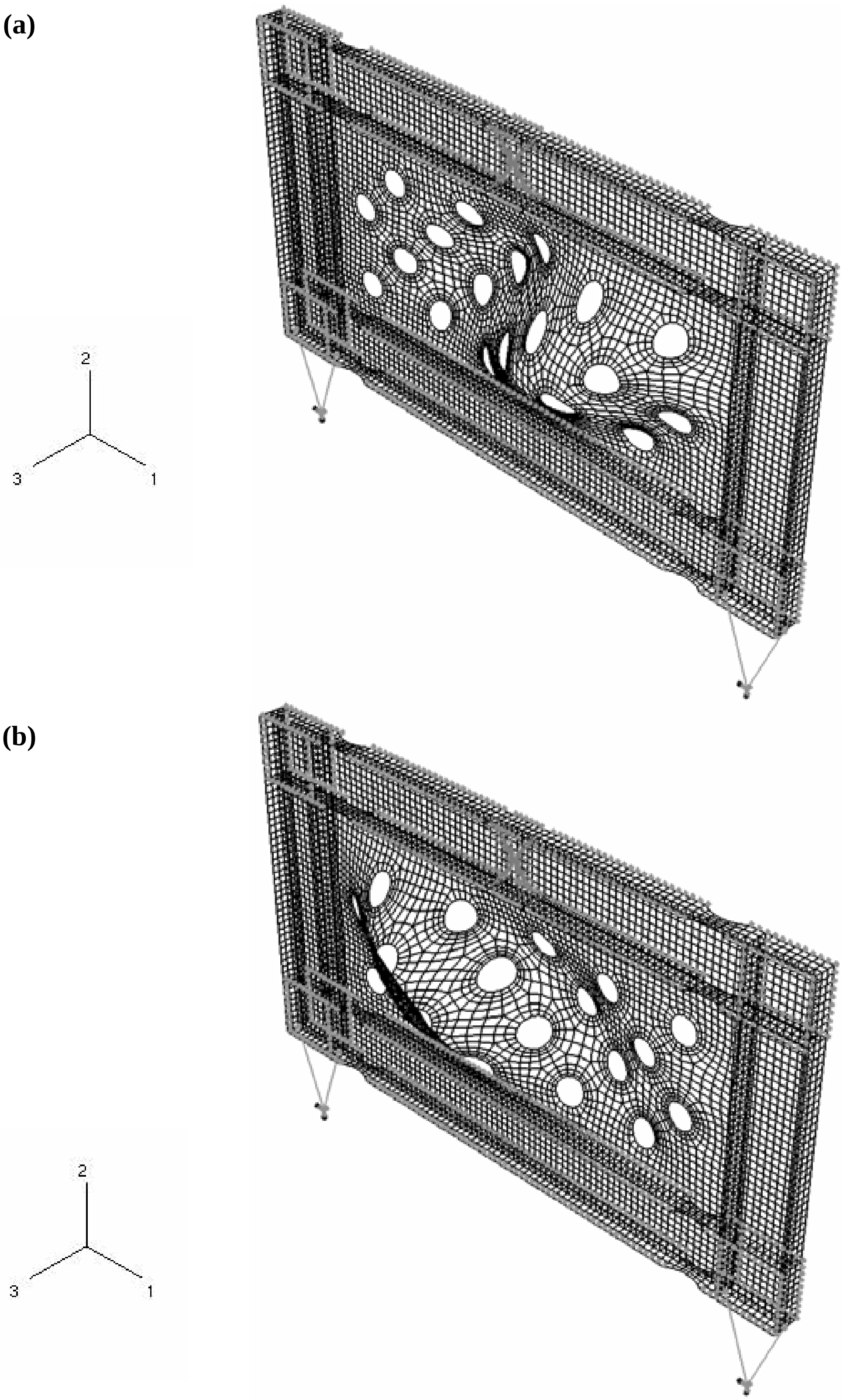

FIGURE 4-5 Perforated Panel Buckling Mode (a) 1st Mode Shape; (b) 2nd Mode Shape (Deformation Scale Factor = 444.9)

(a)

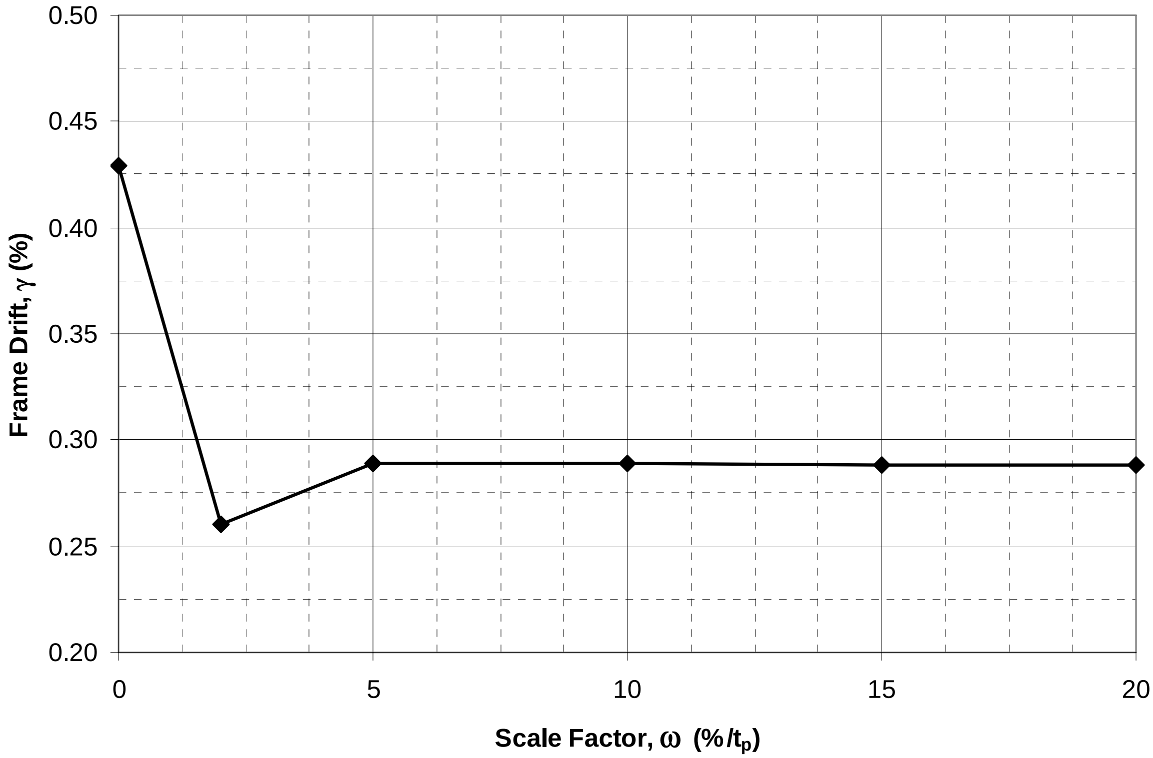

(b)

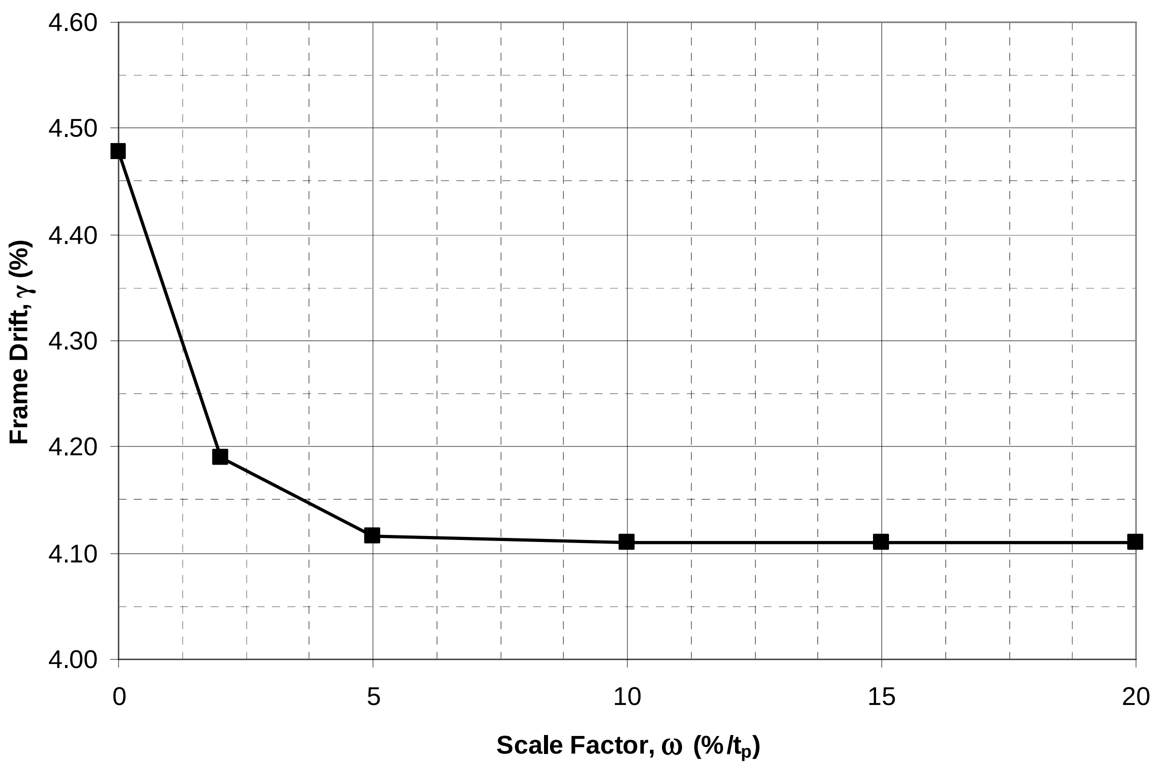

FIGURE 4-6 Frame Drift γ versus Scale Factor ω at (a) Maximum Local Strain ε_{max} = 1%; (b) Maximum Local Strain ε_{max} = 15%

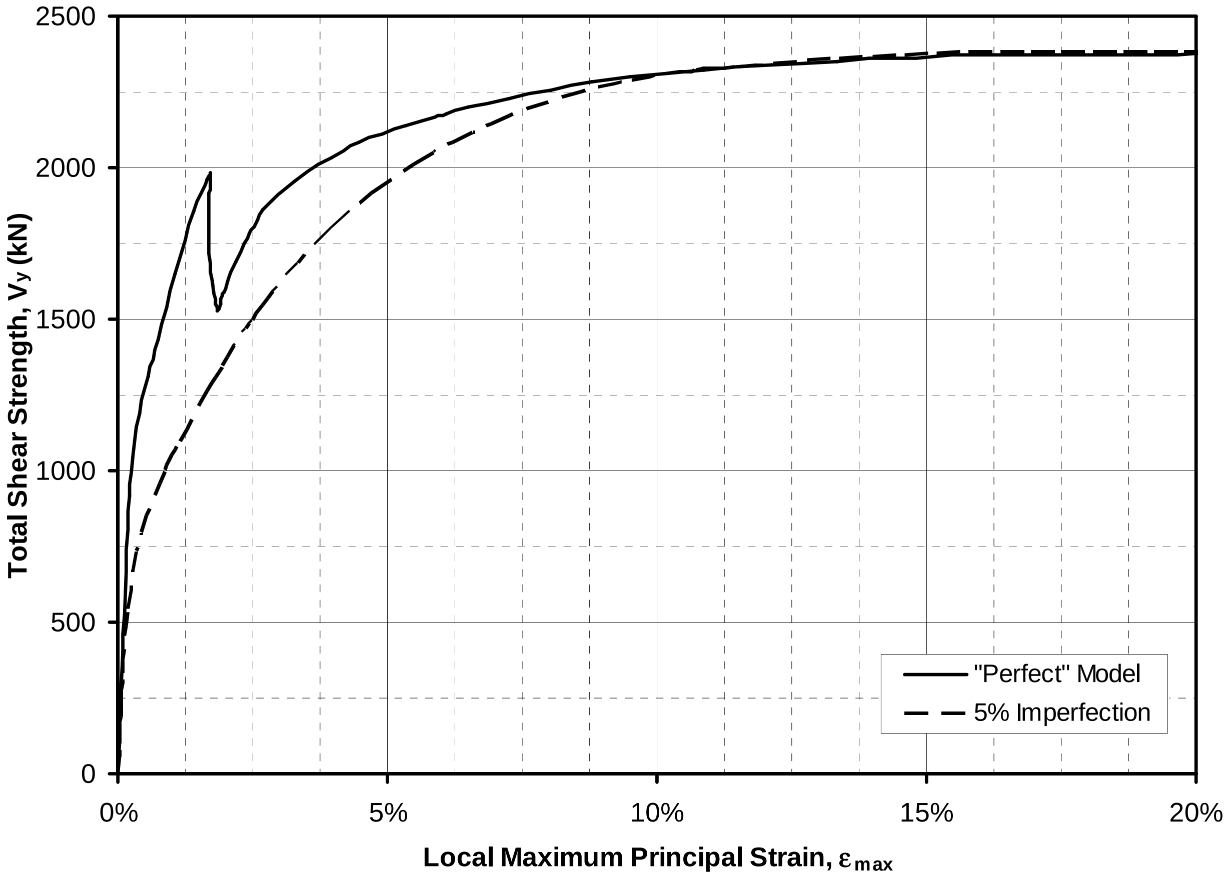

FIGURE 4-7 Total Shear Strength History of the "Perfect" and 5% Imperfection Model

result, a higher load was required to yield the infill plate, at this point the overall shear strength of the perforated panels $V_{yp.perf}$ equal to 1611 kN, than for the imperfect infill plate which only required a shear load $V_{yp.perf}$ of 1044 kN. For the former, as strain increased and shear yielding occurred, tension field action suddenly developed, marked by a shear drop in strength. Eventually the two models developed approximately the same shear strength (i.e., $V_{yp.perf}$ = 2366 kN and 2376 kN, respectively, at maximum local strain ε_{max} = 15%).

Furthermore, note that the first four eigenvalues as listed in table 4-1 are closely spaced and might have impacted the postbuckling response. Further analysis, however, has proved that setting the highest scale factor on the first four eigenmodes (and a decreasing percentage for higher eigenmodes) did not change significantly the postbuckling response. For example, at the scale factor ω_i = 10% and ε_{max} = 1% and 15%, the frame drift magnitude only differed by 7% and 2%, respectively.

TABLE 4-1 Eigenmodes and Corresponding Eigenvalue of the "Perfect" Structure

MODE NO	EIGENVALUE
1	31.484
2	-31.548
3	32.424
4	-33.311
5	42.299
6	-44.887
7	-50.988
8	54.369
9	67.896
10	-69.252
11	74.712
12	-76.907
13	86.443
14	-87.964
15	94.150
16	96.992
17	-98.893
18	-102.090
19	104.300
20	-108.850

Therefore, consideration of the initial imperfections into the model was necessary to capture the correct postbuckling response and the scale factor ω_i was found to be a little sensitive for closely spaced eigenvalues. For simplicity, an initial imperfection amplitude of 1 mm multiplied by the first eigenmodes and decreasing for higher mode was chosen for the rest of the models analyzed in this section.

4.5 Behavior of Perforated SPSW Considering Alternative Models

The behavior of panels in SPSW could be more complex than that of individual strips previously modeled in Section 3, partly because of the continuity between strips, the development of buckling orthogonally to yielding, and the uneven elongation of the "virtual" strips across the panel as a result of the flexibility and strength of the boundary beams and columns. In addition, for a modeling perspective, boundary conditions, mesh size, and perforation diameter as considered in the individual strip analysis also affect the stress and strain distribution results in the panel. Other aspects that may affect the stress and strain distribution in the panel in ways that could not be observed in the individual strip model are non-linearity effects, initial imperfections of the infill plate, boundary element stiffness/rigidity and lateral support, local buckling, and relative infill plate thickness. Sections 4.3 and 4.4 addressed some of these aspects; the remaining will be discussed below and in the subsequent sections.

Vian (2005) reported that the elongation predicted by finite element model of an individual perforated strip and full SPSW, for monitored strain assumed close to perforations edges, was significantly different. The researcher recommended further research to determine the factors that affect this behavior and to improve the design recommendations for perforated SPSW. This significant difference cannot be explained at that time. The objective of this and the following sections, therefore, is to investigate why prior results from panel analysis did not support the predictions from individual strip model analysis and to propose technical answers to this problem.

Three finite element models were studied for this purpose, and are referred to as *Flexible Beam Laterally Braced (FLTB) Model*, *Rigid Floor (RF) Model*, and *Rigid Beam (RB) Model*. The 200 mm perforated panel model four rows of perforation along the diagonal (N_r = 4), as shown in figure 4-2, was chosen for all models in the initial stage of this research. Later in this section, panel models with variation in perforation diameter and infill plate thickness will also be reviewed.

4.5.1 Flexible Beam Laterally Braced (FLTB) Model

The FLTB model is intended to prevent lateral torsional buckling, as described in Section 4.3, by constraining the out-of-plane movement of the boundary nodes at the beams flanges. For that purpose, note that CONN3D2 connector elements were reduced to only 4 connectors instead of 12 connectors as in the previous model. This will avoid redundant constraints (named *Consistent Overconstraints* in ABAQUS) at the four corner nodes while the two middle nodes remain un-constrained. Further analysis had shown that this reduction did not significantly change the overall frame response.

A monotonic pushover displacement was applied to the model. Frame drifts and strips elongations were noted when maximum principal local strain ε_{max} somewhere in the infill plate, usually adjacent to a perforation, reached values of 1, 5, 10, 15, and 20%. Frame drifts were measured from the difference in displacements between the center of the top and bottom panel zones of the two columns and the average of the two were divided by the frame height. Strip elongations, for the strips labeled as STRIP L, 1, 2, 3, 4, and R from the left to right side as shown in figure 4-8, were measured from one point at the interface of the infill plate with the top beam to another corresponding point at the interface of the infill plate with the bottom beam, then multiplied by corresponding cosine or sine of the perforation orientation angle θ to get axial deformation of the strips. The sine component, in this case, is relatively small due to the high moment of inertia of the beams and therefore can be neglected. Only the cosine component of displacement is considered here. Also note that compared to the previous case in which lateral torsional buckling of the beams was not prevented, because of the lateral support, the columns here remained parallel to each other throughout the response.

Figure 4-9 displays the results of total uniform strip elongation ε_{un} ($=\Delta L/L$) for a SPSW having a 5 mm infill plate thickness at each monitored strain value plotted on the vertical axis and for STRIPs 1 to 4 on the horizontal axis. For comparison, results obtained from the individual perforated strip analysis are also plotted on the figure as shown by the five horizontal lines for each monitored strain. Note that STRIPs L and R are not plotted in the figure because both strips have different characteristics, in terms of number of perforations and strip dimensions, from the individual perforated strip model. Incidentally, note that the regular geometry and dimensions of strips considered in Section 3 (e.g., D/S_{diag} = 0.5 for D = 200 mm and S_{diag} = 400 mm) differ somewhat from those considered by Vian (2005); in his tested SPSW, a horizontal and vertical spacing of 300 mm was used resulting in a diagonal strip width or spacing of perforation S_{diag} of

424.26 mm, and perforation ratio D/S_{diag} of 0.471. Hence, for comparison purposes, lines represent the results of individual strip analysis at the same perforation ratio of 0.471.

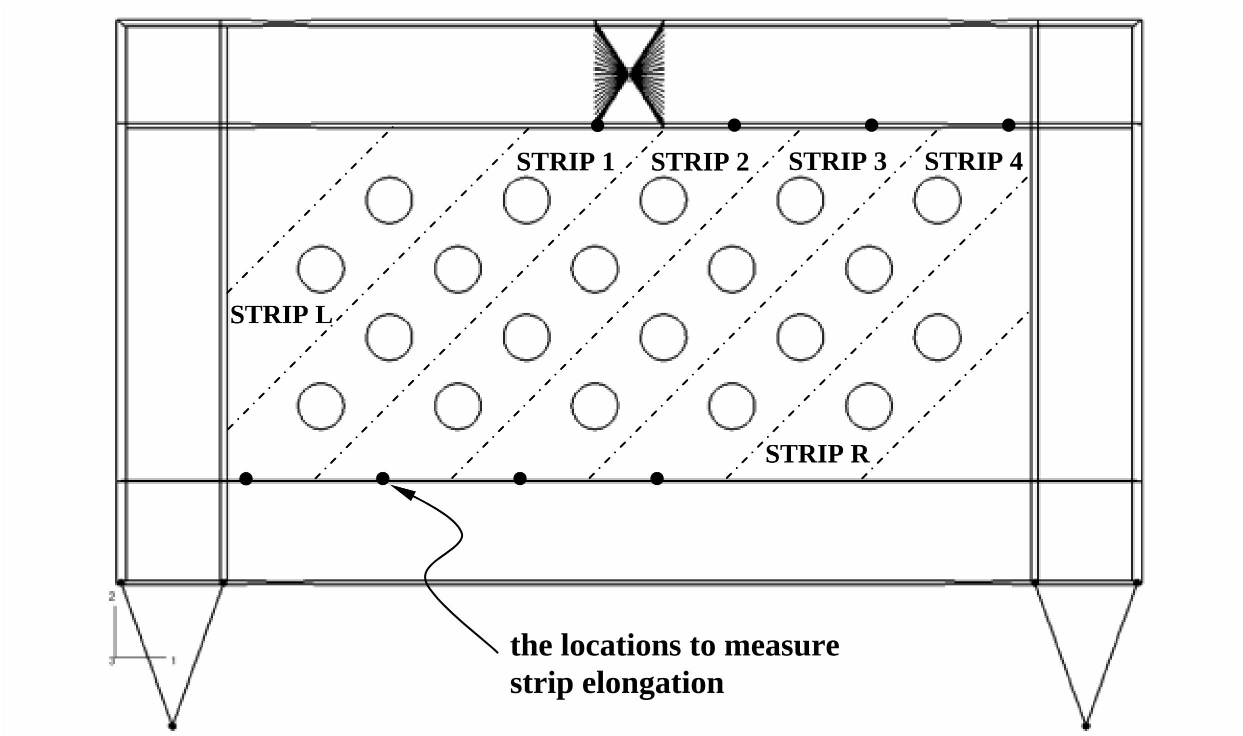

FIGURE 4-8 Strip Annotation on Perforated SPSW

It was originally suspected that each strip would reach the same amount of elongation. However, figure 4-9 shows that this is not the case. Every strip reached a different strip elongation, with only STRIP 1 matching the individual strip results (for reasons unknown at this time), while the elongation observed for the other strips in SPSW panel was less than that for corresponding stand-alone strip. At 20% maximum principal local strain in the infill plate, STRIP 4 elongation was 22% less than that for the individual strip. This behavior can be understood after reviewing the deformed shape of the model plotted in figure 4-10 where the beams deflected due to local buckling and diagonal tension from the infill plate. Note that lateral supports are not shown in the figure. The individual and non-symmetrical beam deflection are shown magnified and schematically in figure 4-10(b). Maximum deflection of the top and bottom beams are 34.6 mm (located 593 mm to the left from the center line) and 27.4 mm (located 1205 mm to the right from the center line), respectively. This leads to the unequal strip axial deformations of 66.9, 60.7, 58.5, and 54.0 mm for STRIPs 1 to 4, respectively.

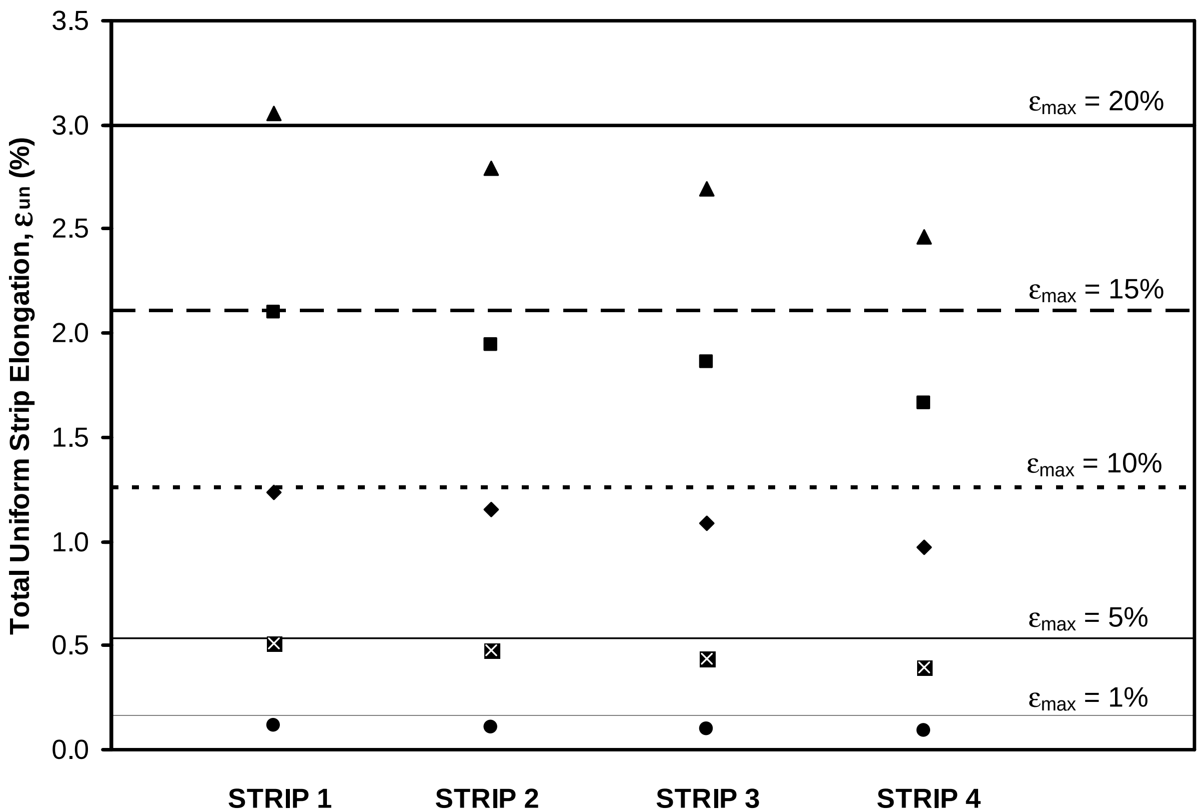

FIGURE 4-9 Uniform Distributed Strip Axial Strain ε_{un} at each Monitored Strip Location (FLTB Model, Fine Mesh, t_p = 5 mm, D = 200 mm, D/S_{diag} = 0.471); Lines Correspond to Individual Strip Analysis

In-plane principal maximum stress contours, strain contours, and strain tensor field of the model are shown in figure 4-11 at 20% monitored strain. A distribution of tension field action around the perforations similar to that observed by Vian (2005) is shown in the figure. Stress and strain concentrations are initiating at the perforation edges, and zones of yielding are radiating out from this location at approximately 45° angles with respect to the diagonal tension field orientation, and then overlapping with yielding zones of adjacent holes from different strips, as shown in figure 4-11(b) and (c), before finally flowing into the RBS connections.

Note that even though presented first, the results described here are actually revisited results obtained after observing the effect of mesh sizes described subsequently in Section 4.5.2. The

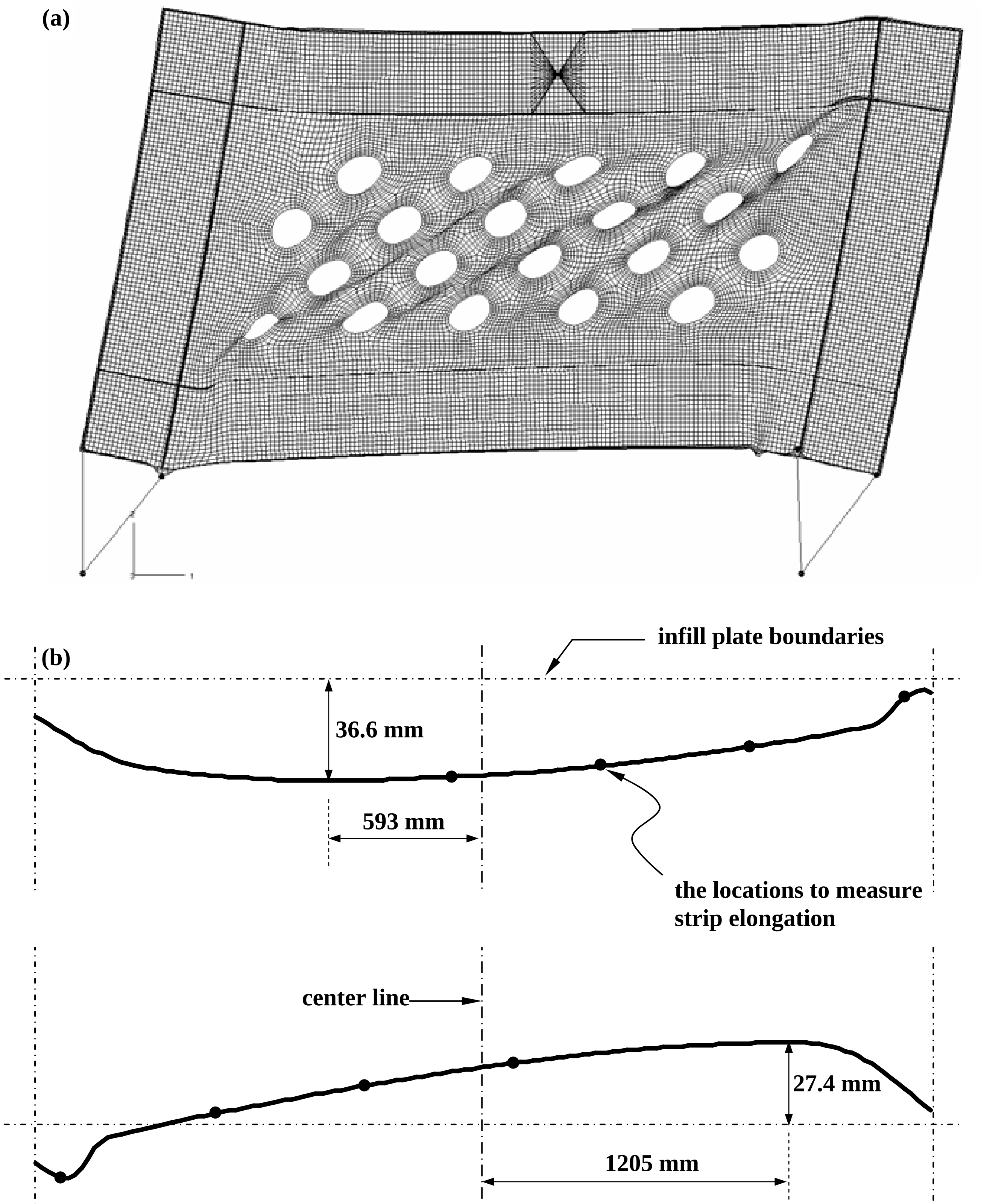

FIGURE 4-10 Deformation Shape of FLTB Model: Uneven Deflection at Top and Bottom Beam (a) Finite Element Results; (b) Schematic Deformation (Deformation Scale Factor = 3.0)

(a)

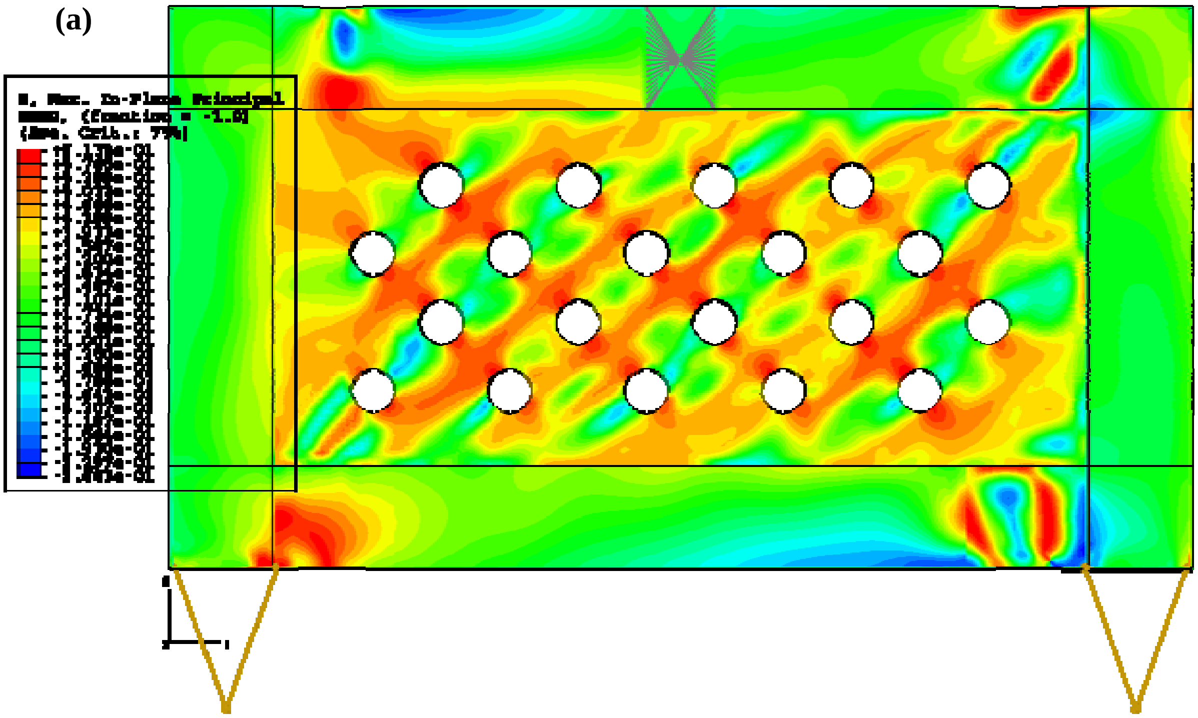

FIGURE 4-11 Perforated Panel Analysis Results at 20% Maximum Local Strain of FLTB Model, Fine Mesh, t_p = 5 mm, D = 200 mm, D/S_{diag} = 0.471 (a) Maximum In-Plane Principal Stress Contours

FLTB model described here was intentionally meshed using fine meshes instead of the coarse meshes used in the previous sections when investigating stability and imperfection sensitivity. Meshes started with 25 x 25 mm shell elements near the boundary elements and gradually reduced to an average dimension of 15 x 15 mm per shell element adjacent to the perforations.

It appears that deformations in the beams play a significant role in affecting the variations in strip elongations in the panel. To investigate the significance of this effect, the two alternative models presented next are considered. In the first case following, rigid-body motions of the beams are considered, as a preliminary way to model rigid floors. This model is named *Rigid Floor (RF) Model*.

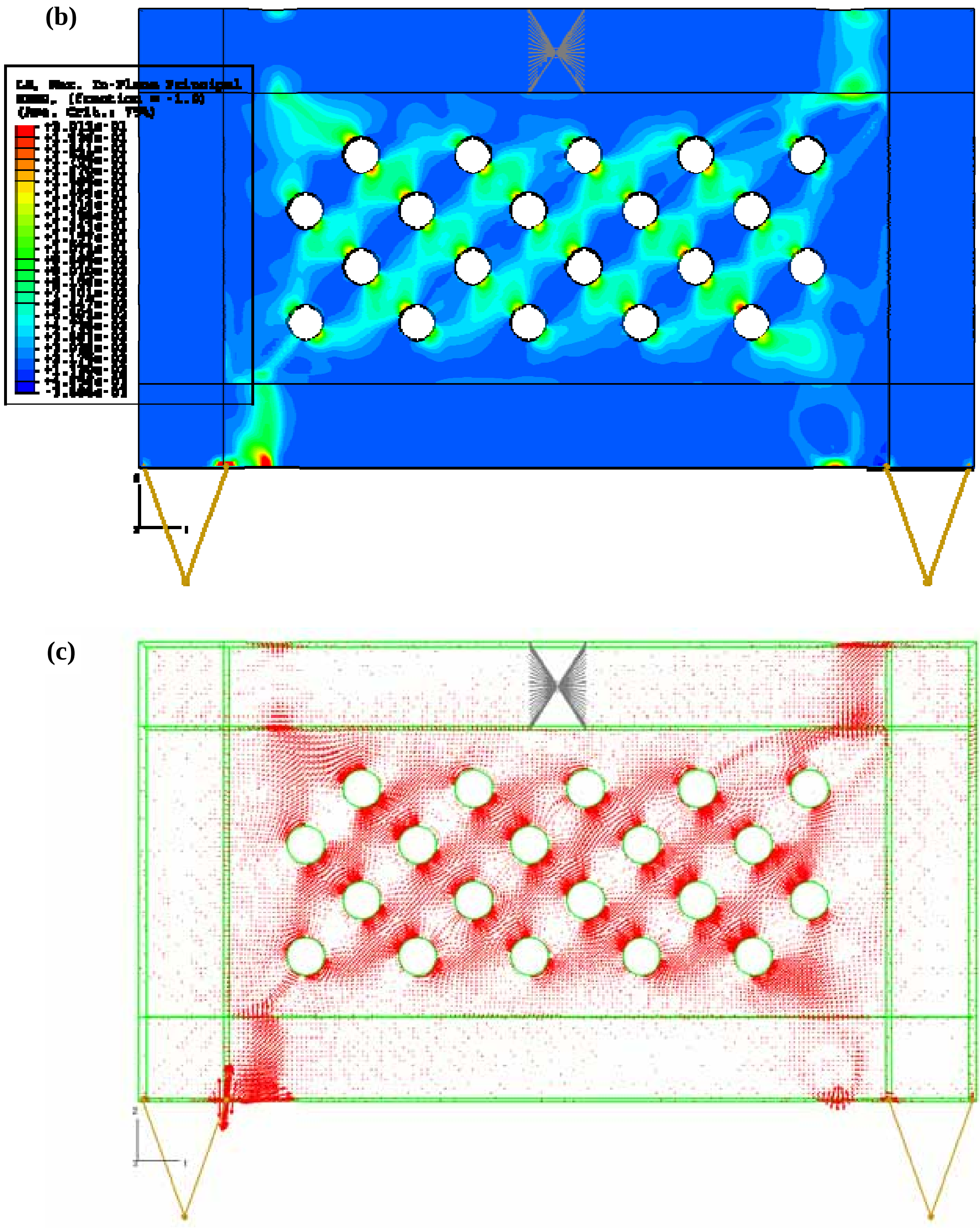

FIGURE 4-11 Perforated Panel Analysis Results at 20% Maximum Local Strain of FLTB Model, Fine Mesh, t_p = 5 mm, D = 200 mm, D/S_{diag} = 0.471 – Cont'd (b) Maximum In-Plane Principal Strain (c) Strain Tensor Field

4.5.2 Rigid Floor (RF) Model

The ABAQUS model described for the FLTB model was modified by adding vertical constraints at the boundary nodes at the beams flanges while the other model properties remain the same. A monotonic pushover displacement was again applied to the model; frame drifts and strips elongations were noted for each monitored strain. In this model, all the nodes in the top and bottom beams moved as a rigid-body motion. Frame drifts were therefore measured from the difference in lateral displacement of the columns at the levels of the top and bottom of the infill plate (i.e., H_{panel} = 1553 mm). Total uniform strip elongation ε_{un} are plotted in figure 4-12 for a 2.6 mm infill plate thickness.

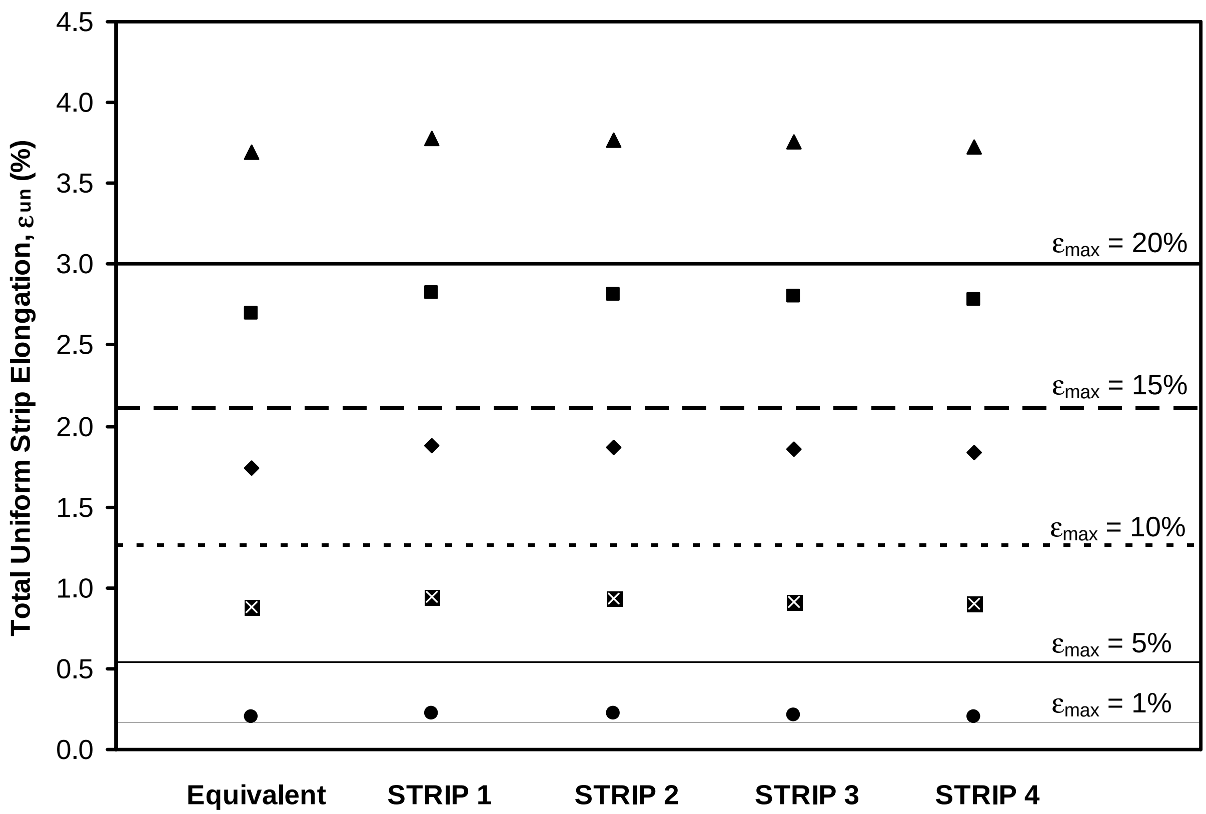

FIGURE 4-12 Uniform Distributed Strip Axial Strain ε_{un} at each Monitored Strip Location (RF Model, Coarse Mesh, t_p = 2.6 mm, D = 200 mm, D/S_{diag} = 0.471); Lines Correspond to Individual Strip Analysis

For comparison, the total uniform strip elongation ε_{un} on the tension field strips of a SPSW having rigid pin-ended frame members can be related to interstory drift through compatibility relations (Vian 2005) by

$$\varepsilon_{un} = \frac{\gamma_F \cdot \sin 2\alpha}{2} \tag{4-2}$$

where γ_F is the frame (interstory) drift and α is the tension field inclination angle which is typically near 45° in SPSW, and certainly close to the value here since the perforation orientation angle θ was set at this angle. The *Rigid Floor Model* was developed as a way to approximate (using finite element analysis) the theoretical case of SPSW with rigid pin-ended boundary elements, and the equivalent strip elongation calculated from (4-2) is therefore also plotted in figure 4-12 under the label *Equivalent*. To further complete the comparison, results for the individual strips analyzed in Section 3 are also shown on this figure.

It can be observed from figure 4-12 that, in this case, all strips reached about the same elongation. At 20% maximum principal local strain in the infill plate, on average, the SPSW strips have elongated 3.76%. Furthermore, the equivalent strip elongation calculated using (4-2) consistently closely matched the SPSW strip elongations with 3.69% elongation at the maximum principal local strain, i.e., less than a 1% difference from the SPSW strips average elongation. At the other monitored strain levels, this difference varied between 2% and 5%. However, SPSW results varied more considerably from the individual strip results. For example, at 20% maximum principal local strain, the SPSW average strip elongation results (i.e., 3.76%) are 23% higher than that for the individual strip model which only elongated 3.00%. At that time, one possible reason for this observed difference speculated to be possibly attributable to the mesh sizes that were used in the model. This was a point deemed worthy of further consideration, particularly given that the limit state driving the qualification of system performance in this case is a maximum local strain that is by definition generally sensitive to mesh size. To investigate this possibility, various mesh sizes were considered.

To this point, the SPSW plate was modeled using coarse meshes, starting with 50 x 50 mm shell elements near the boundary elements and gradually reducing to an average dimension of 35 x 35 mm per shell element adjacent to the perforations. A refined mesh model was then used, with mesh such that plate elements started at a size of 25 x 25 mm near the boundary elements and gradually reduced to an average of 15 x 15 mm adjacent to the perforations. This later model has 27099 elements (four times more elements) and was computationally more expensive than the previous model). The results obtained with this refined model are plotted in figure 4-13. In this case, it is shown that the SPSW total uniform strip elongation results match the results obtained for the individual strip model. At monitored strain $\varepsilon_{max} \geq 5\%$, the difference between the results for the two models is less than 2%.

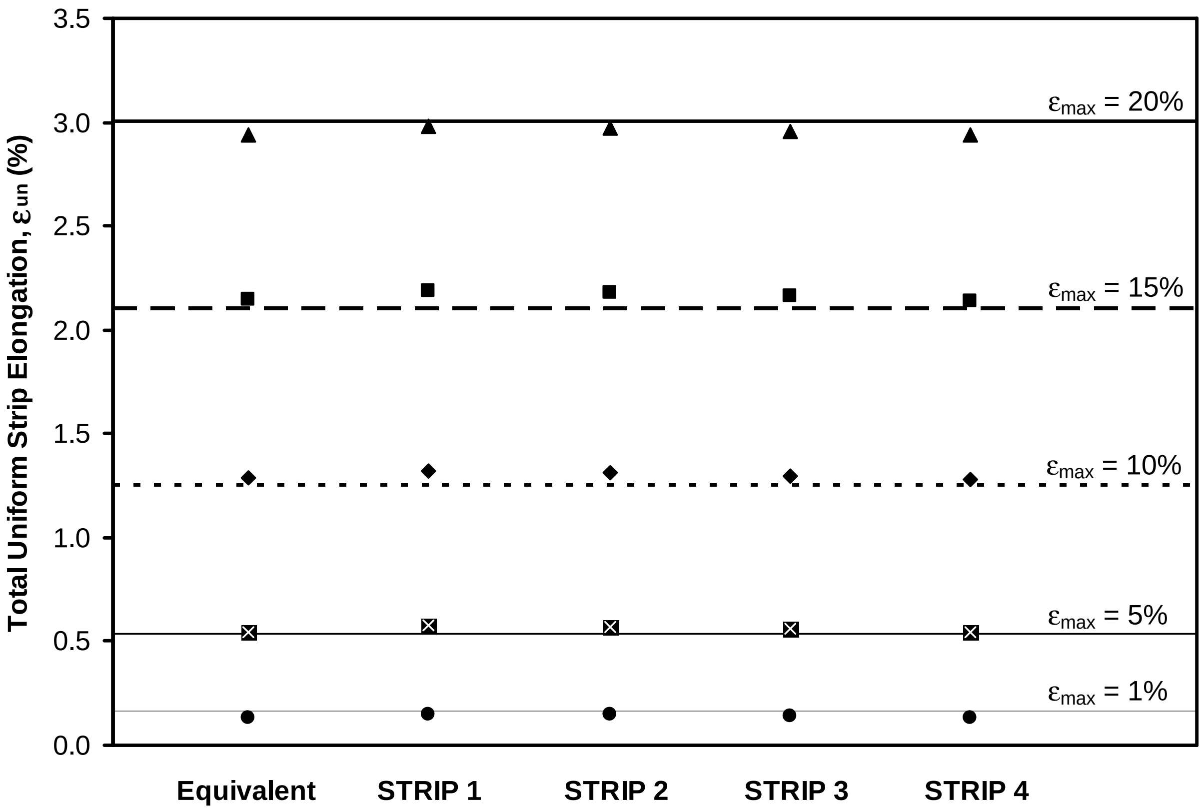

FIGURE 4-13 Uniform Distributed Strip Axial Strain ε_{un} at each Monitored Strip Location (RF Model, Fine Mesh, t_p = 2.6 mm, D = 200 mm, D/S_{diag} = 0.471); Lines Correspond to Individual Strip Analysis

Deformed shape (both front and rear view) for the RF model having a perforated infill plate with 200 mm diameter holes is shown in figure 4-14, while in-plane principal maximum stress contours, strain contours and strain tensor field are shown in figure 4-15. Note that both figures are plotted at 20% maximum strain. The regularity of the observed deformed shape, with peaks at the strips lines and valley between them, illustrates how each strip reached the same elongation.

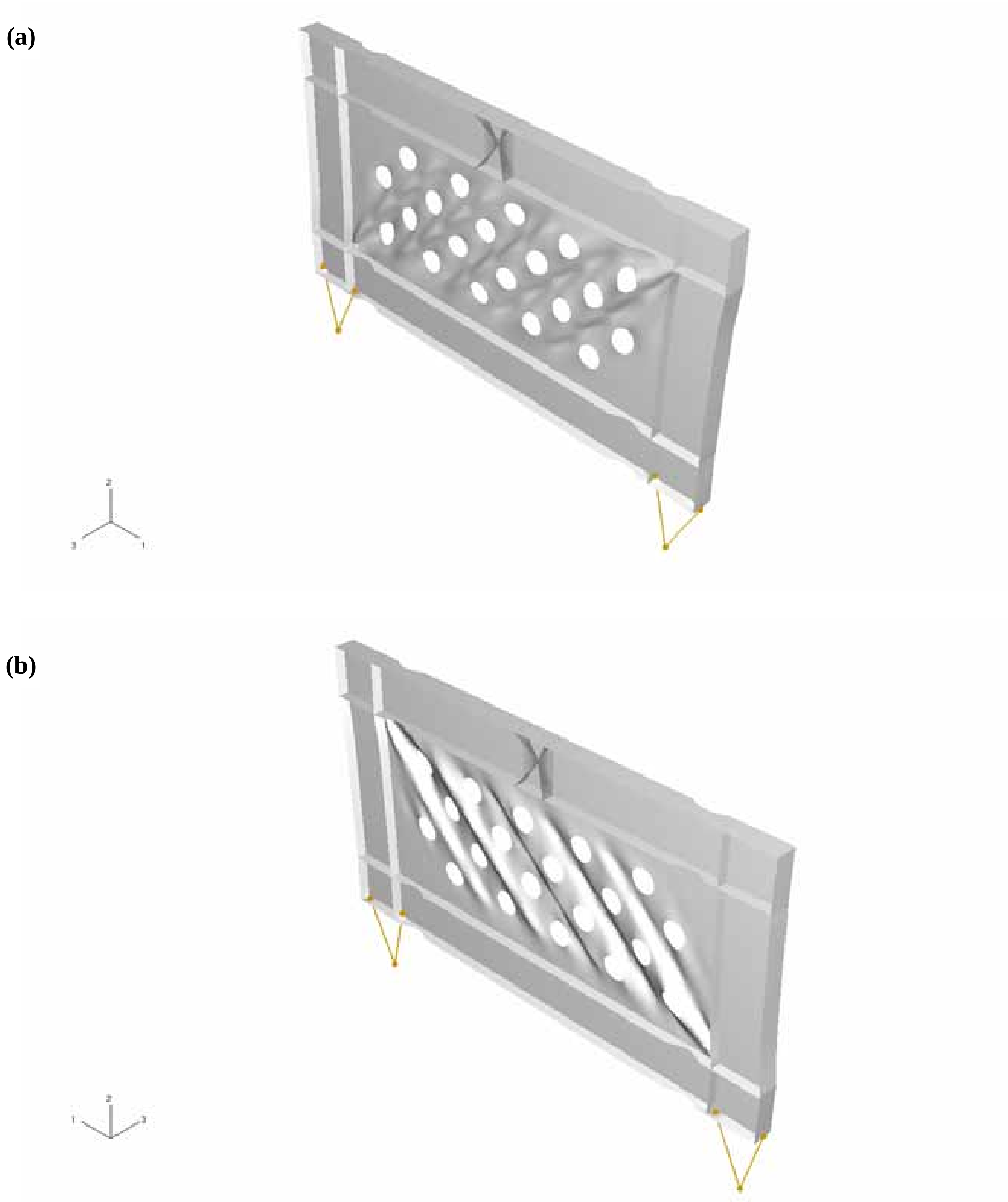

FIGURE 4-14 Deformed Shape of RF Model (a) Front View; (b) Rear View (Deformation Scale Factor = 1.0)

(c)

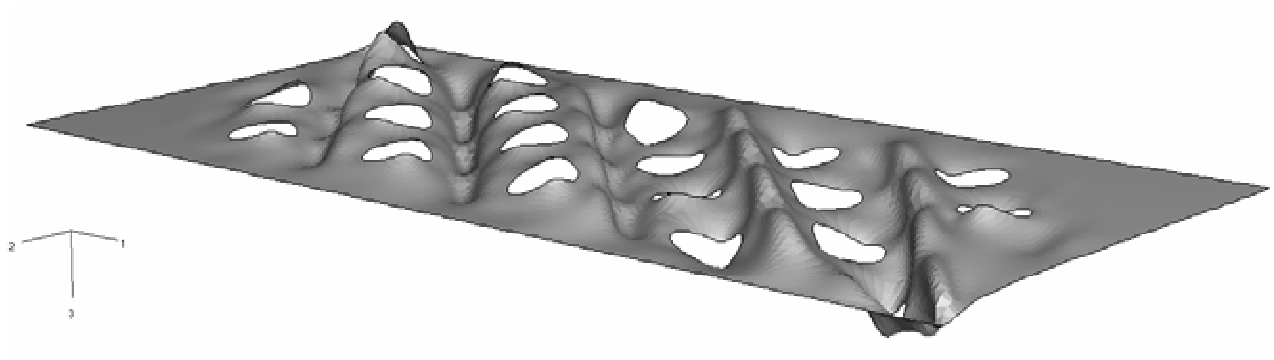

FIGURE 4-14 Deformed Shape of RF Model – Cont'd (c) Infill Plate Deformation Shaped (Deformation Scale Factor = 2.0)

(a)

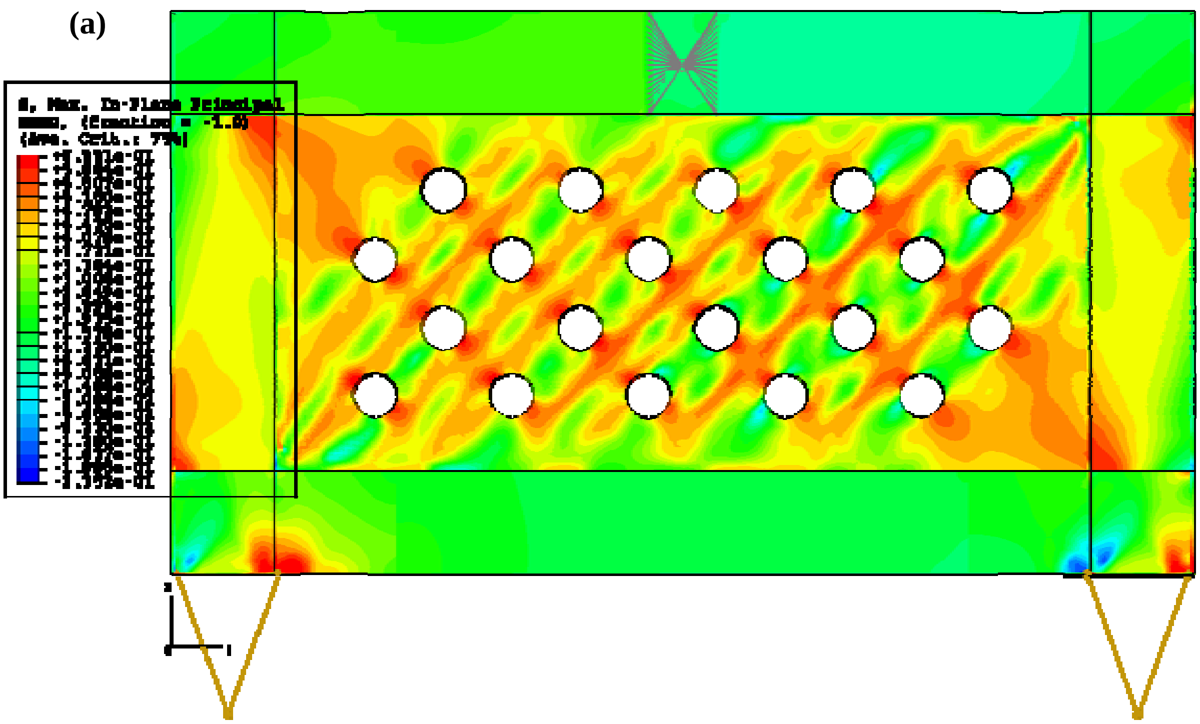

FIGURE 4-15 Perforated Panel Analysis Results at 20% Maximum Local Strain of RF Model, Fine Mesh, t_p = 2.6 mm, D = 200 mm, D/S_{diag} = 0.471 (a) Maximum In-Plane Principal Stress Contours

(b)

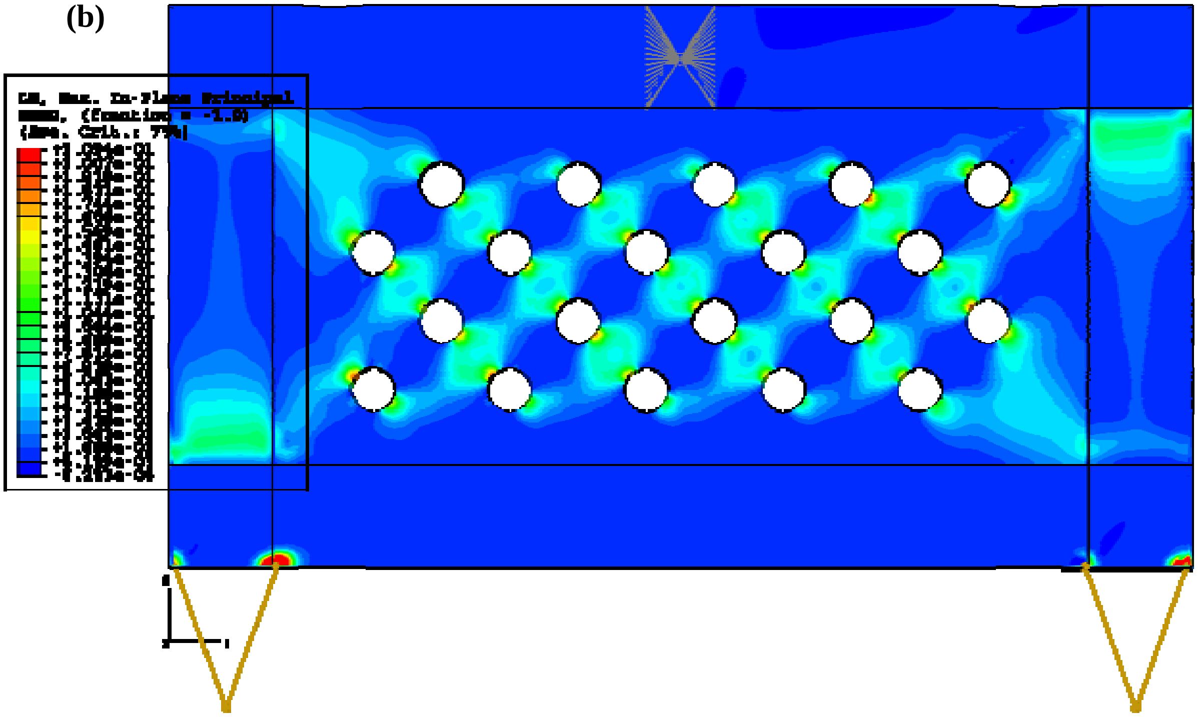

(c)

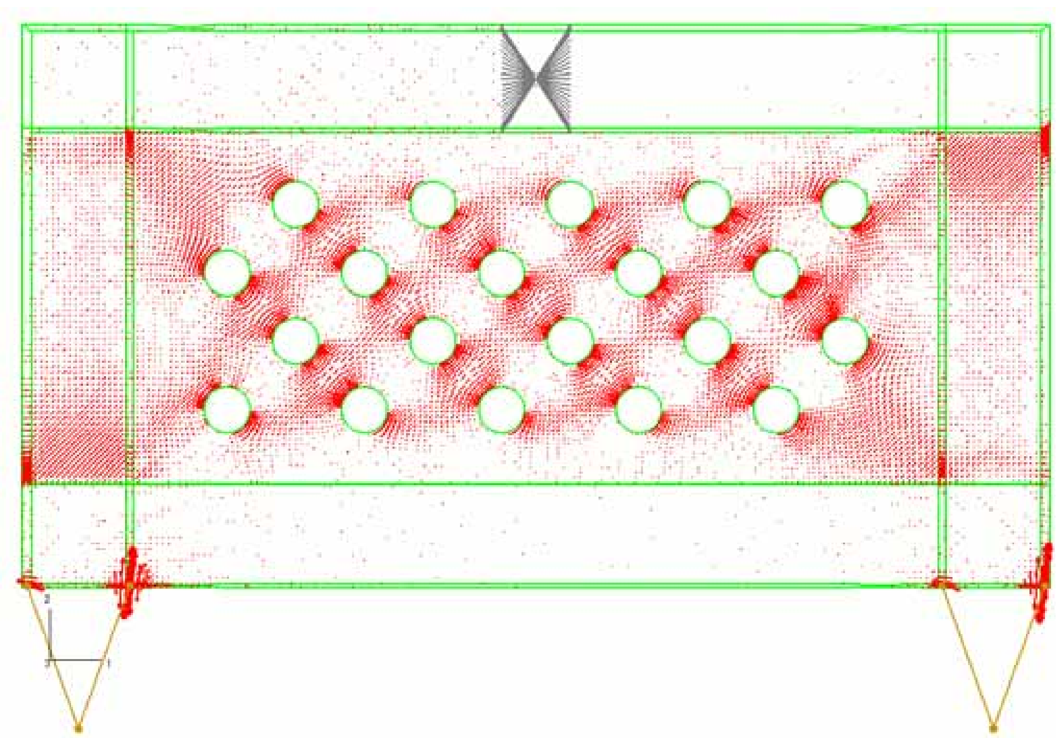

FIGURE 4-15 Perforated Panel Analysis Results at 20% Maximum Local Strain of RF Model, Fine Mesh, t_p = 2.6 mm, D = 200 mm, D/S_{diag} = 0.471 (b) Maximum In-Plane Principal Strain; (c) Strain Tensor Field

The maximum peak and valley are 67.9 mm (at the upper left corner) and – 67.5 mm (at the lower right corner), respectively. On the middle strip, the maximum peak and valley are 40.99 mm and – 38.31 mm, respectively. Note that all points along a given peak “ridge” do not reach the same maximum out of plane deformation. Indeed, the magnified deformations shown in figure 4-14(c) illustrate that the maximum value for the peaks occur along the ridge at the location furthest away from holes, where as some reduction in the amplitude of the out-of-plane buckle occurs at the point closest to two adjacent holes. For example, adjacent to and on each side of the maximum peak of 40.99 mm, along the buckling fold, the maximum out-of-plane deformation drops to 32.68 mm and 31.80 mm between holes. This behavior illustrates that the boundary conditions between each individual strip is unrestrained by adjacent strips. As such, each strip behaves as shown in figure 3.7 (rather than what is shown in figure 3.14), and the variation of amplitude of out-of-plane deformation along a buckling fold occurs as a result of the reduction of effective width due to Poisson’s-ratio effect that develops as the strip elongates. The distribution of tension field action around the perforations similar to that observed by Vian (2005) is again seen on the figure, where stress and strain concentrations initiate at the perforation edges and zones of yielding radiate out from this location at approximately 45° angles with respect to the diagonal tension field orientation. Note that in this model, plastic hinges were constrained to occur in the columns by artificially making the beams infinitely rigid across the entire width of the SPSW. This was done as an interim measure to establish the linkages between full plate behavior and the simplified individual strips. As demonstrated above, such a match exists and difference between results for actual unconstrained SPSW and individual strips are primarily due to flexibility of the top and bottom beams, and not some of the other factors enunciated earlier (e.g. plate buckling, initial imperfections, etc).

To further the understanding of how strip elongations in actual SPSW relate to the individual strip model, another intermediate step is considered, this time using a model in which a rigid-body motion on the beams is considered, but for which plastic hinges occur at the RBS connections (as would be expected in correctly designed SPSW). The next section describes this model named the *Rigid Beam (RB) Model*.

4.5.3 Rigid Beam (RB) Model

The RB Model is a modification of the refined RF Model in which the beams boundary conditions are changed while all other model properties, including the lateral supports, remain the same. In this model, a very stiff beam between the RBS is modeled by increasing the thickness of the flanges and webs to be 10 times thicker than for the actual beam. The RBS segments remained at their actual thickness and unconstrained. This allows the rigid-body motions of the beams (translations and rotations) and development of plastic hinges at the RBS connections. As before, pushover displacements were applied. figure 4-16 shows resulting displacement and deformed shape of the RB model, where plastic hinges occurred at the RBS connections and the beams between the RBS rotated but remained almost parallel (i.e., with less than 0.2° difference) through their rigid-body-motions. Total uniform strip elongation ε_{un} for the 2.6 mm thick infill plate for each monitored strain is plotted in figure 4-17.

It can be observed from the figure 4-17 that STRIPs 2 and 3 elongated by almost the same amount reaching 2.75 and 2.69%, respectively, at 20% maximum principal local strain, while STRIPs 1 and 4 only reached elongation of 2.59 and 2.34%, respectively. This could be attributed to the "kink" that occurred at the RBS connections that are the reference points from which the STRIPs 1 and 4 axial deformations are measured. In this case, the absolute axial elongations of STRIPs 1 to 4 are 56.7, 60.0, 58.6., 51.3 mm, respectively. At lower monitored strain (i.e., ε_{max} = 5%), however, the difference was significantly less since the RBS connections are not severely yielded. Nevertheless, the STRIPs 2 and 3 elongations are yet 8% and 11% lower than that the individual strip, respectively, at the monitored strain $\varepsilon_{max} \geq 10\%$. The effect of mesh size was again investigated as one possible reason for the observed difference in elongation between strips. Further analysis, however, did not confirm this hypothesis. The use of a refined mesh with the infill plate modeled with 12.5 x 12.5 mm shell elements near the boundary elements and on average 7.5 x 7.5 mm shell elements adjacent to the perforations (with a total of 108819 elements this model was seven times more computationally intensive) insignificantly changed the results presented in figure 4-17.

To investigate the possible reason for some of the difference in elongation between strips, as well as the lower elongation for the SPSW strip compared to the individual strip results obtained in

(a)

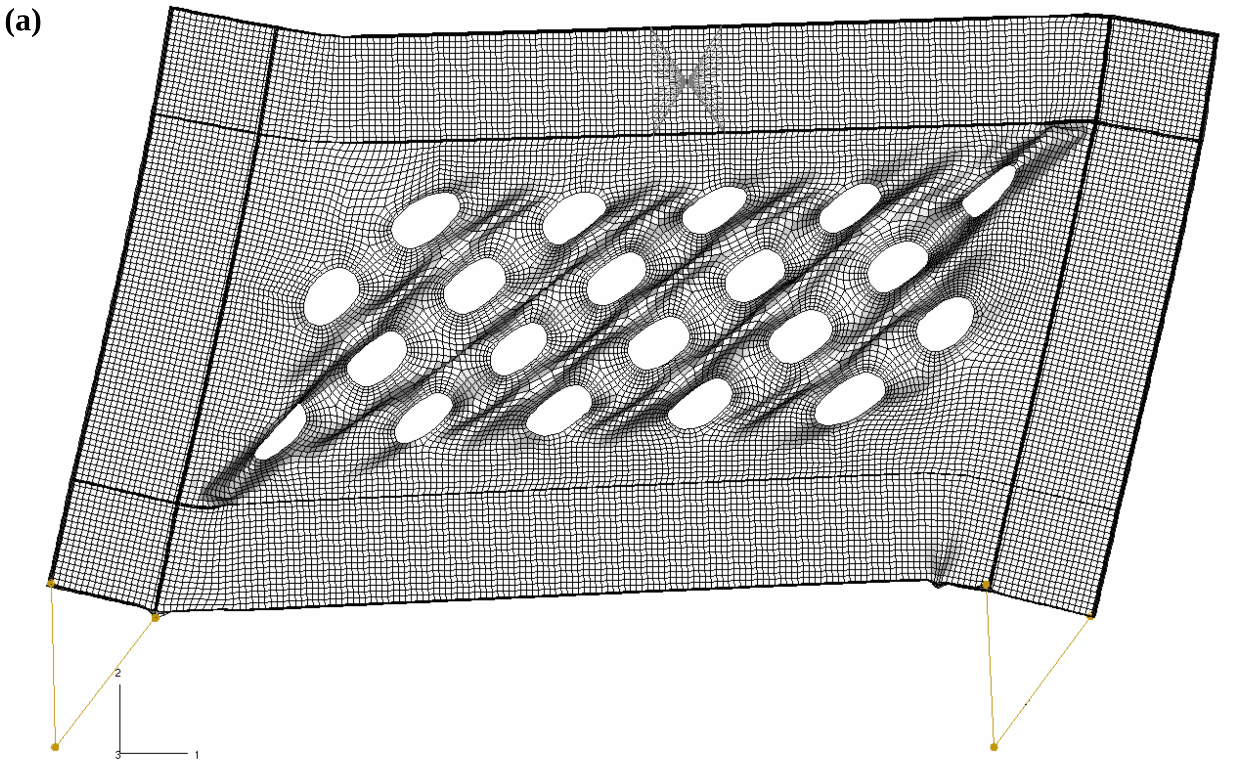

(b)

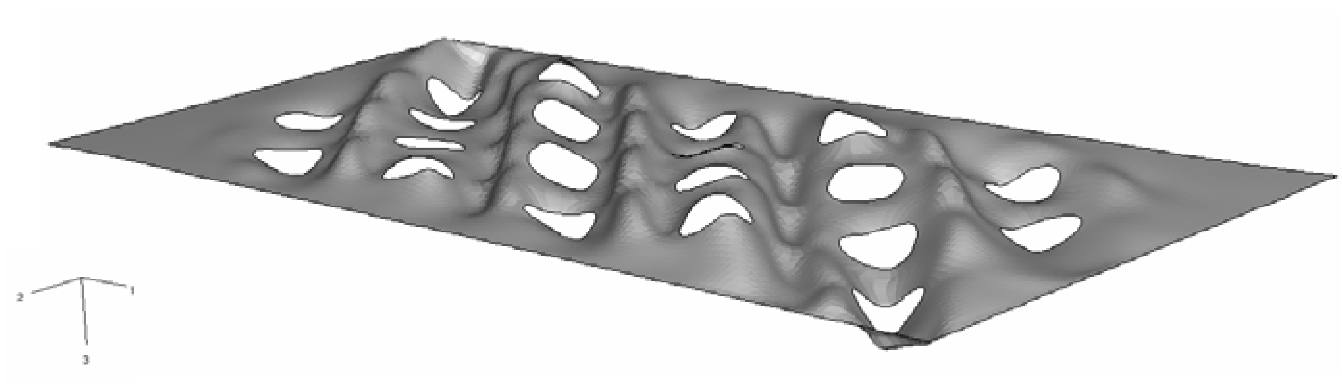

FIGURE 4-16 Deformed Shape of RB Model (a) Parallel Deflection at Top and Bottom Beam (Deformed Shape Scale Factor = 5.0); (b) Infill Plate Deformation Shaped (Deformation Scale Factor = 2.0)

(c)

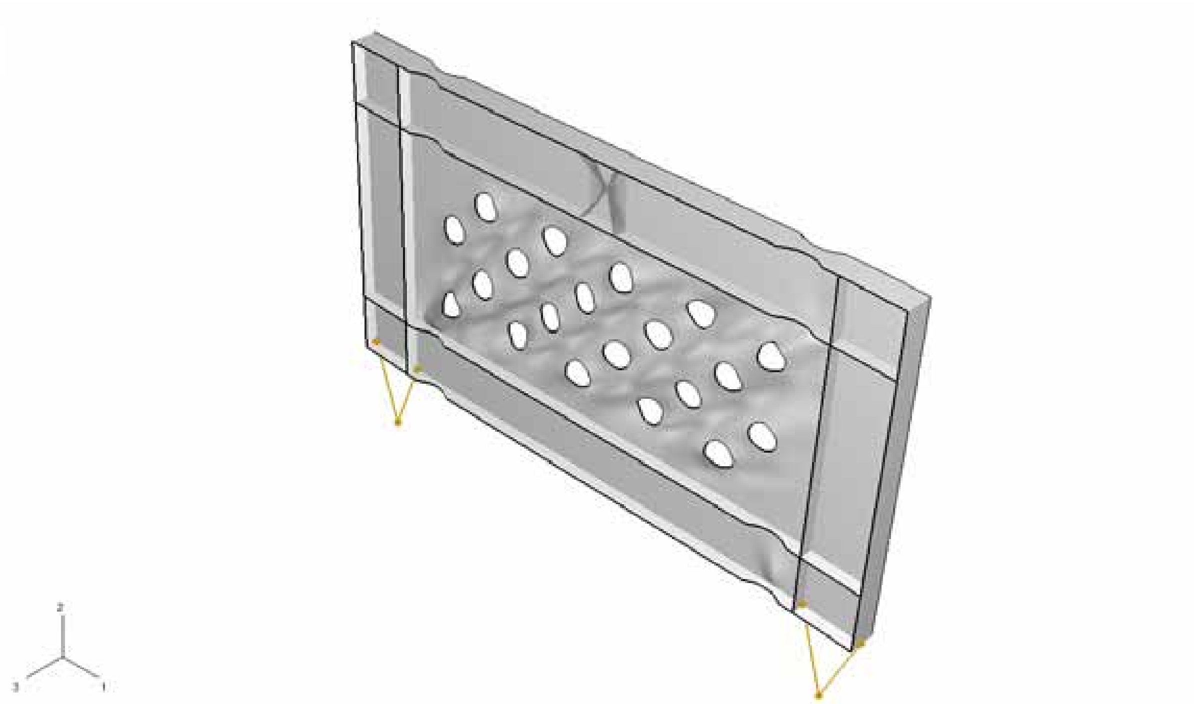

(d)

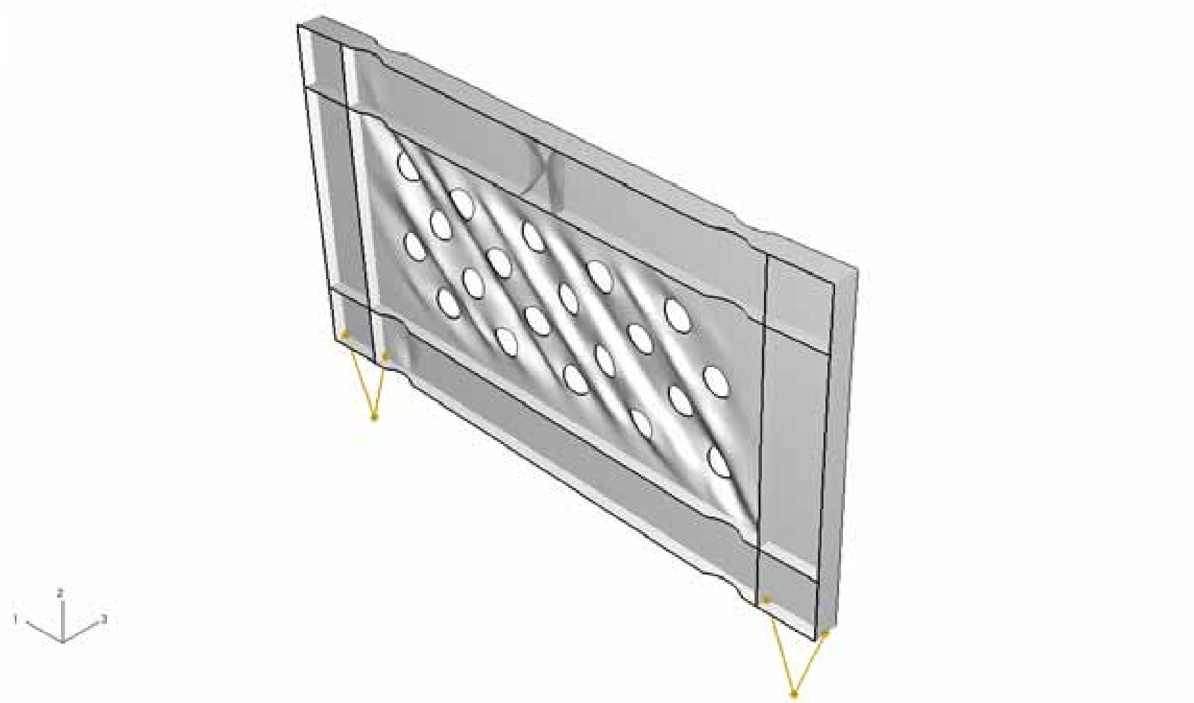

FIGURE 4-16 Deformed Shape of RB Model – Cont'd (c) Front View; (d) Rear View (Deformation Scale Factor = 1.0)

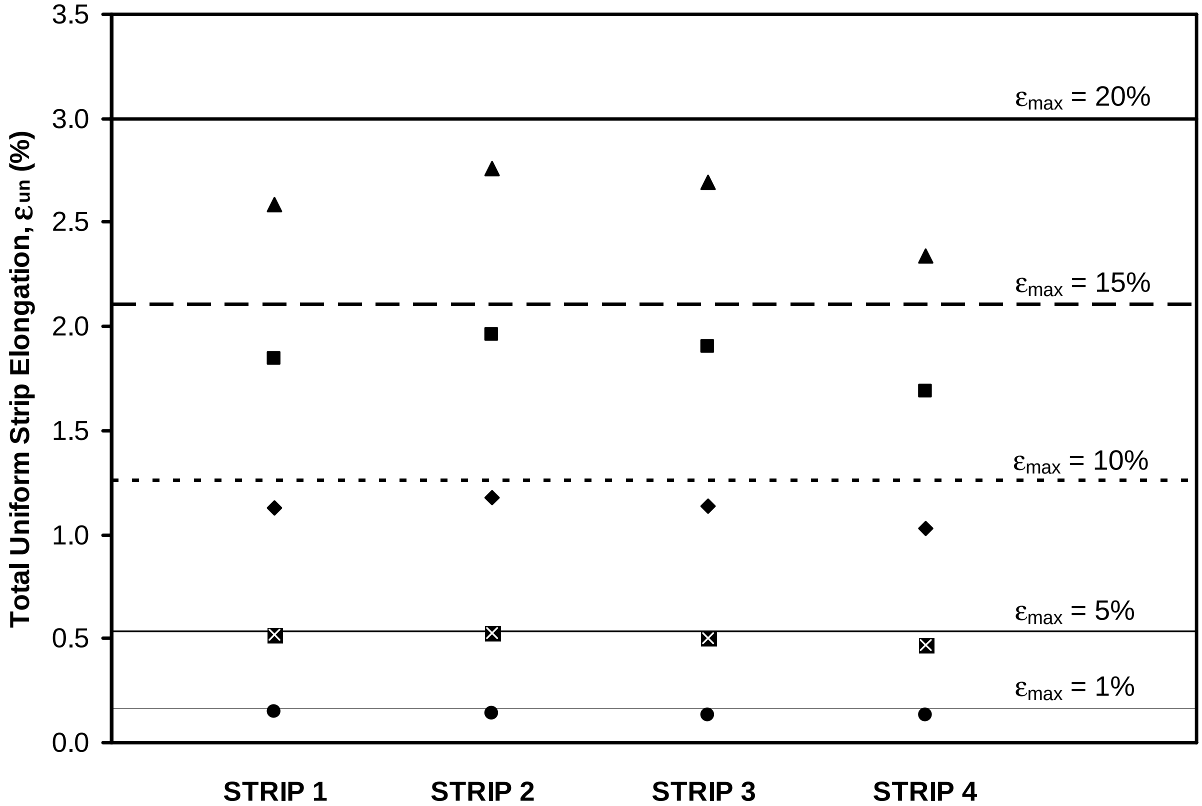

FIGURE 4-17 Uniform Distributed Strip Axial Strain ε_{un} at each Monitored Strip Location (RB Model, Fine Mesh, t_p = 2.6 mm, D = 200 mm, D/S_{diag} = 0.471); Lines Correspond to Individual Strip Analysis

Section 3, close attention was paid to the location of maximum principal local strain. Figure 4-18 presents in-plane principal maximum stress contours, strain contours and strain tensor fields at 20% monitored strain. As shown in the figure 4-18(b), larger strains developed in one of the edge strips compared to any value anywhere else on the plate. In fact, when the 20% maximum principal local strain occurred at the “edge” strip (STRIP R), the “full-length” strips only reached 17.2%, 16.1%, 16.7, and 18.4% strain for STRIPs 1 to 4, respectively. Note that in all cases considered so far, all results were plotted when the target maximum principal local strain was reached at one single location anywhere in the SPSW infill plate, irrespective of where that maximum value was located. It was therefore decided to continue the pushover analysis of the SPSW until one of the “full” strips reached 20% strain next to a perforation. This led to corresponding strip elongations of 2.89, 3.12, 3.06, and 2.60% for the same respective strips as shown in figure 4-19. This provides a better match between the SPSW strip results and that of

(a)

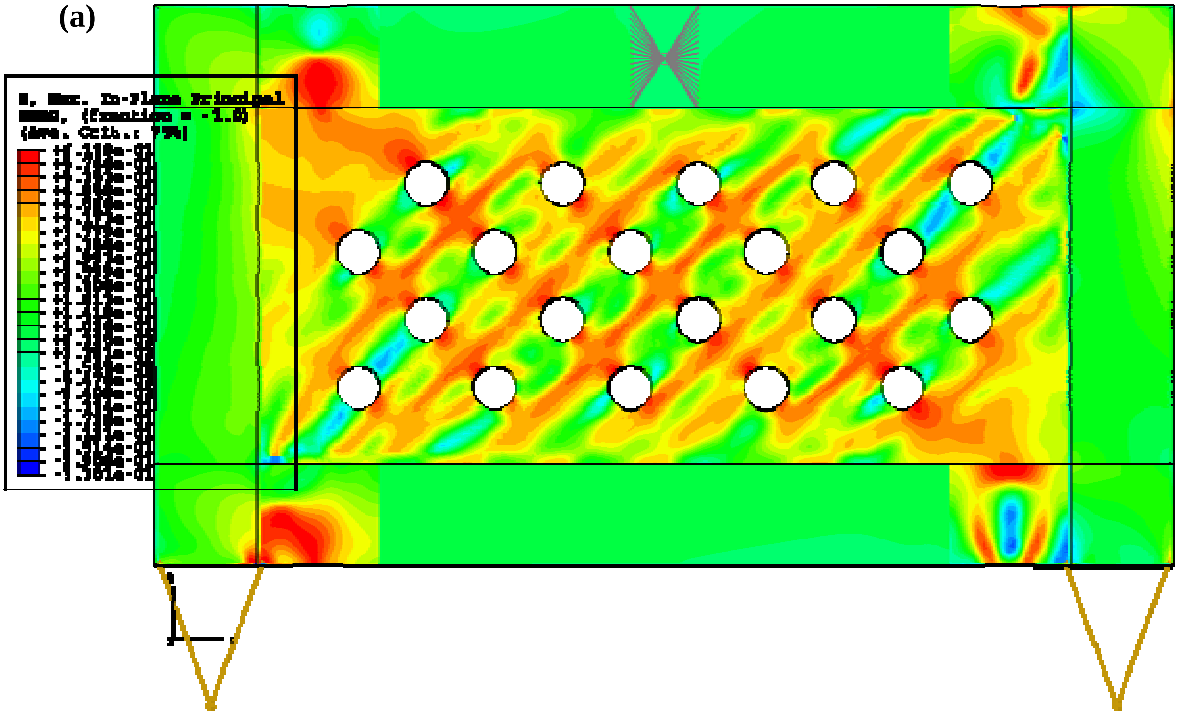

FIGURE 4-18 Perforated Panel Analysis Results at 20% Maximum Local Strain of RB Model, Fine Mesh, t_p = 2.6 mm, D = 200 mm, D/S_{diag} = 0.471 (a) Maximum In-Plane Principal Stress Contours

individual strips, but still does not fully explain the relative difference in results between the various strips in the SPSW (other than what was discussed earlier). It is not clear either why the maximum strain occurs in an edge strip, but it is speculated to be due to some combination of biaxial stress condition due to constraints at the corner of the plate. Elongation of the RBS flange, compounded with the infill plate elongation, and possibly some artifact due to the rigid beam modeling next to the RBS, may all contribute to this "corner effect". A detailed study of this localized phenomenon is beyond the scope of this study. However, from here on in this study, results in figure 4-17 are used and the 15% differences between individual strip results are considered acceptable for all practical purposes.

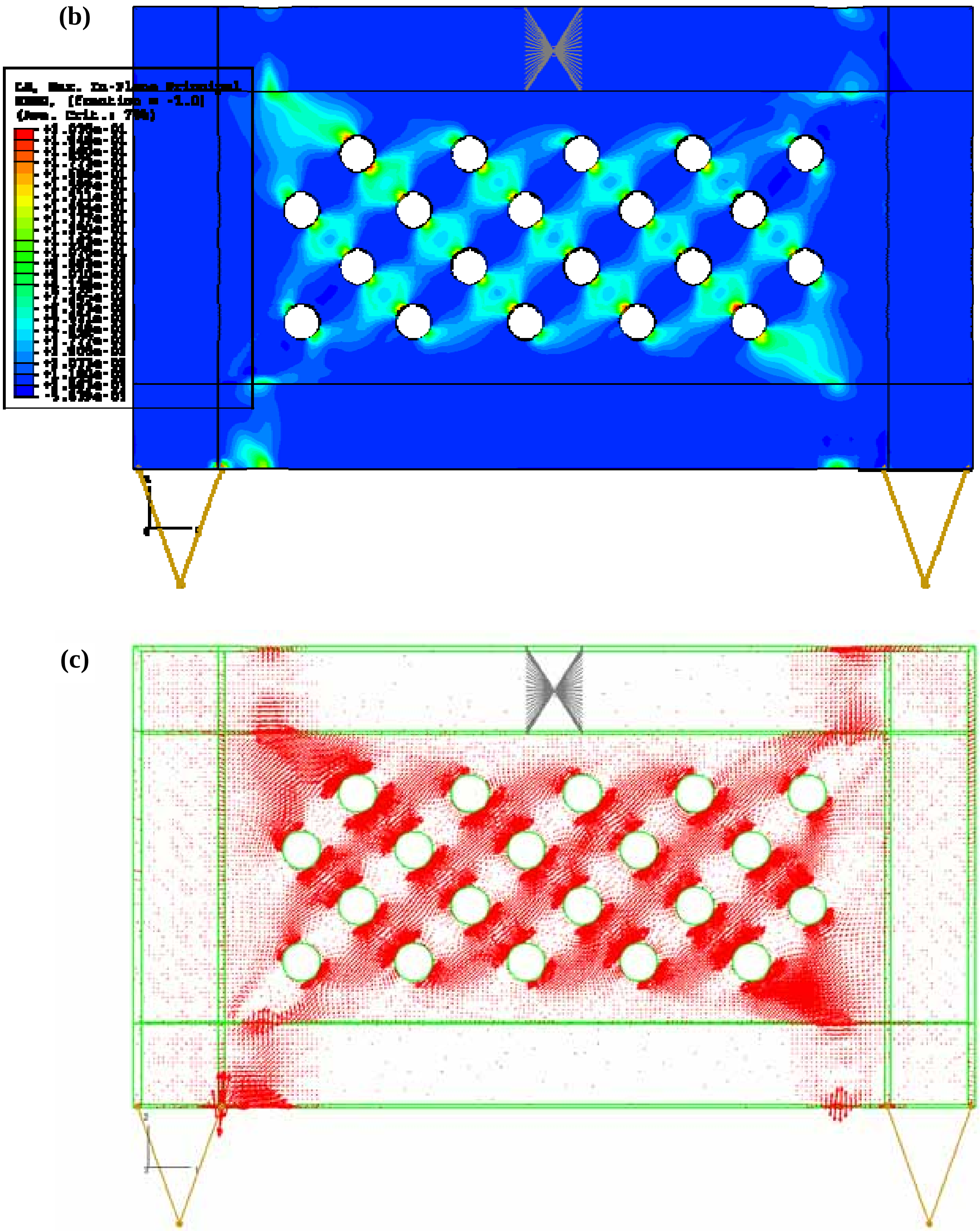

FIGURE 4-18 Perforated Panel Analysis Results at 20% Maximum Local Strain of RB Model, Fine Mesh, t_p = 2.6 mm, D = 200 mm, D/S_{diag} = 0.471; (b) Maximum In-Plane Principal Strain (c) Strain Tensor Field

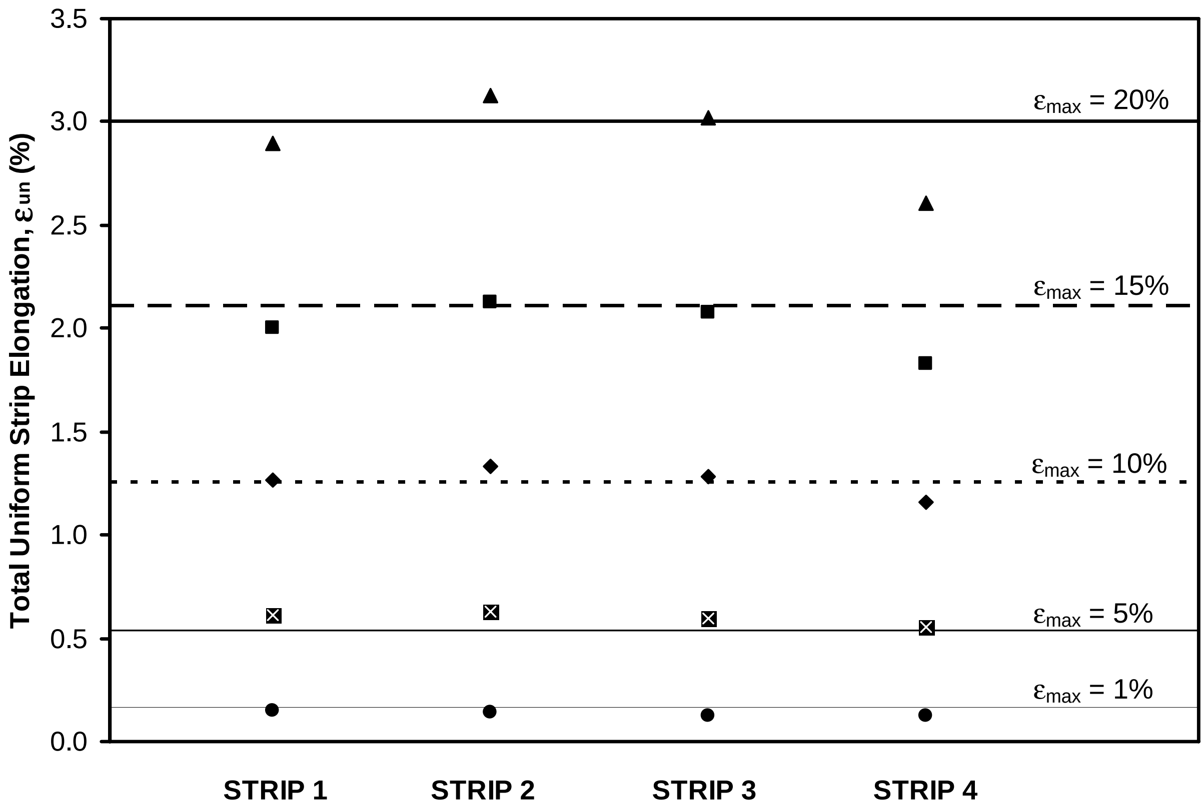

FIGURE 4-19 Uniform Distributed Strip Axial Strain ε_{un} at each Monitored Strip Location (Extended RB Model, Fine Mesh, t_p = 2.6 mm, D = 200 mm, D/S_{diag} = 0.471); Lines Correspond to Individual Strip Analysis

4.6 Behavior of Perforated SPSW of Various Infill Plate Thicknesses

To examine the effect of relative thickness in perforated SPSW, the three analyzed models were re-analyzed using several different infill plate thicknesses from 1 to 5 mm. The results were monitored for the same strain limit states, and the total uniform strip elongation ε_{un} was measured at the STRIP 2 for the FLTB and RB models. For the RF model, the *Equivalent* strip elongation was calculated from (4-2), chosen for expediency, which for this model is similar to the actual SPSW strip elongations.

4.6.1 Flexible Beam Laterally Braced (FLTB) Model

Figure 4-20 presents the total uniform strip elongation ε_{un} for several different infill plate thicknesses. The results of the FLTB show that strip elongation did not fluctuate much as the

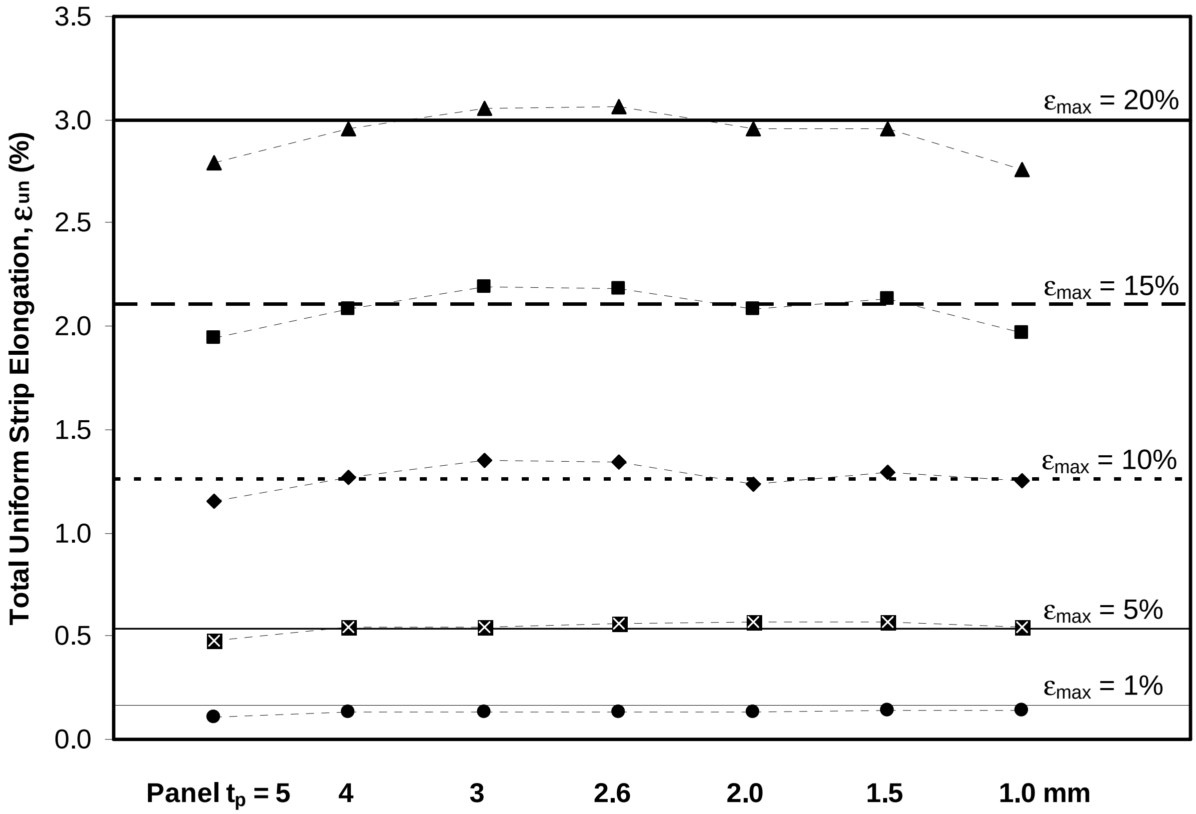

FIGURE 4-20 Uniform Distributed Strip Axial Strain ε_{un} Measured at STRIP 2 for Various Infill Plate Thickness (FLTB Model, Fine Mesh, D = 200 mm, D/S_{diag} = 0.471); Lines Correspond to Individual Strip Analysis

infill plate thickness changed from 1 mm to 5 mm. For example, at ε_{max}= 20%, the 2.6 mm and 5 mm panel elongated 2.79% and 3.06%, respectively, and the difference between the two is only 10%. Moreover, the panel with infill thickness from 1.5 mm to 4 mm apparently matched the individual strip results. However, that later observation is not necessary true for all strips in light of the results plotted in figure 4-9 where every strip reached a different strip elongation.

4.6.2 Rigid Floor (RF) Model

Figure 4-21 presents the total uniform strip elongation ε_{un} for several different infill plate thicknesses. The results of the RF model show that, except for relatively thin plates (i.e. smaller than 1.5 mm here), strip elongation or frame drift was not much affected by the infill plate thickness. For example, at ε_{max} = 20%, the 2 mm and 5 mm thickness panel elongated 2.93% and

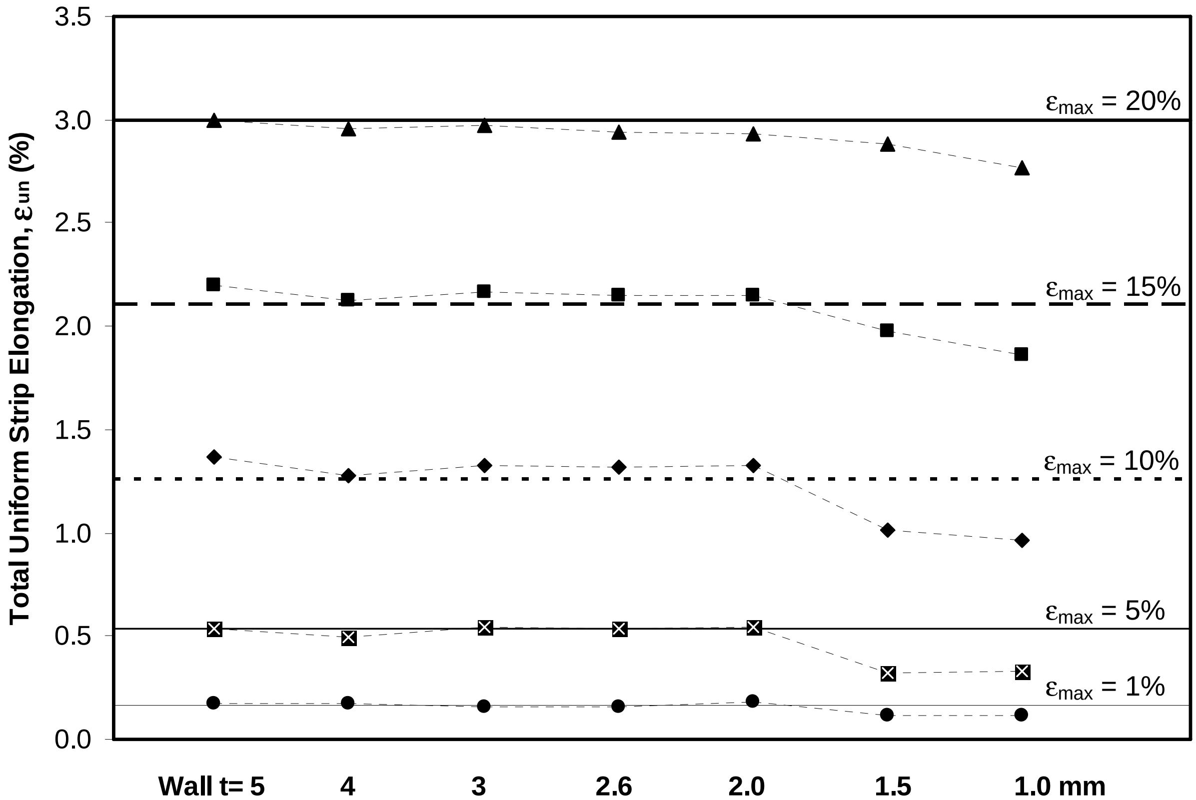

FIGURE 4-21 Equivalent Uniform Distributed Strip Axial Strain ε_{un} for Various Infill Plate Thickness (RF Model, Fine Mesh, D = 200 mm, D/S_{diag} = 0.471); Lines Correspond to Individual Strip Analysis

3.00%, respectively (corresponding to a frame drift of 5.86% and 6.00%, respectively). For comparison, the 1 mm thickness panel reached the same monitored strain earlier at 2.78% strip elongation (or 5.56% frame drift), which is 8% less.

Observation of the strain contours revealed why the relatively thin plates reached a certain maximum principal local strain earlier than the thicker plates. The location in the plate where the 20% maximum principal local strain occurred for the various infill plate thicknesses considered is marked in figure 4-22. These locations for the thicker plates, $t_p \geq 2$ mm, occurred in one of the “full-length” strips, while it occurred in an “edge” strip for the thinner plates. Note that for the latter case, for the 1 mm thickness panel, the maximum strain in STRIPs 1 to 4 is 16.4, 18.2, 17.9, and 16.3%, respectively. As was done previously for the RB model, the pushover displacement

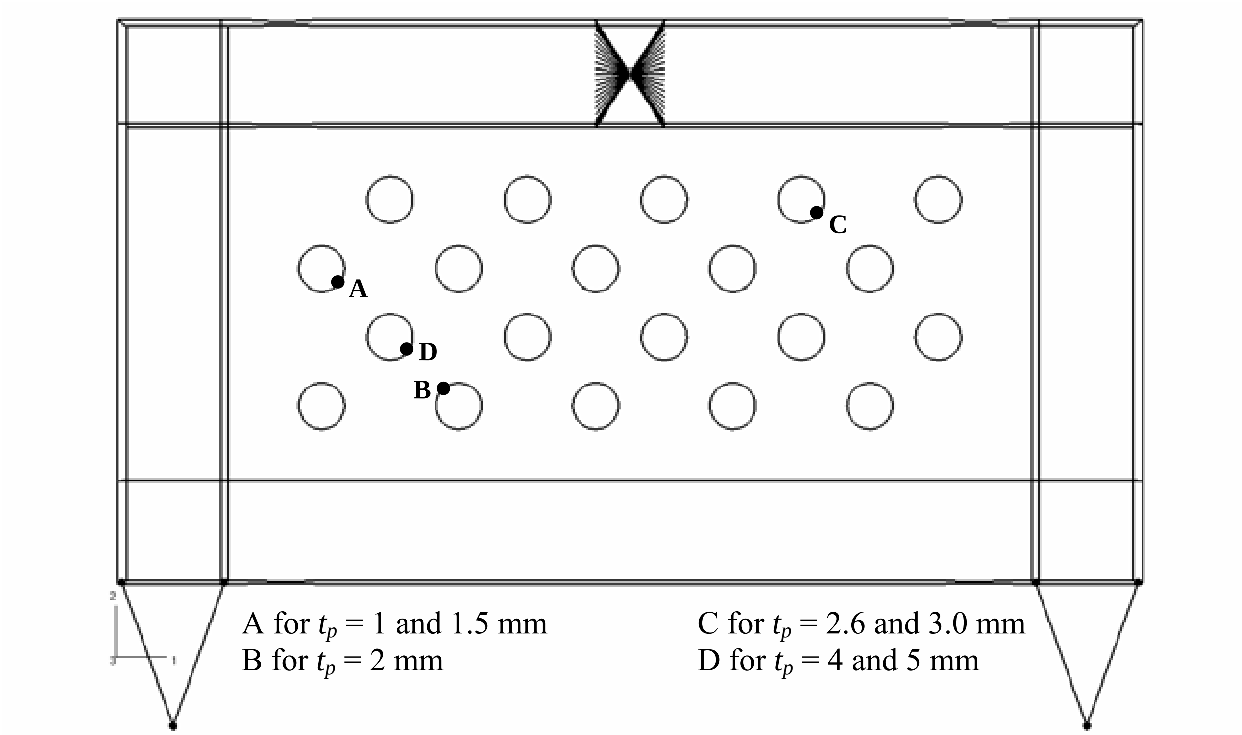

FIGURE 4-22 Location of the 20% ε_{max} Occurred for Various Infill Plate Thickness

analysis could be continued until one of the "full-length" strips reached 20% strain which would give larger system strip elongations (and frame drifts) for the SPSW with thinner plates. When 20% monitored strain occurred at the STRIP 2, the strip elongated 3.04% (corresponding to a frame drift of 6.08%).

Berman and Bruneau (2003) investigated the use of plastic analysis as an alternative for the design of SPSW. The researchers developed the base shear equation using kinematic collapse mechanism. In this mechanism, for a given drift, every strip in the infill plate would reach the same local strain. However, the results here did not confirm the same fact; the local strain was higher next to a corner. Three reasons could partly explain this phenomenon. First, there seems to be some local effect developing at the "edge" strip that is not explained further as part of scope of this study. Note that the difference between "edge" and "full" strip behavior is small of little significance in light of other assumptions made. Second, the "kink" that occurs at the columns as a result of plastic hinging there may have an impact both on the aforementioned local effect, and in creating unequal strip elongations. Third, nodes in the infill plate close to the RBS connections elongated more than along the rest of the beam and are thus subjected to large strains in more than one direction.

4.6.3 Rigid Beam (RB) Model

The total uniform strip elongation ε_{un} for several different infill plate thicknesses is plotted in figure 4-23 for the RB model. The results in the figure show that strip elongation did not fluctuate as the infill plate thickness changed from 1 mm to 5 mm, as also observed for the other two models. For example, at ε_{max} = 20%, the 1.5 mm and 5 mm panel elongated 2.54% and 2.84%, respectively, and the difference between the two is only 12%.

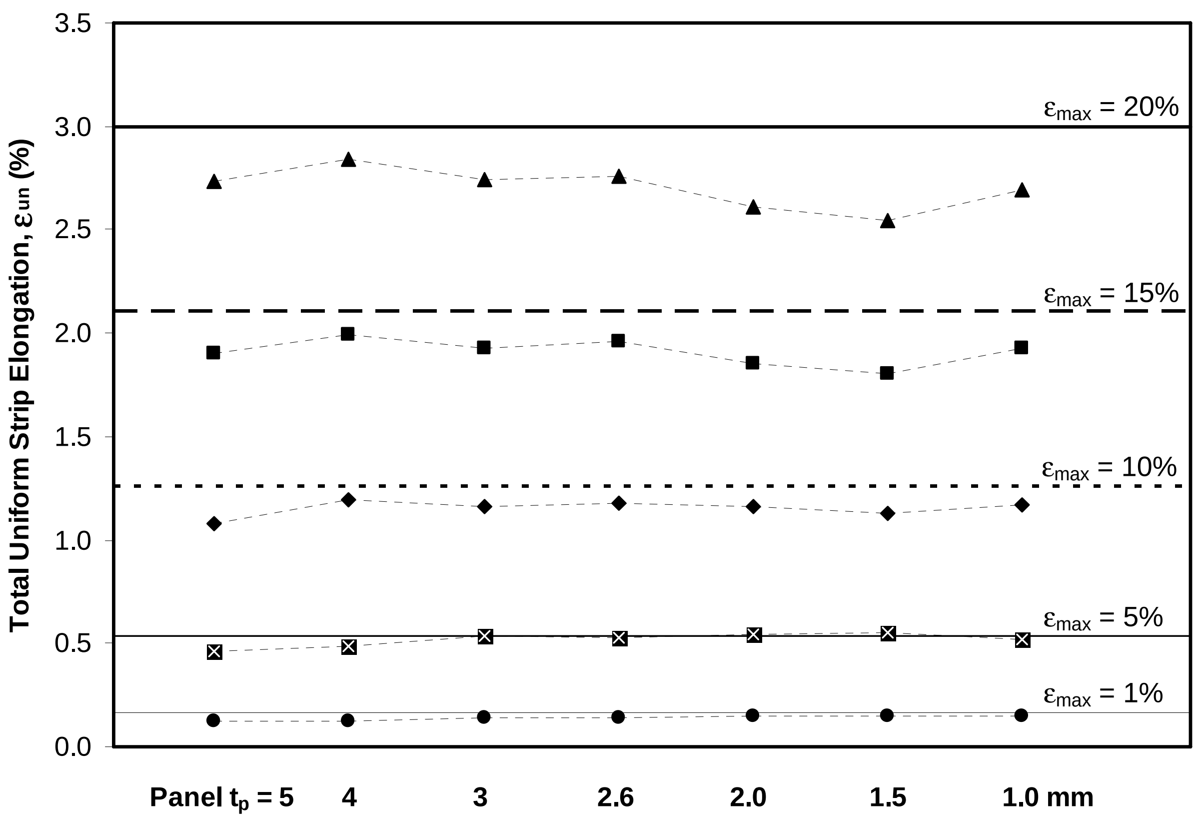

FIGURE 4-23 Equivalent Uniform Distributed Strip Axial Strain ε_{un} for Various Infill Plate Thickness (RB Model, Fine Mesh, *D* = 200 mm, D/S_{diag} = 0.471); Lines Correspond to Individual Strip Analysis

4.7 Effects of Perforation Ratios and Number of Perforations

To examine the effect of perforation ratios and number of perforations, a series of SPSW using the three analyzed models with several panel perforation diameter D = 50, 100, 150, 200, 250, and 300 mm was developed and analyzed. This data set allows observation of the trends in SPSW behavior compared to the individual strip results plotted in figure 3.10. Note that the total uniform strip elongation ε_{un} presented here were also measured at the same location previously described in Section 4.6, at the STRIP 2 for the FLTB and RB models and using (4-2) for the RF model.

4.7.1 Flexible Beam Laterally Braced (FLTB) Model

Figure 4-24 shows the results for the FLTB model with refined mesh for STRIP 2. The strip elongation reached 1.12, 1.73, 2.06, 2.18, 2.27, and 1.97% when the maximum local strain reached 15% maximum principal local strain, and 1.79, 2.46, 2.87, 3.05, 3.17, and 2.67% when the maximum principal local strain reached 20% for the respective perforation diameters of 50, 100, 150, 200, 250, and 300 mm. Some differences between the SPSW panel strips and the individual strips results are observed at 15 and 20% monitored strain for smaller perforation diameters (i.e., 50, 100, and 150 mm). For example at 20% monitored strain and 100 mm perforation diameter, the differences between the two are as much as 23%. Some variation in those results is expected for the other strips of the FLTB model, consistently with the trends shown in figure 4-9. Note that the results presented here are obtained from the perforated SPSW having infill plate of 2.6 mm thick. When using infill plate of 5 mm thick for the perforation diameter of 200 mm as in Section 4.5.1, a 10% difference was observed at 20% monitored strain.

4.7.2 Rigid Floor (RF) Model

Figure 4-25 shows the results for the RF model with refined mesh. Note that since strip elongation can be related to frame drift using (4-2), both strip elongation and frame drift are given on the left and right vertical axes, respectively. For example, to illustrate interpretation of the results, it can be seen in the figure that to reach a 15% maximum principal local strain, the frame has to achieve 2.21, 3.02, 3.78, 4.29, 4.73, and 3.78% drifts, and the strip reached 1.11, 1.51, 1.89, 2.15, 2.37, 1.89% elongations for the same respective perforation diameters. As described in Section 4.5.2, the RF model having perforated panel with the 200 mm diameter holes matched

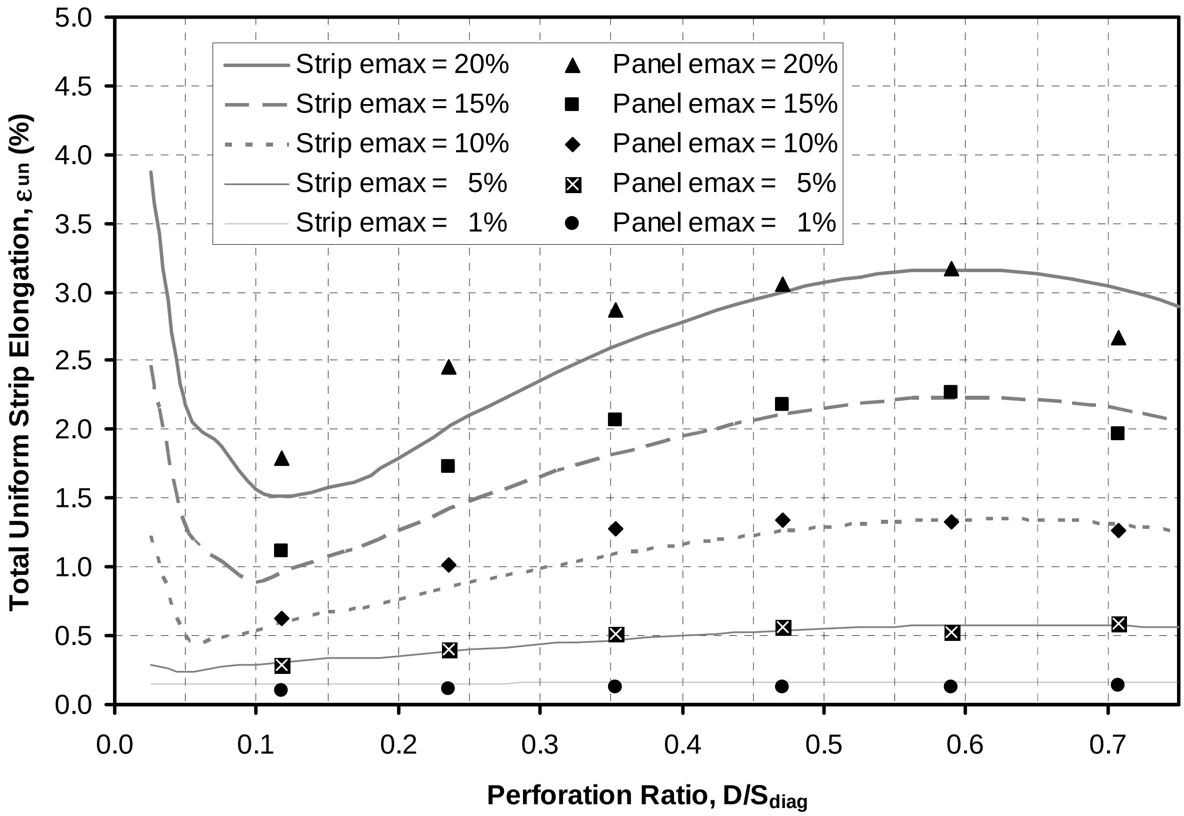

FIGURE 4-24 Uniform Distributed Strip Axial Strain ε_{un} versus Perforation Ratio D/S_{diag} (FLTB Model, Fine Mesh, t_p = 2.6 mm)

well the individual strip model results; figure 4-25 further confirms the same result for various perforation ratios. Some insignificant differences occurred at the smaller perforation ratio D/S_{diag} = 0.118 and 0.236 (which correspond to D = 50 mm and 100 mm, respectively) at the 5 and 10% monitored strain levels.

4.7.3 Rigid Beam (RB) Model

Figure 4-26 shows the results for the RB model with refined mesh. For the same selected cases considered previously, the strip elongated 1.15, 1.52, 1.85, 1.96, 2.11, and 1.87% to reach a 15% maximum principal local strain, and 1.75, 2.26, 2.65, 2.75, 2.96, and 2.60% to reach a 20% maximum principal local strain for the same respective perforation diameters. Note that (4-2), which relates strip elongation to frame drift, is not valid for the RB model. Though some differences between the SPSW panel strips and the individual strip results are observed at the

20% monitored strain, at lower monitored strain however the two models are in a good agreement. A less than 15% difference is observed and considered acceptable.

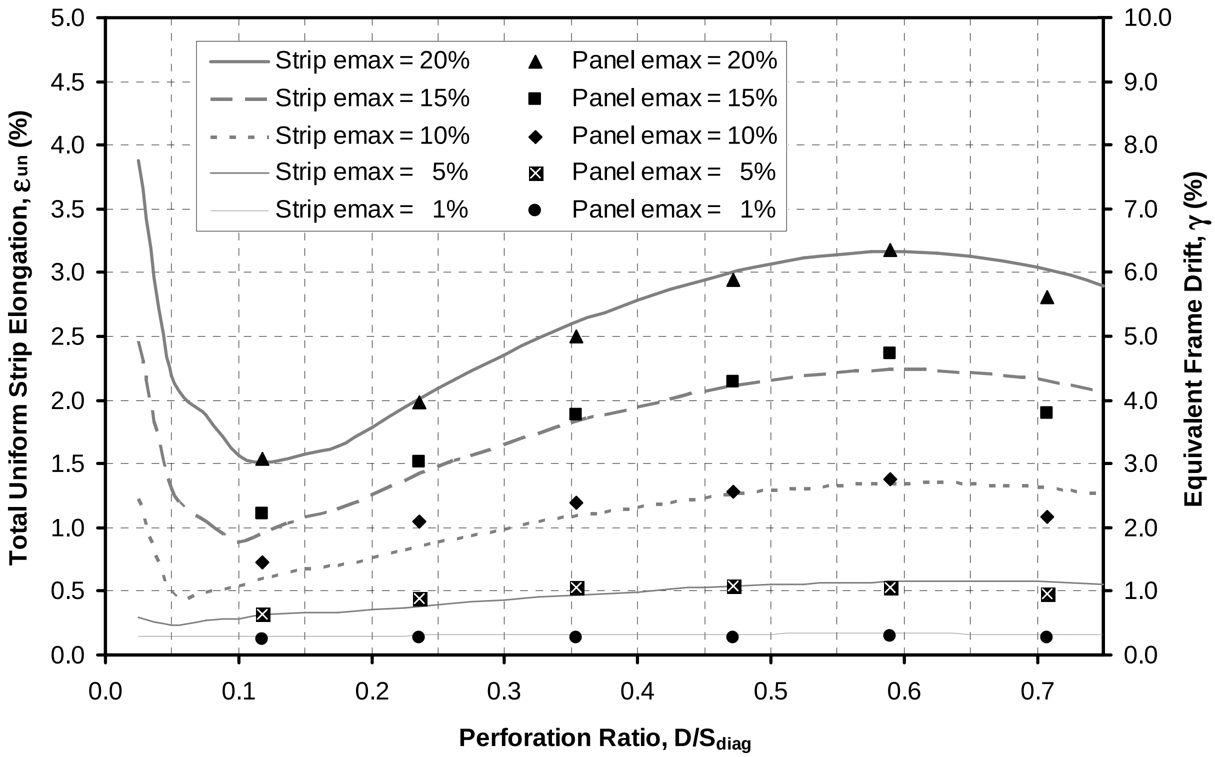

FIGURE 4-25 Uniform Distributed Strip Axial Strain ε_{un} versus Perforation Ratio D/S_{diag} (RF Model, Fine Mesh, t_p = 2.6 mm)

4.7.4 Discussion on the 300 mm Perforation Diameter

No substantial efforts were invested to investigate why for all models considered, the results for the case with 300 mm perforations (D/S_{diag} = 0.707) were consistently different from the individual strip results at all monitored strains. As shown in figure 4-27, strain contours show that the zones of yielding propagate more directly from hole to hole instead of radiating out more broadly from the perforation edges in 45° angles as observed for the typical strain distributions plotted in the figures 4-11, 4-15, and 4-18 for the FLTB, RF and RB model, respectively. However, strain contours of the individual strip at the same perforation ratio shown in figure 4-28 exhibited the same yielding pattern so the match between the results should be better. The difference might be attributable to a "corner effect" of the type previously described and possibly

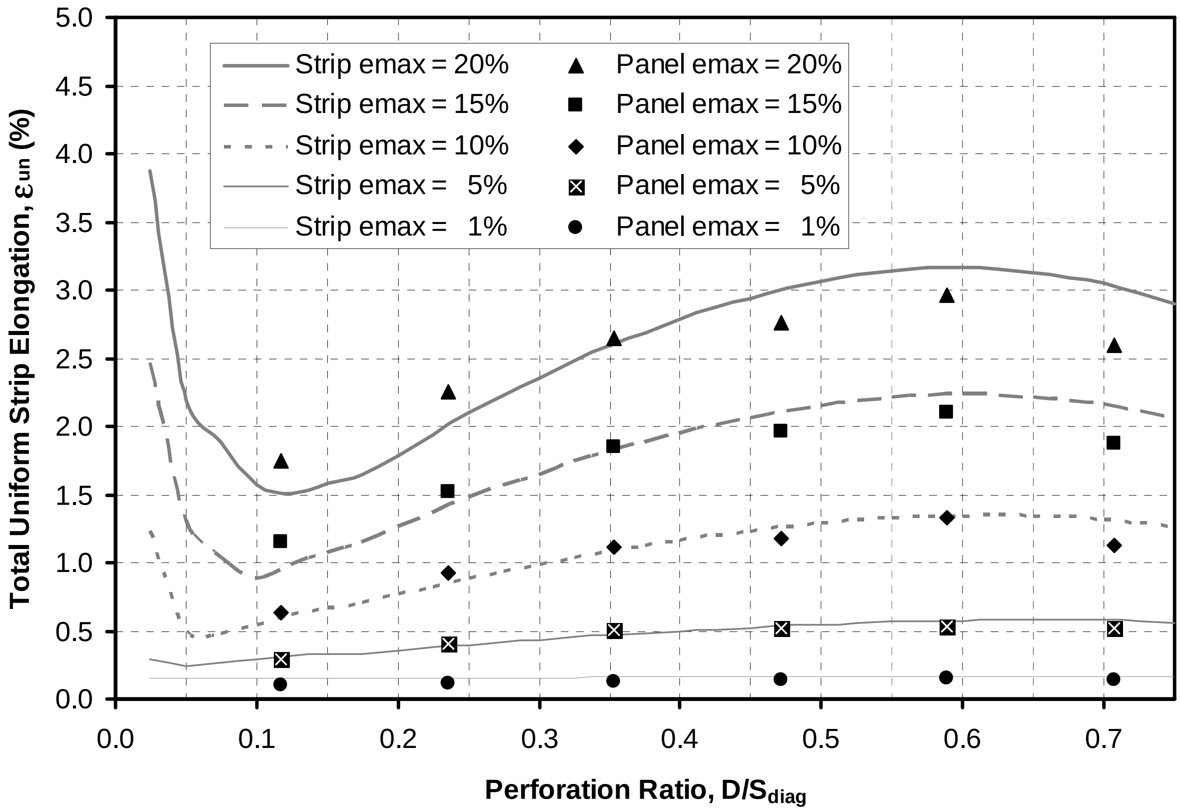

FIGURE 4-26 Uniform Distributed Strip Axial Strain ε_{un} versus Perforation Ratio D/S_{diag} (RB Model, Fine Mesh, t_p = 2.6 mm)

magnified as the size of holes become relatively more significant. However, a more detailed investigation of this particular case is beyond the scope of this study. For this reason, in designing a perforated SPSW, it is recommended at this time to limit the perforation ratio $D/S_{diag} \leq 0.6$ (i.e. the range over which good match in results was obtained) which is a range that should accommodate most practical needs.

For completeness of understanding the effect of perforation ratios and number of perforations, the normalized strip elongations of all models are also plotted in figures 4-29 to 4-31. This can be done by dividing the total uniform elongation ε_{un} by the ratio $N_r{\cdot}D/L$ as also performed in Section 3. In this case too, the results for the SPSW panel strips and individual strips are in good agreement, for all models considered.

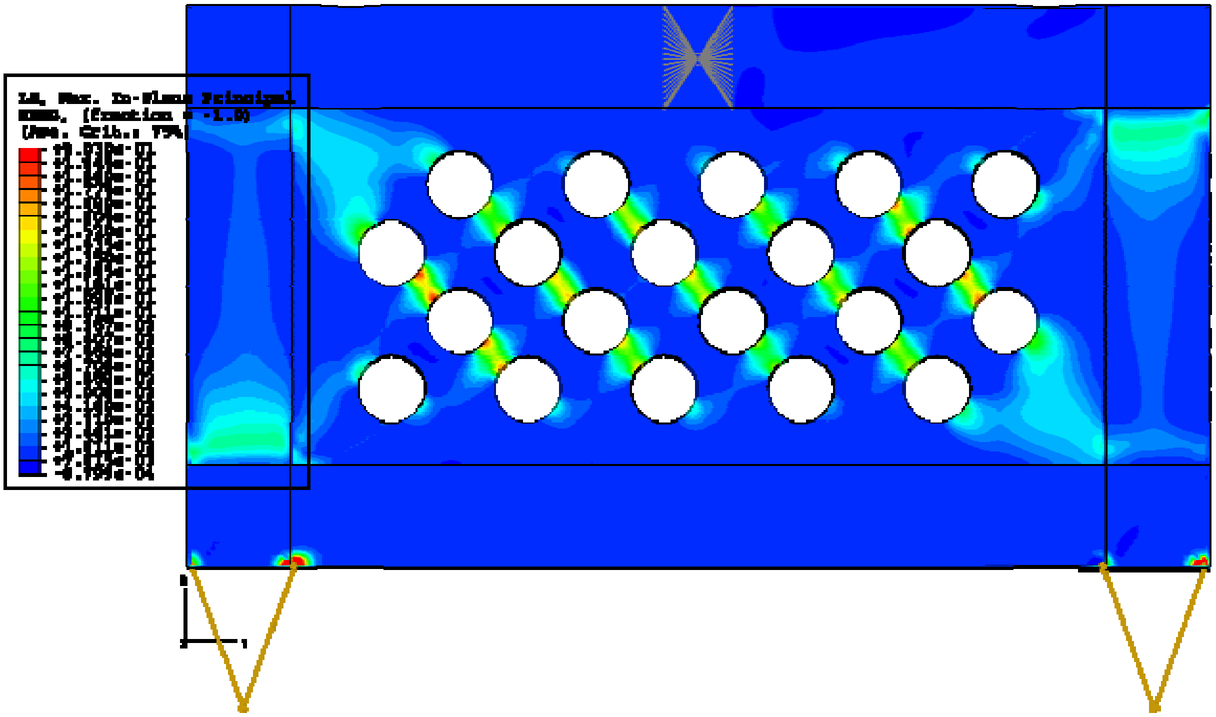

FIGURE 4-27 Maximum In-Plane Principal Strain of RF Model at 20% Maximum Local Strain, Fine Mesh, t_p = 2.6 mm, D = 300 mm, D/S_{diag} = 0.707

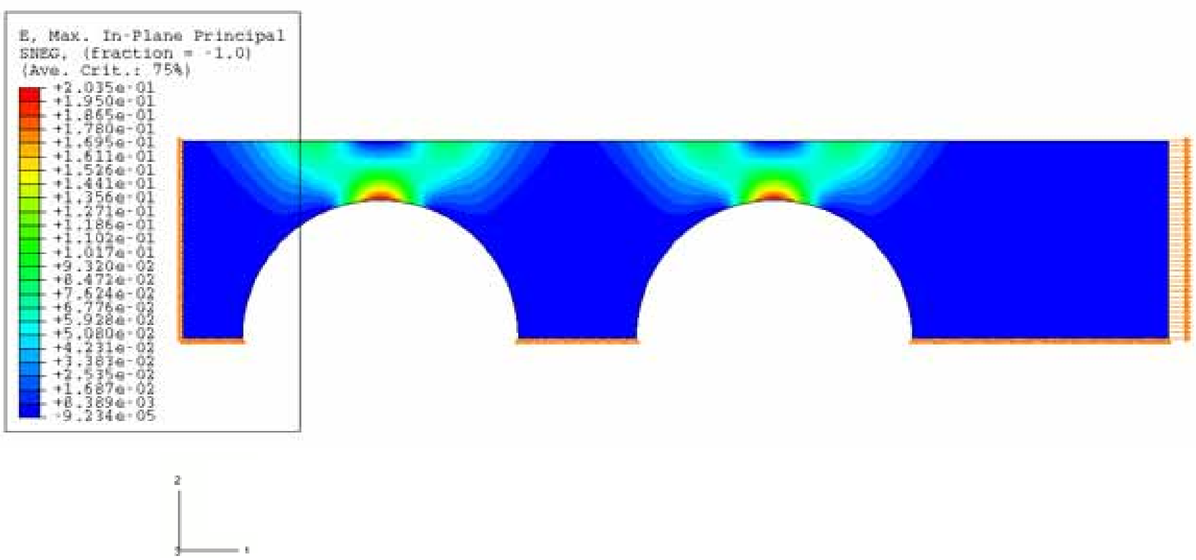

FIGURE 4-28 Maximum In-Plane Principal Strain of Strip Model at 20% Maximum Local Strain D = 280 mm, D/S_{diag} = 0.700

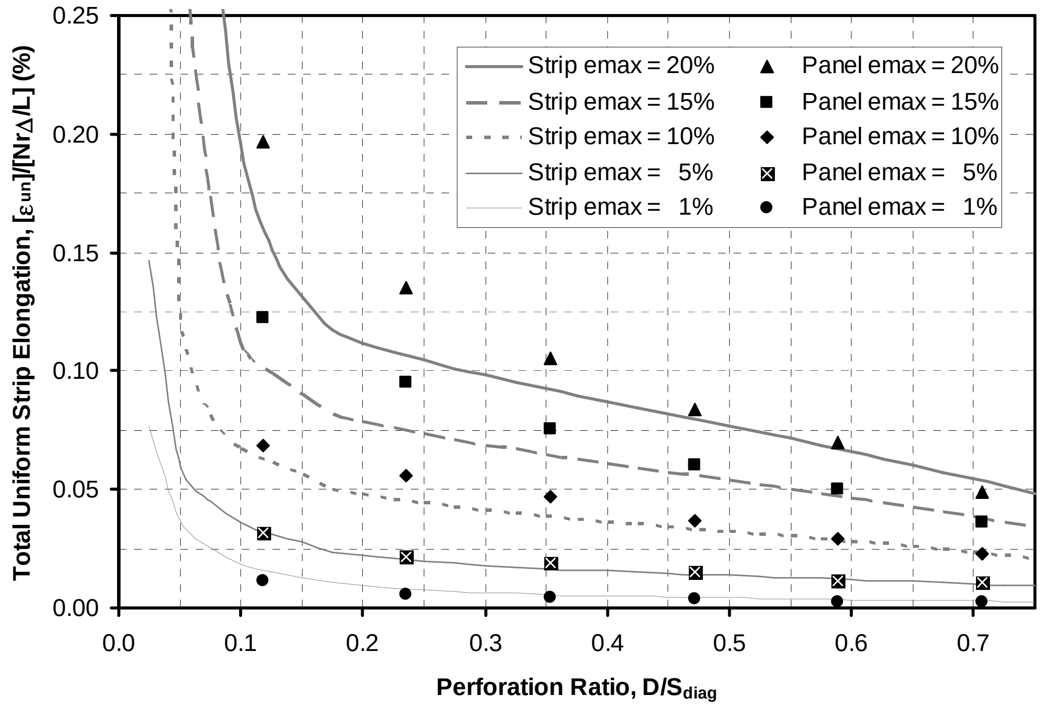

FIGURE 4-29 Normalized Strip Elongation [$\mathcal{E}_{un}$]/[*Nr·D/L*] versus Perforation Ratio *D/S_{diag}* (FLTB Model, Fine Mesh, t_p = 2.6 mm)

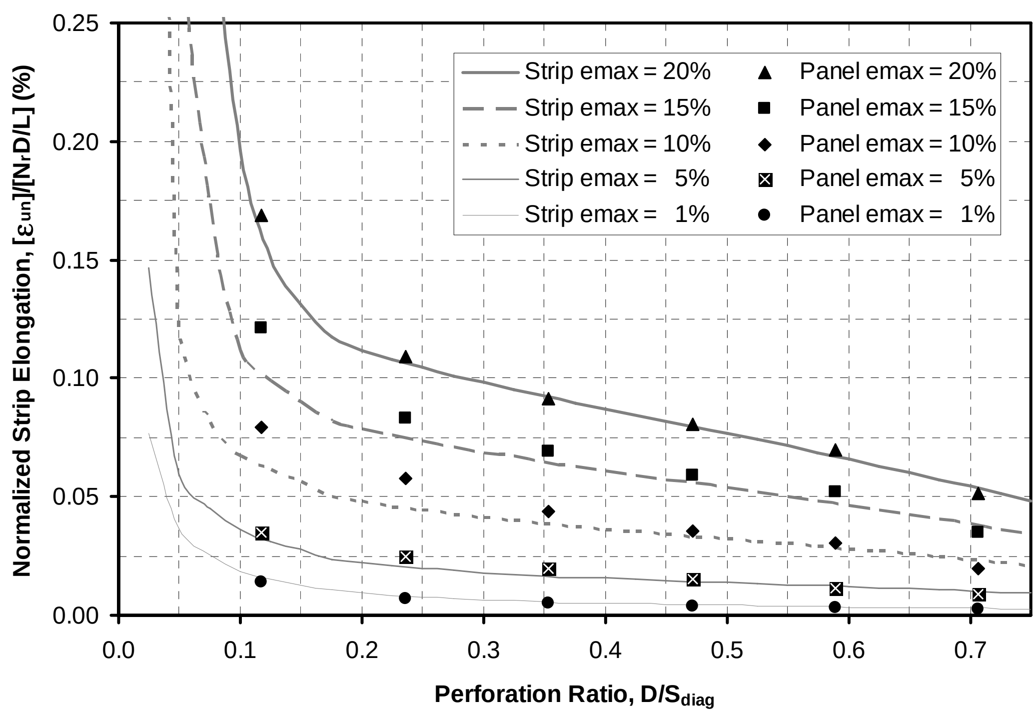

FIGURE 4-30 Normalized Strip Elongation [$\mathcal{E}_{un}$]/[*Nr·D/L*] versus Perforation Ratio *D/S_{diag}* (RF Model, Fine Mesh, t_p = 2.6 mm)

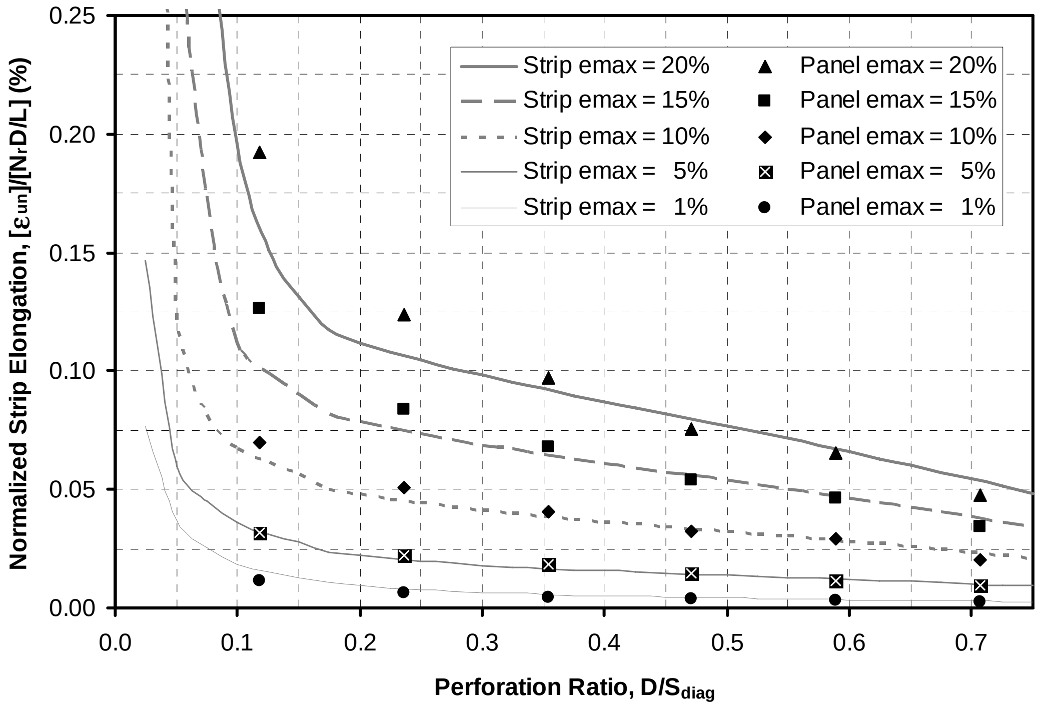

FIGURE 4-31 Normalized Strip Elongation [ε_{un}]/[$Nr{\cdot}D/L$] versus Perforation Ratio D/S_{diag} (RB Model, Fine Mesh, t_p = 2.6 mm)

4.8 Panel Strength Design Equation

Roberts and Sabouri-Ghomi (1992) proposed the following equation to approximate the strength of a perforated panel

$$V_{yp.perf} = \left[1 - \frac{D}{d}\right] \cdot V_{yp} \tag{4-3}$$

where $V_{yp.perf}$ and V_{yp} are the strength of a perforated and solid panel specimen, respectively. D is the perforation diameter, and d is the panel depth. However, Vian (2005) found the equation to provide a conservative estimate of the strength of perforated panels of the type considered here, provided that d in (4-3) is replaced by S_{diag}. The proposed equation was developed from a single holed panel. The objective of this section is to re-assess the applicability of (4-3) for SPSW panels having multiple perforations taking into account the refinements in analysis considered in this study. For this purpose, the series of perforated wall models previously considered in Section 4.7 was again observed. For comparison purposes, a SPSW having a solid infill panel was also analyzed. Results and discussion are only presented for the last two models considered: the RF model is presented first, followed by the RB model.

4.8.1 Rigid Floor (RF) Model

For the purpose of the following calculations, the overall shear strength V_y of a wall was taken by summing the horizontal reaction in horizontal direction at the two hinged base. Figure 4-32 shows results from the pushover analyses for all SPSW considered (a) as a function of maximum principal local strain ε_{max} (occurring anywhere in the infill plate) and (b) as a function of frame drift γ.

In figure 4-32(a), the overall shear strength of the perforated panels $V_{yp.perf}$ gradually increase as maximum principal local strain ε_{max} also increase. This behavior is consistent with the observed the stress-strain contour for the perforated walls, as shown in figure 4-15. Localized stress and strain concentrations at edges adjacent to the perforations develop as soon as lateral drifts are applied to the frame. These localized strains account for the rapid development of a difference between the strength curves for the solid and perforated panels, even at low magnitude of strains. Note that for the SPSW with solid panel, stresses and strains are distributed almost uniformly to the entire wall and the monitored strain considered in this case occurred close to the RBS connections. On the other hand in figure 4-32(b), pushover curve for all systems considered smoothly increase both in overall shear strength V_y and frame drift γ with progressively larger differences as the relative magnitude of perforations increase.

To study the applicability of (4-3) to perforated walls, the overall strength of each perforated model $V_{yp.perf}$ was reported when the maximum principal local strain ε_{max} reached values of 1, 5, 10, 15 and 20%, and compared to the corresponding overall strength of the solid panel V_{yp} at the same ε_{max} rate. The resulting ratio $V_{yp.perf}/V_{yp}$ is plotted in figure 4-33 as a function of the perforation ratio D/S_{diag}, together with the ratios calculated using (4-3). In addition, these results are also presented by comparing the ratios of the actual value obtained from the finite element analysis results divided by the value predicted by (4-3). This ratio of actual-to-predicted results is denoted as η and shown in figure 4-34.

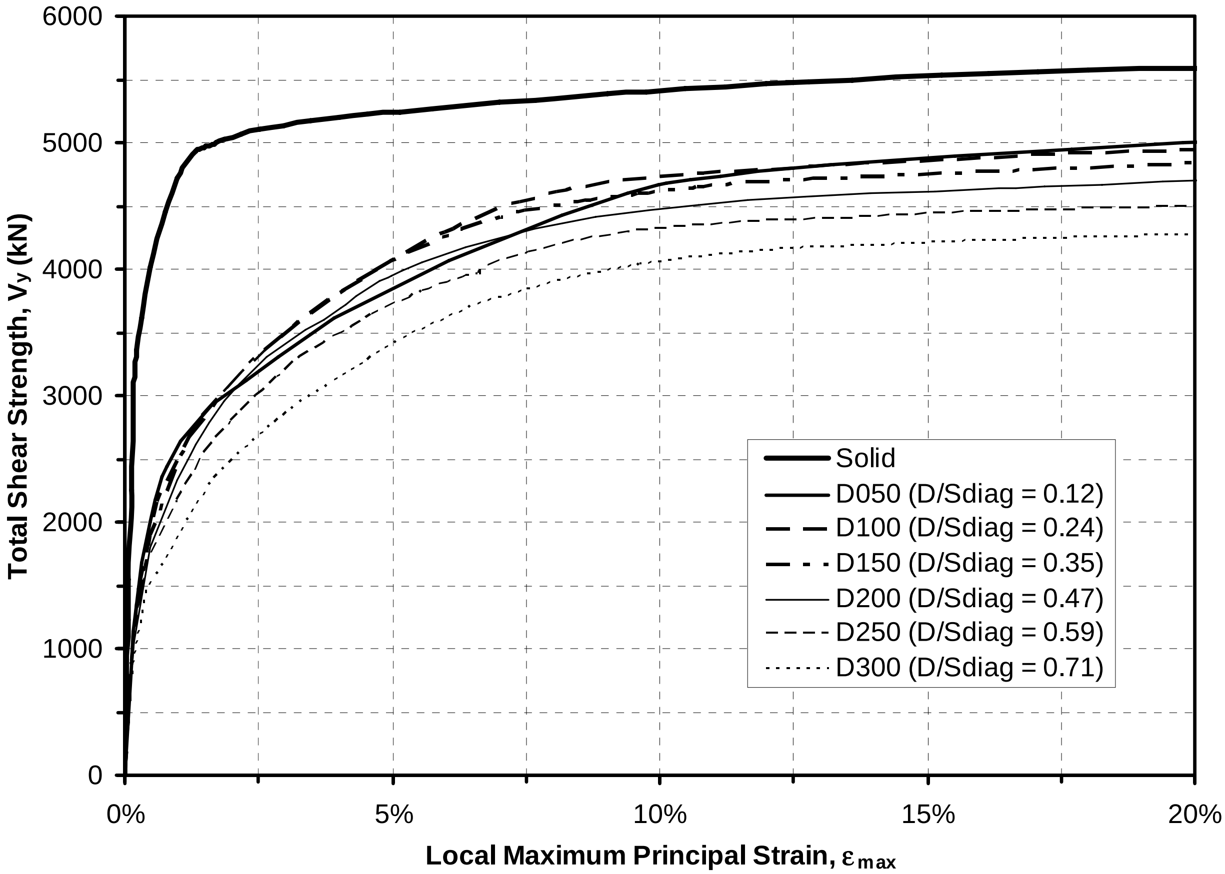

FIGURE 4-32(a) Overall Shear Strength V_y versus Local Maximum Principal Strain ε_{max} (RF Model, Fine Mesh, t_p = 2.6 mm)

These two figures show that for small perforation ratio and lower maximum principal local strain values, the actual values obtained from finite element analysis can deviates significantly from the predicted value, with values of η as low as 0.63 for some of the cases considered. Better matches are obtained as $\eta \approx 1.00$ at higher maximum principal local strain (ε_{max} equal to 10, 15, and 20%) for the same small perforation ratios. However, as the perforation diameter increase, so does η, with value of η as high as 2.6 for the largest perforation ratio considered.

It may be more appropriate and rational, instead of comparing the overall shear strength of the SPSW (which includes infill plate and boundary elements), to compare only the infill plate shear strength. For this reason, a bare frame model consisting of only the boundary elements was developed and analyzed. By assuming that the SPSW overall strength can be approximated by

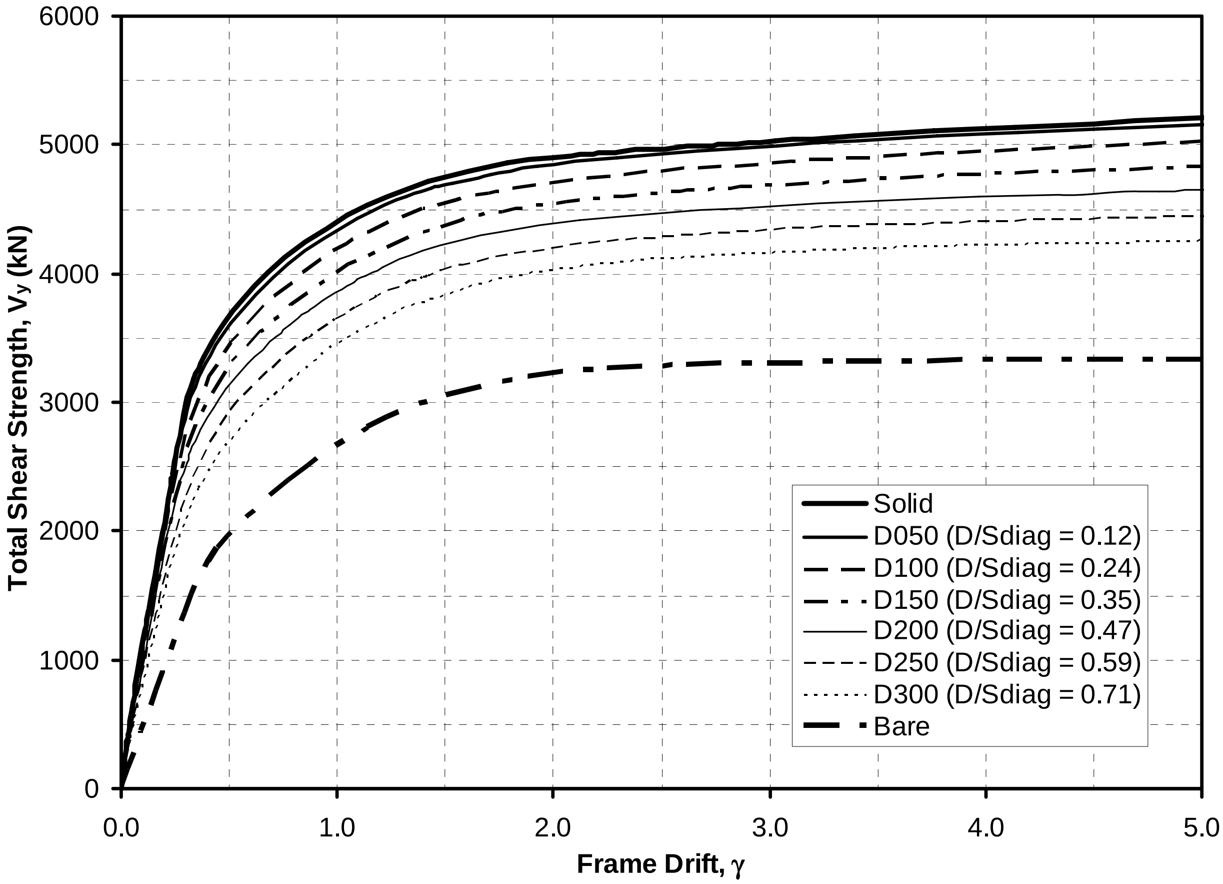

FIGURE 4-32(b) Overall Shear Strength V_y versus Frame Drift γ
(RF Model, Fine Mesh, t_p = 2.6 mm)

the summation of the bare frame and the infill plate strengths, it is possible to estimate the infill plate strength by subtraction of the bare frame strength from the total SPSW strength. Note that this is an approximation given that this approach does not satisfy the compatibility of deformations at the frame and plate interface for the SPSW versus bare frame system. These revised values so obtained are plotted in figures 4-35 and 4-36 in the same format as before. These two figures show a pattern of behavior similar to the previous one, but with different magnitudes for η as a function of the perforation ratios, and with a reversal of the relationship of η as a function of the monitored strain (for example, larger values of η occurring at the smaller ε_{max} in figure 4-36, whereas smaller values of η occurring at that strain in figure 4-34).

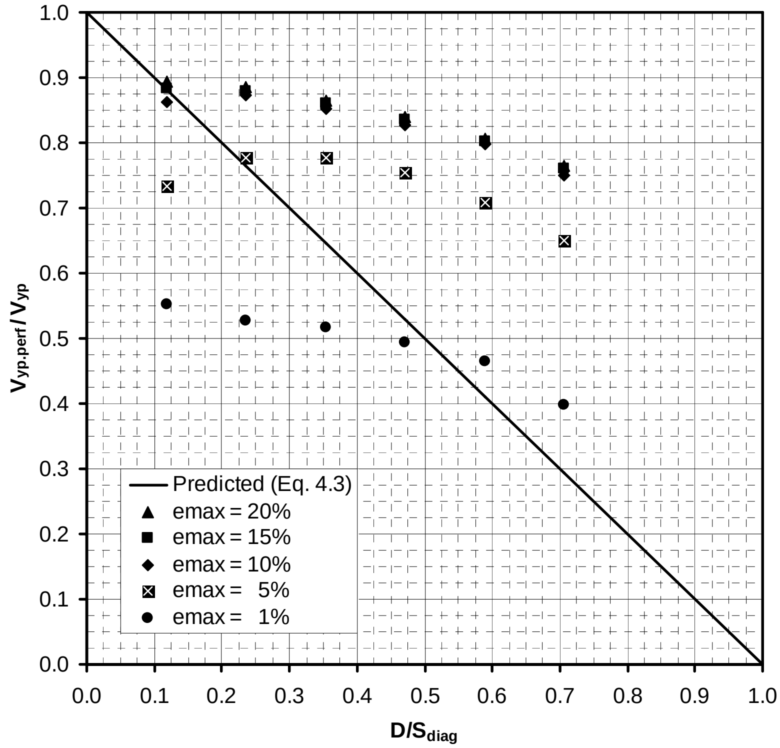

FIGURE 4-33 Overall Strength Ratio of Perforated over Solid Panel $V_{yp.perf} / V_{yp}$ versus Perforation Ratio D/S_{diag} – *Strain Criteria*, RF Model

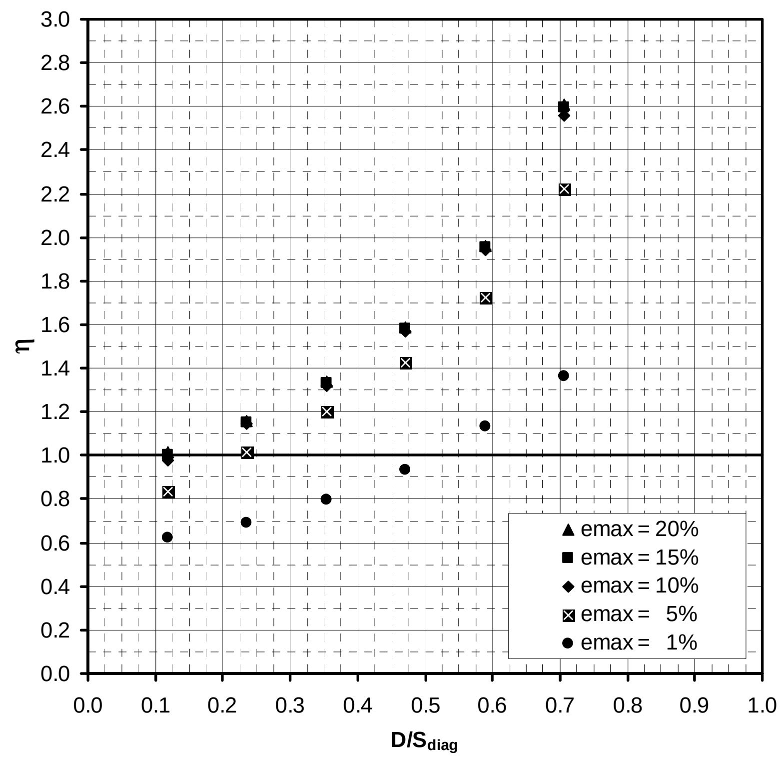

FIGURE 4-34 Overall Strength Ratios of Actual over Predicted Value η versus Perforation Ratio D/S_{diag} – *Strain Criteria*, RF Model

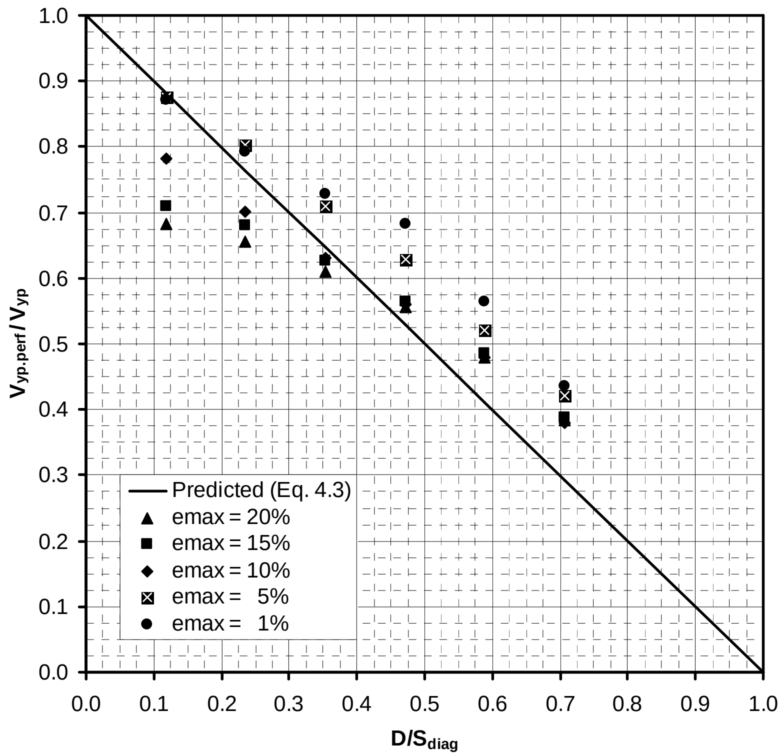

FIGURE 4-35 Infill Plate Strength Ratios of Perforated Panel and Solid Panel $V_{yp.perf}$ /V_{yp} versus Perforation Ratio D/S_{diag} – *Strain Criteria* RF Model

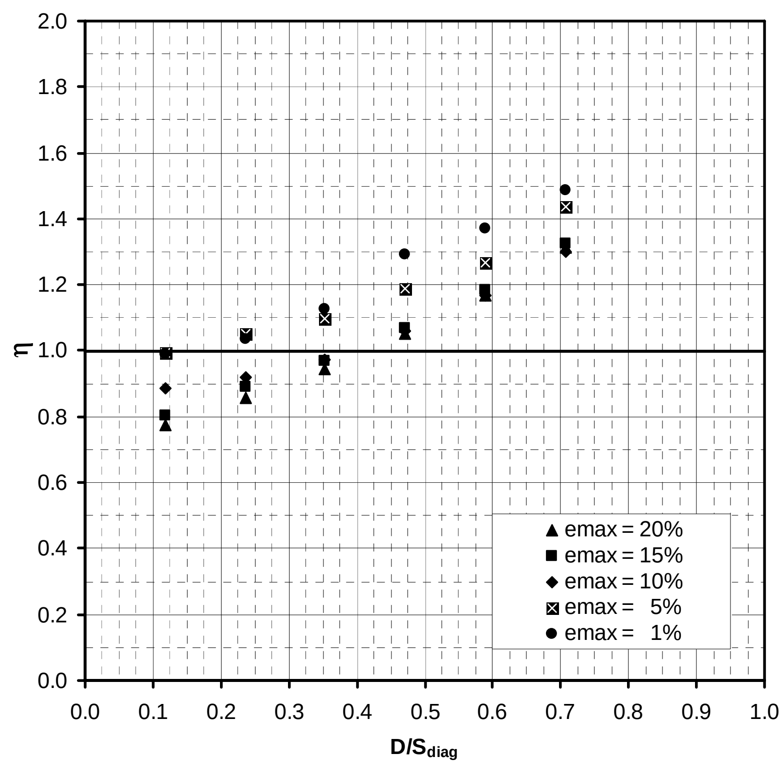

FIGURE 4-36 Infill Plate Strength Ratios of Actual and Predicted Value η versus Perforation Ratio D/S_{diag} – *Strain Criteria* RF Model

The above results show some challenges in using (4-3) on the basis of a specified maximum principal local strain. One particular problem is that panels with different perforation diameter reach particular maximum principal local strain (i.e., ε_{max} = 20%) at different drifts. In subtracting the bare frame strength from the full SPSW strength, this can only be done at the same drift value which creates the need to adapt the results obtained in terms of ε_{max}. For this reason, probably, establishing applicability of (4-3) based on a *strain criteria* does not work well.

To overcome this situation, a *drift approach* is used instead. In this case, overall strength of each perforated model $V_{yp.perf}$ was reported when the frame drift γ reached values of 1 to 5% and then compared to the corresponding overall strength of the solid panel V_{yp} at the same frame drift γ rate. The ratio $V_{yp.perf}/V_{yp}$ and the ratio of actual-to-predicted values versus perforation ratio D/S_{diag} are again plotted in figure 4-37 and 4-38, respectively. In this case, very consistent and systematic trends were observed. For all value of drifts considered, for small perforation ratio, values of η started at 1.12 and increased parabolically as a function of perforation ratio, up to $\eta \approx 2.78$ for the cases considered. Visual extrapolation also seems to indicate a smooth convergence to $\eta = 1.0$ at D = 0.

In reviewing figure 4-37, one might question why only such a small reduction in SPSW strength occurs for a wall with 300 mm diameter perforation in the panel compared to the solid SPSW strength; for example, when the frame has drifted 5%, the reduction between the two is only 18.2%, or as much as 950 kN from a total of 5204 kN. This could be answered by considering the strength contribution from each component in a SPSW. As perforation diameters increase, the contribution of the infill plate to the total SPSW strength decreases while boundary frame strength almost remains the same (since the same boundary frame is used for all cases considered). For example comparing the SPSW with solid panel to the perforated SPSW with 300 mm diameter holes in the panel, the infill plates contribute 36% (1768 kN) and 21% (858 kN), respectively, to the SPSW overall strength; strength of the bare frame contributes in a significant portion to total strength. As such, it is again more appropriate to compare instead the relative strength of only the infill plates in the cases considered. In this case, since the comparison is made at equal drifts, it is more straightforward to subtract the bare frame strength from the total SPSW strength at the same drift reference for all models.

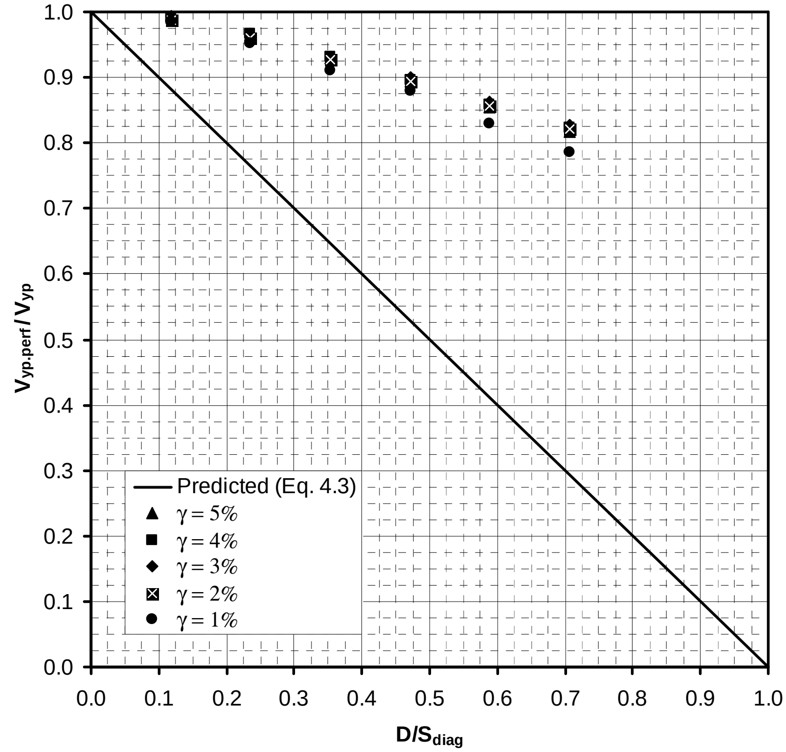

FIGURE 4-37 Overall Plate Strength Ratios of Perforated Panel and Solid Panel $V_{yp.perf} / V_{yp}$ versus Perforation Ratio D/S_{diag} – *Drift Criteria* RF Model

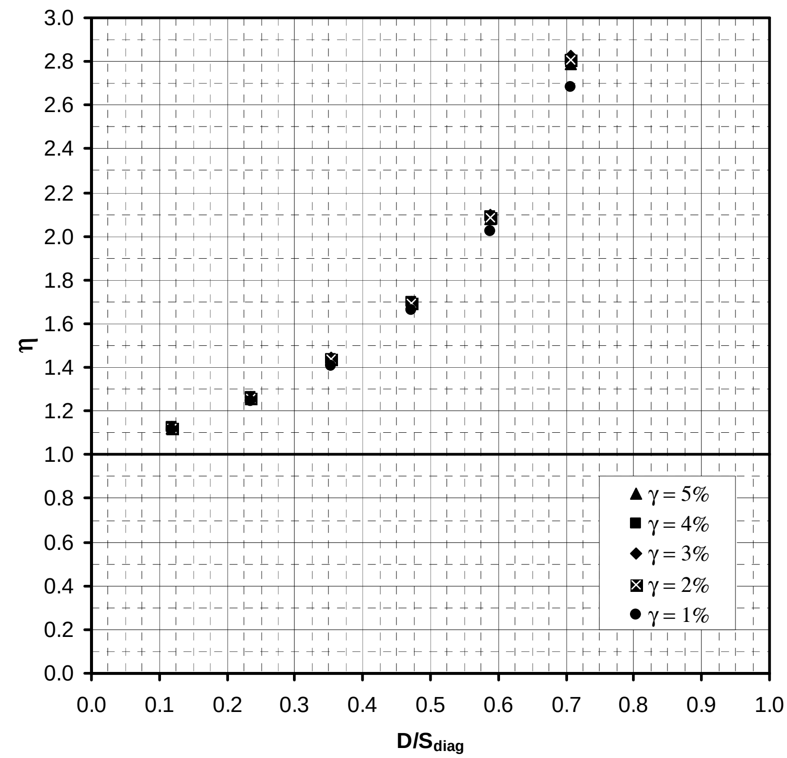

FIGURE 4-38 Overall Plate Strength Ratios of Actual and Predicted Value η versus Perforation Ratio D/S_{diag} – *Drift Criteria* RF Model

Figures 4-39 and 4-40 show the results from that operation: in this case, the actual strength obtained from finite element analysis is always larger than the value predicted by (4-3). At 50 and 300 mm perforated panel, the actual value deviates 10% and 66% from the predicted value, respectively. As shown in figure 4-39, the infill plate strength of SPSW with the 300 mm perforated panel (with D/S_{diag} = 0.707) on average lost 51.5% strength compared to that of the solid panel (with $V_{yp.perf}/V_{yp}$ = 0.485).

4.8.2 Rigid Beam (RB) Model

Results obtained using the RB model exhibited the same behavior as the RF model. The pushover curves of RB model are plotted in figure 4-41 for the same respective variables. Figures 4-42 to 4-45 used to examine the applicability of (4-3) are plotted only in terms of *drift*. From figures 4-42 and 4-43, for small perforation ratio, values of η started at 1.12 and increased parabolically as a function of perforation ratio, up to $\eta \approx 2.55$ for the case considered. A smooth convergence, visual extrapolation, to $\eta = 0$ at D = 0 are also observed. When the frame has drifted 5%, the strength of SPSW with 300 mm diameter perforation in the panel reduced as much as 717 kN (or 25.2%) from the solid panel strength of 2714 kN. In addition, observing only the infill plate strength plotted in figures 4-44 and 4-45, the actual value of infill plate having 50 mm and 300 mm diameter perforation deviate 10% and 66% from the predicted values, respectively. As shown in figure 4-44, the infill plate strength of SPSW with the 300 mm perforated panel on average lost 51.5% strength compared to that of the solid panel. Observation in the RB model confirmed the same results as in the RF model.

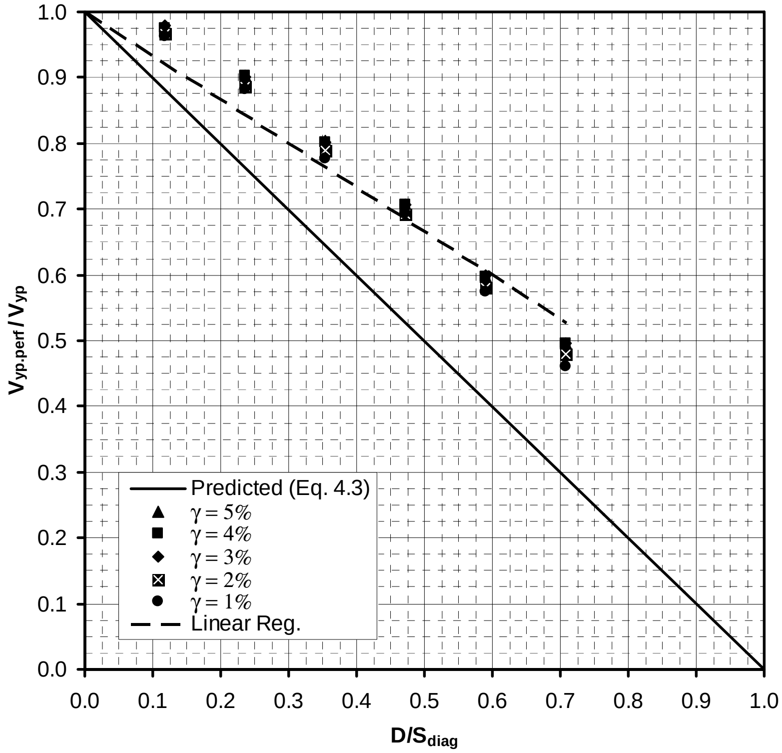

FIGURE 4-39 Infill Plate Strength Ratios of Perforated Panel and Solid Panel $V_{yp.perf} / V_{yp}$ versus Perforation Ratio D/S_{diag} – *Drift Criteria* RF Model

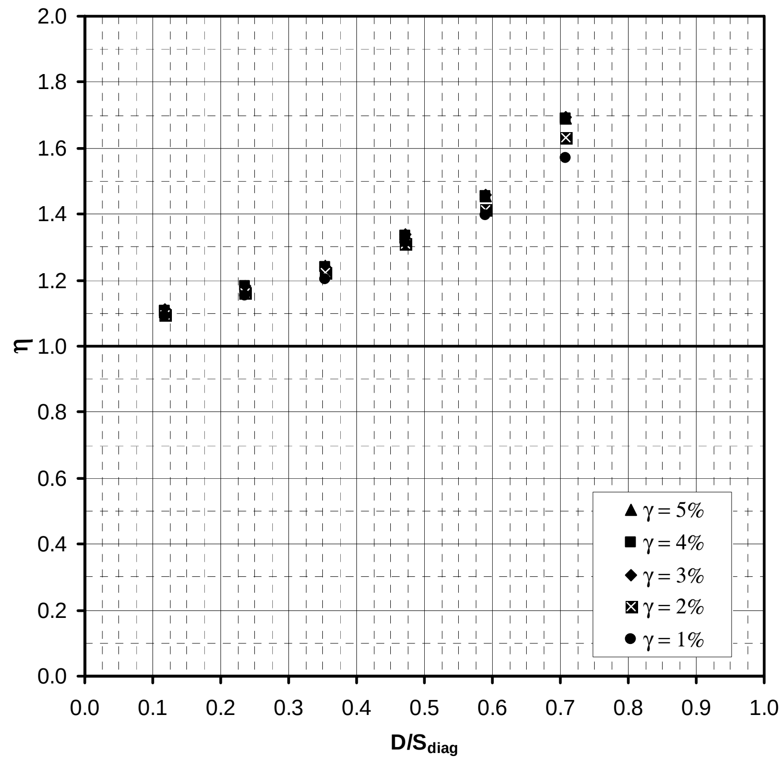

FIGURE 4-40 Infill Plate Strength Ratios of Actual and Predicted Value η versus Perforation Ratio D/S_{diag} – *Drift Criteria* RF Model

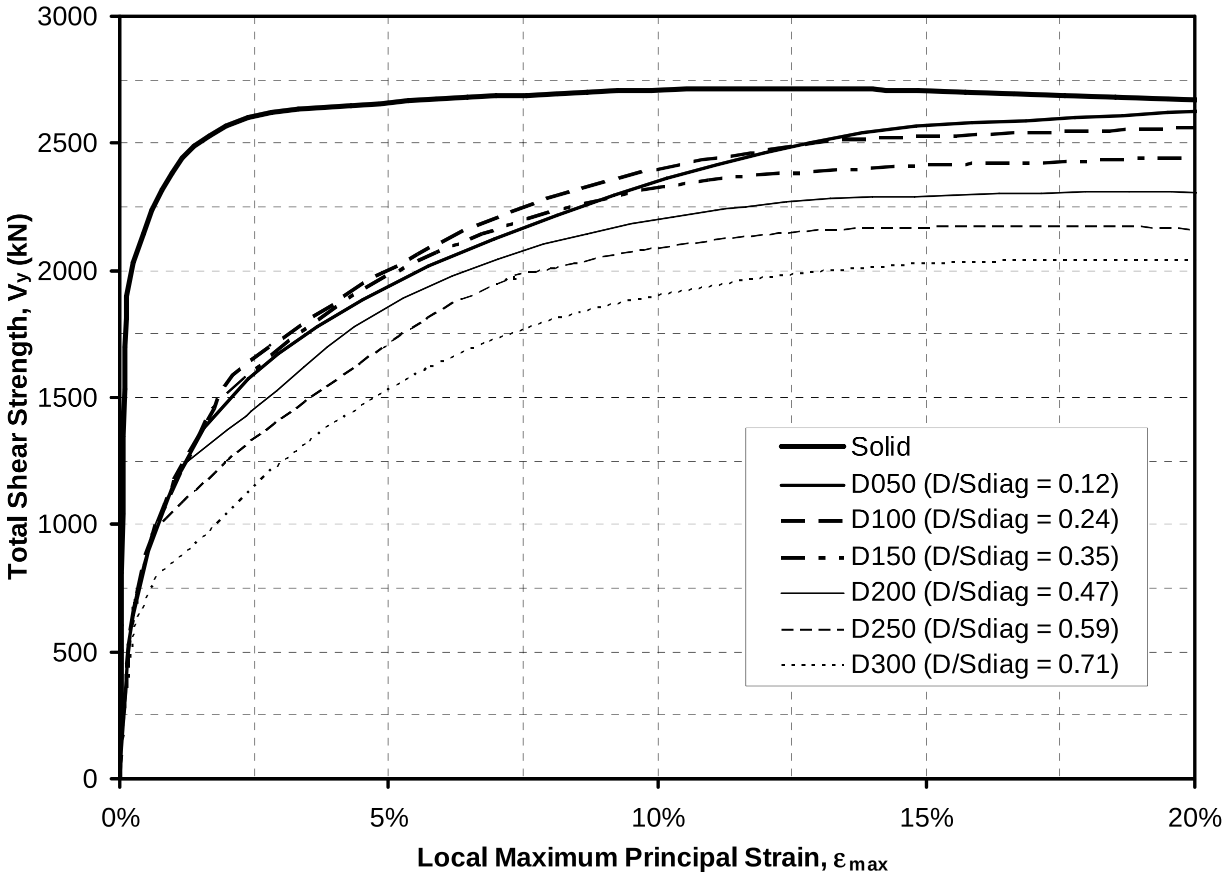

FIGURE 4-41(a) Overall Shear Strength V_y versus Local Maximum Principal Strain ε_{max} (RB Model, Fine Mesh, t_p = 2.6 mm)

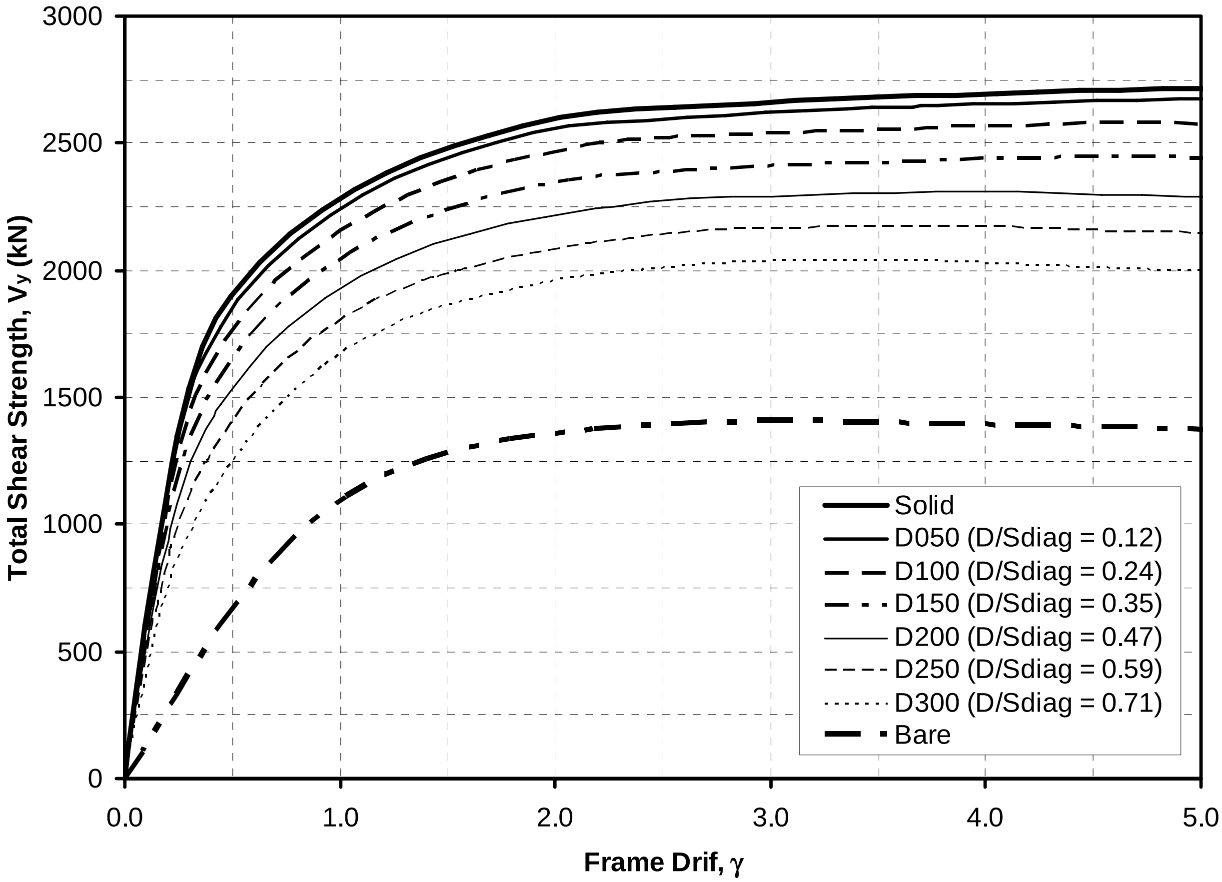

FIGURE 4-41(b) Overall Shear Strength V_y versus Frame Drift γ
(RB Model, Fine Mesh, t_p = 2.6 mm)

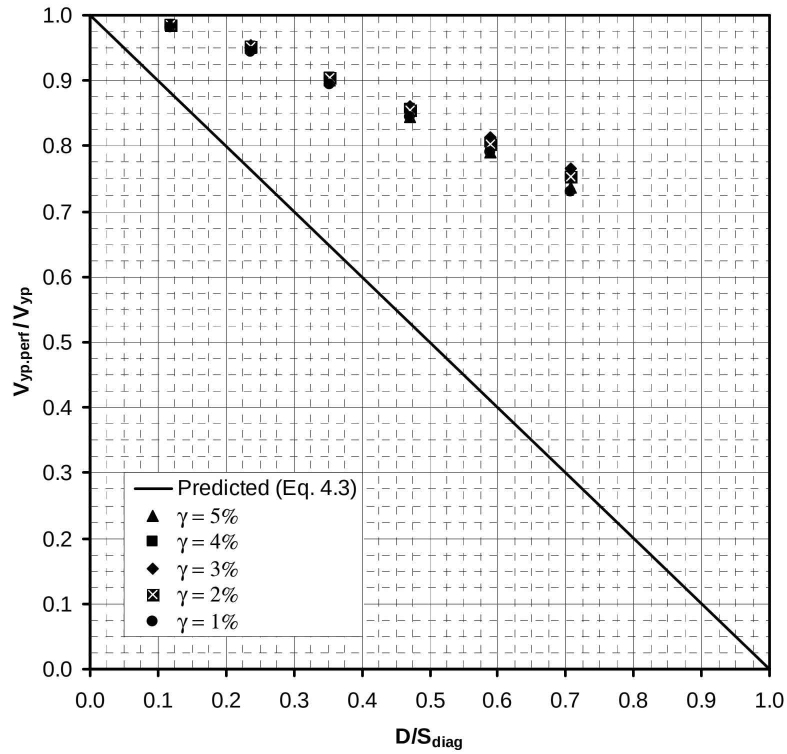

FIGURE 4-42 Overall Plate Strength Ratios of Perforated Panel and Solid Panel $V_{yp.perf} / V_{yp}$ versus Perforation Ratio D/S_{diag} – *Drift Criteria* RB Model

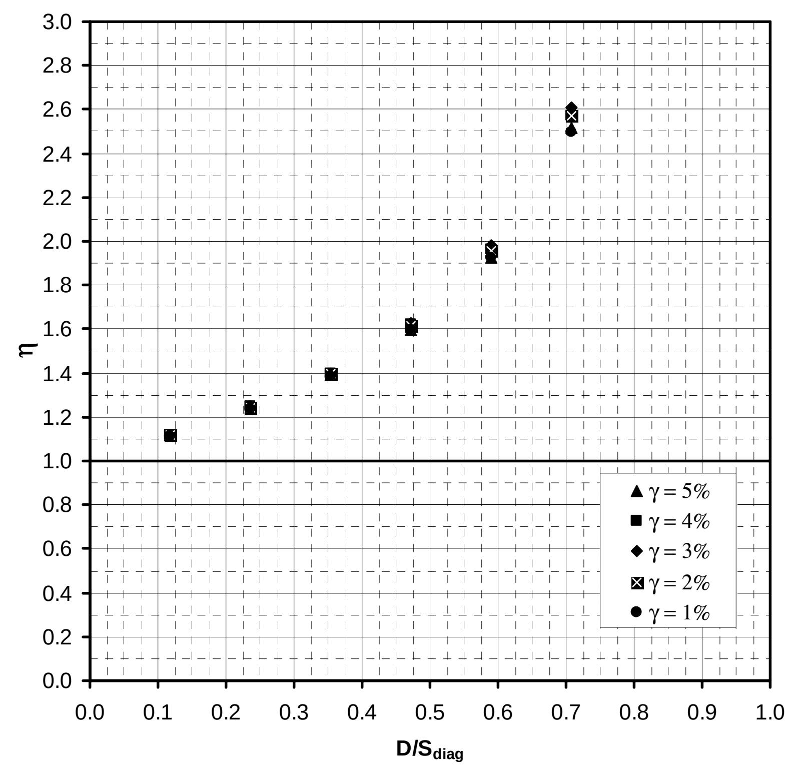

FIGURE 4-43 Overall Plate Strength Ratios of Actual and Predicted Value η versus Perforation Ratio D/S_{diag} – *Drift Criteria* RB Model

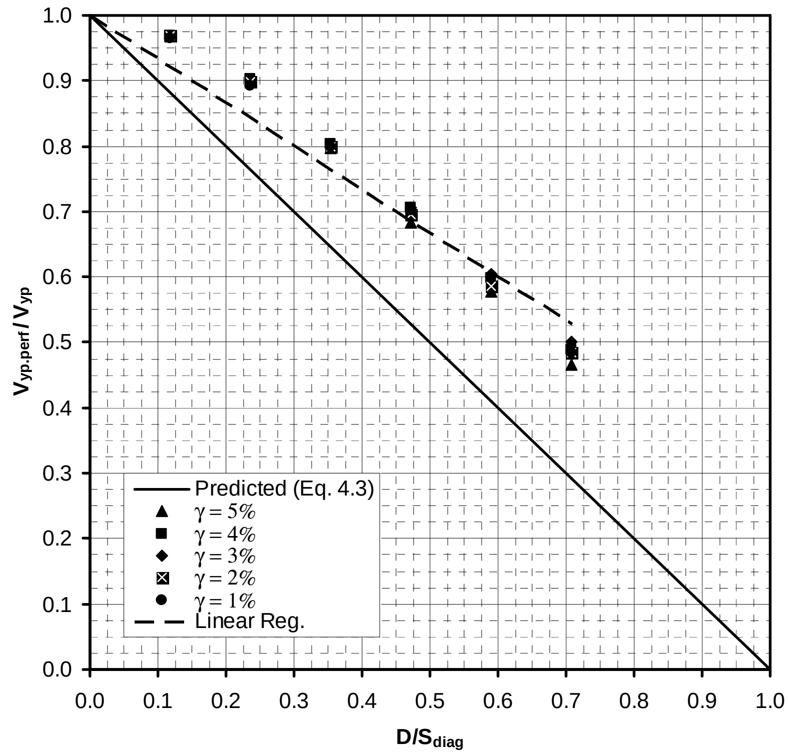

FIGURE 4-44 Infill Plate Strength Ratios of Perforated Panel and Solid Panel $V_{yp.perf}$ /V_{yp} versus Perforation Ratio D/S_{diag} – *Drift Criteria* RB Model

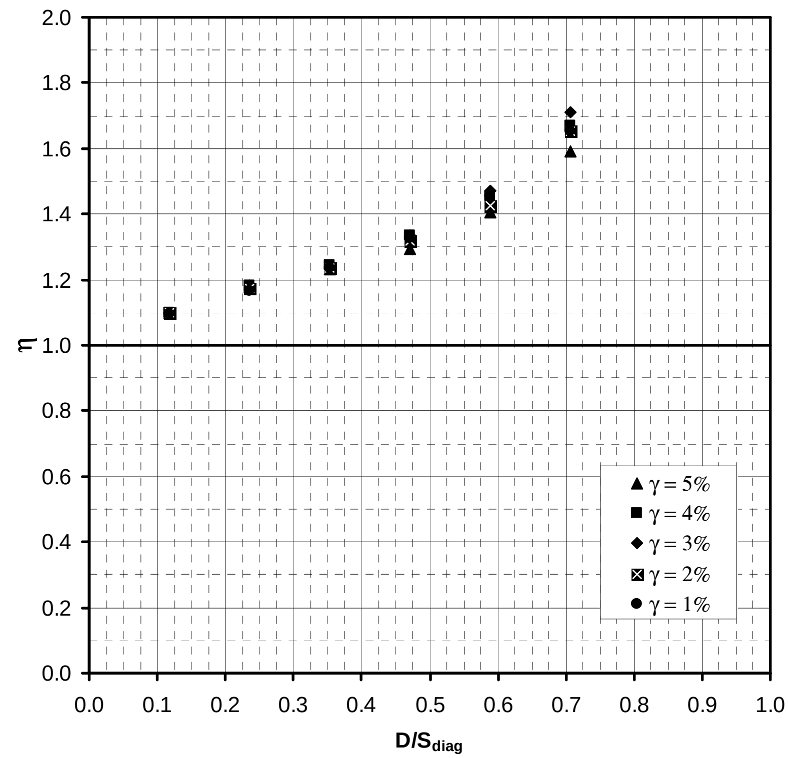

FIGURE 4-45 Infill Plate Strength Ratios of Actual and Predicted Value η versus Perforation Ratio D/S_{diag} – *Drift Criteria* RB Model

4.8.3 Regression Analysis

From the two models considered, it can be observed that polynomial regression would provide good correlation with the actual data in developing an equation to predict the strength of the perforated infill plate. However, for simplicity, linear regression was applied on a new proposed equation as follows:

$$V_{yp.perf} = \left[1 - \alpha \frac{D}{S_{diag}}\right] \cdot V_{yp} \tag{4-4}$$

where α is a proposed regression factor equal to 0.70. Equation (4-4) is only applicable to SPSW having multiple perforations of the type and configuration considered here. This equation acceptably matches, with a 5% deviation on average, the actual data series as shown in figures 4-39 and 4-44.

4.9 Example

It is helpful to illustrate how frame drift correlated to the corresponding local maximum strain in the infill plate for the system considered. Figure 4-46 shows this relationship between the two for the RB system. In a design perspective, this figure also provides structural engineers some insight of how high local strain in the infill plate relates to design drift and vise versa. In part (a) of that figure, for a perforated SPSW plate limited to a certain elongation and for a given perforation diameter, the corresponding frame drift can be predicted. In part (b), for a selected design drift and for a given perforation diameter, local maximum strain in the infill plate can be determined. Note that figure 4-46(a) actually somewhat is generated by summing the figure 4-41(b) and a 90-degree clockwise-rotation of figure 4-26 starting from perforation ratio $D/S_{diag} > 0.1$.

In addition, the following example explains a design process on perforated SPSW. Assume that the 4000 mm by 2000 mm building frame (used in this study) is designed to resist lateral shear load V_{design} of 2300 kN. A572 Gr. 50 steel (F_y = 345 MPa) is used for both boundary frame and infill plate of 2.6 mm thick. The design objective is to determine how big the perforation diameter should be used such that the frame drifts are less than 1% and maximum strain in the infill plate are less than 20%.

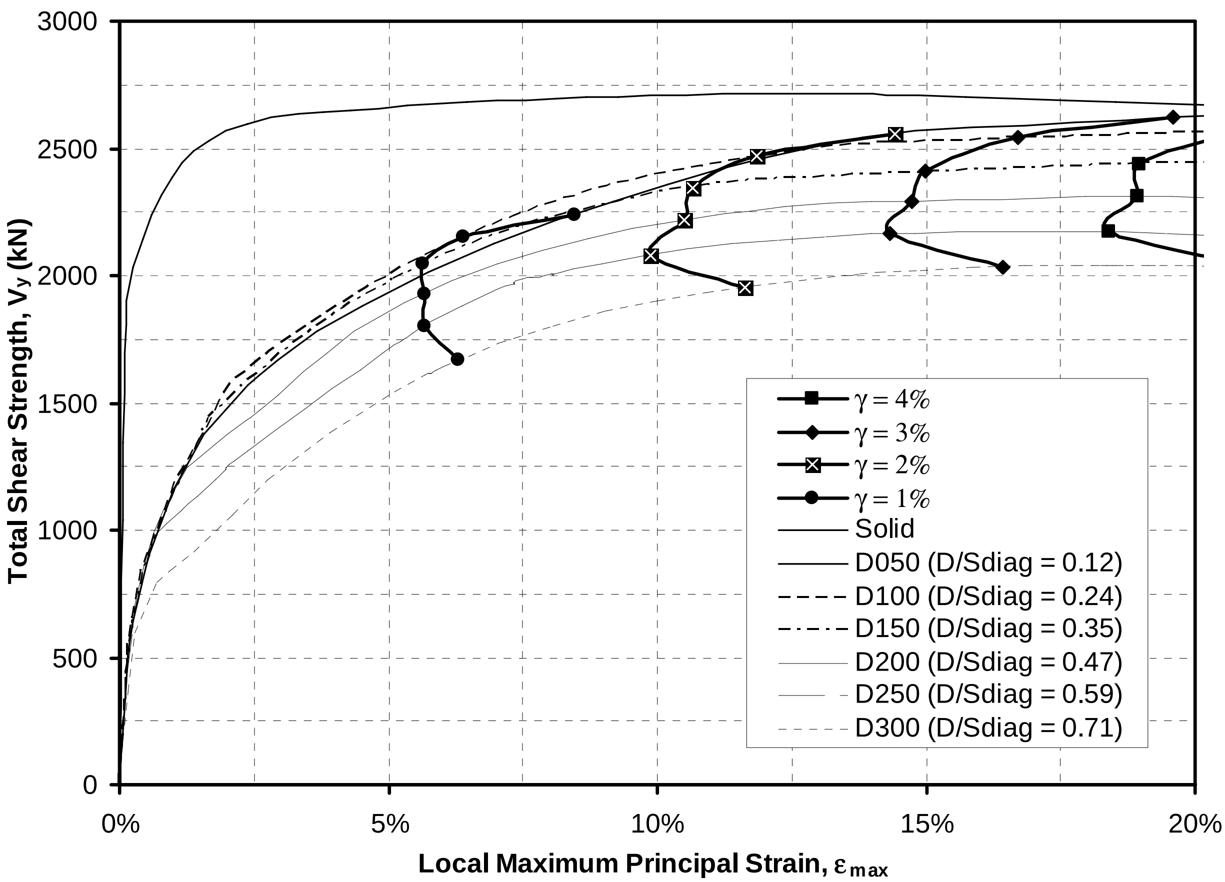

FIGURE 4-46(a) Overall Shear Strength V_y versus Local Maximum Principal Strain ε_{max} and Link to the Corresponding Frame Drift γ for RB Model

From simple plastic analysis, the strength of the bare frame (without infill plate) is given by

$$V_{yf} = \frac{4 \cdot M_p}{\left(H + h_{hinge}\right)} \tag{4-5}$$

where M_p is the plastic moment of the W18X65 used for the beams, h_{hinge} is the height between the centerlines of floor hinge and bottom beam, and H is the frame story height between beam centerlines. According to Thorburn and Kulak (1983), the strength of the infill plate is given by

$$V_{yp} = \frac{1}{2} \cdot F_y \cdot t_p \cdot W_{panel} \cdot \sin 2\alpha \tag{4-6}$$

where W_{panel} is the width of infill panel between column flanges. The bare frame and infill plate contributions to the strength of the SPSW system are V_{yf} = 1055 kN and V_{yp} = 1593 kN, respectively. Total system strength is therefore 2648 kN which is considerably higher than required by the design and perforations on the infill plate are then added.

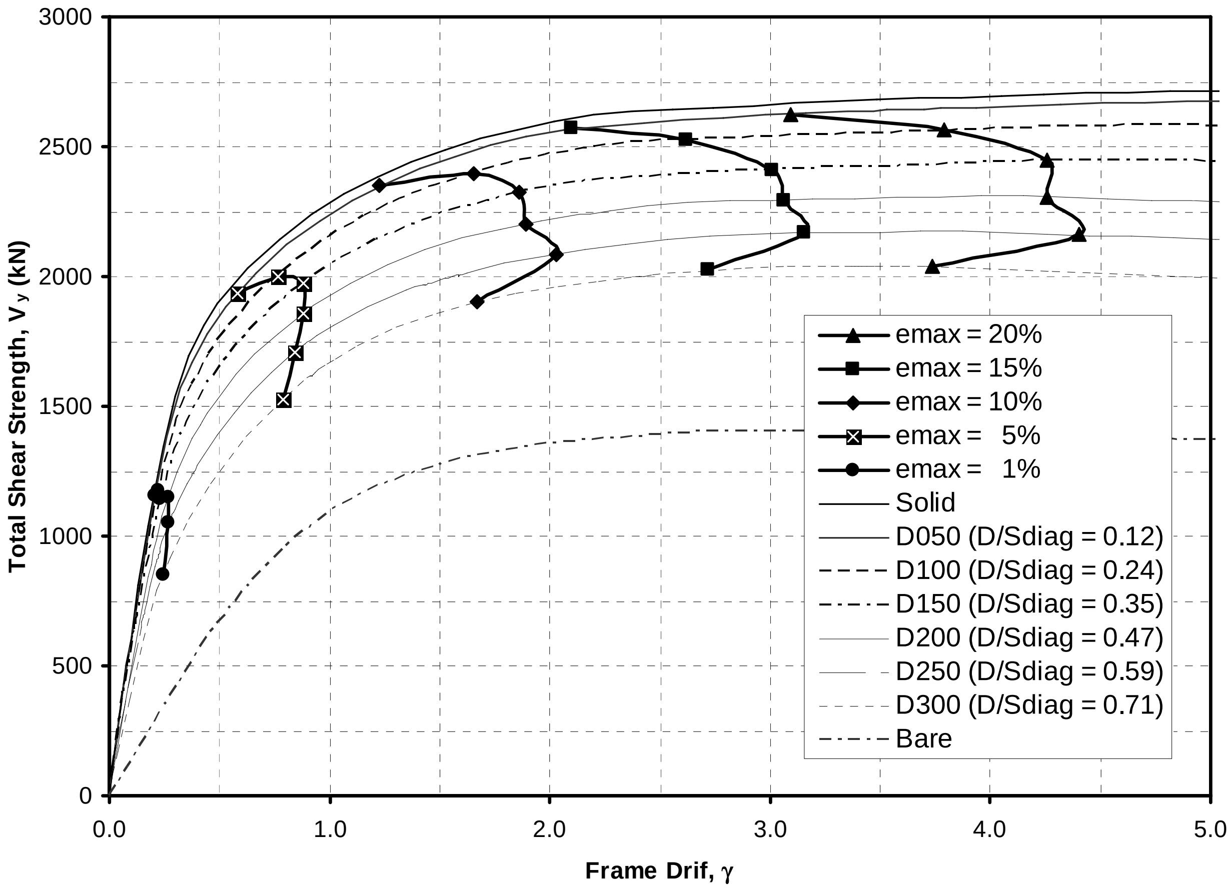

FIGURE 4-46(b) Overall Shear Strength V_y versus Frame Drift γ and Link to the Corresponding Local Maximum Principal Strain ε_{max} for RB Model

Assume that the perforation layout (used in this study) with 4 perforations along the strip length and 300 mm center-to-center spacing along both the vertical and horizontal directions, or S_{diag} of 424.26 mm are applied in the design. Therefore, perforation diameter needed to reduce the infill plate shear strength can be calculated using (4-4) and obtained $D \approx 130$ mm. By plotting V_{design} of 2300 kN and D of 130 mm (or D/S_{diag} = 0.31) into figure 4-46(b), frame drifts $\gamma \approx 1.4\%$ and maximum strain $\varepsilon_{max} \approx 7.5\%$ are obtained.

The results obtained do not satisfy the design objective where the frame drifts is higher than 1%. One way to revise the design results is by changing the properties of the infill plate using smaller perforation diameter, or by changing the number of perforation along the strip length per design procedure specified by Vian (2005). Note that in this design example, the present of RBS connections and uncertainty in steel material used are not considered.

4.10 Case Study on Element and Material Definitions

This study of perforated SPSW was also extended to examine the effects of different element and material definitions in the model. In this case study, the S4 shell elements replaced the S4R shell elements. The S4 shell element is a four-node doubly curve general-purpose shell element with full integration. Despite of being more computationally expensive, the S4 shell elements should give higher solution accuracy than the S4R shell elements and the objective here is to investigate how significant this change affects the previous results. In this study, the refined RF model with 200 mm diameter perforations and 2.6 mm infill plate thickness is used. The results are compared in table 4-2.

TABLE 4-2 Result Comparison of Models using S4 and S4R Shell Elements when Frame Reached 3% Drifts

Model[(1)]	Number of Elements	S_{max} (MPa)	E_{max} (%)	RF11[(1)] (kN)	CPU Time (hh:mm:ss)
S4	27099	455.53	11.70	4530.99	05:48:15
S4R	27099	455.53	10.66	4522.73	01:40:17

Note: [1)] The RF model: Fine Mesh, D = 200 mm, t_p = 2.6 mm
[2)] Total shear strength of the model

Table 4-2 presents the maximum in plane principal stress (S_{max}) and strain (E_{max}), and total shear strength of the model (RF11) when the frame experienced 3% drift. The stress and strain are monitored at the location where maximum value occurred. Point C from figure 4-22 is selected in this case. The monitored values of both models analyzed are close to each other, for example, the strain values at 3% drifts are 11.70% and 10.66% for the model with S4 and S4R shell elements, respectively. The total shear strengths at 3% drifts are 4530.00 kN and 4522.73 kN for the same respective models. However, the relative CPU time to run the model with S4 shell elements is roughly four times longer than that with the S4R shell elements. On this basis, the use of S4R elements is justified.

A second case study was conducted to further investigate the impact of material definitions. Here, the cyclic stabilized backbone stress-strain model of A572 Gr. 50 steel (Kauffmann *et al.* 2001) in the infill plate was used to replace the idealized tri-linear stress-strain model to better understand the discrepancy in the results of Vian (2005) between complete SPSW and individual strips results. The RF model with 200 mm diameter perforation and 2.6 mm panel thickness is used in this study and the results are compared in figure 4-47. The figure presents the total strip elongation for material idealizations considered. Recall that the five horizontal lines for each monitored strain represent the results of the individual perforated strip analysis presented in Section 3 at perforation ratio D/S_{diag} of 0.471. The results for the complete SPSW with the RF model are labeled *RF Model* in figure 4-47, reporting the results from figure 4-13. The idealized tri-linear stress-strain model was used for this model and the strip model and a good agreement is obtained (as was reported in Section 4.5.2) For comparison, the results of the complete SPSW and the individual perforated strip analyzed using the cyclic stabilized backbone stress-strain model are plotted in figure 4-47 and labeled *Kauffman* and *Kauff.Strip*, respectively. The total strip elongation reached at each maximum target strain dropped significantly compare to the previous results using the idealized tri-linear stress-strain model. This phenomenon was also reported by Vian (2005) who used the idealized tri-linear stress-strain model on the individual perforated strip and the cyclic stabilized backbone stress-strain model on the complete SPSW. The results reported by Vian (2005) are also plotted in the figure and labeled *Vian Wall* and *Vian Strip* for the complete SPSW and the individual perforated strip, respectively. The results presented in

Figure 4-47 explain the discrepancy in results obtained by Vian (2005) for the wall and strip. In addition, this study demonstrated that the strip model is a good predictor in modeling the behavior of a complete SPSW. The unidirectional idealized tri-linear stress-strain model is an appropriate modeling for the infill plate, which can only yield in tension, and immediately buckles in compression.

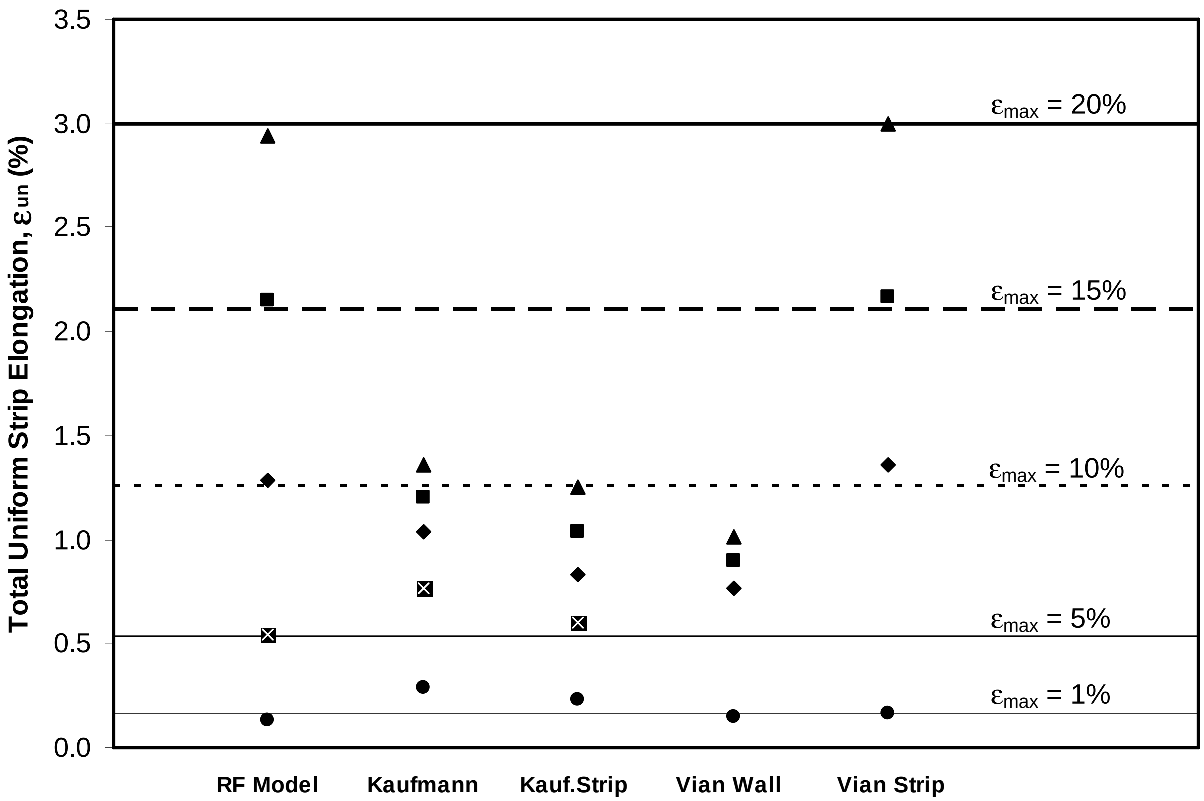

FIGURE 4-47 Uniform Distributed Strip Axial Strain ε_{un} for Material Idealizations Considered (D = 200 mm, D/S_{diag} = 0.471); Lines Correspond to Individual Strip Analysis

4.11 Design Recommendations and Considerations

Design recommendations for perforated SPSW are suggested below as an improvement to the recommendations by Vian (2005).

1. The individual strip analysis can predict the behavior of perforation SPSW provided the hole diameter is less than 60% of the strip width. On that basis, the perforation ratio of SPSW should be limited to $D/S_{diag} \leq 0.6$.
2. The shear strength of perforated infill plate for SPSW of the type considered here (i.e., having multiple regular perforations) is given as:

$$V_{yp.perf} = \left[1 - \alpha \frac{D}{S_{diag}}\right] \cdot V_{yp} \tag{4-7}$$

where α is a proposed correction equal to 0.70.

For panel strength calculated on that basis, the full shear strength of the complete SPSW is obtained by adding to this value the strength of the boundary frame without the infill.

4.12 Summary

A series of SPSW having perforated panels with variation in perforation diameter, infill plate thickness, material properties idealization, and element definitions has been numerically analyzed using the finite element program ABAQUS/Standard. The objective of this analysis was to verify the accuracy of results obtained from finite element analysis of individual perforated strips to predict the strength of SPSW by summing the strength of “simpler” individual strips (as has been widely used in designing SPSW). Specific finite element features to capture the complete SPSW behavior were described. Among them were geometry modeling and mesh algorithm, element definitions, initial imperfection, boundary conditions, non-linear stability, and lateral support to prevent lateral torsional buckling. Several finite element models were considered in investigating the behavior of the SPSW. Good agreement in overall behavior between the three models considered and the individual strip model was observed. The applicability of the equation proposed by previous researchers to approximate the strength of a perforated panel was also re-assessed. Some recommendations were proposed to help design perforated SPSW.

SECTION 5

ADDITIONAL OBSERVATIONS AND DESIGN CONSIDERATIONS FOR CUTOUT CORNER STEEL PLATE SHEAR WALLS

5.1 General

Cutout corner SPSW is another option to accommodate the passage of utilities through the infill plate. This system can also be expected to provide strength and stiffness similar to a solid panel SPSW. Vian (2005) conducted analytical and experimental work on cutout corner SPSW with flat-plate reinforcement along the cutout edges and using a relatively thin fish plate to connect the infill plate to the surrounding boundary frames and to the flat-plate reinforcement. The fish plate usually is not included in finite element models (and neither was in the work by Vian 2005) because a relatively thin fish plate would not significantly affects the analysis results in regular SPSW due to its significant contribution to the large moment of inertia of the beams and columns. This observation was already reported by Driver *et al*. (1997). However, for cutout corner SPSW, potential significant effects might occur if a relatively stiffer and stronger fish plate is provided to the "arching" flat-plate reinforcement along the cutout edges. The additional fish plate would considerably increase the strength and stiffness of the flat-plate reinforcement. As such, one may question whether the fish plate along the flat-plate reinforcement should be modeled. How the fish plate on the flat-plate reinforcement would affect the global behavior of SPSW as well as the local behavior of the arch still needs to be determined. The simplest way to provide the needed fish plate along the cutout corner is to reinforce it using a WT section (instead of a flat plate), with the web of the WT section serving as the fish plate. Due to availability of WT shape, once the needed flange is selected per the procedure described by Vian (2005), limited choices of corresponding webs are available. The web plate could be larger or thicker than needed solely for the purpose of fish plate. This makes the previous question even more relevant.

This section, intended to be an extension of Vian's work, describes analytical work using finite element analysis of cutout corner SPSW with T-section reinforcement modeled by adding a stiffener to the designed flat-plate reinforcement. Finite element considerations of the two systems are only briefly discussed, as most of the finite element features for the perforated SPSW previously described in Section 4 are also applicable here. The behavior of the two systems is observed and compared. Finally, some additional considerations for cutout corner SPSW are presented.

5.2 Finite Element Description of the Two Cutout Corner SPSW

In this section, two cutout corner SPSW models are analyzed using the finite element software ABAQUS/Standard. The first specimen is similar to that investigated by Vian (2005) as shown in figure 2-19. The boundary frame members, the RBS connections, and the hinges located 850 mm below the intersection of the column and lower beam working lines are the same as for the perforated specimen discussed in Section 4. Quarter-circle cutouts of 500 mm radius in the upper corners of the infill plate and 160 mm by 19 mm flat-plate reinforcement along the cutout edges were implemented. A fish plate of 45 mm by 6 mm was added to facilitate attachment of the infill plate to the flat-plate reinforcement and to the surrounding frame. The second specimen has T-section reinforcement along the cutout edges; its model is built by adding a 160 mm by 12 mm plate perpendicularly to the previous flat-plate reinforcement. Note that this stiffener dimension was chosen such that the T-section dimensions approximate the available WT sections listed in the American Institute of Steel Construction (AISC) manual (here corresponding to a WT6X17.5, chosen for expediency). To distinguish the two models considered here, they are labeled CR and CR-T, respectively.

For the finite element models, the thin fish plates are not included in the CR model and the infill plate is connected directly to the flat-plate reinforcement along the cutout corners and surrounding frames. For the CR-T model, the relatively thick web plate of the T-section along the cutout edges is modeled together with the arch plate. Note that in the case of CR-T model, the fish plates along the beams and columns are not included.

In developing the finite element models of the described specimens, all the procedures described in Sections 4.2 to 4.4 were repeated. In the *Part* collection mentioned in Section 4.2.1, the perforated infill plate was replaced by a solid plate with cutout corners, and the cutout edges reinforcement was modeled as a new part. Note that the web of the T-section used as cutout edges reinforcement was simpler to model directly as a *Partition* of the infill plate (adjacent to the cutout corner) for a different thickness from the rest of the infill plate. Note also that to accelerate the modeling process, the partition region is created in both the CR and CR-T finite element model even though the CR model does not need it. Thickness of the partition region was assigned to be 2.6 mm (equal to infill plate thickness) and 12 mm for the CR and CR-T model, respectively. The various part collection are merged into one single model. The arch geometry of the cutout edges reinforcement and the stiffener (the web of the T-section) were meshed using the *Swept Meshing Technique* while other plate regions were meshed with the same technique previously mentioned in Section 4.2.1. The boundary conditions of the RB model, described in Section 4, were applied to both finite element models. The resulting finite element model (i.e., for the CR model) with a maximum 25 x 25 mm shell elements is shown in figure 5-1 and the first two eigenmodes of the model are plotted in figure 5-2. An initial imperfection amplitude of 1 mm multiplied by the first eigenmodes (and decreasing in amplitude for the higher modes) was chosen for the models analyzed in this section.

5.3 Observations on the Two Cutout Corner SPSW Models

Observations on the two models analyzed are presented in terms of global effects, such as frame deformation and shear strength of the systems, as well as in terms of local effects adjacent to the cutout corners, such as local buckling, stress distribution, and forces applied by the cutout edges reinforcement to the beam and columns.

Deformed shapes at 4% frame drift for the CR and CR-T model are compared in figures 5-3 and 5-4 displayed from front and rear views, respectively. The deformed shapes of the two models are generally similar except for some local effects at the right cutout corner. For the CR model, two of the infill plate folds due to buckling end at the corner of the arch plate, while for the CR-T model, the fold lines end at the corner of the stiffener (thus “spreading” the folds a little further apart). No local buckling of the cutout edges reinforcement was observed for both models. Maximum out-of-plane movement of the infill plate equals to 39.0 mm for both the CR and CR-T model.

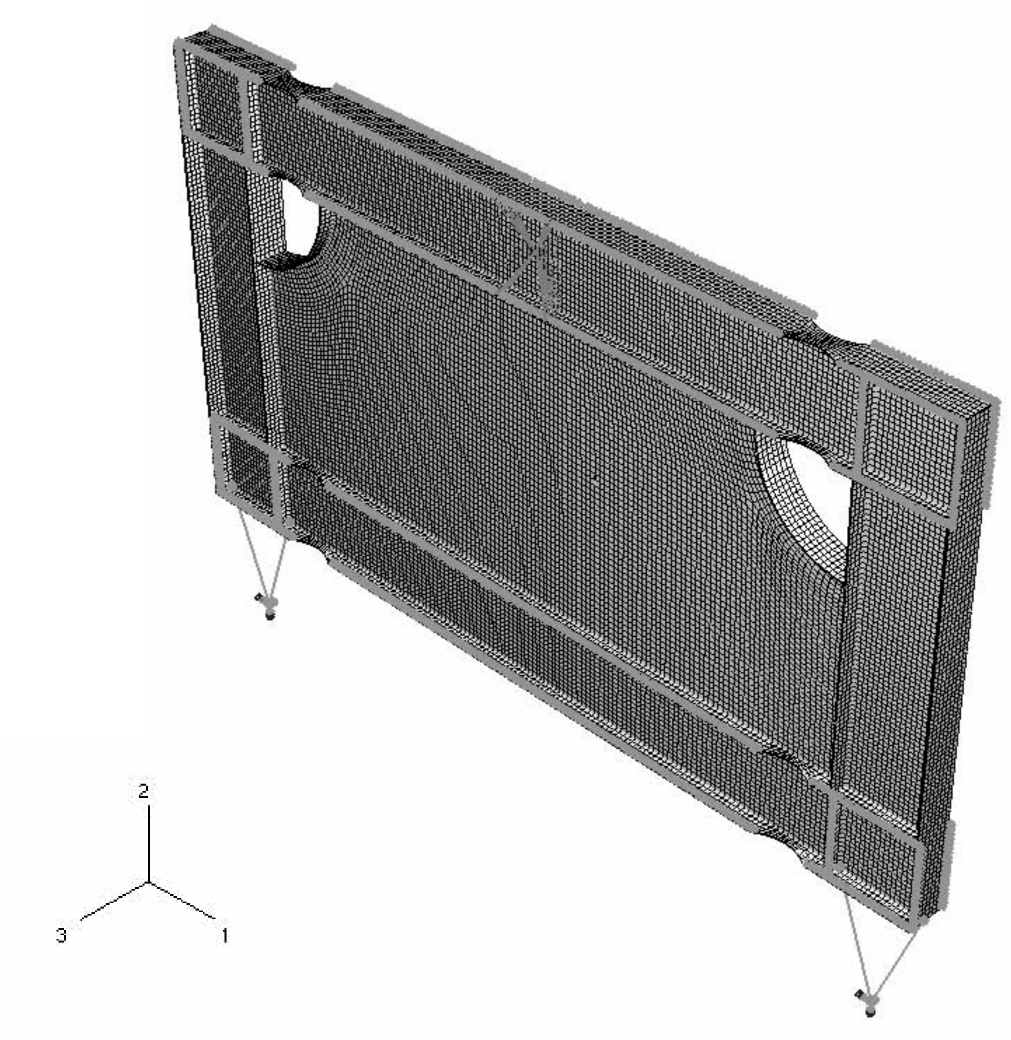

FIGURE 5-1 Finite Element Model of the CR Specimen (Fine Mesh)

(a)

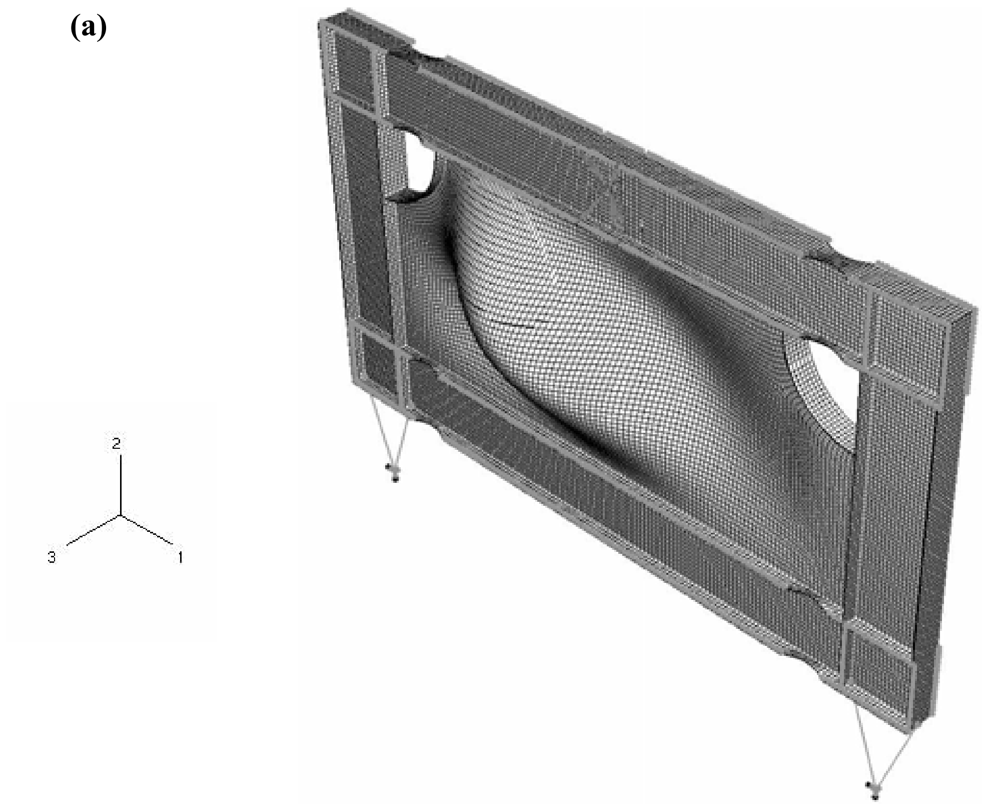

(b)

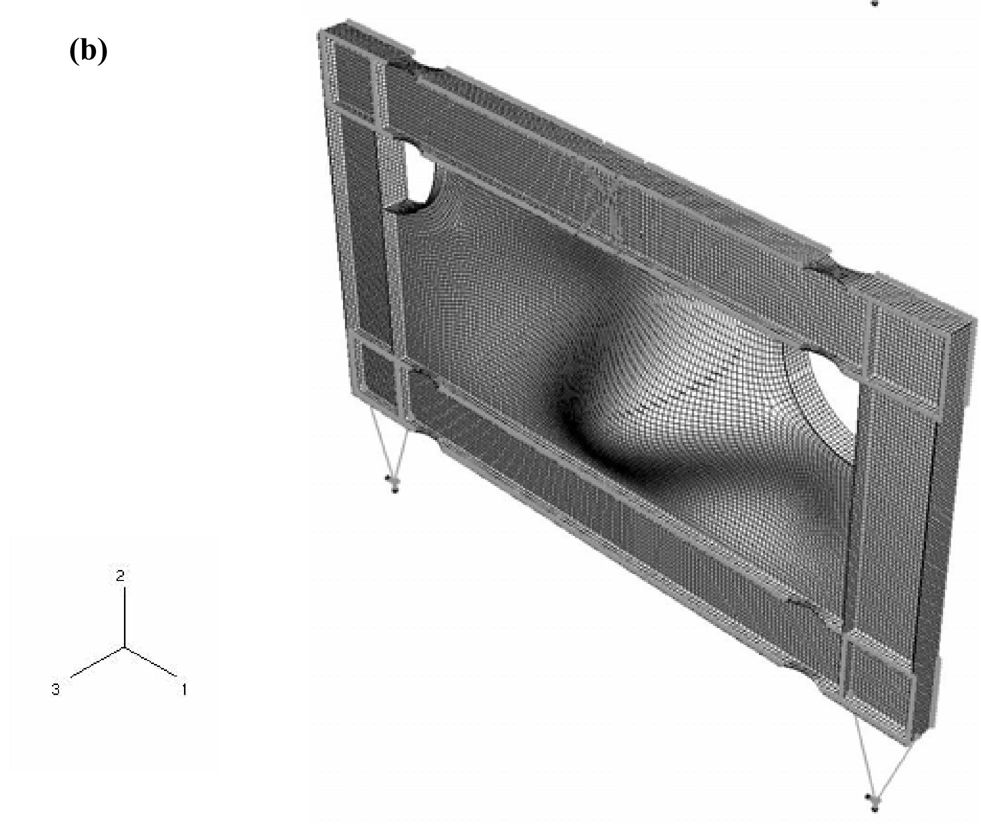

FIGURE 5-2 Perforated Panel Buckling Mode (a) 1st Mode Shape; (b) 2nd Mode Shape (Deformation Scale Factor = 444.9)

(a)

(b)

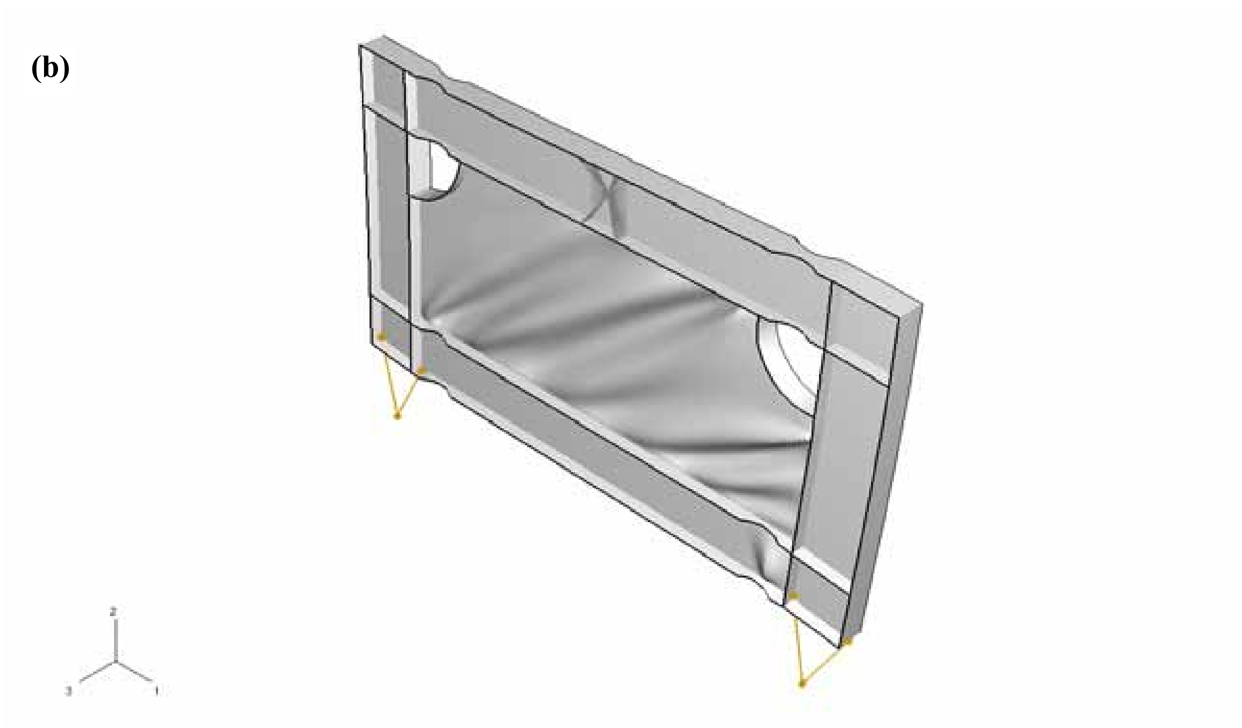

FIGURE 5-3 Front View of the Deformation Shape for the (a) CR Model; (b) CR-T Model (At 4% Frame Drift, Deformation Scale Factor = 2.0)

(a)

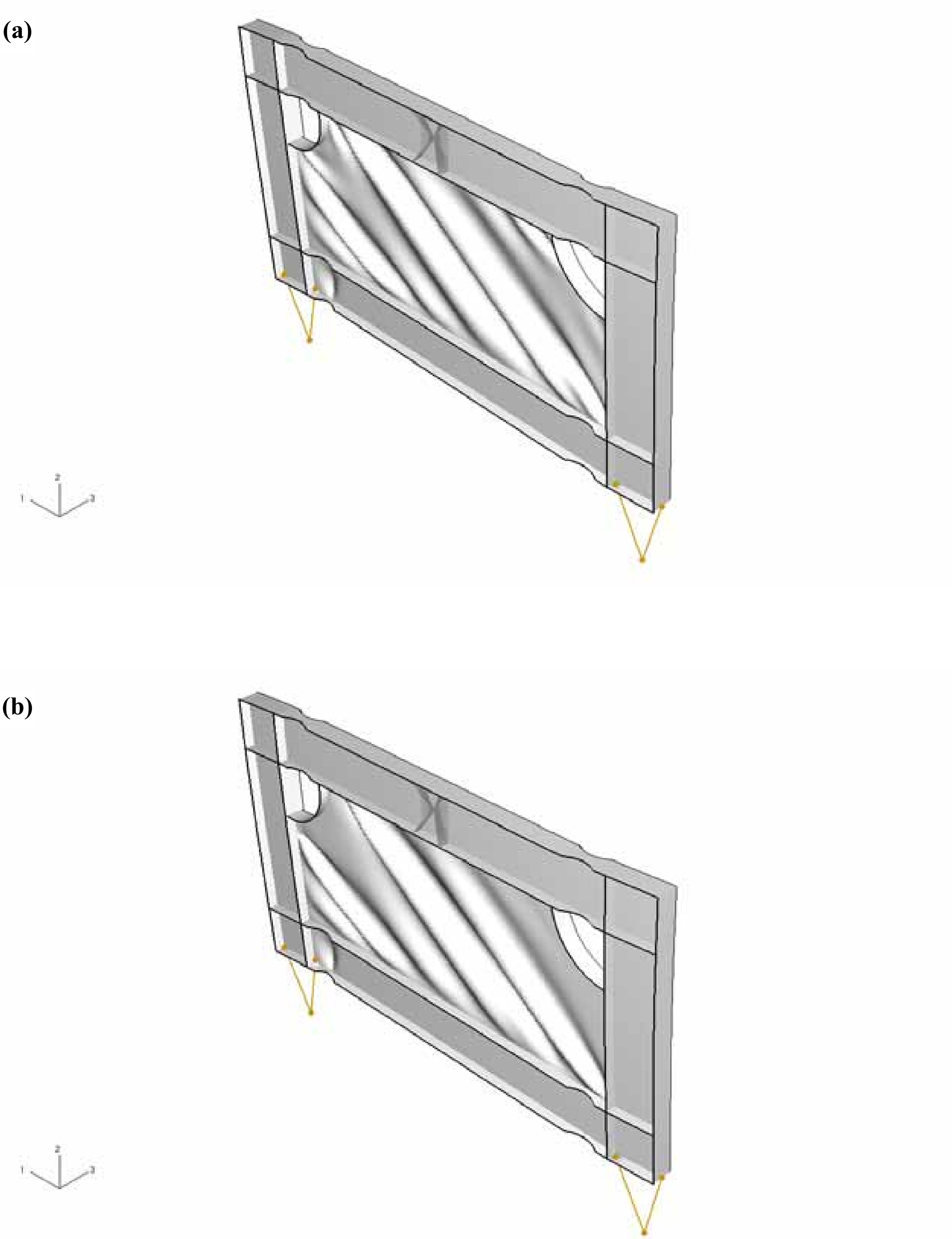

(b)

FIGURE 5-4 Rear View of the Deformation Shape for the (a) CR Model; (b) CR-T Model (At 4% Frame Drift, Deformation Scale Factor = 2.0)

In terms of diagonal displacement δ (the term schematically shown in figure 5-5), the arch plate for the CR model deformed 13.9 mm (arch tensioned) and –24.9 mm (arch compressed) for the left ("opening") corner and right ("closing") corner, respectively. For the stiffened arch plate (i.e., the CR-T model), these diagonal displacements were reduced by as much as 28%, to 10.9 mm and –19.4 mm at the same respective corners.

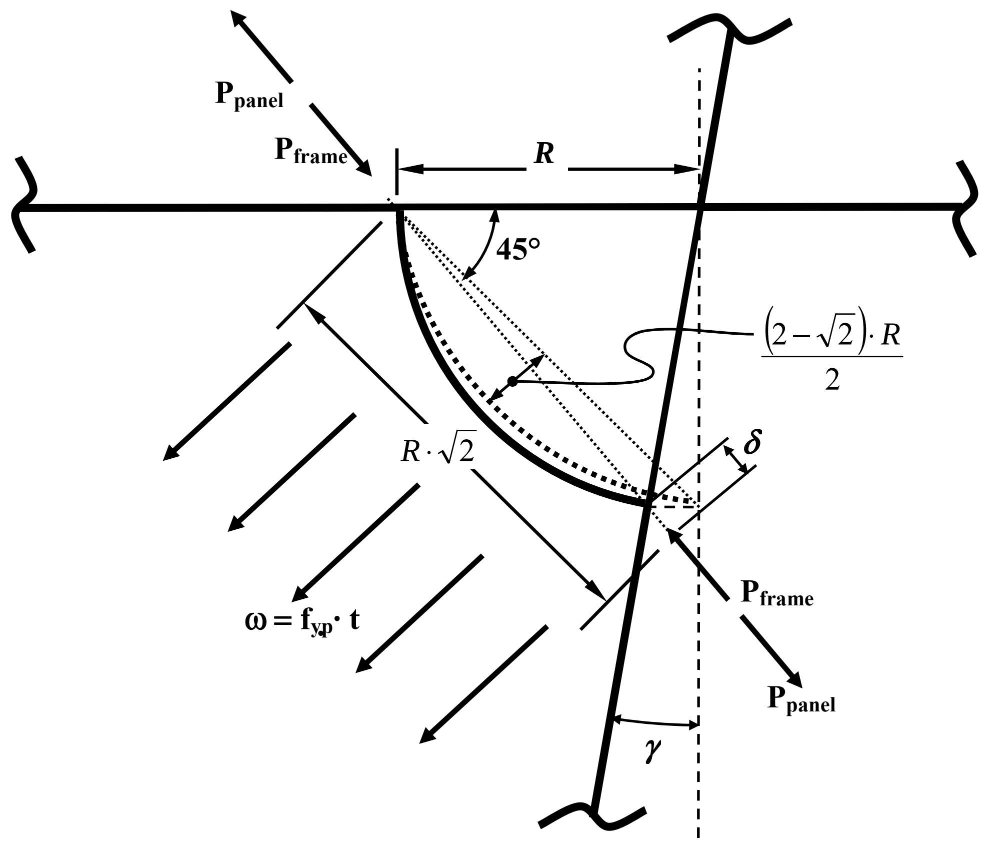

FIGURE 5-5 Deformed Configurations and Forces Acting on Right Arch (Vian 2005)

Figure 5-6 shows the shear strength results obtained from pushover analysis for the CR and CR-T models as a function of frame drift γ. For comparison purposes, the solid panel results observed in the previous section are also included in the figure. Total shear strength of the CR model is somewhat similar to that of the solid panel. For example, at 4% frame drift, the total shear strength of the CR and the solid panel models are 2645 kN and 2695 kN, respectively. Interestingly, the total shear strength of the CR-T model is 11% higher than that of the solid panel model namely 2991 kN at 4% frame drift instead of 2695 kN for the solid panel. One possible reason for this increased strength could be that the arch with the T-section is stiff and strong enough to strengthen the boundary frame by acting somehow as a "corner brace". Note that the corners "braced" the boundary frame at a point equal to about half of the infill plate high ($0.43H_{panel}$ to the end of the web plate), which is significant enough to have an impact on the frame strength.

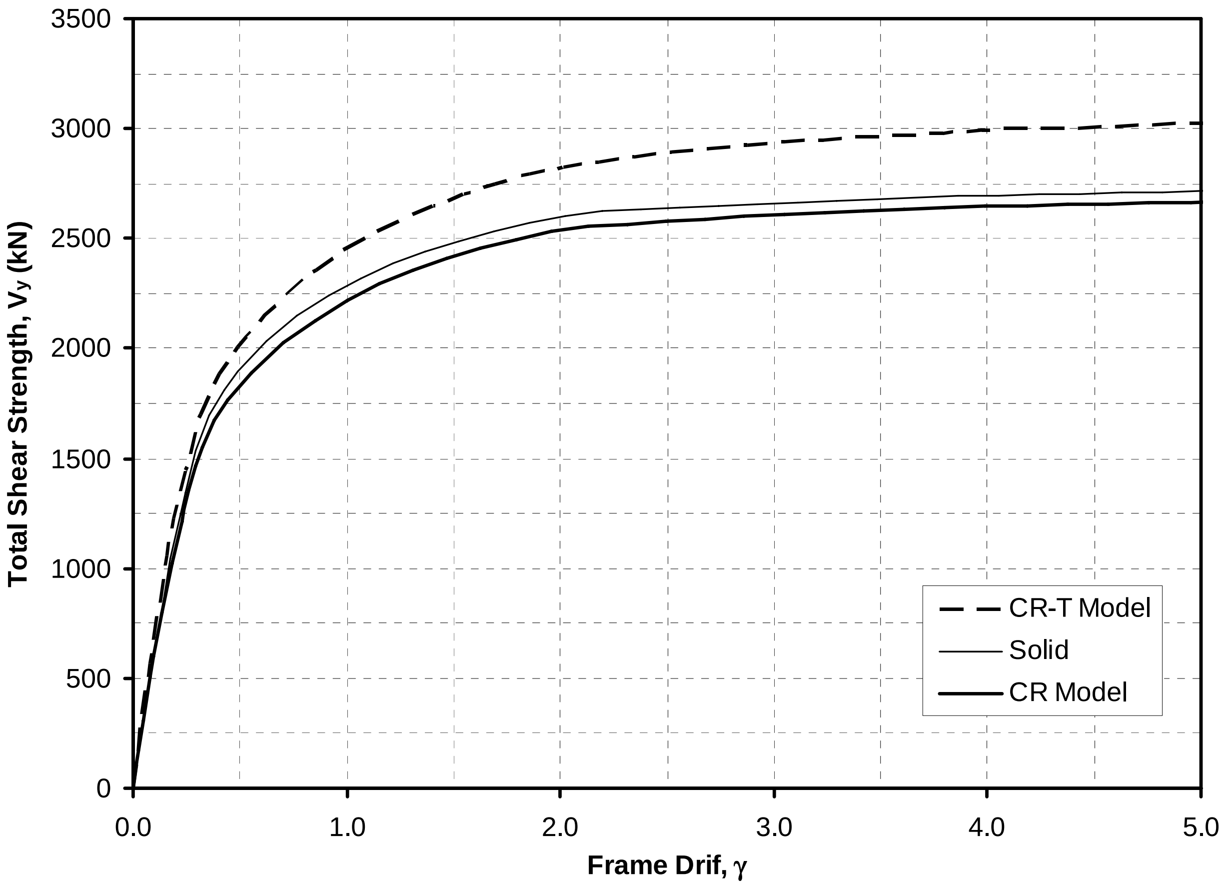

FIGURE 5-6 Total Shear Strength V_y versus Frame Drift γ

Figures 5-7 and 5-8 show maximum in-plane principal stress contours for the CR and CR-T models, respectively, when the frame experienced 4% drift. The stress distributions of the two models are similar with yielding of the top flange of the right RBS connections and on the bottom flange of the left RBS connections, uniform stress distribution on the beams and columns, and stress on the infill plate divided into several zones of tension field action at approximately 45° angles. Some differences are observed locally close to the cutout corners with stress concentration on the boundary frames for the CR-T model and different stress distribution along the length of the arch plate (L_{arch}) as plotted in figure 5-9.

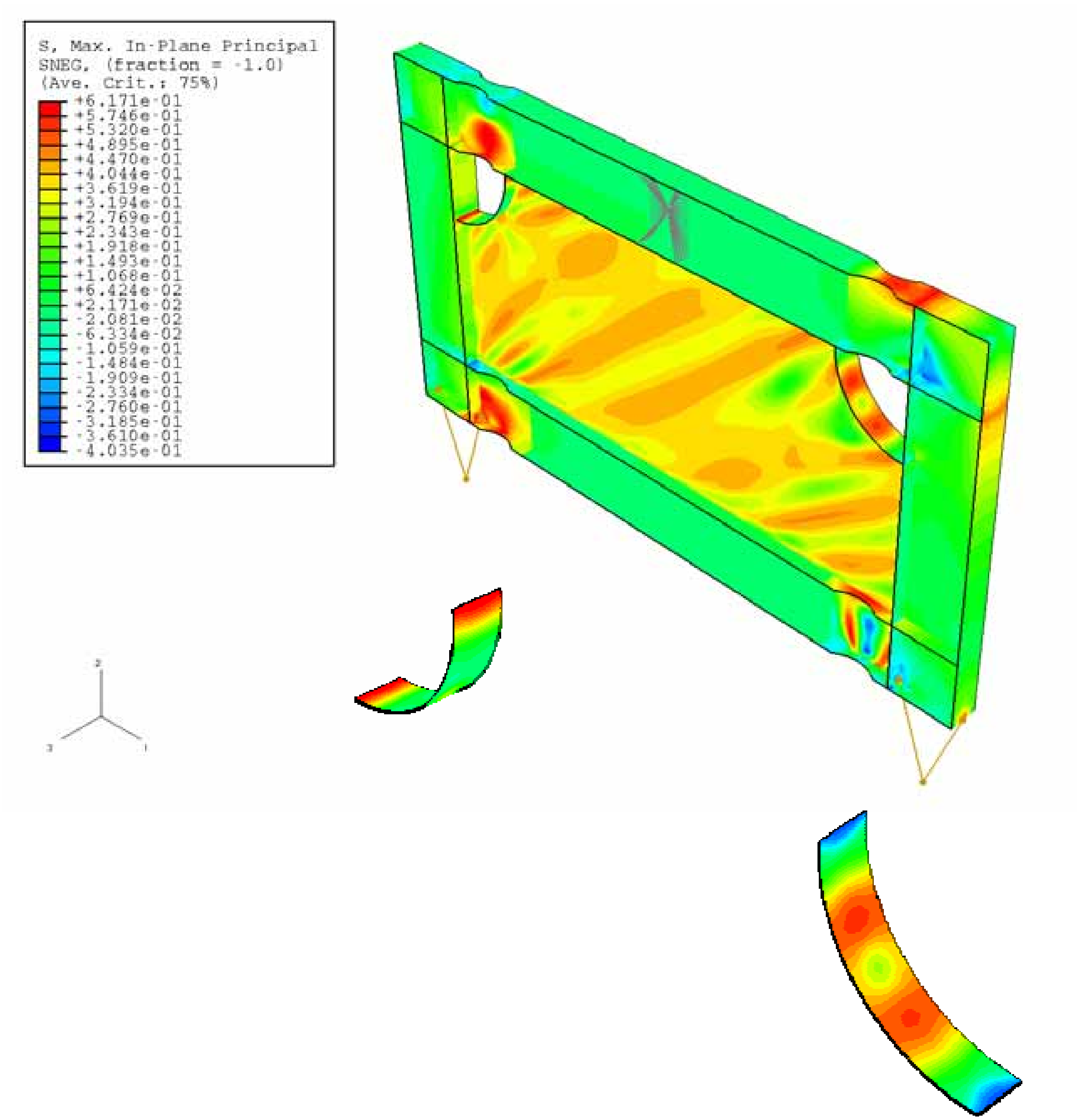

FIGURE 5-7 Maximum In-Plane Principal Stress Contours of CR Model (a) Isometric View; (b) Detail of Left Plate Reinforcement; (c) Detail of Right Plate Reinforcement

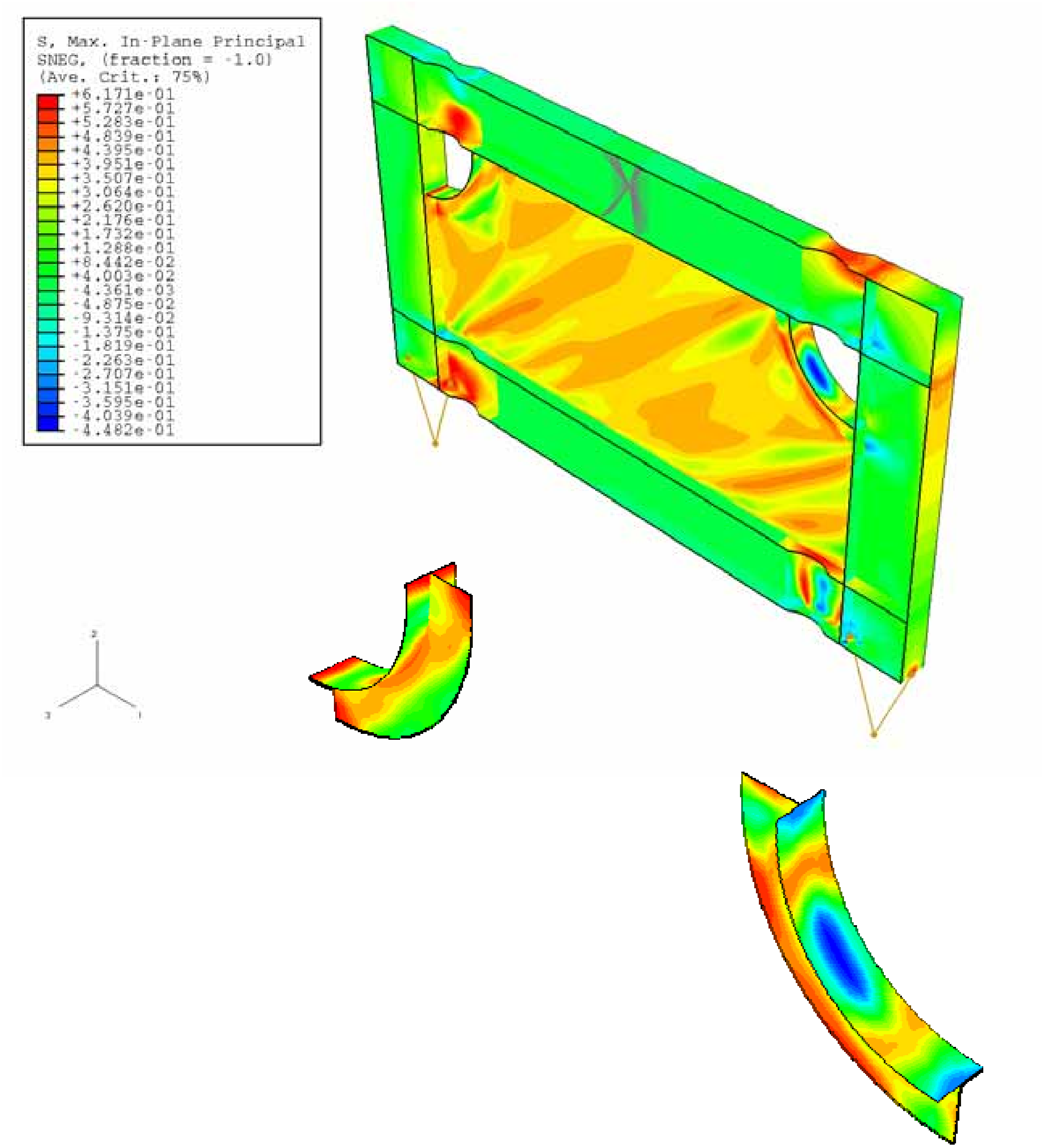

FIGURE 5-8 Maximum In-Plane Principal Stress Contours of CR-T Model (a) Isometric View; (b) Detail of Left T-Reinforcement; (c) Detail of Right T-Reinforcement

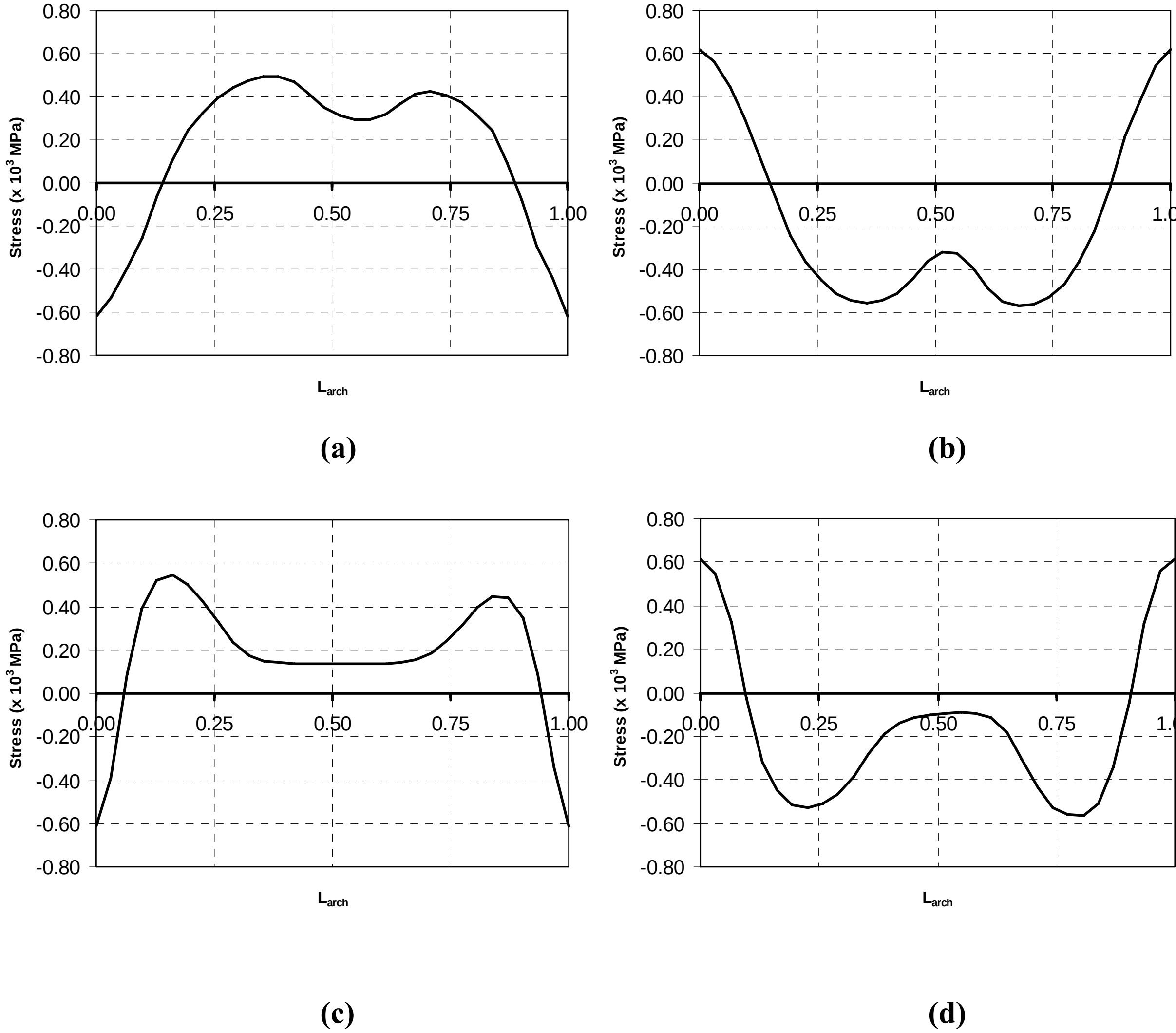

FIGURE 5-9 Stress Diagram along the Length of Plate Reinforcement (a) CR Model: Left Corner; (b) CR Model: Right Corner; (c) CR-T Model: Left Corner; (d) CR-T Model: Right Corner

Although the stress fluctuation along the L_{arch} shown in figure 5-9 is different between the two models, both models experienced relatively the same stress magnitude of 617 MPa at the tip of the arch close to the boundary frame and 568 MPa at points close to $\frac{1}{4}L_{arch}$ or $\frac{3}{4}L_{arch}$. This corresponds to local forces acting on the boundary frame equal to +1875 kN (arch compressed) and –1872 kN (arch tensioned) for the right (“closing”) and left (“opening”) corner, respectively. The boundary frame of the CR-T model experienced an additional force from the stiffener of – 600 kN (arch compressed) and 595 kN (arch tensioned).

5.4 Design Recommendations and Considerations

Total shear strength of the cutout corner SPSW with reinforcement along the cutout edges was higher by as much as 13% from that having flat-plate reinforcement for the case considered. The additional stiffness and strength of the fish plate component of the T-section reinforcement (160 mm by 12 mm) partly contributed to this increment by strengthening the "corner-brace" effect on the frame. However, the shear strength of the infill plate was not significantly different for both specimens considered. Therefore, it is acceptable, conservative, and recommended, in the perspective of global behavior, that the infill plate with cutout corners be designed per the design procedure specified by Vian (2005) for a solid infill plate.

While the stiffener (the web of the T-section) decreased the arch diagonal displacement δ by as much as 28%, it did not significantly improve the behavior of the cutout corners, as local deformation and stress distribution remained relatively the same there. Based on these results, it is recommended to design the cutout reinforcement only considering a flat plate arch (as proposed by Vian 2005). However, given that a fish plate is needed along that cutout reinforcement, the minimum fish plate needed is considered adequate to reinforce the cutout edges.

Finally, the "corner-brace" action on the boundary frame could induce high tension/compression forces from the cutout edges reinforcement to the beams and columns, and it is important to consider the actual stiffness and strength of the cutout corner (with the T-section) to determine if web stiffeners to prevent local buckling in the boundary frame.

5.5 Summary

Finite element models of the two cutout corner steel plate shear walls considered have been analyzed using ABAQUS/Standard. The first model replicated the cutout corner SPSW specimen tested by Vian (2005) with flat-plate reinforcement of 160 mm and 19 mm installed along the cutout edges. The second model introduced an additional stiffener (160 mm by 12 mm) perpendicular to the flat-plate reinforcement and formed reinforcement to the cutout edges. The latter model was intended to study the effects of the additional stiffener on the behavior of cutout corner SPSW both in terms of global and local effects. The SPSW modeled considering the T-section reinforcement exhibited a slightly higher strength. No significant difference between the two models was observed in terms of frame deformations and stress distributions along the cutout corner SPSW. Some local effects however were observed along the cutout corners in terms of diagonal displacements and stress distributions along the length of the arches. Some recommendations were proposed to help design cutout corner SPSW.

SECTION 6

SUMMARY, CONCLUSIONS, AND RECOMMENDATIONS

6.1 Summary

Analytical study using the finite element program ABAQUS/Standard was performed to investigate the behavior of unstiffened thin SPSW having openings on the infill plate under monotonic pushover displacement. To accommodate the passage of utilities, two designs proposed by Vian (2005), namely the perforated and the cutout corner SPSW, are revisited to investigate and resolve some concerns reported by Vian (2005).

As a sub-element that drives the behavior of the perforated infill plate of the type considered by Vian (2005), individual perforated strips 2000 mm by 400 mm with 4 perforations along the strip length and perforation diameters *D* ranging from 10 mm to 300 mm were first analyzed to develop a fundamental understanding of the behavior of complete perforated SPSW. Using finite element models of individual perforated strips having 100 mm diameter perforations, the effect of mesh refinement on the convergence of solutions was investigated before evaluating various perforated strip models with different perforation diameters, boundary conditions, and material idealizations. The results were presented in terms of stress-strain distribution throughout the strip section as well as in terms of global deformations.

After gaining this preliminary knowledge on the behavior of individual perforated strips, a series of 4000 mm by 2000 mm one-story SPSW having multiple perforations on panels was then considered, with variation in perforation diameter, boundary conditions, infill plate thickness, material properties idealization, and element definition. The objective of this analysis was to verify the accuracy of results obtained from finite element analysis of individual perforated strips to predict the strength of complete SPSW by summing the strength of "simpler" individual strips. Shell elements were used to model the infill plates as well as the boundary frame member webs and flanges. Specific finite element features to capture the complete SPSW behavior were also described. Among them were geometry modeling, element and material definitions, meshes size, initial imperfection, non-linear stability, boundary conditions, and lateral support to prevent lateral torsional buckling. Good agreement in overall behavior between the three models considered and the individual perforated strip model was observed. The applicability of the equation proposed by previous researchers to approximate the strength of a perforated panel was also re-assessed.

Two cutout corner SPSW models were investigated in this study. A first model replicated the cutout corner SPSW specimen tested by Vian (2005) in which a flat-plate reinforcement was introduced along the cutout edges (in that model, the fish plate added to facilitate attachment of the infill plate to the plate-reinforcement and to the surrounding frame was neglected). A second model considered had a T-section reinforcement along the cutout edges; this model was built by adding a new plate perpendicularly to the previous flat-plate reinforcement. The latter model was intended to study the effects of the additional stiffener on the behavior of cutout corner SPSW both in terms of global and local effects. The SPSW model considering the T-section reinforcement exhibited a slightly higher strength. No significant difference between the two models was observed in terms of frame deformations and stress distributions along the cutout corner SPSW. Some local effects however were observed adjacent to the cutout corner, in terms of diagonal displacement of the cutout reinforcement plate and stress distribution along the length of the plates.

Finally, some additional recommendations and considerations improving on those previously made by Vian (2005) were proposed to help design perforated and cutout corner SPSW.

6.2 Conclusions

After generating a large number of analysis results capturing the key response parameters of individual perforated strips using models having fine finite element mesh sizes, “smooth” curves of total uniform strip elongation versus perforation ratio were obtained, improving those previously developed by Vian (2005). It was also found that results on the behavior of individual perforated strips can accurately predict the behavior of complete perforated SPSW provided the holes diameter is less than 60% of the strip width. On that basis, if performance of complete

SPSW systems is to be evaluated using simpler models, it is recommended that the ratio between perforation diameter D and strip width S_{diag} be limited to $D/S_{diag} \leq 0.6$. It was found that no interaction exists between adjacent strips that could affect the stress distribution within an individual strip, i.e., each strip in a SPSW behaves as an independent strip. Material properties should duly model strain hardening to properly capture the spread of yielding in this system needed to accommodate the drifts demands in perforated SPSW.

Shear strength of the infill plate in a perforated SPSW having multiple circular perforations regularly spaced throughout the infill plate can be calculated by reducing the shear strength of the plate in a solid panel SPSW by a factor $\left(1 - \alpha \cdot D / S_{diag}\right)$, where α is a proposed correction factor equal to 0.70. For panel strength calculated on that basis, the full shear strength of the complete SPSW is obtained by adding to this value the strength of the boundary frame without the infill.

For both cutout corner SPSW considered, the shear strength of the infill plate was not significantly different. Therefore, it is acceptable, conservative, and recommended, in the perspective of global behavior, that the infill plate with cutout corners be designed per the design procedure specified by Vian (2005) for a solid infill plate.

The global behavior of cutout corner SPSW having T-section reinforcement along the cutout edges was not significantly different from that having flat-plate reinforcement. Some local effects however were observed adjacent to the cutout corner. The flat-plate reinforcement along the cutout edges (with a minimum fish plate) is considered adequate and sufficient to reinforce the cutout edges. The “corner-brace” action on the boundary frame could induce high tension/compression forces from the cutout edges reinforcement to the beams and columns. Web stiffeners may be required to prevent web crippling, web buckling, and flange bending in the boundary frame.

6.3 Recommendations for Future Research

There are some cases where the strip elongation predicted by finite element analysis of an individual perforated strip for a monitored maximum strain assumed to develop close to the perforation differs from that predicted by finite element analysis of a complete SPSW. When this occurred, it was observed that the maximum strains in the full SPSW occurred either in the edge strip, or near the RBS in the beam, or near the wall corners. These have commonly been called "corner effect" here. There are currently no reasons to believe that this would detrimentally affect the behavior of SPSW, but would nonetheless benefit from further studies. This difference should be studied further to determine the influence of this "corner effect".

The effect of beam flexibility on the reported results in absence of RBS in the beam should be further investigated, as the beam flexibility might affect the relative elongation of adjacent strips more significantly in those cases. Similarly, the presence of concrete slab should also be considered (composite or partially-composite), as in this case, the relative elongation of adjacent strips might be more similar. Furthermore, beam with semi-rigid and flexible connections deserve further study (including how to develop simplified boundary conditions that capture the behavior of these connections in finite element modeling).

Further experimental studies of SPSW having regular grade infill steels (e.g., ASTM A572 Gr. 50 or A36) would also allow to further verify that the proposed limit maximum strain of 20% is a reasonable limit state for the behavior of the infill plate. A better understanding of the ultimate limit state of the infill plate is desirable.

Finally, the design of cutout corners directly accounting for a WT reinforcement during the design process might give strength, stiffness, and ultimate behavior comparable to the case where the flat-plat reinforcement alone is used. Here, only the impact of having a thick fish plate (through a thick WT web) has been investigated.

SECTION 7

REFERENCES

AISC. (2001). "LRFD Manual of Steel Construction.", 3rd Edition, American Institute of Steel Construction, Inc., Chicago, Illinois.

Astaneh-Asl, A. (2001). "Seismic Behavior of Steel Plate Shear Walls." *Steel Tips Report,* Structural Steel Education Council, Moraga, California.

Behbahanifard, M. R., Grondin, G. Y., and Elwi, A. E. (2003). "Experimental and Numerical Investigation of Steel Plate Shear Wall." *Structural Engineering Report 254,* Department of Civil Engineering, University of Alberta, Edmonton, Alberta, Canada.

Berman, J. W. and Bruneau, M. (2003a). "Experimental Investigation of Light-Gauge Steel Plate Shear Walls for the Seismic Retrofit Of Buildings." *Technical Report MCEER-03-0001,* Multidisciplinary Center for Earthquake Engineering Research, Buffalo, New York.

Berman, J. W. and Bruneau, M. (2003b). "Plastic Analysis and Design of Steel Plate Shear Walls." *Journal of Structural Engineering*, ASCE, Vol. 129, No. 11, pp. 1148-1156.

Berman, J. W. and Bruneau, M. (2005). "Experimental Investigation of Light-Gauge Steel Plate Shear Walls." *Journal of Structural Engineering*, ASCE, Vol. 131, No. 2, pp. 259-267.

Cook, R., D., Malkus, D., S., Plesha, M., E., and Witt, R., J. (2002). "Concepts and Applications of Finite Element Analysis." 4th Edition, John Wiley and Sons, Inc., New York.

Driver, R. G., Kulak, G. L., Kennedy, D. J. L., and Elwi, A. E. (1997). "Seismic Behavior of Steel Plate Shear Walls." *Structural Engineering Report 215,* Department of Civil Engineering, University of Alberta, Edmonton, Alberta, Canada.

Driver, R. G., Kulak, G. L., Kennedy, D. J. L., and Elwi, A. E. (1998a). "Cyclic Test of Four-Story Steel Plate Shear Walls." *Journal of Structural Engineering,* ASCE, Vol. 124, No. 2, pp. 112-120.

Driver, R. G., Kulak, G. L., Kennedy, D. J. L., and Elwi, A. E. (1998b). "FE and Simplified Models of Steel Plate Shear Walls." *Journal of Structural Engineering,* ASCE, Vol. 124, No. 2, pp. 121-130.

Fillippa, C. A. (2004). "Introduction to Finite Element Methods", Department of Aerospace Engineering Sciences and Center for Aerospace Structures, University of Colorado, Boulder. 2004.

Hibbitt, Karlsson, and Sorenson, Inc. (HKS) (2004a). "ABAQUS/CAE Users Manual." Version 6.5-1, Hibbitt, Karlsson, and Sorenson, Inc., Pawtucket, Rhode Island.

Hibbitt, Karlsson, and Sorenson, Inc. (HKS) (2004b). “ABAQUS/Standard Users Manual.” Version 6.5-1, Hibbitt, Karlsson, and Sorenson, Inc., Pawtucket, Rhode Island.

Hitaka, T. and Matsui, C. (2003). “Experimental Study on Steel Shear Wall with Slits.” *Journal of Structural Engineering*, ASCE, Vol. 129, No. 5, pp. 586-595.

Kaufmann, E. J., Metrovich, B., Pense, A. W. (2001). “Characterization of Cyclic Inelastic Strain Behavior On Properties of A572 Gr. 50 and A913 Gr. 50 Rolled Sections.” *ATLSS Report No. 01-13,* National Center for Engineering Research on Advanced Technology for Large Structural Systems, Lehigh University, Bethlehem, Pennsylvania.

Roberts, T. and Sabouri-Ghomi, S. (1991). “Hysteretic characteristics of unstiffened plate shear panels.” *Thin Walled Structures*, Vol. 12, No. 2, pp. 145-162.

Roberts, T. and Sabouri-Ghomi, S. (1992). “Hysteretic characteristics of unstiffened perforated steel plate shear panels.” *Thin Walled Structures*, Vol. 14, pp. 139-151.

Scheirmeier, J.E., Housner, J. M., Aminpour, M.A., Stroud, W. J. (1996). “The application of Interface Elements to Dissimilar Meshes in Global/Local Analysis”, The 1996 MSC World Users’ Conference, California.

Shishkin, J. J., Driver, R. G., and Grondin, G. Y. “Analysis of Steel Plate Shear Walls using the Modified Strip Model.”, Structural Engineering Report No. 261, Department of Civil Engineering, University of Alberta, Edmonton, Alberta, Canada.

Thorburn, L. Jane, Kulak, G. L., and Montgomery, C. J. (1983). “Analysis of Steel Plate Shear Walls.” *Structural Engineering Report No. 107,* Department of Civil Engineering, University of Alberta, Edmonton, Alberta, Canada.

Timler, P. A. and Kulak, G. L. (1983). “Experimental Study of Steel Plate Shear Walls.” *Structural Engineering Report No. 114,* Department of Civil Engineering, University of Alberta, Edmonton, Alberta, Canada.

Timler, P.A., Ventura, C.E., Prion, H., and Anjam, R. (1998). “Experimental and Analytical Studies of Steel Plate Shear Walls as Applied to the Design of Tall Buildings.”, *Structural Design of Tall Buildings*, Vol. 7, pp. 233-249.

Tromposch, E.W., and Kulak, G.L. (1987). “Cyclic and Static Behavior of Thin Panel Steel Plate Shear Walls.”, Structural Engineering Report No. 145, Department of Civil Engineering, University of Alberta, Edmonton, Alberta, Canada.

Vian, D. (2005). “Steel Plate Shear Walls for Seismic Design and Retrofit of Building Structures.”, Ph.D Dissertation, University at Buffalo, New York.

Yang, T.Y. & Whittaker, A.S. (2002). “MCEER demonstration hospitals - Mathematical models and preliminary analysis results.”, (http://civil.eng.buffalo.edu/hospital/MCEER%20Report.pdf), Department of Civil, Structural, and Environmental Engineering, University at Buffalo, New York.

MCEER Technical Reports

MCEER publishes technical reports on a variety of subjects written by authors funded through MCEER. These reports are available from both MCEER Publications and the National Technical Information Service (NTIS). Requests for reports should be directed to MCEER Publications, MCEER, University at Buffalo, State University of New York, Red Jacket Quadrangle, Buffalo, New York 14261. Reports can also be requested through NTIS, 5285 Port Royal Road, Springfield, Virginia 22161. NTIS accession numbers are shown in parenthesis, if available.

NCEER-87-0001 "First-Year Program in Research, Education and Technology Transfer," 3/5/87, (PB88-134275, A04, MF-A01).

NCEER-87-0002 "Experimental Evaluation of Instantaneous Optimal Algorithms for Structural Control," by R.C. Lin, T.T. Soong and A.M. Reinhorn, 4/20/87, (PB88-134341, A04, MF-A01).

NCEER-87-0003 "Experimentation Using the Earthquake Simulation Facilities at University at Buffalo," by A.M. Reinhorn and R.L. Ketter, to be published.

NCEER-87-0004 "The System Characteristics and Performance of a Shaking Table," by J.S. Hwang, K.C. Chang and G.C. Lee, 6/1/87, (PB88-134259, A03, MF-A01). This report is available only through NTIS (see address given above).

NCEER-87-0005 "A Finite Element Formulation for Nonlinear Viscoplastic Material Using a Q Model," by O. Gyebi and G. Dasgupta, 11/2/87, (PB88-213764, A08, MF-A01).

NCEER-87-0006 "Symbolic Manipulation Program (SMP) - Algebraic Codes for Two and Three Dimensional Finite Element Formulations," by X. Lee and G. Dasgupta, 11/9/87, (PB88-218522, A05, MF-A01).

NCEER-87-0007 "Instantaneous Optimal Control Laws for Tall Buildings Under Seismic Excitations," by J.N. Yang, A. Akbarpour and P. Ghaemmaghami, 6/10/87, (PB88-134333, A06, MF-A01). This report is only available through NTIS (see address given above).

NCEER-87-0008 "IDARC: Inelastic Damage Analysis of Reinforced Concrete Frame - Shear-Wall Structures," by Y.J. Park, A.M. Reinhorn and S.K. Kunnath, 7/20/87, (PB88-134325, A09, MF-A01). This report is only available through NTIS (see address given above).

NCEER-87-0009 "Liquefaction Potential for New York State: A Preliminary Report on Sites in Manhattan and Buffalo," by M. Budhu, V. Vijayakumar, R.F. Giese and L. Baumgras, 8/31/87, (PB88-163704, A03, MF-A01). This report is available only through NTIS (see address given above).

NCEER-87-0010 "Vertical and Torsional Vibration of Foundations in Inhomogeneous Media," by A.S. Veletsos and K.W. Dotson, 6/1/87, (PB88-134291, A03, MF-A01). This report is only available through NTIS (see address given above).

NCEER-87-0011 "Seismic Probabilistic Risk Assessment and Seismic Margins Studies for Nuclear Power Plants," by Howard H.M. Hwang, 6/15/87, (PB88-134267, A03, MF-A01). This report is only available through NTIS (see address given above).

NCEER-87-0012 "Parametric Studies of Frequency Response of Secondary Systems Under Ground-Acceleration Excitations," by Y. Yong and Y.K. Lin, 6/10/87, (PB88-134309, A03, MF-A01). This report is only available through NTIS (see address given above).

NCEER-87-0013 "Frequency Response of Secondary Systems Under Seismic Excitation," by J.A. HoLung, J. Cai and Y.K. Lin, 7/31/87, (PB88-134317, A05, MF-A01). This report is only available through NTIS (see address given above).

NCEER-87-0014 "Modelling Earthquake Ground Motions in Seismically Active Regions Using Parametric Time Series Methods," by G.W. Ellis and A.S. Cakmak, 8/25/87, (PB88-134283, A08, MF-A01). This report is only available through NTIS (see address given above).

NCEER-87-0015 "Detection and Assessment of Seismic Structural Damage," by E. DiPasquale and A.S. Cakmak, 8/25/87, (PB88-163712, A05, MF-A01). This report is only available through NTIS (see address given above).

NCEER-87-0016 "Pipeline Experiment at Parkfield, California," by J. Isenberg and E. Richardson, 9/15/87, (PB88-163720, A03, MF-A01). This report is available only through NTIS (see address given above).

NCEER-87-0017 "Digital Simulation of Seismic Ground Motion," by M. Shinozuka, G. Deodatis and T. Harada, 8/31/87, (PB88-155197, A04, MF-A01). This report is available only through NTIS (see address given above).

NCEER-87-0018 "Practical Considerations for Structural Control: System Uncertainty, System Time Delay and Truncation of Small Control Forces," J.N. Yang and A. Akbarpour, 8/10/87, (PB88-163738, A08, MF-A01). This report is only available through NTIS (see address given above).

NCEER-87-0019 "Modal Analysis of Nonclassically Damped Structural Systems Using Canonical Transformation," by J.N. Yang, S. Sarkani and F.X. Long, 9/27/87, (PB88-187851, A04, MF-A01).

NCEER-87-0020 "A Nonstationary Solution in Random Vibration Theory," by J.R. Red-Horse and P.D. Spanos, 11/3/87, (PB88-163746, A03, MF-A01).

NCEER-87-0021 "Horizontal Impedances for Radially Inhomogeneous Viscoelastic Soil Layers," by A.S. Veletsos and K.W. Dotson, 10/15/87, (PB88-150859, A04, MF-A01).

NCEER-87-0022 "Seismic Damage Assessment of Reinforced Concrete Members," by Y.S. Chung, C. Meyer and M. Shinozuka, 10/9/87, (PB88-150867, A05, MF-A01). This report is available only through NTIS (see address given above).

NCEER-87-0023 "Active Structural Control in Civil Engineering," by T.T. Soong, 11/11/87, (PB88-187778, A03, MF-A01).

NCEER-87-0024 "Vertical and Torsional Impedances for Radially Inhomogeneous Viscoelastic Soil Layers," by K.W. Dotson and A.S. Veletsos, 12/87, (PB88-187786, A03, MF-A01).

NCEER-87-0025 "Proceedings from the Symposium on Seismic Hazards, Ground Motions, Soil-Liquefaction and Engineering Practice in Eastern North America," October 20-22, 1987, edited by K.H. Jacob, 12/87, (PB88-188115, A23, MF-A01). This report is available only through NTIS (see address given above).

NCEER-87-0026 "Report on the Whittier-Narrows, California, Earthquake of October 1, 1987," by J. Pantelic and A. Reinhorn, 11/87, (PB88-187752, A03, MF-A01). This report is available only through NTIS (see address given above).

NCEER-87-0027 "Design of a Modular Program for Transient Nonlinear Analysis of Large 3-D Building Structures," by S. Srivastav and J.F. Abel, 12/30/87, (PB88-187950, A05, MF-A01). This report is only available through NTIS (see address given above).

NCEER-87-0028 "Second-Year Program in Research, Education and Technology Transfer," 3/8/88, (PB88-219480, A04, MF-A01).

NCEER-88-0001 "Workshop on Seismic Computer Analysis and Design of Buildings With Interactive Graphics," by W. McGuire, J.F. Abel and C.H. Conley, 1/18/88, (PB88-187760, A03, MF-A01). This report is only available through NTIS (see address given above).

NCEER-88-0002 "Optimal Control of Nonlinear Flexible Structures," by J.N. Yang, F.X. Long and D. Wong, 1/22/88, (PB88-213772, A06, MF-A01).

NCEER-88-0003 "Substructuring Techniques in the Time Domain for Primary-Secondary Structural Systems," by G.D. Manolis and G. Juhn, 2/10/88, (PB88-213780, A04, MF-A01).

NCEER-88-0004 "Iterative Seismic Analysis of Primary-Secondary Systems," by A. Singhal, L.D. Lutes and P.D. Spanos, 2/23/88, (PB88-213798, A04, MF-A01).

NCEER-88-0005 "Stochastic Finite Element Expansion for Random Media," by P.D. Spanos and R. Ghanem, 3/14/88, (PB88-213806, A03, MF-A01).

NCEER-88-0006 "Combining Structural Optimization and Structural Control," by F.Y. Cheng and C.P. Pantelides, 1/10/88, (PB88-213814, A05, MF-A01).

NCEER-88-0007 "Seismic Performance Assessment of Code-Designed Structures," by H.H-M. Hwang, J-W. Jaw and H-J. Shau, 3/20/88, (PB88-219423, A04, MF-A01). This report is only available through NTIS (see address given above).

NCEER-88-0008 "Reliability Analysis of Code-Designed Structures Under Natural Hazards," by H.H-M. Hwang, H. Ushiba and M. Shinozuka, 2/29/88, (PB88-229471, A07, MF-A01). This report is only available through NTIS (see address given above).

NCEER-88-0009 "Seismic Fragility Analysis of Shear Wall Structures," by J-W Jaw and H.H-M. Hwang, 4/30/88, (PB89-102867, A04, MF-A01).

NCEER-88-0010 "Base Isolation of a Multi-Story Building Under a Harmonic Ground Motion - A Comparison of Performances of Various Systems," by F-G Fan, G. Ahmadi and I.G. Tadjbakhsh, 5/18/88, (PB89-122238, A06, MF-A01). This report is only available through NTIS (see address given above).

NCEER-88-0011 "Seismic Floor Response Spectra for a Combined System by Green's Functions," by F.M. Lavelle, L.A. Bergman and P.D. Spanos, 5/1/88, (PB89-102875, A03, MF-A01).

NCEER-88-0012 "A New Solution Technique for Randomly Excited Hysteretic Structures," by G.Q. Cai and Y.K. Lin, 5/16/88, (PB89-102883, A03, MF-A01).

NCEER-88-0013 "A Study of Radiation Damping and Soil-Structure Interaction Effects in the Centrifuge," by K. Weissman, supervised by J.H. Prevost, 5/24/88, (PB89-144703, A06, MF-A01).

NCEER-88-0014 "Parameter Identification and Implementation of a Kinematic Plasticity Model for Frictional Soils," by J.H. Prevost and D.V. Griffiths, to be published.

NCEER-88-0015 "Two- and Three- Dimensional Dynamic Finite Element Analyses of the Long Valley Dam," by D.V. Griffiths and J.H. Prevost, 6/17/88, (PB89-144711, A04, MF-A01).

NCEER-88-0016 "Damage Assessment of Reinforced Concrete Structures in Eastern United States," by A.M. Reinhorn, M.J. Seidel, S.K. Kunnath and Y.J. Park, 6/15/88, (PB89-122220, A04, MF-A01). This report is only available through NTIS (see address given above).

NCEER-88-0017 "Dynamic Compliance of Vertically Loaded Strip Foundations in Multilayered Viscoelastic Soils," by S. Ahmad and A.S.M. Israil, 6/17/88, (PB89-102891, A04, MF-A01).

NCEER-88-0018 "An Experimental Study of Seismic Structural Response With Added Viscoelastic Dampers," by R.C. Lin, Z. Liang, T.T. Soong and R.H. Zhang, 6/30/88, (PB89-122212, A05, MF-A01). This report is available only through NTIS (see address given above).

NCEER-88-0019 "Experimental Investigation of Primary - Secondary System Interaction," by G.D. Manolis, G. Juhn and A.M. Reinhorn, 5/27/88, (PB89-122204, A04, MF-A01).

NCEER-88-0020 "A Response Spectrum Approach For Analysis of Nonclassically Damped Structures," by J.N. Yang, S. Sarkani and F.X. Long, 4/22/88, (PB89-102909, A04, MF-A01).

NCEER-88-0021 "Seismic Interaction of Structures and Soils: Stochastic Approach," by A.S. Veletsos and A.M. Prasad, 7/21/88, (PB89-122196, A04, MF-A01). This report is only available through NTIS (see address given above).

NCEER-88-0022 "Identification of the Serviceability Limit State and Detection of Seismic Structural Damage," by E. DiPasquale and A.S. Cakmak, 6/15/88, (PB89-122188, A05, MF-A01). This report is available only through NTIS (see address given above).

NCEER-88-0023 "Multi-Hazard Risk Analysis: Case of a Simple Offshore Structure," by B.K. Bhartia and E.H. Vanmarcke, 7/21/88, (PB89-145213, A05, MF-A01).

NCEER-88-0024 "Automated Seismic Design of Reinforced Concrete Buildings," by Y.S. Chung, C. Meyer and M. Shinozuka, 7/5/88, (PB89-122170, A06, MF-A01). This report is available only through NTIS (see address given above).

NCEER-88-0025 "Experimental Study of Active Control of MDOF Structures Under Seismic Excitations," by L.L. Chung, R.C. Lin, T.T. Soong and A.M. Reinhorn, 7/10/88, (PB89-122600, A04, MF-A01).

NCEER-88-0026 "Earthquake Simulation Tests of a Low-Rise Metal Structure," by J.S. Hwang, K.C. Chang, G.C. Lee and R.L. Ketter, 8/1/88, (PB89-102917, A04, MF-A01).

NCEER-88-0027 "Systems Study of Urban Response and Reconstruction Due to Catastrophic Earthquakes," by F. Kozin and H.K. Zhou, 9/22/88, (PB90-162348, A04, MF-A01).

NCEER-88-0028 "Seismic Fragility Analysis of Plane Frame Structures," by H.H-M. Hwang and Y.K. Low, 7/31/88, (PB89-131445, A06, MF-A01).

NCEER-88-0029 "Response Analysis of Stochastic Structures," by A. Kardara, C. Bucher and M. Shinozuka, 9/22/88, (PB89-174429, A04, MF-A01).

NCEER-88-0030 "Nonnormal Accelerations Due to Yielding in a Primary Structure," by D.C.K. Chen and L.D. Lutes, 9/19/88, (PB89-131437, A04, MF-A01).

NCEER-88-0031 "Design Approaches for Soil-Structure Interaction," by A.S. Veletsos, A.M. Prasad and Y. Tang, 12/30/88, (PB89-174437, A03, MF-A01). This report is available only through NTIS (see address given above).

NCEER-88-0032 "A Re-evaluation of Design Spectra for Seismic Damage Control," by C.J. Turkstra and A.G. Tallin, 11/7/88, (PB89-145221, A05, MF-A01).

NCEER-88-0033 "The Behavior and Design of Noncontact Lap Splices Subjected to Repeated Inelastic Tensile Loading," by V.E. Sagan, P. Gergely and R.N. White, 12/8/88, (PB89-163737, A08, MF-A01).

NCEER-88-0034 "Seismic Response of Pile Foundations," by S.M. Mamoon, P.K. Banerjee and S. Ahmad, 11/1/88, (PB89-145239, A04, MF-A01).

NCEER-88-0035 "Modeling of R/C Building Structures With Flexible Floor Diaphragms (IDARC2)," by A.M. Reinhorn, S.K. Kunnath and N. Panahshahi, 9/7/88, (PB89-207153, A07, MF-A01).

NCEER-88-0036 "Solution of the Dam-Reservoir Interaction Problem Using a Combination of FEM, BEM with Particular Integrals, Modal Analysis, and Substructuring," by C-S. Tsai, G.C. Lee and R.L. Ketter, 12/31/88, (PB89-207146, A04, MF-A01).

NCEER-88-0037 "Optimal Placement of Actuators for Structural Control," by F.Y. Cheng and C.P. Pantelides, 8/15/88, (PB89-162846, A05, MF-A01).

NCEER-88-0038 "Teflon Bearings in Aseismic Base Isolation: Experimental Studies and Mathematical Modeling," by A. Mokha, M.C. Constantinou and A.M. Reinhorn, 12/5/88, (PB89-218457, A10, MF-A01). This report is available only through NTIS (see address given above).

NCEER-88-0039 "Seismic Behavior of Flat Slab High-Rise Buildings in the New York City Area," by P. Weidlinger and M. Ettouney, 10/15/88, (PB90-145681, A04, MF-A01).

NCEER-88-0040 "Evaluation of the Earthquake Resistance of Existing Buildings in New York City," by P. Weidlinger and M. Ettouney, 10/15/88, to be published.

NCEER-88-0041 "Small-Scale Modeling Techniques for Reinforced Concrete Structures Subjected to Seismic Loads," by W. Kim, A. El-Attar and R.N. White, 11/22/88, (PB89-189625, A05, MF-A01).

NCEER-88-0042 "Modeling Strong Ground Motion from Multiple Event Earthquakes," by G.W. Ellis and A.S. Cakmak, 10/15/88, (PB89-174445, A03, MF-A01).

NCEER-88-0043 "Nonstationary Models of Seismic Ground Acceleration," by M. Grigoriu, S.E. Ruiz and E. Rosenblueth, 7/15/88, (PB89-189617, A04, MF-A01).

NCEER-88-0044 "SARCF User's Guide: Seismic Analysis of Reinforced Concrete Frames," by Y.S. Chung, C. Meyer and M. Shinozuka, 11/9/88, (PB89-174452, A08, MF-A01).

NCEER-88-0045 "First Expert Panel Meeting on Disaster Research and Planning," edited by J. Pantelic and J. Stoyle, 9/15/88, (PB89-174460, A05, MF-A01).

NCEER-88-0046 "Preliminary Studies of the Effect of Degrading Infill Walls on the Nonlinear Seismic Response of Steel Frames," by C.Z. Chrysostomou, P. Gergely and J.F. Abel, 12/19/88, (PB89-208383, A05, MF-A01).

NCEER-88-0047 "Reinforced Concrete Frame Component Testing Facility - Design, Construction, Instrumentation and Operation," by S.P. Pessiki, C. Conley, T. Bond, P. Gergely and R.N. White, 12/16/88, (PB89-174478, A04, MF-A01).

NCEER-89-0001 "Effects of Protective Cushion and Soil Compliancy on the Response of Equipment Within a Seismically Excited Building," by J.A. HoLung, 2/16/89, (PB89-207179, A04, MF-A01).

NCEER-89-0002 "Statistical Evaluation of Response Modification Factors for Reinforced Concrete Structures," by H.H-M. Hwang and J-W. Jaw, 2/17/89, (PB89-207187, A05, MF-A01).

NCEER-89-0003 "Hysteretic Columns Under Random Excitation," by G-Q. Cai and Y.K. Lin, 1/9/89, (PB89-196513, A03, MF-A01).

NCEER-89-0004 "Experimental Study of `Elephant Foot Bulge' Instability of Thin-Walled Metal Tanks," by Z-H. Jia and R.L. Ketter, 2/22/89, (PB89-207195, A03, MF-A01).

NCEER-89-0005 "Experiment on Performance of Buried Pipelines Across San Andreas Fault," by J. Isenberg, E. Richardson and T.D. O'Rourke, 3/10/89, (PB89-218440, A04, MF-A01). This report is available only through NTIS (see address given above).

NCEER-89-0006 "A Knowledge-Based Approach to Structural Design of Earthquake-Resistant Buildings," by M. Subramani, P. Gergely, C.H. Conley, J.F. Abel and A.H. Zaghw, 1/15/89, (PB89-218465, A06, MF-A01).

NCEER-89-0007 "Liquefaction Hazards and Their Effects on Buried Pipelines," by T.D. O'Rourke and P.A. Lane, 2/1/89, (PB89-218481, A09, MF-A01).

NCEER-89-0008 "Fundamentals of System Identification in Structural Dynamics," by H. Imai, C-B. Yun, O. Maruyama and M. Shinozuka, 1/26/89, (PB89-207211, A04, MF-A01).

NCEER-89-0009 "Effects of the 1985 Michoacan Earthquake on Water Systems and Other Buried Lifelines in Mexico," by A.G. Ayala and M.J. O'Rourke, 3/8/89, (PB89-207229, A06, MF-A01).

NCEER-89-R010 "NCEER Bibliography of Earthquake Education Materials," by K.E.K. Ross, Second Revision, 9/1/89, (PB90-125352, A05, MF-A01). This report is replaced by NCEER-92-0018.

NCEER-89-0011 "Inelastic Three-Dimensional Response Analysis of Reinforced Concrete Building Structures (IDARC-3D), Part I - Modeling," by S.K. Kunnath and A.M. Reinhorn, 4/17/89, (PB90-114612, A07, MF-A01). This report is available only through NTIS (see address given above).

NCEER-89-0012 "Recommended Modifications to ATC-14," by C.D. Poland and J.O. Malley, 4/12/89, (PB90-108648, A15, MF-A01).

NCEER-89-0013 "Repair and Strengthening of Beam-to-Column Connections Subjected to Earthquake Loading," by M. Corazao and A.J. Durrani, 2/28/89, (PB90-109885, A06, MF-A01).

NCEER-89-0014 "Program EXKAL2 for Identification of Structural Dynamic Systems," by O. Maruyama, C-B. Yun, M. Hoshiya and M. Shinozuka, 5/19/89, (PB90-109877, A09, MF-A01).

NCEER-89-0015 "Response of Frames With Bolted Semi-Rigid Connections, Part I - Experimental Study and Analytical Predictions," by P.J. DiCorso, A.M. Reinhorn, J.R. Dickerson, J.B. Radziminski and W.L. Harper, 6/1/89, to be published.

NCEER-89-0016 "ARMA Monte Carlo Simulation in Probabilistic Structural Analysis," by P.D. Spanos and M.P. Mignolet, 7/10/89, (PB90-109893, A03, MF-A01).

NCEER-89-P017 "Preliminary Proceedings from the Conference on Disaster Preparedness - The Place of Earthquake Education in Our Schools," Edited by K.E.K. Ross, 6/23/89, (PB90-108606, A03, MF-A01).

NCEER-89-0017 "Proceedings from the Conference on Disaster Preparedness - The Place of Earthquake Education in Our Schools," Edited by K.E.K. Ross, 12/31/89, (PB90-207895, A012, MF-A02). This report is available only through NTIS (see address given above).

NCEER-89-0018 "Multidimensional Models of Hysteretic Material Behavior for Vibration Analysis of Shape Memory Energy Absorbing Devices, by E.J. Graesser and F.A. Cozzarelli, 6/7/89, (PB90-164146, A04, MF-A01).

NCEER-89-0019 "Nonlinear Dynamic Analysis of Three-Dimensional Base Isolated Structures (3D-BASIS)," by S. Nagarajaiah, A.M. Reinhorn and M.C. Constantinou, 8/3/89, (PB90-161936, A06, MF-A01). This report has been replaced by NCEER-93-0011.

NCEER-89-0020 "Structural Control Considering Time-Rate of Control Forces and Control Rate Constraints," by F.Y. Cheng and C.P. Pantelides, 8/3/89, (PB90-120445, A04, MF-A01).

NCEER-89-0021 "Subsurface Conditions of Memphis and Shelby County," by K.W. Ng, T-S. Chang and H-H.M. Hwang, 7/26/89, (PB90-120437, A03, MF-A01).

NCEER-89-0022 "Seismic Wave Propagation Effects on Straight Jointed Buried Pipelines," by K. Elhmadi and M.J. O'Rourke, 8/24/89, (PB90-162322, A10, MF-A02).

NCEER-89-0023 "Workshop on Serviceability Analysis of Water Delivery Systems," edited by M. Grigoriu, 3/6/89, (PB90-127424, A03, MF-A01).

NCEER-89-0024 "Shaking Table Study of a 1/5 Scale Steel Frame Composed of Tapered Members," by K.C. Chang, J.S. Hwang and G.C. Lee, 9/18/89, (PB90-160169, A04, MF-A01).

NCEER-89-0025 "DYNA1D: A Computer Program for Nonlinear Seismic Site Response Analysis - Technical Documentation," by Jean H. Prevost, 9/14/89, (PB90-161944, A07, MF-A01). This report is available only through NTIS (see address given above).

NCEER-89-0026 "1:4 Scale Model Studies of Active Tendon Systems and Active Mass Dampers for Aseismic Protection," by A.M. Reinhorn, T.T. Soong, R.C. Lin, Y.P. Yang, Y. Fukao, H. Abe and M. Nakai, 9/15/89, (PB90-173246, A10, MF-A02). This report is available only through NTIS (see address given above).

NCEER-89-0027 "Scattering of Waves by Inclusions in a Nonhomogeneous Elastic Half Space Solved by Boundary Element Methods," by P.K. Hadley, A. Askar and A.S. Cakmak, 6/15/89, (PB90-145699, A07, MF-A01).

NCEER-89-0028 "Statistical Evaluation of Deflection Amplification Factors for Reinforced Concrete Structures," by H.H.M. Hwang, J-W. Jaw and A.L. Ch'ng, 8/31/89, (PB90-164633, A05, MF-A01).

NCEER-89-0029 "Bedrock Accelerations in Memphis Area Due to Large New Madrid Earthquakes," by H.H.M. Hwang, C.H.S. Chen and G. Yu, 11/7/89, (PB90-162330, A04, MF-A01).

NCEER-89-0030 "Seismic Behavior and Response Sensitivity of Secondary Structural Systems," by Y.Q. Chen and T.T. Soong, 10/23/89, (PB90-164658, A08, MF-A01).

NCEER-89-0031 "Random Vibration and Reliability Analysis of Primary-Secondary Structural Systems," by Y. Ibrahim, M. Grigoriu and T.T. Soong, 11/10/89, (PB90-161951, A04, MF-A01).

NCEER-89-0032 "Proceedings from the Second U.S. - Japan Workshop on Liquefaction, Large Ground Deformation and Their Effects on Lifelines, September 26-29, 1989," Edited by T.D. O'Rourke and M. Hamada, 12/1/89, (PB90-209388, A22, MF-A03).

NCEER-89-0033 "Deterministic Model for Seismic Damage Evaluation of Reinforced Concrete Structures," by J.M. Bracci, A.M. Reinhorn, J.B. Mander and S.K. Kunnath, 9/27/89, (PB91-108803, A06, MF-A01).

NCEER-89-0034 "On the Relation Between Local and Global Damage Indices," by E. DiPasquale and A.S. Cakmak, 8/15/89, (PB90-173865, A05, MF-A01).

NCEER-89-0035 "Cyclic Undrained Behavior of Nonplastic and Low Plasticity Silts," by A.J. Walker and H.E. Stewart, 7/26/89, (PB90-183518, A10, MF-A01).

NCEER-89-0036 "Liquefaction Potential of Surficial Deposits in the City of Buffalo, New York," by M. Budhu, R. Giese and L. Baumgrass, 1/17/89, (PB90-208455, A04, MF-A01).

NCEER-89-0037 "A Deterministic Assessment of Effects of Ground Motion Incoherence," by A.S. Veletsos and Y. Tang, 7/15/89, (PB90-164294, A03, MF-A01).

NCEER-89-0038 "Workshop on Ground Motion Parameters for Seismic Hazard Mapping," July 17-18, 1989, edited by R.V. Whitman, 12/1/89, (PB90-173923, A04, MF-A01).

NCEER-89-0039 "Seismic Effects on Elevated Transit Lines of the New York City Transit Authority," by C.J. Costantino, C.A. Miller and E. Heymsfield, 12/26/89, (PB90-207887, A06, MF-A01).

NCEER-89-0040 "Centrifugal Modeling of Dynamic Soil-Structure Interaction," by K. Weissman, Supervised by J.H. Prevost, 5/10/89, (PB90-207879, A07, MF-A01).

NCEER-89-0041 "Linearized Identification of Buildings With Cores for Seismic Vulnerability Assessment," by I-K. Ho and A.E. Aktan, 11/1/89, (PB90-251943, A07, MF-A01).

NCEER-90-0001 "Geotechnical and Lifeline Aspects of the October 17, 1989 Loma Prieta Earthquake in San Francisco," by T.D. O'Rourke, H.E. Stewart, F.T. Blackburn and T.S. Dickerman, 1/90, (PB90-208596, A05, MF-A01).

NCEER-90-0002 "Nonnormal Secondary Response Due to Yielding in a Primary Structure," by D.C.K. Chen and L.D. Lutes, 2/28/90, (PB90-251976, A07, MF-A01).

NCEER-90-0003 "Earthquake Education Materials for Grades K-12," by K.E.K. Ross, 4/16/90, (PB91-251984, A05, MF-A05). This report has been replaced by NCEER-92-0018.

NCEER-90-0004 "Catalog of Strong Motion Stations in Eastern North America," by R.W. Busby, 4/3/90, (PB90-251984, A05, MF-A01).

NCEER-90-0005 "NCEER Strong-Motion Data Base: A User Manual for the GeoBase Release (Version 1.0 for the Sun3)," by P. Friberg and K. Jacob, 3/31/90 (PB90-258062, A04, MF-A01).

NCEER-90-0006 "Seismic Hazard Along a Crude Oil Pipeline in the Event of an 1811-1812 Type New Madrid Earthquake," by H.H.M. Hwang and C-H.S. Chen, 4/16/90, (PB90-258054, A04, MF-A01).

NCEER-90-0007 "Site-Specific Response Spectra for Memphis Sheahan Pumping Station," by H.H.M. Hwang and C.S. Lee, 5/15/90, (PB91-108811, A05, MF-A01).

NCEER-90-0008 "Pilot Study on Seismic Vulnerability of Crude Oil Transmission Systems," by T. Ariman, R. Dobry, M. Grigoriu, F. Kozin, M. O'Rourke, T. O'Rourke and M. Shinozuka, 5/25/90, (PB91-108837, A06, MF-A01).

NCEER-90-0009 "A Program to Generate Site Dependent Time Histories: EQGEN," by G.W. Ellis, M. Srinivasan and A.S. Cakmak, 1/30/90, (PB91-108829, A04, MF-A01).

NCEER-90-0010 "Active Isolation for Seismic Protection of Operating Rooms," by M.E. Talbott, Supervised by M. Shinozuka, 6/8/9, (PB91-110205, A05, MF-A01).

NCEER-90-0011 "Program LINEARID for Identification of Linear Structural Dynamic Systems," by C-B. Yun and M. Shinozuka, 6/25/90, (PB91-110312, A08, MF-A01).

NCEER-90-0012 "Two-Dimensional Two-Phase Elasto-Plastic Seismic Response of Earth Dams," by A.N. Yiagos, Supervised by J.H. Prevost, 6/20/90, (PB91-110197, A13, MF-A02).

NCEER-90-0013 "Secondary Systems in Base-Isolated Structures: Experimental Investigation, Stochastic Response and Stochastic Sensitivity," by G.D. Manolis, G. Juhn, M.C. Constantinou and A.M. Reinhorn, 7/1/90, (PB91-110320, A08, MF-A01).

NCEER-90-0014 "Seismic Behavior of Lightly-Reinforced Concrete Column and Beam-Column Joint Details," by S.P. Pessiki, C.H. Conley, P. Gergely and R.N. White, 8/22/90, (PB91-108795, A11, MF-A02).

NCEER-90-0015 "Two Hybrid Control Systems for Building Structures Under Strong Earthquakes," by J.N. Yang and A. Danielians, 6/29/90, (PB91-125393, A04, MF-A01).

NCEER-90-0016 "Instantaneous Optimal Control with Acceleration and Velocity Feedback," by J.N. Yang and Z. Li, 6/29/90, (PB91-125401, A03, MF-A01).

NCEER-90-0017 "Reconnaissance Report on the Northern Iran Earthquake of June 21, 1990," by M. Mehrain, 10/4/90, (PB91-125377, A03, MF-A01).

NCEER-90-0018 "Evaluation of Liquefaction Potential in Memphis and Shelby County," by T.S. Chang, P.S. Tang, C.S. Lee and H. Hwang, 8/10/90, (PB91-125427, A09, MF-A01).

NCEER-90-0019 "Experimental and Analytical Study of a Combined Sliding Disc Bearing and Helical Steel Spring Isolation System," by M.C. Constantinou, A.S. Mokha and A.M. Reinhorn, 10/4/90, (PB91-125385, A06, MF-A01). This report is available only through NTIS (see address given above).

NCEER-90-0020 "Experimental Study and Analytical Prediction of Earthquake Response of a Sliding Isolation System with a Spherical Surface," by A.S. Mokha, M.C. Constantinou and A.M. Reinhorn, 10/11/90, (PB91-125419, A05, MF-A01).

NCEER-90-0021 "Dynamic Interaction Factors for Floating Pile Groups," by G. Gazetas, K. Fan, A. Kaynia and E. Kausel, 9/10/90, (PB91-170381, A05, MF-A01).

NCEER-90-0022 "Evaluation of Seismic Damage Indices for Reinforced Concrete Structures," by S. Rodriguez-Gomez and A.S. Cakmak, 9/30/90, PB91-171322, A06, MF-A01).

NCEER-90-0023 "Study of Site Response at a Selected Memphis Site," by H. Desai, S. Ahmad, E.S. Gazetas and M.R. Oh, 10/11/90, (PB91-196857, A03, MF-A01).

NCEER-90-0024 "A User's Guide to Strongmo: Version 1.0 of NCEER's Strong-Motion Data Access Tool for PCs and Terminals," by P.A. Friberg and C.A.T. Susch, 11/15/90, (PB91-171272, A03, MF-A01).

NCEER-90-0025 "A Three-Dimensional Analytical Study of Spatial Variability of Seismic Ground Motions," by L-L. Hong and A.H.-S. Ang, 10/30/90, (PB91-170399, A09, MF-A01).

NCEER-90-0026 "MUMOID User's Guide - A Program for the Identification of Modal Parameters," by S. Rodriguez-Gomez and E. DiPasquale, 9/30/90, (PB91-171298, A04, MF-A01).

NCEER-90-0027 "SARCF-II User's Guide - Seismic Analysis of Reinforced Concrete Frames," by S. Rodriguez-Gomez, Y.S. Chung and C. Meyer, 9/30/90, (PB91-171280, A05, MF-A01).

NCEER-90-0028 "Viscous Dampers: Testing, Modeling and Application in Vibration and Seismic Isolation," by N. Makris and M.C. Constantinou, 12/20/90 (PB91-190561, A06, MF-A01).

NCEER-90-0029 "Soil Effects on Earthquake Ground Motions in the Memphis Area," by H. Hwang, C.S. Lee, K.W. Ng and T.S. Chang, 8/2/90, (PB91-190751, A05, MF-A01).

NCEER-91-0001 "Proceedings from the Third Japan-U.S. Workshop on Earthquake Resistant Design of Lifeline Facilities and Countermeasures for Soil Liquefaction, December 17-19, 1990," edited by T.D. O'Rourke and M. Hamada, 2/1/91, (PB91-179259, A99, MF-A04).

NCEER-91-0002 "Physical Space Solutions of Non-Proportionally Damped Systems," by M. Tong, Z. Liang and G.C. Lee, 1/15/91, (PB91-179242, A04, MF-A01).

NCEER-91-0003 "Seismic Response of Single Piles and Pile Groups," by K. Fan and G. Gazetas, 1/10/91, (PB92-174994, A04, MF-A01).

NCEER-91-0004 "Damping of Structures: Part 1 - Theory of Complex Damping," by Z. Liang and G. Lee, 10/10/91, (PB92-197235, A12, MF-A03).

NCEER-91-0005 "3D-BASIS - Nonlinear Dynamic Analysis of Three Dimensional Base Isolated Structures: Part II," by S. Nagarajaiah, A.M. Reinhorn and M.C. Constantinou, 2/28/91, (PB91-190553, A07, MF-A01). This report has been replaced by NCEER-93-0011.

NCEER-91-0006 "A Multidimensional Hysteretic Model for Plasticity Deforming Metals in Energy Absorbing Devices," by E.J. Graesser and F.A. Cozzarelli, 4/9/91, (PB92-108364, A04, MF-A01).

NCEER-91-0007 "A Framework for Customizable Knowledge-Based Expert Systems with an Application to a KBES for Evaluating the Seismic Resistance of Existing Buildings," by E.G. Ibarra-Anaya and S.J. Fenves, 4/9/91, (PB91-210930, A08, MF-A01).

NCEER-91-0008 "Nonlinear Analysis of Steel Frames with Semi-Rigid Connections Using the Capacity Spectrum Method," by G.G. Deierlein, S-H. Hsieh, Y-J. Shen and J.F. Abel, 7/2/91, (PB92-113828, A05, MF-A01).

NCEER-91-0009 "Earthquake Education Materials for Grades K-12," by K.E.K. Ross, 4/30/91, (PB91-212142, A06, MF-A01). This report has been replaced by NCEER-92-0018.

NCEER-91-0010 "Phase Wave Velocities and Displacement Phase Differences in a Harmonically Oscillating Pile," by N. Makris and G. Gazetas, 7/8/91, (PB92-108356, A04, MF-A01).

NCEER-91-0011 "Dynamic Characteristics of a Full-Size Five-Story Steel Structure and a 2/5 Scale Model," by K.C. Chang, G.C. Yao, G.C. Lee, D.S. Hao and Y.C. Yeh," 7/2/91, (PB93-116648, A06, MF-A02).

NCEER-91-0012 "Seismic Response of a 2/5 Scale Steel Structure with Added Viscoelastic Dampers," by K.C. Chang, T.T. Soong, S-T. Oh and M.L. Lai, 5/17/91, (PB92-110816, A05, MF-A01).

NCEER-91-0013 "Earthquake Response of Retaining Walls; Full-Scale Testing and Computational Modeling," by S. Alampalli and A-W.M. Elgamal, 6/20/91, to be published.

NCEER-91-0014 "3D-BASIS-M: Nonlinear Dynamic Analysis of Multiple Building Base Isolated Structures," by P.C. Tsopelas, S. Nagarajaiah, M.C. Constantinou and A.M. Reinhorn, 5/28/91, (PB92-113885, A09, MF-A02).

NCEER-91-0015 "Evaluation of SEAOC Design Requirements for Sliding Isolated Structures," by D. Theodossiou and M.C. Constantinou, 6/10/91, (PB92-114602, A11, MF-A03).

NCEER-91-0016 "Closed-Loop Modal Testing of a 27-Story Reinforced Concrete Flat Plate-Core Building," by H.R. Somaprasad, T. Toksoy, H. Yoshiyuki and A.E. Aktan, 7/15/91, (PB92-129980, A07, MF-A02).

NCEER-91-0017 "Shake Table Test of a 1/6 Scale Two-Story Lightly Reinforced Concrete Building," by A.G. El-Attar, R.N. White and P. Gergely, 2/28/91, (PB92-222447, A06, MF-A02).

NCEER-91-0018 "Shake Table Test of a 1/8 Scale Three-Story Lightly Reinforced Concrete Building," by A.G. El-Attar, R.N. White and P. Gergely, 2/28/91, (PB93-116630, A08, MF-A02).

NCEER-91-0019 "Transfer Functions for Rigid Rectangular Foundations," by A.S. Veletsos, A.M. Prasad and W.H. Wu, 7/31/91, to be published.

NCEER-91-0020 "Hybrid Control of Seismic-Excited Nonlinear and Inelastic Structural Systems," by J.N. Yang, Z. Li and A. Danielians, 8/1/91, (PB92-143171, A06, MF-A02).

NCEER-91-0021 "The NCEER-91 Earthquake Catalog: Improved Intensity-Based Magnitudes and Recurrence Relations for U.S. Earthquakes East of New Madrid," by L. Seeber and J.G. Armbruster, 8/28/91, (PB92-176742, A06, MF-A02).

NCEER-91-0022 "Proceedings from the Implementation of Earthquake Planning and Education in Schools: The Need for Change - The Roles of the Changemakers," by K.E.K. Ross and F. Winslow, 7/23/91, (PB92-129998, A12, MF-A03).

NCEER-91-0023 "A Study of Reliability-Based Criteria for Seismic Design of Reinforced Concrete Frame Buildings," by H.H.M. Hwang and H-M. Hsu, 8/10/91, (PB92-140235, A09, MF-A02).

NCEER-91-0024 "Experimental Verification of a Number of Structural System Identification Algorithms," by R.G. Ghanem, H. Gavin and M. Shinozuka, 9/18/91, (PB92-176577, A18, MF-A04).

NCEER-91-0025 "Probabilistic Evaluation of Liquefaction Potential," by H.H.M. Hwang and C.S. Lee," 11/25/91, (PB92-143429, A05, MF-A01).

NCEER-91-0026 "Instantaneous Optimal Control for Linear, Nonlinear and Hysteretic Structures - Stable Controllers," by J.N. Yang and Z. Li, 11/15/91, (PB92-163807, A04, MF-A01).

NCEER-91-0027 "Experimental and Theoretical Study of a Sliding Isolation System for Bridges," by M.C. Constantinou, A. Kartoum, A.M. Reinhorn and P. Bradford, 11/15/91, (PB92-176973, A10, MF-A03).

NCEER-92-0001 "Case Studies of Liquefaction and Lifeline Performance During Past Earthquakes, Volume 1: Japanese Case Studies," Edited by M. Hamada and T. O'Rourke, 2/17/92, (PB92-197243, A18, MF-A04).

NCEER-92-0002 "Case Studies of Liquefaction and Lifeline Performance During Past Earthquakes, Volume 2: United States Case Studies," Edited by T. O'Rourke and M. Hamada, 2/17/92, (PB92-197250, A20, MF-A04).

NCEER-92-0003 "Issues in Earthquake Education," Edited by K. Ross, 2/3/92, (PB92-222389, A07, MF-A02).

NCEER-92-0004 "Proceedings from the First U.S. - Japan Workshop on Earthquake Protective Systems for Bridges," Edited by I.G. Buckle, 2/4/92, (PB94-142239, A99, MF-A06).

NCEER-92-0005 "Seismic Ground Motion from a Haskell-Type Source in a Multiple-Layered Half-Space," A.P. Theoharis, G. Deodatis and M. Shinozuka, 1/2/92, to be published.

NCEER-92-0006 "Proceedings from the Site Effects Workshop," Edited by R. Whitman, 2/29/92, (PB92-197201, A04, MF-A01).

NCEER-92-0007 "Engineering Evaluation of Permanent Ground Deformations Due to Seismically-Induced Liquefaction," by M.H. Baziar, R. Dobry and A-W.M. Elgamal, 3/24/92, (PB92-222421, A13, MF-A03).

NCEER-92-0008 "A Procedure for the Seismic Evaluation of Buildings in the Central and Eastern United States," by C.D. Poland and J.O. Malley, 4/2/92, (PB92-222439, A20, MF-A04).

NCEER-92-0009 "Experimental and Analytical Study of a Hybrid Isolation System Using Friction Controllable Sliding Bearings," by M.Q. Feng, S. Fujii and M. Shinozuka, 5/15/92, (PB93-150282, A06, MF-A02).

NCEER-92-0010 "Seismic Resistance of Slab-Column Connections in Existing Non-Ductile Flat-Plate Buildings," by A.J. Durrani and Y. Du, 5/18/92, (PB93-116812, A06, MF-A02).

NCEER-92-0011 "The Hysteretic and Dynamic Behavior of Brick Masonry Walls Upgraded by Ferrocement Coatings Under Cyclic Loading and Strong Simulated Ground Motion," by H. Lee and S.P. Prawel, 5/11/92, to be published.

NCEER-92-0012 "Study of Wire Rope Systems for Seismic Protection of Equipment in Buildings," by G.F. Demetriades, M.C. Constantinou and A.M. Reinhorn, 5/20/92, (PB93-116655, A08, MF-A02).

NCEER-92-0013 "Shape Memory Structural Dampers: Material Properties, Design and Seismic Testing," by P.R. Witting and F.A. Cozzarelli, 5/26/92, (PB93-116663, A05, MF-A01).

NCEER-92-0014 "Longitudinal Permanent Ground Deformation Effects on Buried Continuous Pipelines," by M.J. O'Rourke, and C. Nordberg, 6/15/92, (PB93-116671, A08, MF-A02).

NCEER-92-0015 "A Simulation Method for Stationary Gaussian Random Functions Based on the Sampling Theorem," by M. Grigoriu and S. Balopoulou, 6/11/92, (PB93-127496, A05, MF-A01).

NCEER-92-0016 "Gravity-Load-Designed Reinforced Concrete Buildings: Seismic Evaluation of Existing Construction and Detailing Strategies for Improved Seismic Resistance," by G.W. Hoffmann, S.K. Kunnath, A.M. Reinhorn and J.B. Mander, 7/15/92, (PB94-142007, A08, MF-A02).

NCEER-92-0017 "Observations on Water System and Pipeline Performance in the Limón Area of Costa Rica Due to the April 22, 1991 Earthquake," by M. O'Rourke and D. Ballantyne, 6/30/92, (PB93-126811, A06, MF-A02).

NCEER-92-0018 "Fourth Edition of Earthquake Education Materials for Grades K-12," Edited by K.E.K. Ross, 8/10/92, (PB93-114023, A07, MF-A02).

NCEER-92-0019 "Proceedings from the Fourth Japan-U.S. Workshop on Earthquake Resistant Design of Lifeline Facilities and Countermeasures for Soil Liquefaction," Edited by M. Hamada and T.D. O'Rourke, 8/12/92, (PB93-163939, A99, MF-E11).

NCEER-92-0020 "Active Bracing System: A Full Scale Implementation of Active Control," by A.M. Reinhorn, T.T. Soong, R.C. Lin, M.A. Riley, Y.P. Wang, S. Aizawa and M. Higashino, 8/14/92, (PB93-127512, A06, MF-A02).

NCEER-92-0021 "Empirical Analysis of Horizontal Ground Displacement Generated by Liquefaction-Induced Lateral Spreads," by S.F. Bartlett and T.L. Youd, 8/17/92, (PB93-188241, A06, MF-A02).

NCEER-92-0022 "IDARC Version 3.0: Inelastic Damage Analysis of Reinforced Concrete Structures," by S.K. Kunnath, A.M. Reinhorn and R.F. Lobo, 8/31/92, (PB93-227502, A07, MF-A02).

NCEER-92-0023 "A Semi-Empirical Analysis of Strong-Motion Peaks in Terms of Seismic Source, Propagation Path and Local Site Conditions, by M. Kamiyama, M.J. O'Rourke and R. Flores-Berrones, 9/9/92, (PB93-150266, A08, MF-A02).

NCEER-92-0024 "Seismic Behavior of Reinforced Concrete Frame Structures with Nonductile Details, Part I: Summary of Experimental Findings of Full Scale Beam-Column Joint Tests," by A. Beres, R.N. White and P. Gergely, 9/30/92, (PB93-227783, A05, MF-A01).

NCEER-92-0025 "Experimental Results of Repaired and Retrofitted Beam-Column Joint Tests in Lightly Reinforced Concrete Frame Buildings," by A. Beres, S. El-Borgi, R.N. White and P. Gergely, 10/29/92, (PB93-227791, A05, MF-A01).

NCEER-92-0026 "A Generalization of Optimal Control Theory: Linear and Nonlinear Structures," by J.N. Yang, Z. Li and S. Vongchavalitkul, 11/2/92, (PB93-188621, A05, MF-A01).

NCEER-92-0027 "Seismic Resistance of Reinforced Concrete Frame Structures Designed Only for Gravity Loads: Part I - Design and Properties of a One-Third Scale Model Structure," by J.M. Bracci, A.M. Reinhorn and J.B. Mander, 12/1/92, (PB94-104502, A08, MF-A02).

NCEER-92-0028 "Seismic Resistance of Reinforced Concrete Frame Structures Designed Only for Gravity Loads: Part II - Experimental Performance of Subassemblages," by L.E. Aycardi, J.B. Mander and A.M. Reinhorn, 12/1/92, (PB94-104510, A08, MF-A02).

NCEER-92-0029 "Seismic Resistance of Reinforced Concrete Frame Structures Designed Only for Gravity Loads: Part III - Experimental Performance and Analytical Study of a Structural Model," by J.M. Bracci, A.M. Reinhorn and J.B. Mander, 12/1/92, (PB93-227528, A09, MF-A01).

NCEER-92-0030 "Evaluation of Seismic Retrofit of Reinforced Concrete Frame Structures: Part I - Experimental Performance of Retrofitted Subassemblages," by D. Choudhuri, J.B. Mander and A.M. Reinhorn, 12/8/92, (PB93-198307, A07, MF-A02).

NCEER-92-0031 "Evaluation of Seismic Retrofit of Reinforced Concrete Frame Structures: Part II - Experimental Performance and Analytical Study of a Retrofitted Structural Model," by J.M. Bracci, A.M. Reinhorn and J.B. Mander, 12/8/92, (PB93-198315, A09, MF-A03).

NCEER-92-0032 "Experimental and Analytical Investigation of Seismic Response of Structures with Supplemental Fluid Viscous Dampers," by M.C. Constantinou and M.D. Symans, 12/21/92, (PB93-191435, A10, MF-A03). This report is available only through NTIS (see address given above).

NCEER-92-0033 "Reconnaissance Report on the Cairo, Egypt Earthquake of October 12, 1992," by M. Khater, 12/23/92, (PB93-188621, A03, MF-A01).

NCEER-92-0034 "Low-Level Dynamic Characteristics of Four Tall Flat-Plate Buildings in New York City," by H. Gavin, S. Yuan, J. Grossman, E. Pekelis and K. Jacob, 12/28/92, (PB93-188217, A07, MF-A02).

NCEER-93-0001 "An Experimental Study on the Seismic Performance of Brick-Infilled Steel Frames With and Without Retrofit," by J.B. Mander, B. Nair, K. Wojtkowski and J. Ma, 1/29/93, (PB93-227510, A07, MF-A02).

NCEER-93-0002 "Social Accounting for Disaster Preparedness and Recovery Planning," by S. Cole, E. Pantoja and V. Razak, 2/22/93, (PB94-142114, A12, MF-A03).

NCEER-93-0003 "Assessment of 1991 NEHRP Provisions for Nonstructural Components and Recommended Revisions," by T.T. Soong, G. Chen, Z. Wu, R-H. Zhang and M. Grigoriu, 3/1/93, (PB93-188639, A06, MF-A02).

NCEER-93-0004 "Evaluation of Static and Response Spectrum Analysis Procedures of SEAOC/UBC for Seismic Isolated Structures," by C.W. Winters and M.C. Constantinou, 3/23/93, (PB93-198299, A10, MF-A03).

NCEER-93-0005 "Earthquakes in the Northeast - Are We Ignoring the Hazard? A Workshop on Earthquake Science and Safety for Educators," edited by K.E.K. Ross, 4/2/93, (PB94-103066, A09, MF-A02).

NCEER-93-0006 "Inelastic Response of Reinforced Concrete Structures with Viscoelastic Braces," by R.F. Lobo, J.M. Bracci, K.L. Shen, A.M. Reinhorn and T.T. Soong, 4/5/93, (PB93-227486, A05, MF-A02).

NCEER-93-0007 "Seismic Testing of Installation Methods for Computers and Data Processing Equipment," by K. Kosar, T.T. Soong, K.L. Shen, J.A. HoLung and Y.K. Lin, 4/12/93, (PB93-198299, A07, MF-A02).

NCEER-93-0008 "Retrofit of Reinforced Concrete Frames Using Added Dampers," by A. Reinhorn, M. Constantinou and C. Li, to be published.

NCEER-93-0009 "Seismic Behavior and Design Guidelines for Steel Frame Structures with Added Viscoelastic Dampers," by K.C. Chang, M.L. Lai, T.T. Soong, D.S. Hao and Y.C. Yeh, 5/1/93, (PB94-141959, A07, MF-A02).

NCEER-93-0010 "Seismic Performance of Shear-Critical Reinforced Concrete Bridge Piers," by J.B. Mander, S.M. Waheed, M.T.A. Chaudhary and S.S. Chen, 5/12/93, (PB93-227494, A08, MF-A02).

NCEER-93-0011 "3D-BASIS-TABS: Computer Program for Nonlinear Dynamic Analysis of Three Dimensional Base Isolated Structures," by S. Nagarajaiah, C. Li, A.M. Reinhorn and M.C. Constantinou, 8/2/93, (PB94-141819, A09, MF-A02).

NCEER-93-0012 "Effects of Hydrocarbon Spills from an Oil Pipeline Break on Ground Water," by O.J. Helweg and H.H.M. Hwang, 8/3/93, (PB94-141942, A06, MF-A02).

NCEER-93-0013 "Simplified Procedures for Seismic Design of Nonstructural Components and Assessment of Current Code Provisions," by M.P. Singh, L.E. Suarez, E.E. Matheu and G.O. Maldonado, 8/4/93, (PB94-141827, A09, MF-A02).

NCEER-93-0014 "An Energy Approach to Seismic Analysis and Design of Secondary Systems," by G. Chen and T.T. Soong, 8/6/93, (PB94-142767, A11, MF-A03).

NCEER-93-0015 "Proceedings from School Sites: Becoming Prepared for Earthquakes - Commemorating the Third Anniversary of the Loma Prieta Earthquake," Edited by F.E. Winslow and K.E.K. Ross, 8/16/93, (PB94-154275, A16, MF-A02).

NCEER-93-0016 "Reconnaissance Report of Damage to Historic Monuments in Cairo, Egypt Following the October 12, 1992 Dahshur Earthquake," by D. Sykora, D. Look, G. Croci, E. Karaesmen and E. Karaesmen, 8/19/93, (PB94-142221, A08, MF-A02).

NCEER-93-0017 "The Island of Guam Earthquake of August 8, 1993," by S.W. Swan and S.K. Harris, 9/30/93, (PB94-141843, A04, MF-A01).

NCEER-93-0018 "Engineering Aspects of the October 12, 1992 Egyptian Earthquake," by A.W. Elgamal, M. Amer, K. Adalier and A. Abul-Fadl, 10/7/93, (PB94-141983, A05, MF-A01).

NCEER-93-0019 "Development of an Earthquake Motion Simulator and its Application in Dynamic Centrifuge Testing," by I. Krstelj, Supervised by J.H. Prevost, 10/23/93, (PB94-181773, A-10, MF-A03).

NCEER-93-0020 "NCEER-Taisei Corporation Research Program on Sliding Seismic Isolation Systems for Bridges: Experimental and Analytical Study of a Friction Pendulum System (FPS)," by M.C. Constantinou, P. Tsopelas, Y-S. Kim and S. Okamoto, 11/1/93, (PB94-142775, A08, MF-A02).

NCEER-93-0021 "Finite Element Modeling of Elastomeric Seismic Isolation Bearings," by L.J. Billings, Supervised by R. Shepherd, 11/8/93, to be published.

NCEER-93-0022 "Seismic Vulnerability of Equipment in Critical Facilities: Life-Safety and Operational Consequences," by K. Porter, G.S. Johnson, M.M. Zadeh, C. Scawthorn and S. Eder, 11/24/93, (PB94-181765, A16, MF-A03).

NCEER-93-0023 "Hokkaido Nansei-oki, Japan Earthquake of July 12, 1993, by P.I. Yanev and C.R. Scawthorn, 12/23/93, (PB94-181500, A07, MF-A01).

NCEER-94-0001 "An Evaluation of Seismic Serviceability of Water Supply Networks with Application to the San Francisco Auxiliary Water Supply System," by I. Markov, Supervised by M. Grigoriu and T. O'Rourke, 1/21/94, (PB94-204013, A07, MF-A02).

NCEER-94-0002 "NCEER-Taisei Corporation Research Program on Sliding Seismic Isolation Systems for Bridges: Experimental and Analytical Study of Systems Consisting of Sliding Bearings, Rubber Restoring Force Devices and Fluid Dampers," Volumes I and II, by P. Tsopelas, S. Okamoto, M.C. Constantinou, D. Ozaki and S. Fujii, 2/4/94, (PB94-181740, A09, MF-A02 and PB94-181757, A12, MF-A03).

NCEER-94-0003 "A Markov Model for Local and Global Damage Indices in Seismic Analysis," by S. Rahman and M. Grigoriu, 2/18/94, (PB94-206000, A12, MF-A03).

NCEER-94-0004 "Proceedings from the NCEER Workshop on Seismic Response of Masonry Infills," edited by D.P. Abrams, 3/1/94, (PB94-180783, A07, MF-A02).

NCEER-94-0005 "The Northridge, California Earthquake of January 17, 1994: General Reconnaissance Report," edited by J.D. Goltz, 3/11/94, (PB94-193943, A10, MF-A03).

NCEER-94-0006 "Seismic Energy Based Fatigue Damage Analysis of Bridge Columns: Part I - Evaluation of Seismic Capacity," by G.A. Chang and J.B. Mander, 3/14/94, (PB94-219185, A11, MF-A03).

NCEER-94-0007 "Seismic Isolation of Multi-Story Frame Structures Using Spherical Sliding Isolation Systems," by T.M. Al-Hussaini, V.A. Zayas and M.C. Constantinou, 3/17/94, (PB94-193745, A09, MF-A02).

NCEER-94-0008 "The Northridge, California Earthquake of January 17, 1994: Performance of Highway Bridges," edited by I.G. Buckle, 3/24/94, (PB94-193851, A06, MF-A02).

NCEER-94-0009 "Proceedings of the Third U.S.-Japan Workshop on Earthquake Protective Systems for Bridges," edited by I.G. Buckle and I. Friedland, 3/31/94, (PB94-195815, A99, MF-A06).

NCEER-94-0010 "3D-BASIS-ME: Computer Program for Nonlinear Dynamic Analysis of Seismically Isolated Single and Multiple Structures and Liquid Storage Tanks," by P.C. Tsopelas, M.C. Constantinou and A.M. Reinhorn, 4/12/94, (PB94-204922, A09, MF-A02).

NCEER-94-0011 "The Northridge, California Earthquake of January 17, 1994: Performance of Gas Transmission Pipelines," by T.D. O'Rourke and M.C. Palmer, 5/16/94, (PB94-204989, A05, MF-A01).

NCEER-94-0012 "Feasibility Study of Replacement Procedures and Earthquake Performance Related to Gas Transmission Pipelines," by T.D. O'Rourke and M.C. Palmer, 5/25/94, (PB94-206638, A09, MF-A02).

NCEER-94-0013 "Seismic Energy Based Fatigue Damage Analysis of Bridge Columns: Part II - Evaluation of Seismic Demand," by G.A. Chang and J.B. Mander, 6/1/94, (PB95-18106, A08, MF-A02).

NCEER-94-0014 "NCEER-Taisei Corporation Research Program on Sliding Seismic Isolation Systems for Bridges: Experimental and Analytical Study of a System Consisting of Sliding Bearings and Fluid Restoring Force/Damping Devices," by P. Tsopelas and M.C. Constantinou, 6/13/94, (PB94-219144, A10, MF-A03).

NCEER-94-0015 "Generation of Hazard-Consistent Fragility Curves for Seismic Loss Estimation Studies," by H. Hwang and J-R. Huo, 6/14/94, (PB95-181996, A09, MF-A02).

NCEER-94-0016 "Seismic Study of Building Frames with Added Energy-Absorbing Devices," by W.S. Pong, C.S. Tsai and G.C. Lee, 6/20/94, (PB94-219136, A10, A03).

NCEER-94-0017 "Sliding Mode Control for Seismic-Excited Linear and Nonlinear Civil Engineering Structures," by J. Yang, J. Wu, A. Agrawal and Z. Li, 6/21/94, (PB95-138483, A06, MF-A02).

NCEER-94-0018 "3D-BASIS-TABS Version 2.0: Computer Program for Nonlinear Dynamic Analysis of Three Dimensional Base Isolated Structures," by A.M. Reinhorn, S. Nagarajaiah, M.C. Constantinou, P. Tsopelas and R. Li, 6/22/94, (PB95-182176, A08, MF-A02).

NCEER-94-0019 "Proceedings of the International Workshop on Civil Infrastructure Systems: Application of Intelligent Systems and Advanced Materials on Bridge Systems," Edited by G.C. Lee and K.C. Chang, 7/18/94, (PB95-252474, A20, MF-A04).

NCEER-94-0020 "Study of Seismic Isolation Systems for Computer Floors," by V. Lambrou and M.C. Constantinou, 7/19/94, (PB95-138533, A10, MF-A03).

NCEER-94-0021 "Proceedings of the U.S.-Italian Workshop on Guidelines for Seismic Evaluation and Rehabilitation of Unreinforced Masonry Buildings," Edited by D.P. Abrams and G.M. Calvi, 7/20/94, (PB95-138749, A13, MF-A03).

NCEER-94-0022 "NCEER-Taisei Corporation Research Program on Sliding Seismic Isolation Systems for Bridges: Experimental and Analytical Study of a System Consisting of Lubricated PTFE Sliding Bearings and Mild Steel Dampers," by P. Tsopelas and M.C. Constantinou, 7/22/94, (PB95-182184, A08, MF-A02).

NCEER-94-0023 "Development of Reliability-Based Design Criteria for Buildings Under Seismic Load," by Y.K. Wen, H. Hwang and M. Shinozuka, 8/1/94, (PB95-211934, A08, MF-A02).

NCEER-94-0024 "Experimental Verification of Acceleration Feedback Control Strategies for an Active Tendon System," by S.J. Dyke, B.F. Spencer, Jr., P. Quast, M.K. Sain, D.C. Kaspari, Jr. and T.T. Soong, 8/29/94, (PB95-212320, A05, MF-A01).

NCEER-94-0025 "Seismic Retrofitting Manual for Highway Bridges," Edited by I.G. Buckle and I.F. Friedland, published by the Federal Highway Administration (PB95-212676, A15, MF-A03).

NCEER-94-0026 "Proceedings from the Fifth U.S.-Japan Workshop on Earthquake Resistant Design of Lifeline Facilities and Countermeasures Against Soil Liquefaction," Edited by T.D. O'Rourke and M. Hamada, 11/7/94, (PB95-220802, A99, MF-E08).

NCEER-95-0001 "Experimental and Analytical Investigation of Seismic Retrofit of Structures with Supplemental Damping: Part 1 - Fluid Viscous Damping Devices," by A.M. Reinhorn, C. Li and M.C. Constantinou, 1/3/95, (PB95-266599, A09, MF-A02).

NCEER-95-0002 "Experimental and Analytical Study of Low-Cycle Fatigue Behavior of Semi-Rigid Top-And-Seat Angle Connections," by G. Pekcan, J.B. Mander and S.S. Chen, 1/5/95, (PB95-220042, A07, MF-A02).

NCEER-95-0003 "NCEER-ATC Joint Study on Fragility of Buildings," by T. Anagnos, C. Rojahn and A.S. Kiremidjian, 1/20/95, (PB95-220026, A06, MF-A02).

NCEER-95-0004 "Nonlinear Control Algorithms for Peak Response Reduction," by Z. Wu, T.T. Soong, V. Gattulli and R.C. Lin, 2/16/95, (PB95-220349, A05, MF-A01).

NCEER-95-0005 "Pipeline Replacement Feasibility Study: A Methodology for Minimizing Seismic and Corrosion Risks to Underground Natural Gas Pipelines," by R.T. Eguchi, H.A. Seligson and D.G. Honegger, 3/2/95, (PB95-252326, A06, MF-A02).

NCEER-95-0006 "Evaluation of Seismic Performance of an 11-Story Frame Building During the 1994 Northridge Earthquake," by F. Naeim, R. DiSulio, K. Benuska, A. Reinhorn and C. Li, to be published.

NCEER-95-0007 "Prioritization of Bridges for Seismic Retrofitting," by N. Basöz and A.S. Kiremidjian, 4/24/95, (PB95-252300, A08, MF-A02).

NCEER-95-0008 "Method for Developing Motion Damage Relationships for Reinforced Concrete Frames," by A. Singhal and A.S. Kiremidjian, 5/11/95, (PB95-266607, A06, MF-A02).

NCEER-95-0009 "Experimental and Analytical Investigation of Seismic Retrofit of Structures with Supplemental Damping: Part II - Friction Devices," by C. Li and A.M. Reinhorn, 7/6/95, (PB96-128087, A11, MF-A03).

NCEER-95-0010 "Experimental Performance and Analytical Study of a Non-Ductile Reinforced Concrete Frame Structure Retrofitted with Elastomeric Spring Dampers," by G. Pekcan, J.B. Mander and S.S. Chen, 7/14/95, (PB96-137161, A08, MF-A02).

NCEER-95-0011 "Development and Experimental Study of Semi-Active Fluid Damping Devices for Seismic Protection of Structures," by M.D. Symans and M.C. Constantinou, 8/3/95, (PB96-136940, A23, MF-A04).

NCEER-95-0012 "Real-Time Structural Parameter Modification (RSPM): Development of Innervated Structures," by Z. Liang, M. Tong and G.C. Lee, 4/11/95, (PB96-137153, A06, MF-A01).

NCEER-95-0013 "Experimental and Analytical Investigation of Seismic Retrofit of Structures with Supplemental Damping: Part III - Viscous Damping Walls," by A.M. Reinhorn and C. Li, 10/1/95, (PB96-176409, A11, MF-A03).

NCEER-95-0014 "Seismic Fragility Analysis of Equipment and Structures in a Memphis Electric Substation," by J-R. Huo and H.H.M. Hwang, 8/10/95, (PB96-128087, A09, MF-A02).

NCEER-95-0015 "The Hanshin-Awaji Earthquake of January 17, 1995: Performance of Lifelines," Edited by M. Shinozuka, 11/3/95, (PB96-176383, A15, MF-A03).

NCEER-95-0016 "Highway Culvert Performance During Earthquakes," by T.L. Youd and C.J. Beckman, available as NCEER-96-0015.

NCEER-95-0017 "The Hanshin-Awaji Earthquake of January 17, 1995: Performance of Highway Bridges," Edited by I.G. Buckle, 12/1/95, to be published.

NCEER-95-0018 "Modeling of Masonry Infill Panels for Structural Analysis," by A.M. Reinhorn, A. Madan, R.E. Valles, Y. Reichmann and J.B. Mander, 12/8/95, (PB97-110886, MF-A01, A06).

NCEER-95-0019 "Optimal Polynomial Control for Linear and Nonlinear Structures," by A.K. Agrawal and J.N. Yang, 12/11/95, (PB96-168737, A07, MF-A02).

NCEER-95-0020 "Retrofit of Non-Ductile Reinforced Concrete Frames Using Friction Dampers," by R.S. Rao, P. Gergely and R.N. White, 12/22/95, (PB97-133508, A10, MF-A02).

NCEER-95-0021 "Parametric Results for Seismic Response of Pile-Supported Bridge Bents," by G. Mylonakis, A. Nikolaou and G. Gazetas, 12/22/95, (PB97-100242, A12, MF-A03).

NCEER-95-0022 "Kinematic Bending Moments in Seismically Stressed Piles," by A. Nikolaou, G. Mylonakis and G. Gazetas, 12/23/95, (PB97-113914, MF-A03, A13).

NCEER-96-0001 "Dynamic Response of Unreinforced Masonry Buildings with Flexible Diaphragms," by A.C. Costley and D.P. Abrams," 10/10/96, (PB97-133573, MF-A03, A15).

NCEER-96-0002 "State of the Art Review: Foundations and Retaining Structures," by I. Po Lam, to be published.

NCEER-96-0003 "Ductility of Rectangular Reinforced Concrete Bridge Columns with Moderate Confinement," by N. Wehbe, M. Saiidi, D. Sanders and B. Douglas, 11/7/96, (PB97-133557, A06, MF-A02).

NCEER-96-0004 "Proceedings of the Long-Span Bridge Seismic Research Workshop," edited by I.G. Buckle and I.M. Friedland, to be published.

NCEER-96-0005 "Establish Representative Pier Types for Comprehensive Study: Eastern United States," by J. Kulicki and Z. Prucz, 5/28/96, (PB98-119217, A07, MF-A02).

NCEER-96-0006 "Establish Representative Pier Types for Comprehensive Study: Western United States," by R. Imbsen, R.A. Schamber and T.A. Osterkamp, 5/28/96, (PB98-118607, A07, MF-A02).

NCEER-96-0007 "Nonlinear Control Techniques for Dynamical Systems with Uncertain Parameters," by R.G. Ghanem and M.I. Bujakov, 5/27/96, (PB97-100259, A17, MF-A03).

NCEER-96-0008 "Seismic Evaluation of a 30-Year Old Non-Ductile Highway Bridge Pier and Its Retrofit," by J.B. Mander, B. Mahmoodzadegan, S. Bhadra and S.S. Chen, 5/31/96, (PB97-110902, MF-A03, A10).

NCEER-96-0009 "Seismic Performance of a Model Reinforced Concrete Bridge Pier Before and After Retrofit," by J.B. Mander, J.H. Kim and C.A. Ligozio, 5/31/96, (PB97-110910, MF-A02, A10).

NCEER-96-0010 "IDARC2D Version 4.0: A Computer Program for the Inelastic Damage Analysis of Buildings," by R.E. Valles, A.M. Reinhorn, S.K. Kunnath, C. Li and A. Madan, 6/3/96, (PB97-100234, A17, MF-A03).

NCEER-96-0011 "Estimation of the Economic Impact of Multiple Lifeline Disruption: Memphis Light, Gas and Water Division Case Study," by S.E. Chang, H.A. Seligson and R.T. Eguchi, 8/16/96, (PB97-133490, A11, MF-A03).

NCEER-96-0012 "Proceedings from the Sixth Japan-U.S. Workshop on Earthquake Resistant Design of Lifeline Facilities and Countermeasures Against Soil Liquefaction, Edited by M. Hamada and T. O'Rourke, 9/11/96, (PB97-133581, A99, MF-A06).

NCEER-96-0013 "Chemical Hazards, Mitigation and Preparedness in Areas of High Seismic Risk: A Methodology for Estimating the Risk of Post-Earthquake Hazardous Materials Release," by H.A. Seligson, R.T. Eguchi, K.J. Tierney and K. Richmond, 11/7/96, (PB97-133565, MF-A02, A08).

NCEER-96-0014 "Response of Steel Bridge Bearings to Reversed Cyclic Loading," by J.B. Mander, D-K. Kim, S.S. Chen and G.J. Premus, 11/13/96, (PB97-140735, A12, MF-A03).

NCEER-96-0015 "Highway Culvert Performance During Past Earthquakes," by T.L. Youd and C.J. Beckman, 11/25/96, (PB97-133532, A06, MF-A01).

NCEER-97-0001 "Evaluation, Prevention and Mitigation of Pounding Effects in Building Structures," by R.E. Valles and A.M. Reinhorn, 2/20/97, (PB97-159552, A14, MF-A03).

NCEER-97-0002 "Seismic Design Criteria for Bridges and Other Highway Structures," by C. Rojahn, R. Mayes, D.G. Anderson, J. Clark, J.H. Hom, R.V. Nutt and M.J. O'Rourke, 4/30/97, (PB97-194658, A06, MF-A03).

NCEER-97-0003 “Proceedings of the U.S.-Italian Workshop on Seismic Evaluation and Retrofit,” Edited by D.P. Abrams and G.M. Calvi, 3/19/97, (PB97-194666, A13, MF-A03).

NCEER-97-0004 "Investigation of Seismic Response of Buildings with Linear and Nonlinear Fluid Viscous Dampers," by A.A. Seleemah and M.C. Constantinou, 5/21/97, (PB98-109002, A15, MF-A03).

NCEER-97-0005 "Proceedings of the Workshop on Earthquake Engineering Frontiers in Transportation Facilities," edited by G.C. Lee and I.M. Friedland, 8/29/97, (PB98-128911, A25, MR-A04).

NCEER-97-0006 "Cumulative Seismic Damage of Reinforced Concrete Bridge Piers," by S.K. Kunnath, A. El-Bahy, A. Taylor and W. Stone, 9/2/97, (PB98-108814, A11, MF-A03).

NCEER-97-0007 "Structural Details to Accommodate Seismic Movements of Highway Bridges and Retaining Walls," by R.A. Imbsen, R.A. Schamber, E. Thorkildsen, A. Kartoum, B.T. Martin, T.N. Rosser and J.M. Kulicki, 9/3/97, (PB98-108996, A09, MF-A02).

NCEER-97-0008 "A Method for Earthquake Motion-Damage Relationships with Application to Reinforced Concrete Frames," by A. Singhal and A.S. Kiremidjian, 9/10/97, (PB98-108988, A13, MF-A03).

NCEER-97-0009 "Seismic Analysis and Design of Bridge Abutments Considering Sliding and Rotation," by K. Fishman and R. Richards, Jr., 9/15/97, (PB98-108897, A06, MF-A02).

NCEER-97-0010 "Proceedings of the FHWA/NCEER Workshop on the National Representation of Seismic Ground Motion for New and Existing Highway Facilities," edited by I.M. Friedland, M.S. Power and R.L. Mayes, 9/22/97, (PB98-128903, A21, MF-A04).

NCEER-97-0011 "Seismic Analysis for Design or Retrofit of Gravity Bridge Abutments," by K.L. Fishman, R. Richards, Jr. and R.C. Divito, 10/2/97, (PB98-128937, A08, MF-A02).

NCEER-97-0012 "Evaluation of Simplified Methods of Analysis for Yielding Structures," by P. Tsopelas, M.C. Constantinou, C.A. Kircher and A.S. Whittaker, 10/31/97, (PB98-128929, A10, MF-A03).

NCEER-97-0013 "Seismic Design of Bridge Columns Based on Control and Repairability of Damage," by C-T. Cheng and J.B. Mander, 12/8/97, (PB98-144249, A11, MF-A03).

NCEER-97-0014 "Seismic Resistance of Bridge Piers Based on Damage Avoidance Design," by J.B. Mander and C-T. Cheng, 12/10/97, (PB98-144223, A09, MF-A02).

NCEER-97-0015 “Seismic Response of Nominally Symmetric Systems with Strength Uncertainty,” by S. Balopoulou and M. Grigoriu, 12/23/97, (PB98-153422, A11, MF-A03).

NCEER-97-0016 “Evaluation of Seismic Retrofit Methods for Reinforced Concrete Bridge Columns,” by T.J. Wipf, F.W. Klaiber and F.M. Russo, 12/28/97, (PB98-144215, A12, MF-A03).

NCEER-97-0017 “Seismic Fragility of Existing Conventional Reinforced Concrete Highway Bridges,” by C.L. Mullen and A.S. Cakmak, 12/30/97, (PB98-153406, A08, MF-A02).

NCEER-97-0018 “Loss Asssessment of Memphis Buildings,” edited by D.P. Abrams and M. Shinozuka, 12/31/97, (PB98-144231, A13, MF-A03).

NCEER-97-0019 “Seismic Evaluation of Frames with Infill Walls Using Quasi-static Experiments,” by K.M. Mosalam, R.N. White and P. Gergely, 12/31/97, (PB98-153455, A07, MF-A02).

NCEER-97-0020 “Seismic Evaluation of Frames with Infill Walls Using Pseudo-dynamic Experiments,” by K.M. Mosalam, R.N. White and P. Gergely, 12/31/97, (PB98-153430, A07, MF-A02).

NCEER-97-0021 “Computational Strategies for Frames with Infill Walls: Discrete and Smeared Crack Analyses and Seismic Fragility,” by K.M. Mosalam, R.N. White and P. Gergely, 12/31/97, (PB98-153414, A10, MF-A02).

NCEER-97-0022 "Proceedings of the NCEER Workshop on Evaluation of Liquefaction Resistance of Soils," edited by T.L. Youd and I.M. Idriss, 12/31/97, (PB98-155617, A15, MF-A03).

MCEER-98-0001 "Extraction of Nonlinear Hysteretic Properties of Seismically Isolated Bridges from Quick-Release Field Tests," by Q. Chen, B.M. Douglas, E.M. Maragakis and I.G. Buckle, 5/26/98, (PB99-118838, A06, MF-A01).

MCEER-98-0002 "Methodologies for Evaluating the Importance of Highway Bridges," by A. Thomas, S. Eshenaur and J. Kulicki, 5/29/98, (PB99-118846, A10, MF-A02).

MCEER-98-0003 "Capacity Design of Bridge Piers and the Analysis of Overstrength," by J.B. Mander, A. Dutta and P. Goel, 6/1/98, (PB99-118853, A09, MF-A02).

MCEER-98-0004 "Evaluation of Bridge Damage Data from the Loma Prieta and Northridge, California Earthquakes," by N. Basoz and A. Kiremidjian, 6/2/98, (PB99-118861, A15, MF-A03).

MCEER-98-0005 "Screening Guide for Rapid Assessment of Liquefaction Hazard at Highway Bridge Sites," by T. L. Youd, 6/16/98, (PB99-118879, A06, not available on microfiche).

MCEER-98-0006 "Structural Steel and Steel/Concrete Interface Details for Bridges," by P. Ritchie, N. Kauhl and J. Kulicki, 7/13/98, (PB99-118945, A06, MF-A01).

MCEER-98-0007 "Capacity Design and Fatigue Analysis of Confined Concrete Columns," by A. Dutta and J.B. Mander, 7/14/98, (PB99-118960, A14, MF-A03).

MCEER-98-0008 "Proceedings of the Workshop on Performance Criteria for Telecommunication Services Under Earthquake Conditions," edited by A.J. Schiff, 7/15/98, (PB99-118952, A08, MF-A02).

MCEER-98-0009 "Fatigue Analysis of Unconfined Concrete Columns," by J.B. Mander, A. Dutta and J.H. Kim, 9/12/98, (PB99-123655, A10, MF-A02).

MCEER-98-0010 "Centrifuge Modeling of Cyclic Lateral Response of Pile-Cap Systems and Seat-Type Abutments in Dry Sands," by A.D. Gadre and R. Dobry, 10/2/98, (PB99-123606, A13, MF-A03).

MCEER-98-0011 "IDARC-BRIDGE: A Computational Platform for Seismic Damage Assessment of Bridge Structures," by A.M. Reinhorn, V. Simeonov, G. Mylonakis and Y. Reichman, 10/2/98, (PB99-162919, A15, MF-A03).

MCEER-98-0012 "Experimental Investigation of the Dynamic Response of Two Bridges Before and After Retrofitting with Elastomeric Bearings," by D.A. Wendichansky, S.S. Chen and J.B. Mander, 10/2/98, (PB99-162927, A15, MF-A03).

MCEER-98-0013 "Design Procedures for Hinge Restrainers and Hinge Sear Width for Multiple-Frame Bridges," by R. Des Roches and G.L. Fenves, 11/3/98, (PB99-140477, A13, MF-A03).

MCEER-98-0014 "Response Modification Factors for Seismically Isolated Bridges," by M.C. Constantinou and J.K. Quarshie, 11/3/98, (PB99-140485, A14, MF-A03).

MCEER-98-0015 "Proceedings of the U.S.-Italy Workshop on Seismic Protective Systems for Bridges," edited by I.M. Friedland and M.C. Constantinou, 11/3/98, (PB2000-101711, A22, MF-A04).

MCEER-98-0016 "Appropriate Seismic Reliability for Critical Equipment Systems: Recommendations Based on Regional Analysis of Financial and Life Loss," by K. Porter, C. Scawthorn, C. Taylor and N. Blais, 11/10/98, (PB99-157265, A08, MF-A02).

MCEER-98-0017 "Proceedings of the U.S. Japan Joint Seminar on Civil Infrastructure Systems Research," edited by M. Shinozuka and A. Rose, 11/12/98, (PB99-156713, A16, MF-A03).

MCEER-98-0018 "Modeling of Pile Footings and Drilled Shafts for Seismic Design," by I. PoLam, M. Kapuskar and D. Chaudhuri, 12/21/98, (PB99-157257, A09, MF-A02).

MCEER-99-0001 "Seismic Evaluation of a Masonry Infilled Reinforced Concrete Frame by Pseudodynamic Testing," by S.G. Buonopane and R.N. White, 2/16/99, (PB99-162851, A09, MF-A02).

MCEER-99-0002 "Response History Analysis of Structures with Seismic Isolation and Energy Dissipation Systems: Verification Examples for Program SAP2000," by J. Scheller and M.C. Constantinou, 2/22/99, (PB99-162869, A08, MF-A02).

MCEER-99-0003 "Experimental Study on the Seismic Design and Retrofit of Bridge Columns Including Axial Load Effects," by A. Dutta, T. Kokorina and J.B. Mander, 2/22/99, (PB99-162877, A09, MF-A02).

MCEER-99-0004 "Experimental Study of Bridge Elastomeric and Other Isolation and Energy Dissipation Systems with Emphasis on Uplift Prevention and High Velocity Near-source Seismic Excitation," by A. Kasalanati and M. C. Constantinou, 2/26/99, (PB99-162885, A12, MF-A03).

MCEER-99-0005 "Truss Modeling of Reinforced Concrete Shear-flexure Behavior," by J.H. Kim and J.B. Mander, 3/8/99, (PB99-163693, A12, MF-A03).

MCEER-99-0006 "Experimental Investigation and Computational Modeling of Seismic Response of a 1:4 Scale Model Steel Structure with a Load Balancing Supplemental Damping System," by G. Pekcan, J.B. Mander and S.S. Chen, 4/2/99, (PB99-162893, A11, MF-A03).

MCEER-99-0007 "Effect of Vertical Ground Motions on the Structural Response of Highway Bridges," by M.R. Button, C.J. Cronin and R.L. Mayes, 4/10/99, (PB2000-101411, A10, MF-A03).

MCEER-99-0008 "Seismic Reliability Assessment of Critical Facilities: A Handbook, Supporting Documentation, and Model Code Provisions," by G.S. Johnson, R.E. Sheppard, M.D. Quilici, S.J. Eder and C.R. Scawthorn, 4/12/99, (PB2000-101701, A18, MF-A04).

MCEER-99-0009 "Impact Assessment of Selected MCEER Highway Project Research on the Seismic Design of Highway Structures," by C. Rojahn, R. Mayes, D.G. Anderson, J.H. Clark, D'Appolonia Engineering, S. Gloyd and R.V. Nutt, 4/14/99, (PB99-162901, A10, MF-A02).

MCEER-99-0010 "Site Factors and Site Categories in Seismic Codes," by R. Dobry, R. Ramos and M.S. Power, 7/19/99, (PB2000-101705, A08, MF-A02).

MCEER-99-0011 "Restrainer Design Procedures for Multi-Span Simply-Supported Bridges," by M.J. Randall, M. Saiidi, E. Maragakis and T. Isakovic, 7/20/99, (PB2000-101702, A10, MF-A02).

MCEER-99-0012 "Property Modification Factors for Seismic Isolation Bearings," by M.C. Constantinou, P. Tsopelas, A. Kasalanati and E. Wolff, 7/20/99, (PB2000-103387, A11, MF-A03).

MCEER-99-0013 "Critical Seismic Issues for Existing Steel Bridges," by P. Ritchie, N. Kauhl and J. Kulicki, 7/20/99, (PB2000-101697, A09, MF-A02).

MCEER-99-0014 "Nonstructural Damage Database," by A. Kao, T.T. Soong and A. Vender, 7/24/99, (PB2000-101407, A06, MF-A01).

MCEER-99-0015 "Guide to Remedial Measures for Liquefaction Mitigation at Existing Highway Bridge Sites," by H.G. Cooke and J. K. Mitchell, 7/26/99, (PB2000-101703, A11, MF-A03).

MCEER-99-0016 "Proceedings of the MCEER Workshop on Ground Motion Methodologies for the Eastern United States," edited by N. Abrahamson and A. Becker, 8/11/99, (PB2000-103385, A07, MF-A02).

MCEER-99-0017 "Quindío, Colombia Earthquake of January 25, 1999: Reconnaissance Report," by A.P. Asfura and P.J. Flores, 10/4/99, (PB2000-106893, A06, MF-A01).

MCEER-99-0018 "Hysteretic Models for Cyclic Behavior of Deteriorating Inelastic Structures," by M.V. Sivaselvan and A.M. Reinhorn, 11/5/99, (PB2000-103386, A08, MF-A02).

MCEER-99-0019 "Proceedings of the 7th U.S.- Japan Workshop on Earthquake Resistant Design of Lifeline Facilities and Countermeasures Against Soil Liquefaction," edited by T.D. O'Rourke, J.P. Bardet and M. Hamada, 11/19/99, (PB2000-103354, A99, MF-A06).

MCEER-99-0020 "Development of Measurement Capability for Micro-Vibration Evaluations with Application to Chip Fabrication Facilities," by G.C. Lee, Z. Liang, J.W. Song, J.D. Shen and W.C. Liu, 12/1/99, (PB2000-105993, A08, MF-A02).

MCEER-99-0021 "Design and Retrofit Methodology for Building Structures with Supplemental Energy Dissipating Systems," by G. Pekcan, J.B. Mander and S.S. Chen, 12/31/99, (PB2000-105994, A11, MF-A03).

MCEER-00-0001 "The Marmara, Turkey Earthquake of August 17, 1999: Reconnaissance Report," edited by C. Scawthorn; with major contributions by M. Bruneau, R. Eguchi, T. Holzer, G. Johnson, J. Mander, J. Mitchell, W. Mitchell, A. Papageorgiou, C. Scaethorn, and G. Webb, 3/23/00, (PB2000-106200, A11, MF-A03).

MCEER-00-0002 "Proceedings of the MCEER Workshop for Seismic Hazard Mitigation of Health Care Facilities," edited by G.C. Lee, M. Ettouney, M. Grigoriu, J. Hauer and J. Nigg, 3/29/00, (PB2000-106892, A08, MF-A02).

MCEER-00-0003 "The Chi-Chi, Taiwan Earthquake of September 21, 1999: Reconnaissance Report," edited by G.C. Lee and C.H. Loh, with major contributions by G.C. Lee, M. Bruneau, I.G. Buckle, S.E. Chang, P.J. Flores, T.D. O'Rourke, M. Shinozuka, T.T. Soong, C-H. Loh, K-C. Chang, Z-J. Chen, J-S. Hwang, M-L. Lin, G-Y. Liu, K-C. Tsai, G.C. Yao and C-L. Yen, 4/30/00, (PB2001-100980, A10, MF-A02).

MCEER-00-0004 "Seismic Retrofit of End-Sway Frames of Steel Deck-Truss Bridges with a Supplemental Tendon System: Experimental and Analytical Investigation," by G. Pekcan, J.B. Mander and S.S. Chen, 7/1/00, (PB2001-100982, A10, MF-A02).

MCEER-00-0005 "Sliding Fragility of Unrestrained Equipment in Critical Facilities," by W.H. Chong and T.T. Soong, 7/5/00, (PB2001-100983, A08, MF-A02).

MCEER-00-0006 "Seismic Response of Reinforced Concrete Bridge Pier Walls in the Weak Direction," by N. Abo-Shadi, M. Saiidi and D. Sanders, 7/17/00, (PB2001-100981, A17, MF-A03).

MCEER-00-0007 "Low-Cycle Fatigue Behavior of Longitudinal Reinforcement in Reinforced Concrete Bridge Columns," by J. Brown and S.K. Kunnath, 7/23/00, (PB2001-104392, A08, MF-A02).

MCEER-00-0008 "Soil Structure Interaction of Bridges for Seismic Analysis," I. PoLam and H. Law, 9/25/00, (PB2001-105397, A08, MF-A02).

MCEER-00-0009 "Proceedings of the First MCEER Workshop on Mitigation of Earthquake Disaster by Advanced Technologies (MEDAT-1), edited by M. Shinozuka, D.J. Inman and T.D. O'Rourke, 11/10/00, (PB2001-105399, A14, MF-A03).

MCEER-00-0010 "Development and Evaluation of Simplified Procedures for Analysis and Design of Buildings with Passive Energy Dissipation Systems," by O.M. Ramirez, M.C. Constantinou, C.A. Kircher, A.S. Whittaker, M.W. Johnson, J.D. Gomez and C. Chrysostomou, 11/16/01, (PB2001-105523, A23, MF-A04).

MCEER-00-0011 "Dynamic Soil-Foundation-Structure Interaction Analyses of Large Caissons," by C-Y. Chang, C-M. Mok, Z-L. Wang, R. Settgast, F. Waggoner, M.A. Ketchum, H.M. Gonnermann and C-C. Chin, 12/30/00, (PB2001-104373, A07, MF-A02).

MCEER-00-0012 "Experimental Evaluation of Seismic Performance of Bridge Restrainers," by A.G. Vlassis, E.M. Maragakis and M. Saiid Saiidi, 12/30/00, (PB2001-104354, A09, MF-A02).

MCEER-00-0013 "Effect of Spatial Variation of Ground Motion on Highway Structures," by M. Shinozuka, V. Saxena and G. Deodatis, 12/31/00, (PB2001-108755, A13, MF-A03).

MCEER-00-0014 "A Risk-Based Methodology for Assessing the Seismic Performance of Highway Systems," by S.D. Werner, C.E. Taylor, J.E. Moore, II, J.S. Walton and S. Cho, 12/31/00, (PB2001-108756, A14, MF-A03).

MCEER-01-0001 "Experimental Investigation of P-Delta Effects to Collapse During Earthquakes," by D. Vian and M. Bruneau, 6/25/01, (PB2002-100534, A17, MF-A03).

MCEER-01-0002 "Proceedings of the Second MCEER Workshop on Mitigation of Earthquake Disaster by Advanced Technologies (MEDAT-2)," edited by M. Bruneau and D.J. Inman, 7/23/01, (PB2002-100434, A16, MF-A03).

MCEER-01-0003 "Sensitivity Analysis of Dynamic Systems Subjected to Seismic Loads," by C. Roth and M. Grigoriu, 9/18/01, (PB2003-100884, A12, MF-A03).

MCEER-01-0004 "Overcoming Obstacles to Implementing Earthquake Hazard Mitigation Policies: Stage 1 Report," by D.J. Alesch and W.J. Petak, 12/17/01, (PB2002-107949, A07, MF-A02).

MCEER-01-0005 "Updating Real-Time Earthquake Loss Estimates: Methods, Problems and Insights," by C.E. Taylor, S.E. Chang and R.T. Eguchi, 12/17/01, (PB2002-107948, A05, MF-A01).

MCEER-01-0006 "Experimental Investigation and Retrofit of Steel Pile Foundations and Pile Bents Under Cyclic Lateral Loadings," by A. Shama, J. Mander, B. Blabac and S. Chen, 12/31/01, (PB2002-107950, A13, MF-A03).

MCEER-02-0001 "Assessment of Performance of Bolu Viaduct in the 1999 Duzce Earthquake in Turkey" by P.C. Roussis, M.C. Constantinou, M. Erdik, E. Durukal and M. Dicleli, 5/8/02, (PB2003-100883, A08, MF-A02).

MCEER-02-0002 "Seismic Behavior of Rail Counterweight Systems of Elevators in Buildings," by M.P. Singh, Rildova and L.E. Suarez, 5/27/02. (PB2003-100882, A11, MF-A03).

MCEER-02-0003 "Development of Analysis and Design Procedures for Spread Footings," by G. Mylonakis, G. Gazetas, S. Nikolaou and A. Chauncey, 10/02/02, (PB2004-101636, A13, MF-A03, CD-A13).

MCEER-02-0004 "Bare-Earth Algorithms for Use with SAR and LIDAR Digital Elevation Models," by C.K. Huyck, R.T. Eguchi and B. Houshmand, 10/16/02, (PB2004-101637, A07, CD-A07).

MCEER-02-0005 "Review of Energy Dissipation of Compression Members in Concentrically Braced Frames," by K.Lee and M. Bruneau, 10/18/02, (PB2004-101638, A10, CD-A10).

MCEER-03-0001 "Experimental Investigation of Light-Gauge Steel Plate Shear Walls for the Seismic Retrofit of Buildings" by J. Berman and M. Bruneau, 5/2/03, (PB2004-101622, A10, MF-A03, CD-A10).

MCEER-03-0002 "Statistical Analysis of Fragility Curves," by M. Shinozuka, M.Q. Feng, H. Kim, T. Uzawa and T. Ueda, 6/16/03, (PB2004-101849, A09, CD-A09).

MCEER-03-0003 "Proceedings of the Eighth U.S.-Japan Workshop on Earthquake Resistant Design f Lifeline Facilities and Countermeasures Against Liquefaction," edited by M. Hamada, J.P. Bardet and T.D. O'Rourke, 6/30/03, (PB2004-104386, A99, CD-A99).

MCEER-03-0004 "Proceedings of the PRC-US Workshop on Seismic Analysis and Design of Special Bridges," edited by L.C. Fan and G.C. Lee, 7/15/03, (PB2004-104387, A14, CD-A14).

MCEER-03-0005 "Urban Disaster Recovery: A Framework and Simulation Model," by S.B. Miles and S.E. Chang, 7/25/03, (PB2004-104388, A07, CD-A07).

MCEER-03-0006 "Behavior of Underground Piping Joints Due to Static and Dynamic Loading," by R.D. Meis, M. Maragakis and R. Siddharthan, 11/17/03, (PB2005-102194, A13, MF-A03, CD-A00).

MCEER-03-0007 "Seismic Vulnerability of Timber Bridges and Timber Substructures," by A.A. Shama, J.B. Mander, I.M. Friedland and D.R. Allicock, 12/15/03.

MCEER-04-0001 "Experimental Study of Seismic Isolation Systems with Emphasis on Secondary System Response and Verification of Accuracy of Dynamic Response History Analysis Methods," by E. Wolff and M. Constantinou, 1/16/04 (PB2005-102195, A99, MF-E08, CD-A00).

MCEER-04-0002 "Tension, Compression and Cyclic Testing of Engineered Cementitious Composite Materials," by K. Kesner and S.L. Billington, 3/1/04, (PB2005-102196, A08, CD-A08).

MCEER-04-0003 "Cyclic Testing of Braces Laterally Restrained by Steel Studs to Enhance Performance During Earthquakes," by O.C. Celik, J.W. Berman and M. Bruneau, 3/16/04, (PB2005-102197, A13, MF-A03, CD-A00).

MCEER-04-0004 "Methodologies for Post Earthquake Building Damage Detection Using SAR and Optical Remote Sensing: Application to the August 17, 1999 Marmara, Turkey Earthquake," by C.K. Huyck, B.J. Adams, S. Cho, R.T. Eguchi, B. Mansouri and B. Houshmand, 6/15/04, (PB2005-104888, A10, CD-A00).

MCEER-04-0005 "Nonlinear Structural Analysis Towards Collapse Simulation: A Dynamical Systems Approach," by M.V. Sivaselvan and A.M. Reinhorn, 6/16/04, (PB2005-104889, A11, MF-A03, CD-A00).

MCEER-04-0006 "Proceedings of the Second PRC-US Workshop on Seismic Analysis and Design of Special Bridges," edited by G.C. Lee and L.C. Fan, 6/25/04, (PB2005-104890, A16, CD-A00).

MCEER-04-0007 "Seismic Vulnerability Evaluation of Axially Loaded Steel Built-up Laced Members," by K. Lee and M. Bruneau, 6/30/04, (PB2005-104891, A16, CD-A00).

MCEER-04-0008 "Evaluation of Accuracy of Simplified Methods of Analysis and Design of Buildings with Damping Systems for Near-Fault and for Soft-Soil Seismic Motions," by E.A. Pavlou and M.C. Constantinou, 8/16/04, (PB2005-104892, A08, MF-A02, CD-A00).

MCEER-04-0009 "Assessment of Geotechnical Issues in Acute Care Facilities in California," by M. Lew, T.D. O'Rourke, R. Dobry and M. Koch, 9/15/04, (PB2005-104893, A08, CD-A00).

MCEER-04-0010 "Scissor-Jack-Damper Energy Dissipation System," by A.N. Sigaher-Boyle and M.C. Constantinou, 12/1/04 (PB2005-108221).

MCEER-04-0011 "Seismic Retrofit of Bridge Steel Truss Piers Using a Controlled Rocking Approach," by M. Pollino and M. Bruneau, 12/20/04 (PB2006-105795).

MCEER-05-0001 "Experimental and Analytical Studies of Structures Seismically Isolated with an Uplift-Restraint Isolation System," by P.C. Roussis and M.C. Constantinou, 1/10/05 (PB2005-108222).

MCEER-05-0002 "A Versatile Experimentation Model for Study of Structures Near Collapse Applied to Seismic Evaluation of Irregular Structures," by D. Kusumastuti, A.M. Reinhorn and A. Rutenberg, 3/31/05 (PB2006-101523).

MCEER-05-0003 "Proceedings of the Third PRC-US Workshop on Seismic Analysis and Design of Special Bridges," edited by L.C. Fan and G.C. Lee, 4/20/05, (PB2006-105796).

MCEER-05-0004 "Approaches for the Seismic Retrofit of Braced Steel Bridge Piers and Proof-of-Concept Testing of an Eccentrically Braced Frame with Tubular Link," by J.W. Berman and M. Bruneau, 4/21/05 (PB2006-101524).

MCEER-05-0005 "Simulation of Strong Ground Motions for Seismic Fragility Evaluation of Nonstructural Components in Hospitals," by A. Wanitkorkul and A. Filiatrault, 5/26/05 (PB2006-500027).

MCEER-05-0006 "Seismic Safety in California Hospitals: Assessing an Attempt to Accelerate the Replacement or Seismic Retrofit of Older Hospital Facilities," by D.J. Alesch, L.A. Arendt and W.J. Petak, 6/6/05 (PB2006-105794).

MCEER-05-0007 "Development of Seismic Strengthening and Retrofit Strategies for Critical Facilities Using Engineered Cementitious Composite Materials," by K. Kesner and S.L. Billington, 8/29/05 (PB2006-111701).

MCEER-05-0008 "Experimental and Analytical Studies of Base Isolation Systems for Seismic Protection of Power Transformers," by N. Murota, M.Q. Feng and G-Y. Liu, 9/30/05 (PB2006-111702).

MCEER-05-0009 "3D-BASIS-ME-MB: Computer Program for Nonlinear Dynamic Analysis of Seismically Isolated Structures," by P.C. Tsopelas, P.C. Roussis, M.C. Constantinou, R. Buchanan and A.M. Reinhorn, 10/3/05 (PB2006-111703).

MCEER-05-0010 "Steel Plate Shear Walls for Seismic Design and Retrofit of Building Structures," by D. Vian and M. Bruneau, 12/15/05 (PB2006-111704).

MCEER-05-0011 "The Performance-Based Design Paradigm," by M.J. Astrella and A. Whittaker, 12/15/05 (PB2006-111705).

MCEER-06-0001 "Seismic Fragility of Suspended Ceiling Systems," H. Badillo-Almaraz, A.S. Whittaker, A.M. Reinhorn and G.P. Cimellaro, 2/4/06 (PB2006-111706).

MCEER-06-0002 "Multi-Dimensional Fragility of Structures," by G.P. Cimellaro, A.M. Reinhorn and M. Bruneau, 3/1/06 (PB2007-106974, A09, MF-A02, CD A00).

MCEER-06-0003 "Built-Up Shear Links as Energy Dissipators for Seismic Protection of Bridges," by P. Dusicka, A.M. Itani and I.G. Buckle, 3/15/06 (PB2006-111708).

MCEER-06-0004 "Analytical Investigation of the Structural Fuse Concept," by R.E. Vargas and M. Bruneau, 3/16/06 (PB2006-111709).

MCEER-06-0005 "Experimental Investigation of the Structural Fuse Concept," by R.E. Vargas and M. Bruneau, 3/17/06 (PB2006-111710).

MCEER-06-0006 "Further Development of Tubular Eccentrically Braced Frame Links for the Seismic Retrofit of Braced Steel Truss Bridge Piers," by J.W. Berman and M. Bruneau, 3/27/06 (PB2007-105147).

MCEER-06-0007 "REDARS Validation Report," by S. Cho, C.K. Huyck, S. Ghosh and R.T. Eguchi, 8/8/06 (PB2007-106983).

MCEER-06-0008 "Review of Current NDE Technologies for Post-Earthquake Assessment of Retrofitted Bridge Columns," by J.W. Song, Z. Liang and G.C. Lee, 8/21/06 06 (PB2007-106984).

MCEER-06-0009 "Liquefaction Remediation in Silty Soils Using Dynamic Compaction and Stone Columns," by S. Thevanayagam, G.R. Martin, R. Nashed, T. Shenthan, T. Kanagalingam and N. Ecemis, 8/28/06 06 (PB2007-106985).

MCEER-06-0010 "Conceptual Design and Experimental Investigation of Polymer Matrix Composite Infill Panels for Seismic Retrofitting," by W. Jung, M. Chiewanichakorn and A.J. Aref, 9/21/06 (PB2007-106986).

MCEER-06-0011 "A Study of the Coupled Horizontal-Vertical Behavior of Elastomeric and Lead-Rubber Seismic Isolation Bearings," by G.P. Warn and A.S. Whittaker, 9/22/06 (PB2007-108679).

MCEER-06-0012 "Proceedings of the Fourth PRC-US Workshop on Seismic Analysis and Design of Special Bridges: Advancing Bridge Technologies in Research, Design, Construction and Preservation," Edited by L.C. Fan, G.C. Lee and L. Ziang, 10/12/06.

MCEER-06-0013 "Cyclic Response and Low Cycle Fatigue Characteristics of Plate Steels," by P. Dusicka, A.M. Itani and I.G. Buckle, 11/1/06 06 (PB2007-106987).

MCEER-06-0014 "Proceedings of the Second US-Taiwan Bridge Engineering Workshop," edited by W.P. Yen, J. Shen, J-Y. Chen and M. Wang, 11/15/06.

MCEER-06-0015 "User Manual and Technical Documentation for the REDARS™ Import Wizard," by S. Cho, S. Ghosh, C.K. Huyck and S.D. Werner, 11/30/06.

MCEER-06-0016 "Hazard Mitigation Strategy and Monitoring Technologies for Urban and Infrastructure Public Buildings: Proceedings of the China-US Workshops," edited by X.Y. Zhou, A.L. Zhang, G.C. Lee and M. Tong, 12/12/06.

MCEER-07-0001 "Static and Kinetic Coefficients of Friction for Rigid Blocks," by C. Kafali, S. Fathali, M. Grigoriu and A.S. Whittaker, 3/20/07.

MCEER-07-0002 "Hazard Mitigation Investment Decision Making: Organizational Response to Legislative Mandate," by L.A. Arendt, D.J. Alesch and W.J. Petak, 4/9/07.

MCEER-07-0003 "Seismic Behavior of Bidirectional-Resistant Ductile End Diaphragms with Unbonded Braces in Straight or Skewed Steel Bridges," by O. Celik and M. Bruneau, 4/11/07.

MCEER-07-0004 "Modeling Pile Behavior in Large Pile Groups Under Lateral Loading," by A.M. Dodds and G.R. Martin, 4/16/07.

MCEER-07-0005 "Experimental Investigation of Blast Performance of Seismically Resistant Concrete-Filled Steel Tube Bridge Piers," by S. Fujikura, M. Bruneau and D. Lopez-Garcia, 4/20/07.

MCEER-07-0006 "Seismic Analysis of Conventional and Isolated Liquefied Natural Gas Tanks Using Mechanical Analogs," by I.P. Christovasilis and A.S. Whittaker, 5/1/07.

MCEER-07-0007 "Experimental Seismic Performance Evaluation of Isolation/Restraint Systems for Mechanical Equipment – Part 1: Heavy Equipment Study," by S. Fathali and A. Filiatrault, 6/6/07.

MCEER-07-0008 "Seismic Vulnerability of Timber Bridges and Timber Substructures," by A.A. Sharma, J.B. Mander, I.M. Friedland and D.R. Allicock, 6/7/07.

MCEER-07-0009 "Experimental and Analytical Study of the XY-Friction Pendulum (XY-FP) Bearing for Bridge Applications," by C.C. Marin-Artieda, A.S. Whittaker and M.C. Constantinou, 6/7/07.

MCEER-07-0010 "Proceedings of the PRC-US Earthquake Engineering Forum for Young Researchers," Edited by G.C. Lee and X.Z. Qi, 6/8/07.

MCEER-07-0011 "Design Recommendations for Perforated Steel Plate Shear Walls," by R. Purba and M. Bruneau, 6/18/07.

MCEER
EARTHQUAKE ENGINEERING TO EXTREME EVENTS
University at Buffalo, The State University of New York
Red Jacket Quadrangle ▪ Buffalo, New York 14261
Phone: (716) 645-3391 ▪ Fax: (716) 645-3399
E-mail: *mceer@buffalo.edu* ▪ WWW Site *http://mceer.buffalo.edu*
University at Buffalo *The State University of New York*

ISSN 1520-295X